https://ntrs.nasa.gov/search.jsp?R=19860007754 2020-03-20T16:14:55+00:00Z

DOE/NASA/0305–1
NASA CR–174943

Long-Term Stability and Properties of Zirconia Ceramics for Heavy Duty Diesel Engine Components

N86-17224

(NASA-CR-174943) LONG-TERM STABILITY AND PROPERTIES OF ZIRCONIA CERAMICS FOR HEAVY DUTY DIESEL ENGINE COMPONENTS Final Report (IIT Research Inst.) 263 p HC A12/MF A01 CSCL 13F G3/85

Unclas 05173

David C. Larsen and Jane W. Adams
IIT Research Institute

JAN 1986
RECEIVED
NASA STI FACILITY
ACCESS DEPT.

September 1985

Prepared for
NATIONAL AERONAUTICS AND SPACE ADMINISTRATION
Lewis Research Center
Cleveland, Ohio
Under Contract DEN 3-305

for
U.S. DEPARTMENT OF ENERGY
Conservation and Renewable Energy
Office of Vehicle and Engine R&D

DOE/NASA/0305–1
NASA CR–174943

Long-Term Stability and Properties of Zirconia Ceramics for Heavy Duty Diesel Engine Components

David C. Larsen and Jane W. Adams
IIT Research Institute
Materials and Processing Technology
Nonmetallic Materials and Composites
Chicago, Illinois 60616

September 1985

Prepared for
NATIONAL AERONAUTICS AND SPACE ADMINISTRATION
Lewis Research Center
Cleveland, Ohio 44135
Under Contract DEN 3-305

for
U.S. DEPARTMENT OF ENERGY
Conservation and Renewable Energy
Office of Vehicle and Engine R&D
Washington, D.C. 20585
Under Interagency Agreement DE-AI01-80CS50194

1. Report No.	2. Government Accession No.	3. Recipient's Catalog No.
NASA CR-174943		

4. Title and Subtitle	5. Report Date
Long-Term Stability and Properties of Zirconia Ceramics for Heavy Duty Diesel Engine Components	September 1985
	6. Performing Organization Code

7. Author(s)	8. Performing Organization Report No.
David C. Larsen and Jane W. Adams	
	10. Work Unit No.

9. Performing Organization Name and Address	11. Contract or Grant No.
IIT Research Institute 10 West 35 Street Chicago, Illinois 60616	DEN3-305
	13. Type of Report and Period Covered
	Contractor Report
12. Sponsoring Agency Name and Address U.S. Department of Energy Office of Vehicle and Engine R&D Washington, D.C. 20585	14. Sponsoring Agency Code Report No. DOE/NASA/0305-1

15. Supplementary Notes

Final Report. Performed under Interagency Agreement DE-AI01-80CS50194. Project Manager, James C. Wood, Transportation Propulsion Division, NASA-Lewis Research Center, Cleveland, Ohio 44135.

16. Abstract

Physical, mechanical, and thermal properties of commercially available transformation-toughened zirconia were measured. Behavior was related to the material microstructure and phase assemblage. The stability of the materials was assessed after long-term exposure appropriate for diesel engine application. Properties measured included flexure strength, elastic modulus, fracture toughness, creep, thermal shock, thermal expansion, internal friction, and thermal diffusivity. Stability was assessed by measuring the residual property after 1000 hr/1000°C static exposure. Additionally static fatigue and thermal fatigue testing was performed.

Both yttria-stabilized and magnesia-stabilized materials were compared and contrasted. The major limitations of these materials are short term loss of properties with increasing temperature as the metastable tetragonal phase becomes more stable. Fine grain yttria-stabilized material (TZP) is higher strength and has a more stable microstructure with respect to overaging phenomena. The long-term limitation of Y-TZP is excessive creep deformation. Magnesia-stabilized PSZ has relatively poor stability at elevated temperature. Overaging, decomposition, and/or destabilization effects were observed. The major limitation of Mg-PSZ is controlling unwanted phase changes at elevated temperature.

To utilize the benefits of transformation-toughened zirconia that derive from its high strength, high toughness, and high Weibull modulus, the material must be limited to relatively low temperature applications.

17. Key Words (Suggested by Author(s))	18. Distribution Statement
Ceramics Diesel engine Zirconia Transformation-toughened Mechanical properties Thermal properties	Unclassified-unlimited STAR Category 85

19. Security Classif. (of this report)	20. Security Classif. (of this page)	21. No. of pages	22. Price*
Unclassified	Unclassified	258	

*For sale by the National Technical Information Service, Springfield, Virginia 22161

PRECEDING PAGE BLANK NOT FILMED

FOREWORD

The purpose of this program, "Long-Term Stability and Properties of Zirconia Ceramics for Heavy Duty Diesel Engine Components," Contract DEN3-305, was to: (a) characterize the pertinent physical, mechanical, and thermal properties of available technical grade transformation-toughened zirconia; (b) relate the properties to the material microstructure and phase assemblage; (c) assess the stability of the materials after long-term static exposure at high temperature; and (d) assess the ability of foreign and domestic suppliers to produce component shapes suitable for structural application in a heavy-duty diesel engine.

The authors acknowledge the support of the DOE, Mr. Ed Gregory, Office of Vehicle and Engine Research and Development, and the NASA-Lewis Program Manager, Mr. James C. Wood (formerly Mr. Richard Lancashire and Mr. Harry Davison), Vehicular Gas Turbine and Diesel Project Office, Energy Technology Division.

Thanks are due Coors Porcelain Company for contributing test samples to this program. The principal contact at Coors was Dr. Brian Seegmiller. The cooperation of the other material vendors is also appreciated. They were Mr. Rudy Vallee of Nilsen, Messrs. Ken Umehara and Keith Matsuhiro of NGK, and Dr. Dieter Fingerle of Feldmuhle.

The authors are grateful for the helpful discussions and active collaboration with several people within the ceramics community on various aspects of transformation-toughened zirconia. Special mention is made of Dr. Lise Schioler of AMMRC, Dr. Robert Ruh of AFWAL, Dr. Paul Becher of ONRL, Dr. Robert Ingel of NRL, and Dr. Brian Lawn of NBS. Additionally, Dr. Jim Patten and Mr. Tom Yonushonis of Cummins Engine provided valuable insight from the designer's standpoint.

PRECEDING PAGE BLANK NOT FILMED

PAGE IV INTENTIONALLY BLANK

This is the final report on this contract. It is designated internally as IITRI-M06117-22, and covers work performed over the January 1983-December 1984 time period. The experimental assistance of G. T. Jeka and J. Graf-Teterycz is gratefully acknowledged. Additionally, the authors are indebted to H. Buhay and J. L. Grieser for platinum coating of thermal diffusivity samples.

Respectfully submitted,

IIT RESEARCH INSTITUTE

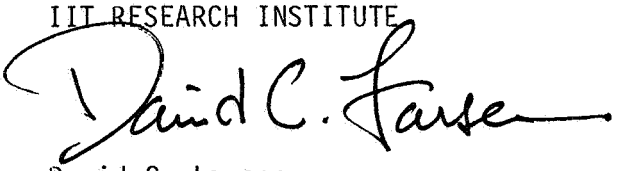

David C. Larsen
Senior Research Engineer

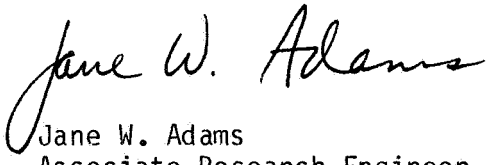

Jane W. Adams
Associate Research Engineer
Nonmetallic Materials and Composites
Materials and Processing Technology

APPROVED:

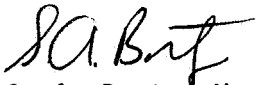

S. A. Bortz, Manager
Nonmetallic Materials and Composites

TABLE OF CONTENTS

LIST OF FIGURES

PAGE VIII INTENTIONALLY BLANK

PRECEDING PAGE BLANK NOT FILMED

LIST OF FIGURES (cont.)

LIST OF FIGURES (cont.)

LIST OF FIGURES (cont.)

LIST OF FIGURES (cont.)

LIST OF FIGURES (cont.)

LIST OF FIGURES (cont.)

LIST OF TABLES

PAGE XVI INTENTIONALLY BLANK

PRECEDING PAGE BLANK NOT FILMED

LIST OF TABLES (cont.)

SUMMARY

The purpose of this work was to (a) characterize the pertinent physical, mechanical, and thermal properties of technical grade transformation-toughened zirconia, (b) relate the properties to the material microstructure and phase assemblage, and (c) assess the stability of the materials after a long-term static exposure at high temperature that is appropriate for diesel engine application.

The materials investigated were NGK Z-191 Y-TZP, Nilsen MS and TS Mg-PSZ, Feldmuhle ZN-40 Mg-PSZ, and Coors Mg-PSZ. Properties measured from 25° to 1000°C included flexure strength, elastic modulus, fracture toughness, creep, thermal shock, thermal expansion, internal friction, and thermal diffusivity. Stability was assessed by measuring the residual property after 1000 hr/1000°C static air exposure. Additionally, static fatigue (stress-rupture) and thermal fatigue testing was performed.

Unique X-ray diffraction and etched reflected light microscopy capabilities were necessary to separate and distinguish the three co-existing crystal phases in these transformation-toughened zirconia (TTZ) materials. The MgO-stabilized materials were found to consist of mainly large (50-100 μm) cubic grains, within which the metstable tetragonal phase is an intragranular precipitate dispersion. X-ray diffraction indicated a composition consisting of nominally and typically 58% cubic, 37% tetragonal, and 5% monoclinic. The Y_2O_3-stabilized material consisted of nominally fully tetragonal polycrystals of average size in the range 1-5 μm (i.e., single-phase fine grain tetragonal).

The fast fracture 4-point bend strength was measured at 25°, 500°, 750°, and 1000°C. The fine-grain NGK Y-TZP has the highest strength (~130 ksi). The room-temperature Weibull moduli are relatively high for structural ceramics (m ~20). This illustrates the greater allowable defect size as the fracture toughness is increased. The predominant fracture origins for all four ZrO_2 materials in this study were large pores and pore agglomerates. It is significant to notice that the flexural strength of all materials decreased

linearly with temperature (50-70% strength reduction at 1000°C). This can be interpreted in terms of increased stability of the metastable tetragonal phase with increasing temperature. This is not to be confused with the related mechanism of overaging, or primary tetragonal-to-monoclinic ($t \rightarrow m$) transformation (and resultant loss of properties) upon extended elevated temperature exposure. This was also investigated on this program. The residual room-temperature bend strength after 1000 hr/1000°C exposure was measured. Y-TZP is much more stable with respect to the overaging phenomenon. In the current tests, only 7% of the strength was lost for Y-TZP after 1000 hr/1000°C exposure. The Mg-PSZ materials experienced 30-70% strength reductions. X-ray diffraction analyses confirm that this is an overaging phenomenon (loss of tetragonal phase). However, XRD results also indicate that destabilization (loss of cubic) and decomposition phenomena are also involved in the long-term elevated temperature degradation of Mg-PSZ materials.

The dynamic elastic modulus of the four as-received materials was found to decrease from approximately 29.5×10^6 psi at room temperature to $\sim 23 \times 10^6$ psi at 1000°C. The residual elastic modulus at 25°C was not affected by the 1000 hr/1000°C aging exposure.

Strong evidence of major microstructural changes was observed for all Mg-PSZ materials after the 1000 hr/1000°C exposure. This was readily seen in thermal expansion curves of typical Mg-PSZ materials before and after aging. There is strong evidence for increased monoclinic phase in the exposed samples, indicating $t \rightarrow m$ transformation to explain the loss in properties. Consistent with its microstructural stability, the Y-TZP showed no evidence of monoclinic phase in the thermal expansion behavior. Reflected light micrographs are similarly interpreted. X-ray diffraction results confirm the degradation mode.

The fracture toughness was measured by the indentation-strength method, and the results were similarly interpreted. Room-temperature values of as-received materials ranged from nominally 7.9 to 11.6 $MPa \cdot m^{1/2}$. The toughness of the Y-TZP was 25% lower than the average value for the three Mg-PSZ materials. Toughness (K_c) decreased to 2.5-5 $MPa \cdot m^{1/2}$ at 1000°C. For Mg-PSZ this decrease was 54-63%. For Y-TZP, the 1000°C toughness was 70% lower than at ambient room temperature. This illustrates that the fracture toughness in

both Y- and Mg-PSZ decreases significantly with temperature as the tetragonal phase becomes more stable. The residual room-temperature fracture toughness after 1000 hr/1000°C exposure was approximately 6.3-7.4 $MPa \cdot m^{1/2}$ for both Y- and Mg-PSZ. For Mg-PSZ, this represents a ~30-50% reduction from the unexposed condition. For Y-TZP, the room-temperature fracture toughness decreased only 6% after 1000 hr/1000°C exposure. These toughness results parallel the strength changes with temperature and exposure.

The creep behavior of these materials was measured at 1000°C. The Y-TZP exhibited over an order-of-magnitude higher creep rates than any of the Mg-PSZ materials. This can perhaps be explained by higher diffusional creep and grain boundary sliding in Y-TZP resulting from (a) greater grain boundary volume and (b) the presence of a SiO_2-rich glassy intergranular phase. However, creep in both Y-TZP and Mg-PSZ was not affected by the 1000°C/1000 hr static exposure. The creep mechanisms are independent of the phase assemblage.

Water quench thermal shock results indicate that the high strength materials from NGK and Nilsen exhibit the highest ΔT_c values (ΔT_c ~400°-450°C). However, all four materials degrade to equivalent levels (ΔT_c ~275°C) after the 1000 hr/1000°C thermal exposure.

Thermal diffusivity was measured at room-temperature (both before and after exposure) by the laser pulse method. Thermal diffusivity for TTZ is very low--nominally 11 x 10^{-3} cm^2 sec^{-1}. Hence, its utility as a thermal insulator for minimum heat rejection or adiabatic diesel engines. For the Mg-PSZ and Y-TZP materials studied, the thermal diffusivity for as-received material only varied ±3%. The thermal diffusivity of NGK Y-TZP was nominally 2% higher than that of the three Mg-PSZ materials. This correlates to its nominally 2% higher density. Apparently, the widely different grain size, dopant and phase content of Mg-PSZ and Y-TZP do not affect the thermal diffusivity. Therefore, in the as-received condition, commercially available transformation-toughened zirconia materials have nominally equivalent values of thermal diffusivity (and thus also thermal conductivity, since the densities are similar and the specific heat is not expected to vary significantly). After 1000 hr/1000°C exposure, the thermal diffusivity increased slightly (in general from 3% to 13%, corresponding to an increase in monoclinic content and associated

microcracking with overaging. The thermal diffusivity of the Coors material, however, increased by as much as 40% upon the extended thermal exposure. These results indicate that thermal diffusivity in transformation-toughened zirconia is more affected by the degree of microcracking that accompanies any degradation than by the grain size and changes in phase content per se.

Static fatigue tests were conducted in flexure at 1000°C. For Y-TZP, it was found that for applied loads as low as 70% of the 1000°C fast fracture strength, excessive deformation (>7%) was obtained in ~200 hr. The particular Y-TZP studied on this program has a very stable microstructure, but exhibits severe creep deformation problems related to its fine grain structure and SiO_2-rich intergranular regions.

Much different behavior was obtained for the Mg-PSZ materials in static fatigue. All such materials survived for periods of nominally 2000 hr at 1000°C while under applied loads of up to 90% of the fast fracture strengths at that temperature. This indicates that classic static fatigue mechanisms such as bulk diffusion, cavity nucleation, creep fracture, or subcritical crack growth are not significantly operable or performance-limiting for Mg-PSZ. However, all Mg-PSZ materials so tested failed during subsequent furnace-cooling under load to room temperature after the successful static fatigue tests. All failures occurred at a furnace temperature almost precisely equivalent to the M_s temperature of each material (as seen in a thermal expansion curve, the temperature of tetragonal-to-monoclinic phase transformation upon cooling). These results are interpreted in terms of the microstructural state of the material at the end of the 2000 hr/1000°C thermal exposure --especially in regard to how much tetragonal phase is available to transform to monoclinic, and how much remains tetragonal and merely becomes more metastable as the temperature is decreased to ambient conditions.

Thermal fatigue tests were conducted by repeated cycling (1115 times) from 25° to 1000°C. The residual strength indicated that total time at elevated temperature is the parameter that controls the degradation. Repeated cycling through the martensitic transformation region was not particularly detrimental, even for the Mg-PSZ material. Any degradation that does occur appears to be related to the total time at elevated temperature. Repeated cycling through temperatures where microcracking occurs does not cause

cumulative damage. In fact, Feldmuhle ZN-40 Mg-PSZ exhibited complete strength retention after the thermal fatigue cycles.

An overall comparison of the two major forms of transformation-toughened zirconia, Mg-PSZ and Y-TZP is provided below.

3% Mg-PSZ (TTZ)	5% Y-PSZ (TZP)
• Cubic with tetragonal precipitates	• All tetragonal
• Large grain size (~50-75 μm)	• Fine grain (1-5 μm)
• Intermediate strength (90 ksi)	• High strength (130 ksi)
• 50% strength reduction at 1000°C	• 70% strength reduction at 1000°C
• Expansion, elastic modulus ~ Y-PSZ	• Expansion, elastic modulus ~ Mg-PSZ
• Poor thermal stability - overaging	• Long-term stability at temperature
• 30-70% strength reduction after 1000 hr/ 1000°C	• Only 7% strength reduction after 1000 hr/ 1000°C
• Good creep resistance	• Thermal expansion unchanged
• Creep unaffected by overaging	• Internal friction unchanged
• Potential destabilization effects	• Potential degradation at 200°C (water vapor)
• Good static fatigue behavior	• Poor creep resistance (SiO_2 intergranular)
• Most failures relate to t → m transformation	• Excessive deformation at temperature

For Y-TZP, excessive creep deformation is the long-term limitation of the material. For Mg-PSZ, all failures or deficiencies are related to unwanted tetragonal-to-monoclinic phase transformation.

When considering the use of these materials in design of structural components, the ceramic technologist would be wise to consider only relatively low temperature applications. There, the high toughness of TTZ leads to flaw tolerance and high Weibull moduli. Therefore, these materials have perhaps a higher probability of design acceptance compared to monolithic ceramics. Life prediction methodologies should be based on the phase structure (e.g., tetragonal retention) rather than strictly on flaw size.

1. INTRODUCTION

The potential benefits to be gained from the use of ceramic components in the hot section of diesel engines include: (a) higher temperature operation leading to increased efficiency; (b) decreased weight when compared to metal (superalloy) components; (c) reduced dependence on strategic materials such as chromium and cobalt; (d) decreased complexity through the use of non-cooled components; and (e) low thermal conductivity components leading to lower heat losses and thereby improved performance.

The low thermal conductivity of ceramics is of particular importance, and has been successfully exploited in the adiabatic or minimum heat rejection diesel engine. The concept is to insulate the high-temperature components of the engine such as the piston cap, head plate, valve hardware, cylinder liner, and exhaust ports. Additional power and improved efficiency result from this concept since thermal energy normally lost to the cooling water and exhaust gas (almost two-thirds of the energy input in a conventional diesel engine) is converted to useful power through the use of turbocompounding. By reducing the lost energy and eliminating the need for a conventional water-cooling system, the adiabatic diesel has been demonstrated to improve fuel economy and increase power output.

This concept of an insulated engine is of particular interest to the DOE for heavy-duty vehicles such as buses and trucks. Those vehicles cannot be downsized as automobiles have been. Therefore, the preferred route to improved fuel economy in such heavy-duty engines is through advanced concepts such as the adiabatic diesel engine. The long-range potential exists for the development of such an engine using ceramic components in the hot section to achieve reduced noise, reduced exhaust emissions, and broader fuel tolerance as well as significant fuel economy improvement.

The performance advances that have been achieved by the adiabatic diesel engine have largely been realized through the use of one generic class of ceramic material, partially stabilized zirconia (PSZ). This particular ceramic has been successful in this application for two reasons: (a) it

possesses a very low thermal conductivity; and (b) significant increase in fracture toughness has been attained in this ceramic material by a phenomenon known as phase transformation-toughening. Much work is currently being done within the ceramics industry on transformation-toughened zirconia (TTZ). Ceramic producers are beginning to supply newly developed materials to various engine demonstration and component development programs. It is now an appropriate time to develop a data base for such zirconia ceramics.

To this end, objectives of this program were:

- characterization of the pertinent thermal and mechanical properties of commercial and developmental zirconia ceramics that are currently available using standardized test methods and procedures
- relate the properties to the material microstructure and phase assemblage
- assessment of the long-term microstructural stability of these materials at elevated temperature
- assessment of the ability of both foreign and domestic sources to produce zirconia components suitable for the intended application.

The program has provided an initial data base of thermal and mechanical properties for various commercially available forms of TTZ. The results demonstrate that the critical technical issue for these materials is the various degradation modes that can potentially occur upon extended elevated temperature exposure. Therefore, preventing phase changes during in-service environmental conditions is the key to retaining the attributes of TTZ, and a necessary condition of insuring their successful structural use in advanced adiabatic diesel engines.

2. MATERIALS AND TEST PLAN

What has made transformation-toughened zirconia potentially acceptable for the intended engine application from a structural materials design standpoint is its high strength and fracture toughness. High toughness leads to flaw tolerance and high Weibull modulus. This attribute is a result of the unique phase assemblage of transformation-toughened zirconia, and how it is controlled. The concept of transformation-toughening involves a finely dispersed metastable tetragonal phase that transforms to monoclinic in the tensile stress field ahead of an advancing crack tip. This results in increased fracture toughness. Current mechanistic interpretations of the improved fracture properties of transformation-toughened zirconia include: (1) deflection of the advancing crack front by interaction with the stress fields around the transformed areas; and/or (2) microcrack generation leading to crack branching and an increase in the energy necessary to continue crack propagation. A third mechanism is sometimes discussed as a minor contributor, i.e., energy absorption by the phase transformation process itself. Whatever the mechanism, it is known that the stress-induced phase transformation in front of an advancing crack tip does absorb energy, arrest crack propagation, and thereby increase the work necessary for fracture and the overall resistance to crack propagation.

This program is structured around measuring the pertinent mechanical and thermal properties, and interpreting the results with respect to the material microstructure and phase assemblage. The properties of interest are listed in Table 1. Note that the basic materials characterization parameters are included: X-ray diffraction to characterize the phase assemblage, reflected light microscopy to reveal grain size and porosity, spectrographic cation impurity analysis, and density/porosity determination. Mechanical and thermal properties were generally measured at 25°-1000°C, and included flexure strength, elastic properties, fracture toughness, creep, thermal expansion, thermal shock, and thermal diffusivity. To assess the long-term stability, these same properties were measured after 1000 hr/1000°C static air exposure. Additionally, static fatigue and thermal fatigue studies were conducted.

TABLE 1. PROPERTIES MEASURED

- Characterization Parameters
  - Phase assemblage
  - Microstructure
  - Spectrographic analysis
  - Density/porosity
- Mechanical and Thermal Properties (25°-1000°C)
  - Flexure strength
  - Fracture origins/mode
  - Elastic modulus
  - Fracture toughness
  - Creep
  - Thermal expansion
  - Thermal shock
  - Thermal diffusivity
  - Internal friction
- Long-Term Stability
  - Properties after 1000 hr/1000°C exposure
  - Static fatigue/stress rupture
  - Thermal fatigue

Processing defects and fracture mode were assessed using the scanning electron microscope. Microstructural stability was assessed by SEM, reflected light microscopy, and X-ray diffraction studies. The overall emphasis and central issue in this program is the stability of the tetragonal zirconia crystal phase; i.e., the phenomenon of overaging upon extended thermal exposure, and resultant loss of toughness. This loss of the metastable tetragonal phase is the major limiting factor for TTZ materials.

The ceramic industry was screened at the inception of this program for potential suppliers of technical-grade zirconia. Four vendors were selected on the basis of their active pursuit of the commercial diesel engine market, their potential ability to scale up to production quantities, and our judgment that their materials are today's most mature toughened zirconia ceramics. The materials investigated were:

- Nilsen MS Mg-PSZ, TS Mg-PSZ*
- NGK Z-191 Y-TZP
- Feldmuhle ZN-40 Mg-PSZ
- Coors Mg-PSZ*

To avoid possible confusion, it is stated now that all materials investigated are partially stabilized zirconia (PSZ) that has been transformation-toughened. Some vendors use a "TT" designation to indicate that the material is indeed transformation-toughened, i.e., TT-ZrO_2. Others prefer to refer to their material as "zirconia" or "partially stabilized zirconia." However, all materials are actually a partially stabilized structure that has been transformation-toughened. Although not generally used by the manufacturers, we prefer to indicate the stabilizer used (i.e., either magnesia or yttria) for each material. For instance, Mg-PSZ and Y-PSZ. As we shall see, this is important in interpreting the properties observed.

---

*Coors and Nilsen (TS) materials were provided to this program at no cost.

3. PHASE, MICROSTRUCTURE, AND CHEMICAL CHARACTERIZATION

The basic materials characterization methods used on this program were X-ray diffraction to determine the crystalline phase assemblage, emission spectrometry for cation impurity analysis, reflected light microscopy of polished and etched sections for microstructural analysis, and an Archimedes water immersion technique to determine density and porosity.

3.1 PHASE ANALYSIS

Zirconia phase analysis was accomplished with IITRI's Rigaku computer-interfaced X-ray diffraction system,* which permits reliable quantitative measurement of the relative amounts of monoclinic, tetragonal, and cubic (coexisting) phases in zirconia. The XRD system is unique for this purpose since (a) it is of higher power than ordinary XRD equipment, which results in better resolution at higher reflected angles, and (b) the software permits separation of shoulders on intensity peaks by fitting to specified intensity-angle distribution functions. This results in a fairly accurate assessment of the percentage of the structure that is tetragonal. The tetragonal content is the primary indicator of toughness, microstructural stability, and overaging phenomena.

The separation of two-phase systems where one of the phases is monoclinic, such as monoclinic and cubic, or monoclinic and tetragonal (e.g., as in NGK Z-191 Y-TZP), is not difficult. The major monoclinic peaks are separated by ~2° 2θ from either cubic or tetragonal peaks within the range 28° to 32° 2θ when using Cu K_α radiation. Consequently, the percent tetragonal (which is the primary quantified measurement desired) is easily calculated by standard X-ray analysis methods.[1,2]

The problem of quantifying the relative amounts of phases when all three phases are present in a TT-ZrO_2 material is documented in the literature.[3-9]

---

*Rigaku 12 kW rotating anode X-ray diffractometer.

PAGE 6 INTENTIONALLY BLANK

PRECEDING PAGE BLANK NOT FILMED

With Cu K_α radiation the cubic and tetragonal phases are difficult to separate, as their major peaks overlap at ~29°-30° 2θ. Separation is possible at higher angles 2θ; however, the intensity of the peaks is lower there. As the tetragonal → monoclinic transformation occurs, the tetragonal (004) and (220) reflections at the higher angles decrease in intensity. The necessary use of solid samples (since tetragonal will convert to monoclinic upon grinding) may also create orientation/extinction problems.

The method with which we have been successful in separating the cubic and tetragonal phases at IITRI, and which we used in this program, involves techniques to enhance peak resolution and a curve-fitting computer program designed specifically for reducing X-ray diffraction data. In our procedure, after scanning a quartz standard and the zirconia sample from 20° to 80° 2θ, the sample is scanned again at the major peak region from ~28° to 32° 2θ using high resolution aperture and receiving slits, high power (5 to 8 kW) and step scanning at 0.01° 2θ/min. The rotating anode of this diffractometer is useful in overcoming orientation problems in solid samples. A curve is produced in which the overlapping cubic and tetragonal peaks may be separated, as shown in Figure 1. Data from both scans are reduced separately using the Alfred University X-ray Powder Diffraction Data Reduction Program. A Gaussian intensity distribution function was assumed as it is easy to model.

The equations commonly used for phase analysis of transformation-toughened zirconia assume only two phases: cubic and monoclinic, or tetragonal and monoclinic. When three phases may be distinguished, the following equations, after Schioler at AMMRC,[9] supply the necessary correction factors in terms of R values for the three phases.

$$V_m + V_c + V_t = 1$$

$$V(m) = \frac{1}{1 + \frac{R(m)}{I(m)} \left[\frac{I(t)}{R(t)} + \frac{I(c)}{R(c)} \right]}$$

$$V(c) = V(m) \left[\frac{I(c)}{R(c)} \approx \left[\frac{R(m)}{I(m)} \right] \right.$$

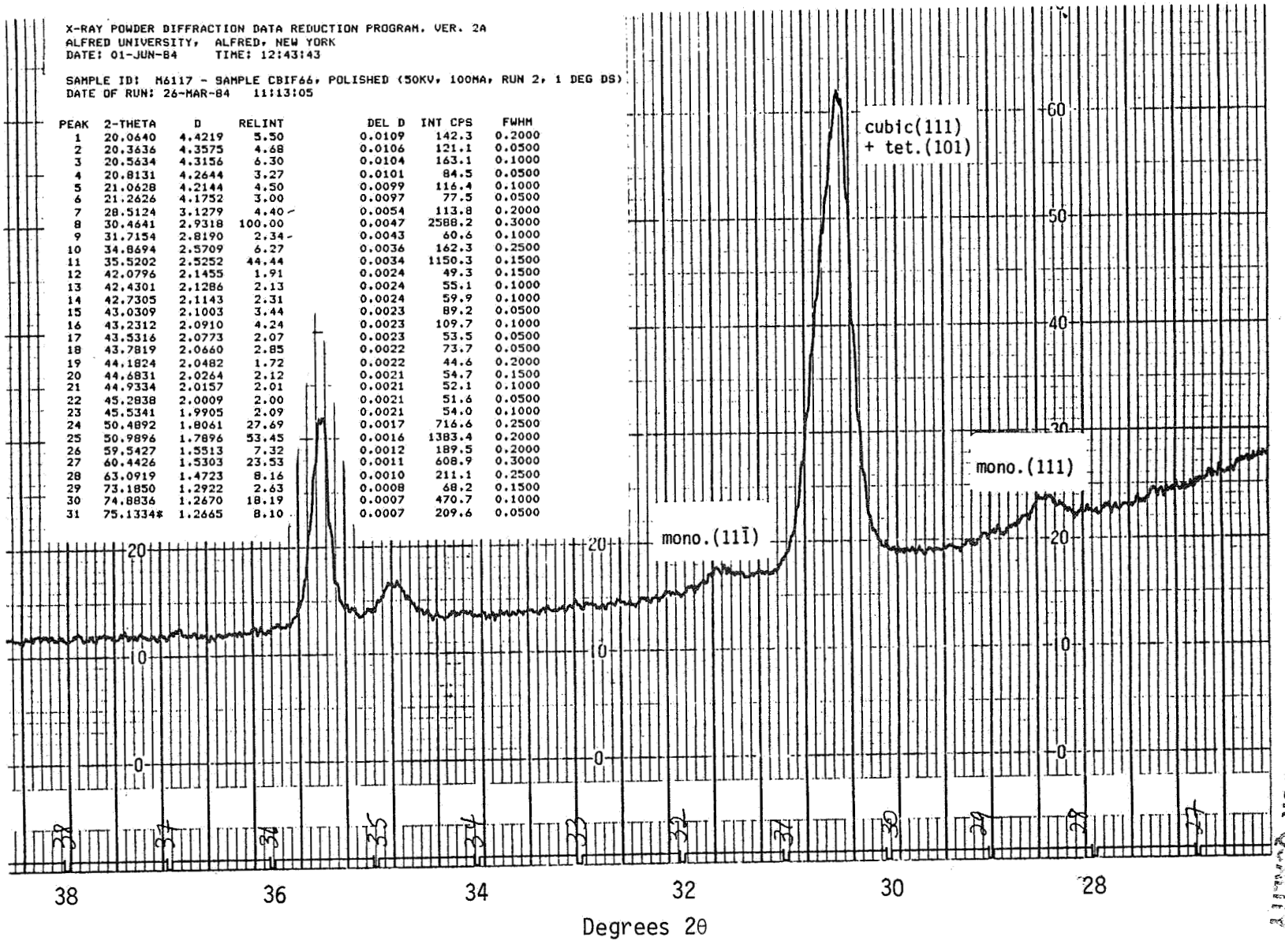

Figure 1a. XRD trace of Coors Mg-PSZ at standard scanning rate over the major peak region of ∿28° to 32° 2θ showing the summing of cubic and tetragonal phases (Cu K_α radiation).

ORIGINAL PAGE IS
OF POOR QUALITY

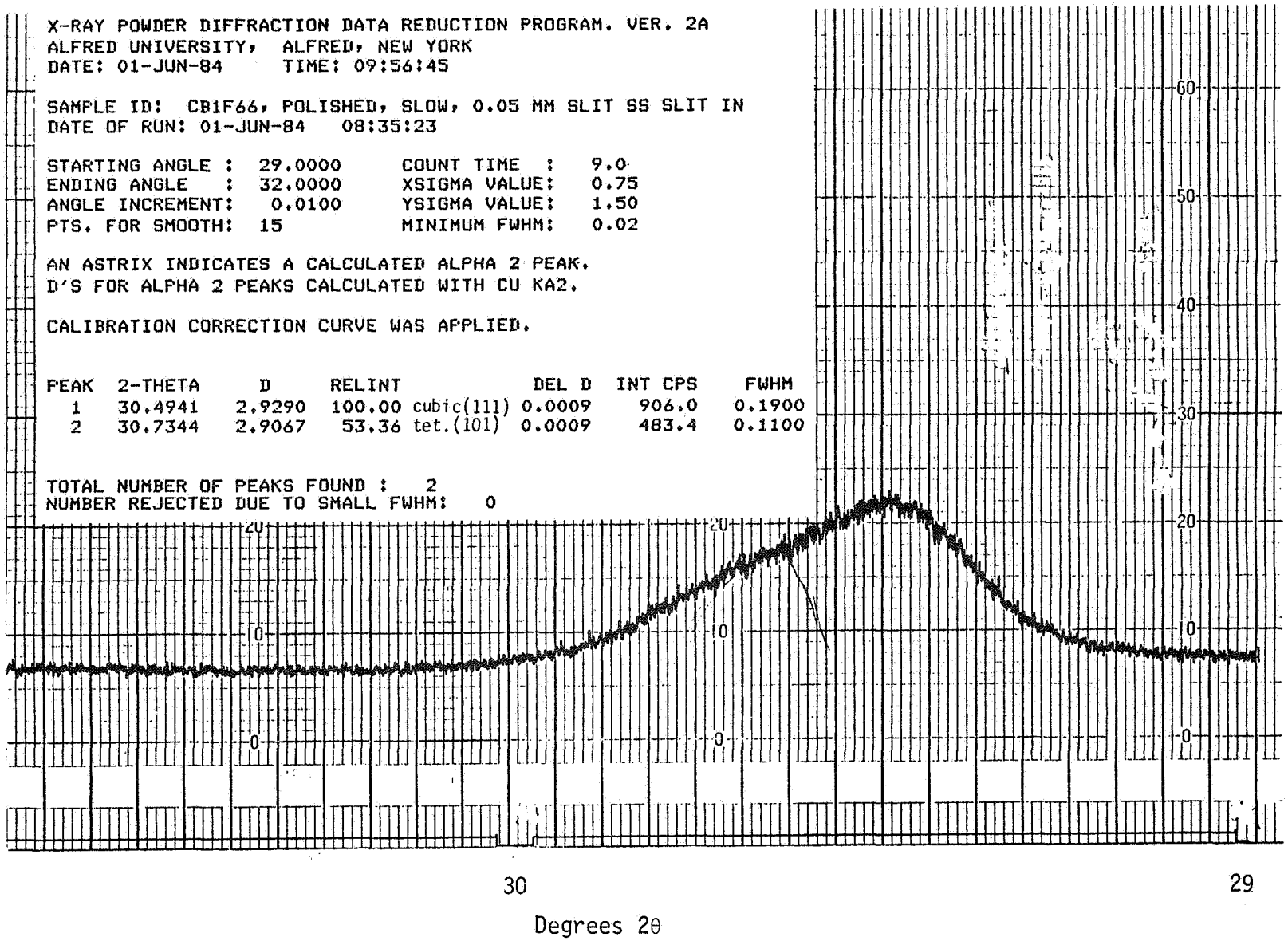

Figure 1b. XRD trace of Coors Mg-PSZ step-scanned at 0.01° 2θ/min at 5 kW over 29° to 30° 2θ to separate the cubic and tetragonal peaks. Fast scan data are renormalized using this information (Cu K_α radiation).

$$V(t) = V(m) \left[\frac{I(t)}{R(t)} \right] \left[\frac{R(m)}{I(m)} \right]$$

where V(m), V(t), and V(c) = volume fraction of monoclinic, tetragonal, and cubic phases, respectively

I(i) = integrated intensity of the peaks of the phases as above, and I(m) = sum of the $(11\bar{1})$ and (111) peaks

R(i) = calculated intensity of the peaks as above.

For Cu radiation:

R(m) = 227.02 [sum of two peaks: $(11\bar{1})$ and (111)]

R(c) = 200.31

R(t) = 187.96

When only two phases are present in a material, as for NGK Z-191 Y-TZP where $V_c = 0$, or when tetragonal and cubic peaks cannot be separated, the equations are:

$$V_{(m)} + V_{(t + c)} = 1$$

$$V_{(m)} = 1 - V_{(t + c)}$$

$$V_{(t + c)} = \frac{1}{1 + \left[\frac{I_{(m)}}{R_{(m)}} \times \frac{R(t + c)}{I_{(t + c)}} \right]}$$

where $R_{(m)}$ = 227.02 [sum of $(11\bar{1})$ and (111) peaks]

$R_{(t + c)}$ = 388.27: for inseparable cubic and tetragonal peaks

$R_{(t)}$ = 187.96: when no cubic phase is present

Baseline as-received samples and materials after exposure were characterized by XRD analysis of polished cross sections and fracture surfaces. The polishing procedure consisted of mounting a cross section of sample in epoxy, then handheld grinding on 220, 360, and 600 grit diamond-bonded wheels,

followed by polishing with 9 μm, 6 μm, 1 μm, and 1/4 μm diamond paste on Buehler napped microcloth. It is recognized that the tetragonal domains in TTZ can be transformed to monoclinic by the stresses involved in the grinding process. However, Pascoe and Garvie[10] demonstrated that the transformed layer resulting from rough grinding can be polished off during the 1 μm diamond paste stage, thus revealing a microstructure representative of the bulk material. Samples were polished with 1 μm and 1/4 μm diamond paste and X-rayed alternately until the diffractometer profile remained unchanged by polishing. All diffraction patterns were obtained at room temperature.

Figure 1a shows normal fast scans over the region of the first four major zirconia peaks for a representative baseline Mg-doped PSZ. The pattern obtained when the sample is slowly scanned over the combined cubic and tetragonal peak at ~30° 2θ is presented in Figure 1b, where the shoulder on the left part of the curve is the tetragonal peak. Similar scans for unexposed Y-PSZ (NGK Z-191) are shown in Figure 2. This material does not contain a cubic zirconia phase; the peak at ~30° 2θ consists of tetragonal material only.

Tabular X-ray diffraction results for the diamond-ground surfaces of as-received materials and their bulk interior, determined by XRD analysis of polished samples, are provided in Table 2. The Mg-PSZ materials are comprised of nominally 60% cubic, 35% tetragonal, and 5% monoclinic zirconia phases. NGK Z-191 Y-PSZ is 100% tetragonal, and therefore is more properly referred to

TABLE 2. BASELINE PHASE ANALYSIS OF TRANSFORMATION-TOUGHENED ZIRCONIA[a]

Material	As-Received, %	
	Ground Surfaces[b]	Polished Bulk[b,c]
Nilsen MS Mg-PSZ	67 (t + c), 33 (m)	37 (t), 58 (c), 5 (m)
Coors Mg-PSZ	49 (t + c), 51 (m)	34 (t), 60 (c), 6 (m)
Feldmuhle ZN-40 Mg-PSZ	79 (t + c), 21 (m)	34 (t), 63 (c), 3 (m)
NGK Z-191 Y-TZP	85 (t), 15 (m)	100 (t)

[a]Performed at IITRI using a Rigaku 12 kW rotating anode diffractometer and the Alfred University XRD data reduction computer program.

[b]Scanned 20°-80° 2θ at 0.5° 2θ/min using Cu K_α radiation.

[c]Step-scanned 28°-32° 2θ at 5 kW, 0.01°/step and 9 sec/step to separate cubic (111) and tetragonal (101) peaks at ~30° 2θ.

ORIGINAL PAGE IS
OF POOR QUALITY

X-RAY POWDER DIFFRACTION DATA REDUCTION PROGRAM. VER. 2A
ALFRED UNIVERSITY, ALFRED, NEW YORK
DATE: 02-JUN-84 TIME: 17:35:34

SAMPLE ID: M6117 - SAMPLE NG1F63, POLISHED (50KV,100MA, 1 DEG DS)
DATE OF RUN: 02-JUN-84 15:11:05

STARTING ANGLE :	20.0000	COUNT TIME :	6.0
ENDING ANGLE :	80.0000	XSIGMA VALUE:	0.75
ANGLE INCREMENT:	0.0500	YSIGMA VALUE:	1.50
PTS. FOR SMOOTH:	3	MINIMUM FWHM:	0.01

AN ASTRIX INDICATES A CALCULATED ALPHA 2 PEAK.
D'S FOR ALPHA 2 PEAKS CALCULATED WITH CU KA2.

CALIBRATION CORRECTION CURVE WAS APPLIED.

PEAK	2-THETA	D	RELINT	DEL D	INT CPS	FWHM
1	20.0640	4.4219	2.54	0.0109	190.6	0.0500
2	20.2637	4.3787	2.18	0.0107	163.5	0.0500
3	20.5634	4.3156	2.08	0.0104	156.6	0.1000
4	20.9629	4.2342	0.96	0.0100	72.0	0.0500
5	21.2127	4.1849	1.93	0.0097	144.9	0.0500
6	21.4624	4.1368	1.04	0.0095	78.4	0.0500
7	21.7122	4.0898	0.83	0.0093	62.2	0.1000
8	27.1616	3.2804	0.87	0.0059	65.5	0.1000
9	30.3640	2.9413	100.00	0.0047	7514.8	0.1500
10	34.7692	2.5780	8.10	0.0036	608.6	0.1500
11	35.1197	2.5531	5.03	0.0035	377.7	0.0500
12	35.3700	2.5356	12.85	0.0035	965.4	0.1500
13	35.8207	2.5047	0.85	0.0034	64.1	0.1500
14	43.1311	2.0956	1.16	0.0023	87.2	0.1500
15	50.3391	1.8112	54.10	0.0017	4065.2	0.2000
16	50.8395	1.7945	18.53	0.0016	1392.4	0.1500
17	59.4427	1.5537	14.98	0.0012	1125.7	0.2500
18	59.8427	1.5442	12.86	0.0012	966.5	0.0500
19	60.2926	1.5338	26.34	0.0012	1979.4	0.2500
20	62.9420	1.4754	7.30	0.0011	548.8	0.2500
21	73.1351	1.2929	2.14	0.0008	160.5	0.2000
22	73.3349*	1.2931	1.06	0.0008	79.8	0.0500
23	73.8844	1.2816	1.79	0.0007	134.7	0.1000
24	74.1342*	1.2811	0.97	0.0007	72.6	0.0500
25	74.5839	1.2713	4.72	0.0007	354.7	0.3000

TOTAL NUMBER OF PEAKS FOUND : 25
NUMBER REJECTED DUE TO SMALL FWHM: 0

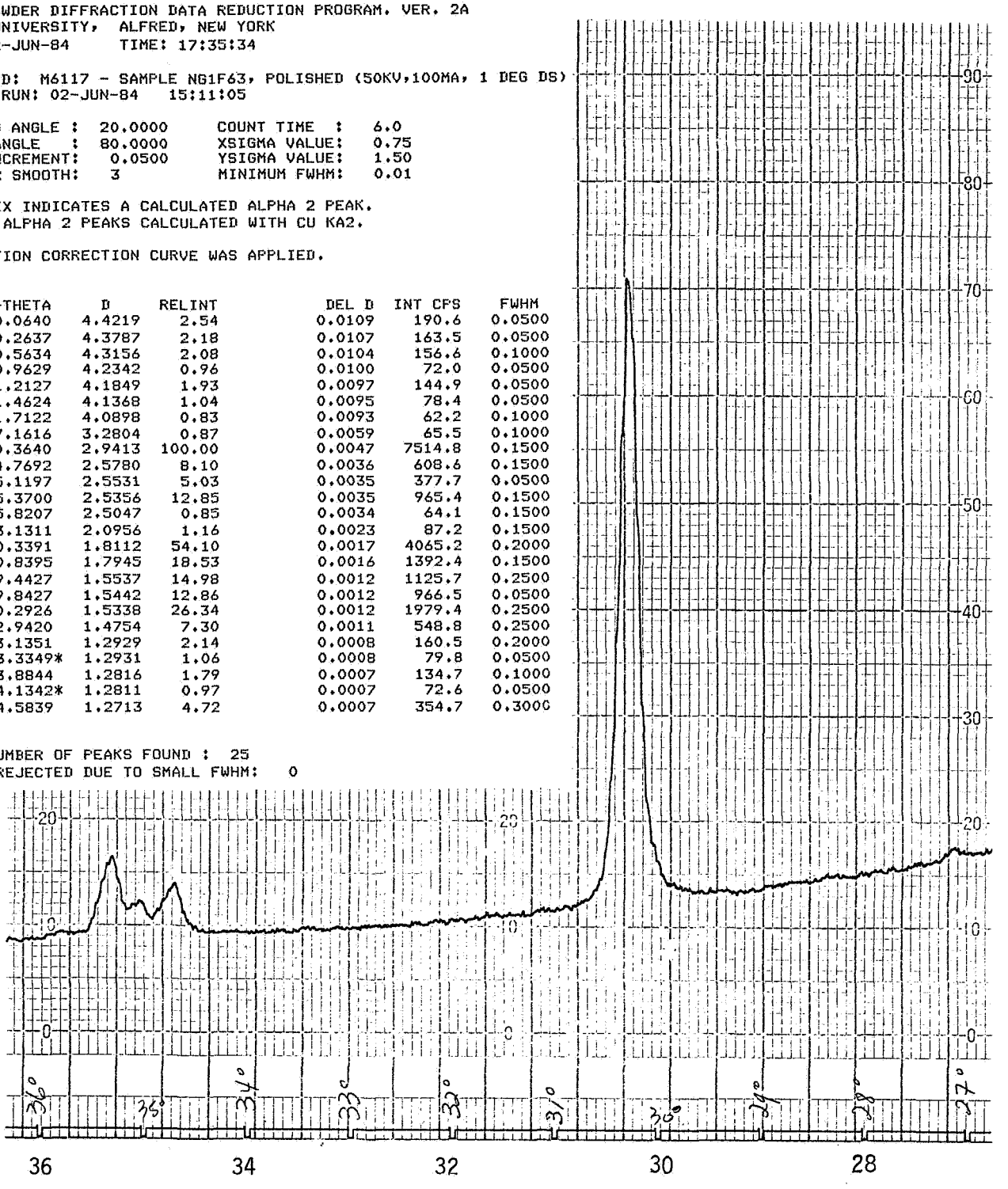

Figure 2a. XRD trace of NGK Z-191 Y-TZP at standard scanning rate over the region ∿28° to 32° 2θ showing the absence of monoclinic peaks.

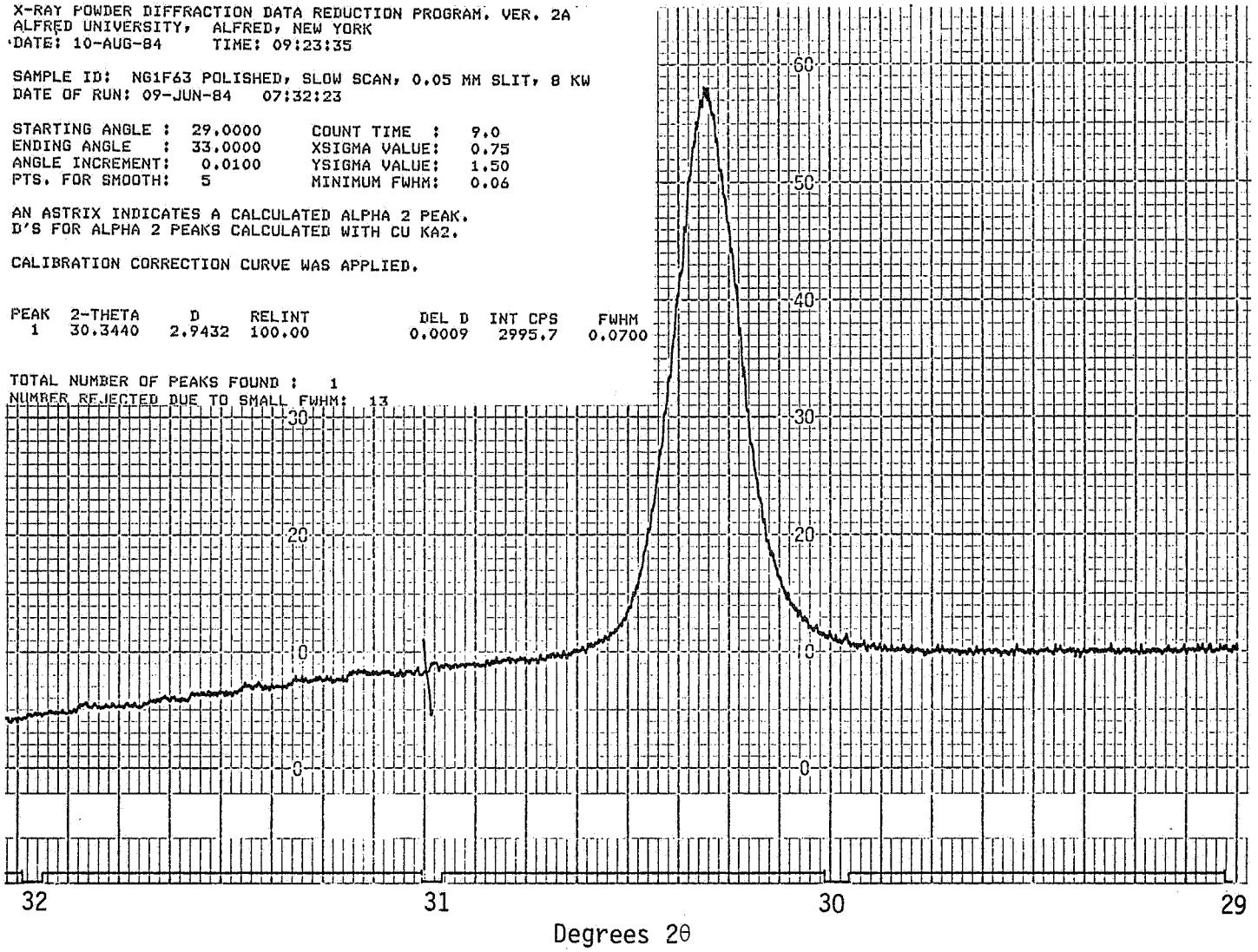

Figure 2b. XRD trace of NGK Z-191 Y-TZP step-scanned at 0.01° 2θ/min at 8 kW over 29° to 32° 2θ indicating tetragonal phase only.

as a TZP (tetragonal zirconia polycrystals). Results for the ground surfaces of all materials illustrate a significant increase in monoclinic, as near-surface tetragonal transforms to monoclinic due to the stress associated with the diamond grinding process.

X-ray phase analysis was also performed on fracture surfaces and polished sections (to reveal the bulk phase assemblage) of representative samples from fast fracture flexure tests conducted at 25°, 500°, 750°, and 1000°C. The results are presented in Tables 3a-3d. There are several important things to notice about these results. First, note that the phase assemblage of all Y-TZP and Mg-PSZ materials is not a function of test temperature (although XRD was performed only post-test at ambient room temperature). This has implications for interpretation of strength-temperature data to be presented in Section 4. Additionally, note in Tables 3a-3d that similar results were obtained on the fracture surfaces as were obtained for the polished bulk material for all fast fracture test conditions. This is somewhat surprising, in that increased monoclinic due to t → m transformation during fracture might be expected to be observed on fresh fracture surfaces. This observation is explained by consideration of the size of the transformation zone in comparison to the expected beam penetration in the X-ray diffraction measurement. The X-ray beam penetration is much greater than the thin zone of transformed material in the wake of the propagating crack tip. Thus, the XRD measurement includes below-surface contributions, which in this case would be the material bulk structure.

X-ray phase analysis was also performed on samples that had been exposed for 1000 hr at 1000°C in static laboratory air. These results are also compiled in Table 3. Note in Table 3a that the TZP material, i.e., NGK Z-191 (Y-PSZ), exhibited precisely the same phase assemblage as it did prior to the exposure. This illustrates the high stability of the Y_2O_3-doped TZP microstructure. Figure 3 illustrates little difference in the exposed and unexposed diffraction patterns for Y_2O_3-doped TZP.

Such microstructural stability was not observed for any of the three 1000 hr/1000°C exposed Mg-PSZ materials, as shown in Tables 3b-3d. The increase in monoclinic and concurrent decrease in tetragonal illustrates the problem of Mg-PSZ materials referred to as overaging. The basic phenomenon is that the

TABLE 3a. X-RAY DIFFRACTION RESULTS[a] FOR NGK Z-191 Y-TZP

Test Condition	Phase Composition, % Cubic	Tetragonal	Monoclinic
A. Fast Fracture			
• Polished Bulk			
25°C	0	100	--
500°C	0	98	2
750°C	0	99	1
1000°C	0	99	1
• Fracture Surface			
25°C	--	--	--
500°C	0	95	5
750°C	0	98	2
1000°C	0	98	2
B. 25°C, Exposed 1000 hr/ 1000°C (polished bulk)	0	99	1

[a]Results determined by calculation for two phases on 8 kW slow step-scan patterns showing evidence of two phases present.

TABLE 3b. X-RAY DIFFRACTION RESULTS[a] FOR NILSEN MS Mg-PSZ

Test Condition	Phase Composition, %		
	Cubic	Tetrag-onal	Mono-clinic
A. Fast Fracture			
• Polished Bulk			
25°C	57	37	5
500°C	56	33	12
750°C	59	32	8
1000°C	60	31	9
• Fracture Surface			
25°C	--	--	--
500°C	57	34	9
750°C	63	31	6
1000°C	66	29	5
B. 25°C, Exposed 1000 hr/ 1000°C (polished bulk)	21	11	69

[a]All results determined by calculations on 8 kW slow step-scan patterns showing evidence of three phases present.

TABLE 3c. X-RAY DIFFRACTION RESULTS[a]
FOR FELDMUHLE ZN-40 Mg-PSZ

Test Condition	Phase Composition, %		
	Cubic	Tetrag-onal	Mono-clinic
A. Fast Fracture			
• Polished Bulk			
25°C	63	34	3
500°C	43	41	16
750°C	56	40	4
1000°C	61	36	4
• Fracture Surface			
25°C	--	--	--
500°C	54	44	2
750°C	67	32	1
1000°C	53	45	2
B. 25°C, Exposed 1000 hr/ 1000°C (polished bulk)	41	0	59

[a]All results determined by calculations on 8 kW slow step-scan patterns showing evidence of three phases present.

TABLE 3d. X-RAY DIFFRACTION RESULTS[a] FOR COORS Mg-PSZ

Test Condition	Phase Composition, % Cubic	Tetragonal	Monoclinic
A. Fast Fracture			
• Polished Bulk			
25°C	60	34	5
500°C	58	39	3
750°C	56	40	4
1000°C	72	25	3
• Fracture Surface			
25°C	--	--	--
500°C	66	30	4
750°C	57	37	6
1000°C	51	46	3
B. 25°C, Exposed 1000 hr/ 1000°C (polished bulk)	10	10	80

[a]All results determined by calculations on 8 kW slow step-scan patterns showing evidence of three phases present.

ORIGINAL PAGE IS
OF POOR QUALITY

SAMPLE ID: M6117-MOUNTED, POLISHED NG1F23,EXPOSED 1000HR/1000C - 5 KW
DATE OF RUN: 14-SEP-84 17:35:05

(036

STARTING ANGLE :	23.0000	COUNT TIME :	6.0
ENDING ANGLE :	80.0000	XSIGMA VALUE:	0.75
ANGLE INCREMENT:	0.0500	YSIGMA VALUE:	1.50
PTS. FOR SMOOTH:	5	MINIMUM FWHM:	0.04

AN ASTRIX INDICATES A CALCULATED ALPHA 2 PEAK.
D'S FOR ALPHA 2 PEAKS CALCULATED WITH CU KA2.

CALIBRATION CORRECTION CURVE WAS APPLIED.

PEAK	2-THETA	D	RELINT		DEL D	INT CPS	FWHM
1	23.0614	3.8535	1.55		0.0082	463.7	0.0500
2	23.4112	3.7967	1.29		0.0080	387.0	0.0500
3	23.6612	3.7571	1.05		0.0078	313.2	0.1000
4	23.9111	3.7184	0.76		0.0076	227.8	0.0500
5	24.2610	3.6656	0.60		0.0074	178.3	0.0500
6	24.6110	3.6142	0.22		0.0072	65.2	0.0500
7	24.9610	3.5643	0.20		0.0070	58.4	0.1000
*8	27.1616	3.2804	0.50		0.0059	148.8	0.1000
*9	28.3623	3.1441	0.27	} mono.	0.0054	80.6	0.1000
10	28.5625	3.1226	0.22		0.0053	64.9	0.0500
11	28.8126	3.0960	0.17		0.0052	49.4	0.1000
12	29.6633	3.0091	0.51		0.0050	151.6	0.0500
*13	30.3139	2.9460	100.00	← tet.	0.0047	29912.9	0.1000
14	31.6153	2.8277	0.06	← mono.	0.0044	18.1	0.0500
*15	34.7192	2.5816	3.57		0.0036	1068.3	0.1500
*16	35.3700	2.5356	5.66		0.0035	1693.2	0.1500
*17	35.8207	2.5047	0.39		0.0034	115.5	0.1000
18	38.7749	2.3204	0.20		0.0029	58.6	0.1000

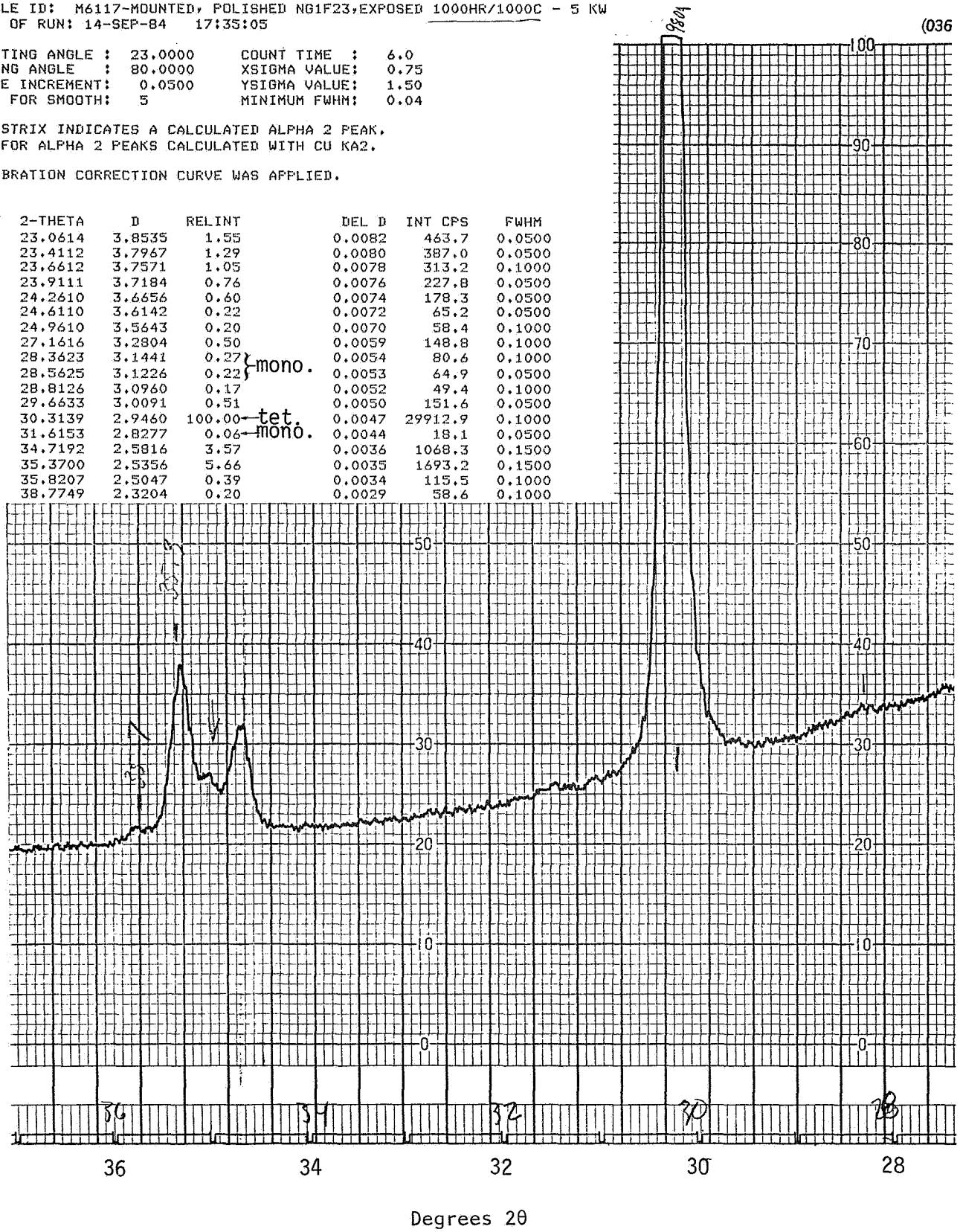

Figure 3a. XRD trace of exposed NGK Z-191 Y-TZP at standard scanning rate over the region ∿28° to 36° 2θ showing the absence of monoclinic peaks.

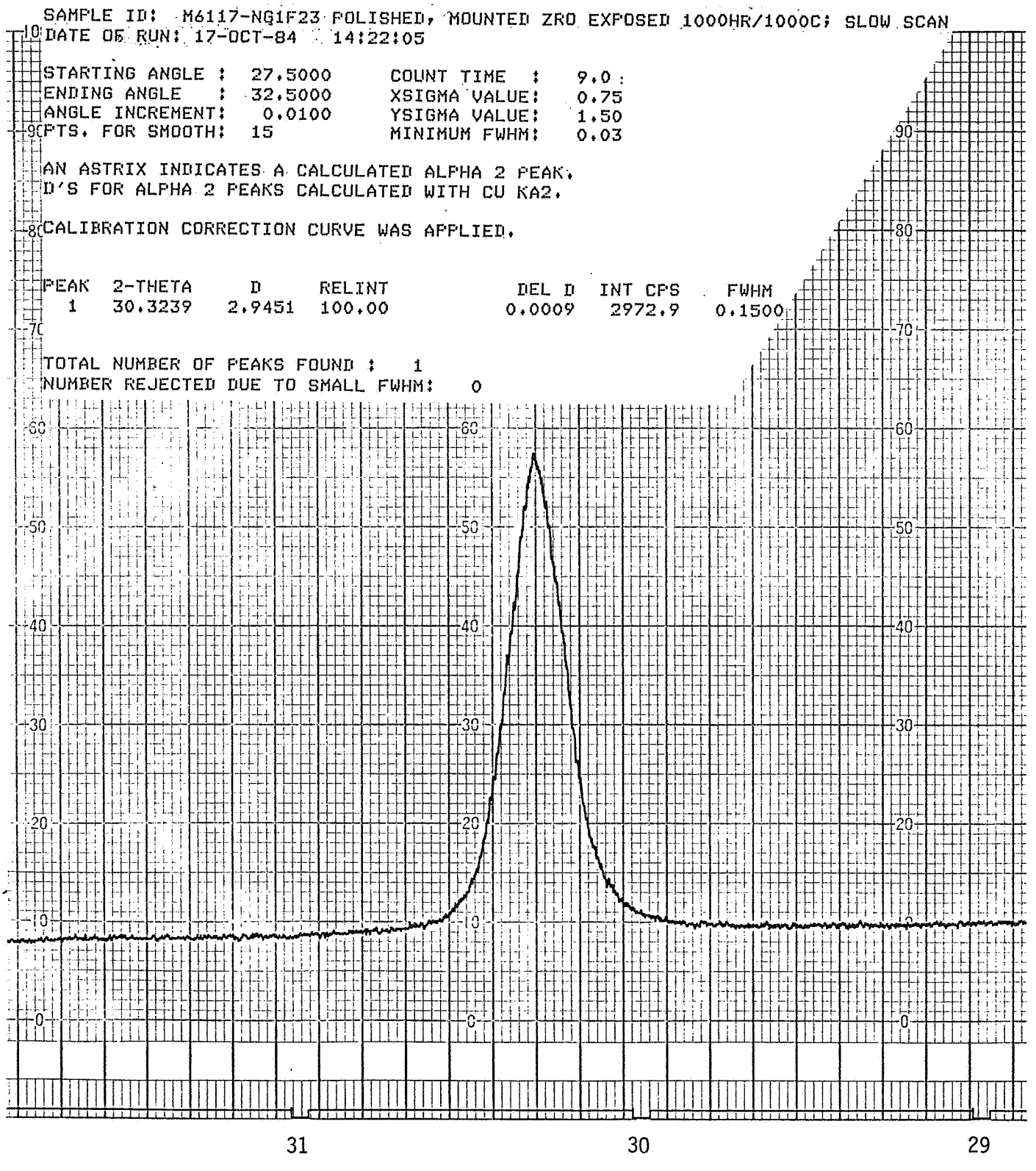

Figure 3b. XRD trace of NGK Z-191 Y-TZP step-scanned at 0.01° 2θ/min at 8 kW over a 29° to 32° 2θ, indicating only tetragonal phase after 1000 hr/1000°C exposure.

tetragonal phase is finely dispersed within large cubic grains and, upon extended exposure at elevated temperature, grows to a size that can no longer be constrained in the metastable tetragonal condition, resulting in subsequent transformation to monoclinic. Representative exposed and unexposed diffraction patterns for Mg-PSZ are shown in Figures 4a and 4b, where definite increase in the monoclinic zirconia phase upon exposure occurs at ~28° and 31° 2θ.

However, examination of the relative amounts of cubic, tetragonal, and monoclinic phases in Mg-PSZ after the 1000 hr/1000°C exposure, and comparison with the unexposed phase assemblage, indicates that more than just t → m overaging must be involved in the degradation of Mg-PSZ materials upon 1000 hr/1000°C exposure. Tables 3b-3d illustrate that the monoclinic content increases at the expense of the cubic phase as well. The transformation of cubic to monoclinic indicates the presence of destabilization and/or decomposition effects, as well as overaging upon exposure.

3.2 MICROSTRUCTURE

The microstructure of the zirconia materials was studied by reflected light microscopy. The polishing procedure consisted of grinding on 220, 360, and 600 grit diamond-bonded wheels, followed by polishing with 9 μm, 6 μm, and 1 μm diamond paste on Buehler napped microcloth. The polished samples were etched at 80°C; the etchant consisted of a solution containing 100 ml water, 8 ml hydrofluoric acid, 8 g ammonium bifluoride, and 1 ml hydrogen peroxide.* It is recognized that the tetragonal domains in TTZ can be transformed to monoclinic by the stresses involved in the grinding process. However, Pascoe and Garvie[10] demonstrated that the transformed layer resulting from rough grinding can be polished-off during the 1 μm diamond paste stage, thus revealing a microstructure representative of the bulk material. This is the procedure used in the current work. This aspect of transformation-toughened zirconia is obviously critical for the preparation of samples for TEM analysis or strength testing; however, even though the tetragonal domains are not visible

*Etchant formula provided by D. Cheever of Coors Porcelain Co., Golden, CO.

SAMPLE ID: M6117-MOUNTED, POLISHED CB1F23, EXPOSED 1000HR/1000C - 5 KW
DATE OF RUN: 14-SEP-84 20:30:05

STARTING ANGLE :	23.0000	COUNT TIME :	6.0
ENDING ANGLE :	80.0000	XSIGMA VALUE:	0.75
ANGLE INCREMENT:	0.0500	YSIGMA VALUE:	1.50
PTS. FOR SMOOTH:	5	MINIMUM FWHM:	0.04

AN ASTRIX INDICATES A CALCULATED ALPHA 2 PEAK.
D'S FOR ALPHA 2 PEAKS CALCULATED WITH CU KA2.

CALIBRATION CORRECTION CURVE WAS APPLIED.

ORIGINAL PAGE IS
OF POOR QUALITY

PEAK	2-THETA	D	RELINT		DEL D	INT CPS	FWHM
1	23.0614	3.8535	17.89		0.0082	522.2	0.1000
2	23.5112	3.7807	10.03		0.0079	292.7	0.1500
3	23.8611	3.7261	7.08		0.0077	206.7	0.0500
-4	24.3610	3.6507	17.21		0.0074	502.2	0.1500
-5	24.7610	3.5927	11.60		0.0071	338.6	0.1000
-6	28.5124	3.1279	100.00	mono.	0.0054	2918.3	0.2000
7	29.2130	3.0545	2.39		0.0051	69.7	0.0500
-8	30.4641	2.9318	16.30	tet.+c.	0.0047	475.8	0.2500
-9	31.0146	2.8810	17.05		0.0045	497.5	0.1000
-10	31.7655	2.8146	61.35	mono.	0.0043	1790.4	0.2000
-11	34.4188	2.6035	12.99		0.0037	379.0	0.2000
12	34.7692	2.5780	6.50		0.0036	189.6	0.1000
-13	35.6204	2.5184	17.05		0.0034	497.7	0.1500

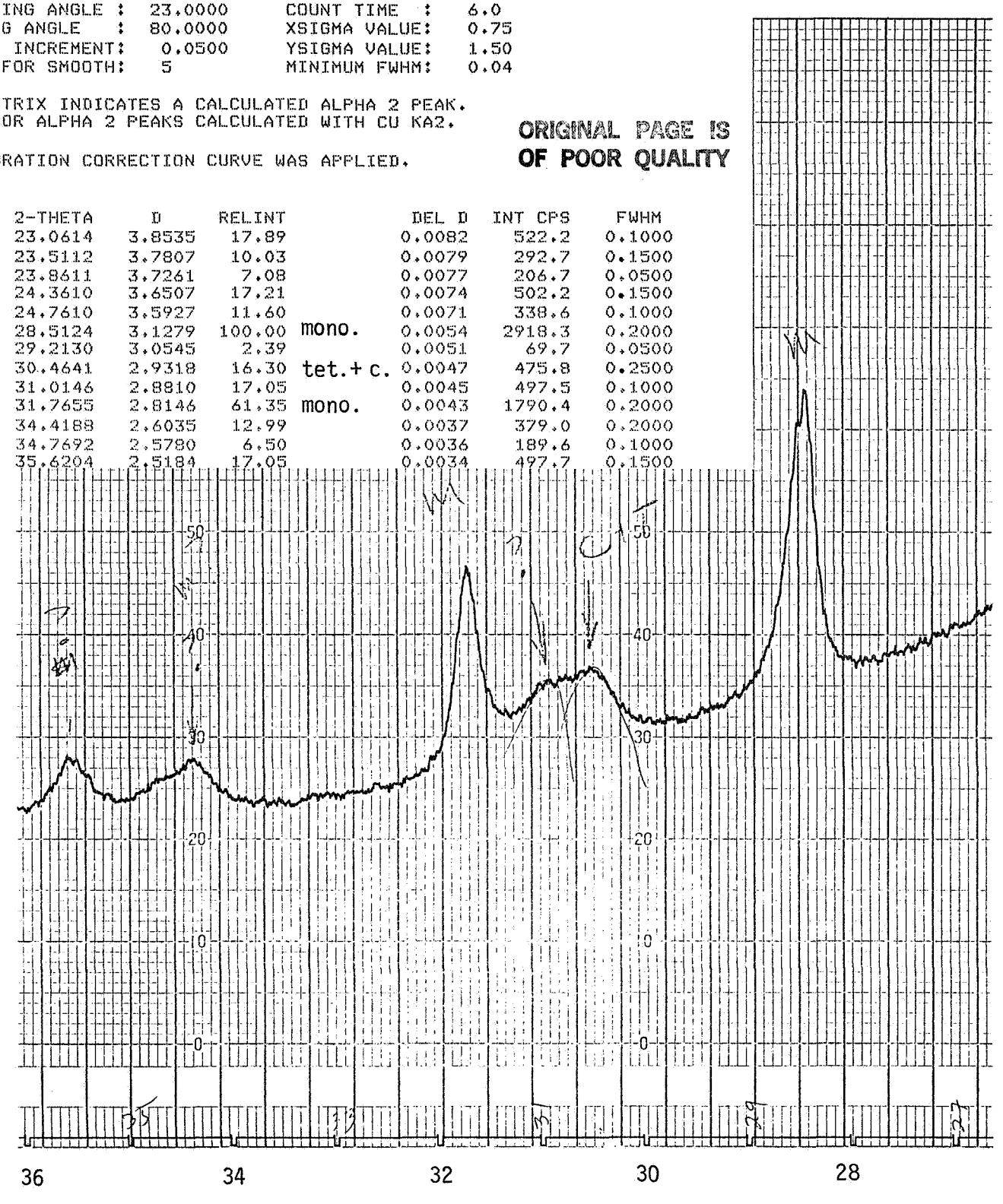

Figure 4a. XRD trace of exposed Coors Mg-PSZ at standard scanning rate over the major peak region of ∿28° to 36° 2θ showing the decrease of the summed cubic and tetragonal phases and the increased monoclinic peaks (Cu K_α radiation).

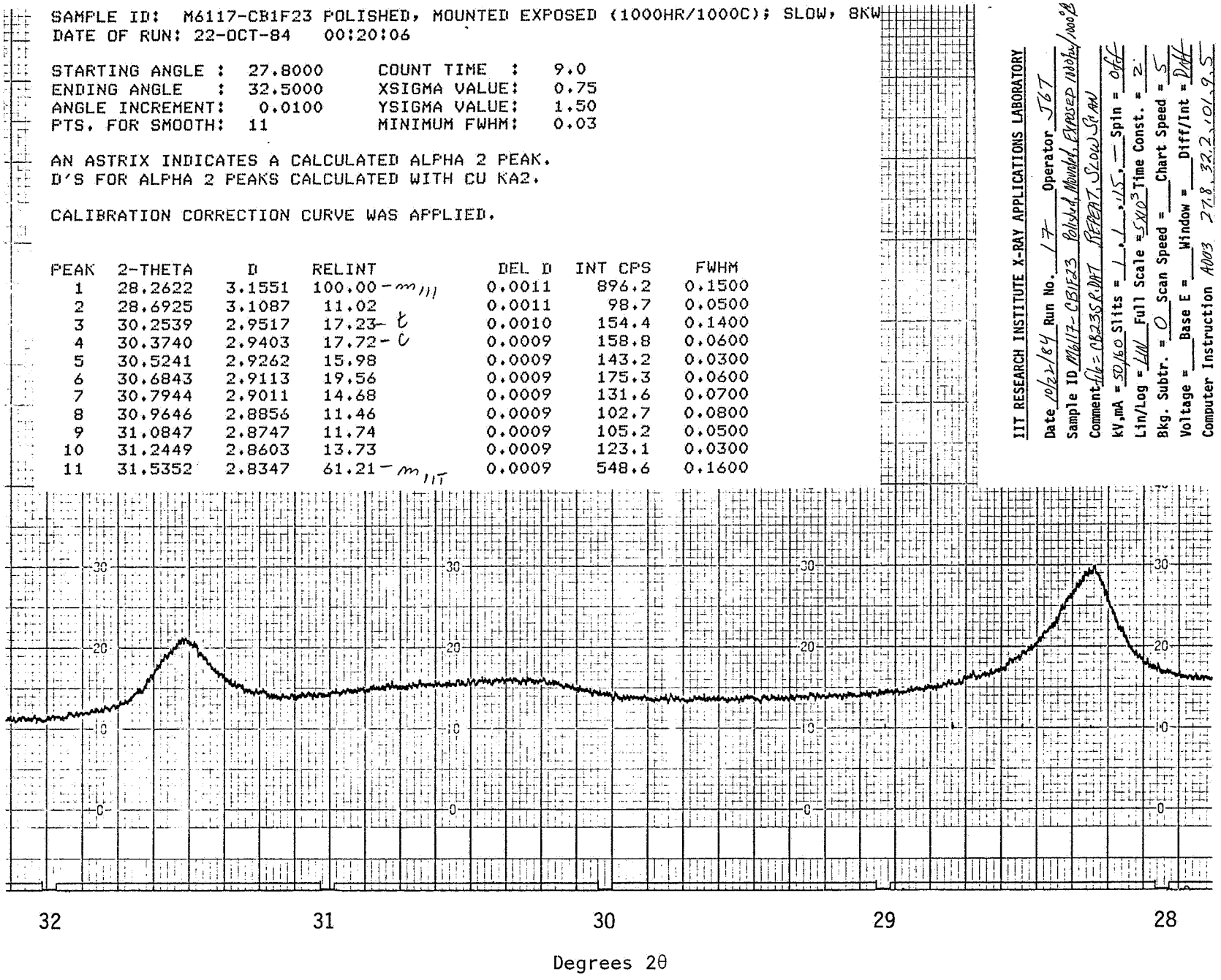

Figure 4b. XRD trace of exposed Coors Mg-PSZ step-scanned at 0.01° 2θ/min at 5 kW over 28° to 32° 2θ to separate the cubic and tetragonal peaks (Cu K_α radiation).

in low-magnification optical microscopy, it is recommended practice to be aware of the grinding stress induced transformation. This was the procedure used for obtaining the X-ray phase assemblage of the below-surface bulk material, described in the previous section.

The pre- and post-exposure microstructure of each material is presented in Figures 5-8. The Mg-PSZ materials (Figures 5-7) look similar. The primary phase in each material both before and after exposure is large (50 to 100 μm), light gray grains which are cubic (refer to XRD phase analysis). The lighter phase which surrounds the large grains is monoclinic, and the darkest phase is porosity. At optical microscope magnifications, the intragranular tetragonal phase (within cubic grains) cannot be seen. Note that the Feldmuhle and Coors materials have considerably larger grain size and more porosity compared to the Nilsen material. Thus, lower strength is expected. The unexposed MgO-doped materials have monoclinic phases surrounding cubic grains in bands of 1 to 5 μm thicknesses.

After 1000 hr/1000°C exposure, the intergranular regions in Mg-PSZ have grown to thicknesses of 10 to 15 microns in cubic grain boundaries, and to regions of ~25 μm diameter at grain triple points. XRD results confirm the increased volume of monoclinic material after exposure for these Mg-PSZ materials. The metastable tetragonal precipitates have transformed to monoclinic upon 1000 hr/1000°C exposure (overaging), and the cubic matrix has decomposed and/or destabilized, as evidenced by the development of a monoclinic grain boundary phase. Note that Figures 5 and 7 illustrate that the Nilsen and Coors materials appeared to decompose more than did the Feldmuhle ZrO_2, at least as indicated by the microstructure revealed by reflected light microscopy. This will be correlated with their relative strength retention in Section 4.

The microstructure of the NGK material is illustrated in Figure 8. This is a very fine-grained material, the approximate average grain size being 1-5 μm. The microstructure shown in Figure 8 gives no optical indication of a monoclinic phase. The tetragonal phase in Y-PSZ is not a precipitate as in Mg-PSZ, but rather a discrete phase. In fact, the NGK Y-PSZ is composed primarily of discrete tetragonal grains (a TZP). X-ray diffraction confirms 100% tetragonal single phase. Interestingly, after 1000 hr/1000°C exposure

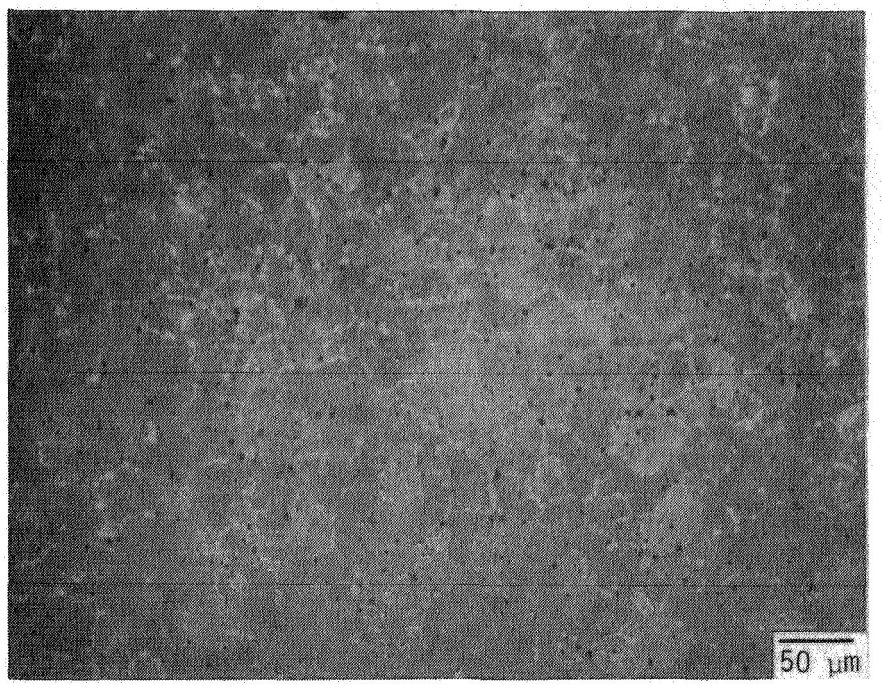

(a) Unexposed, etched 1.25 min.

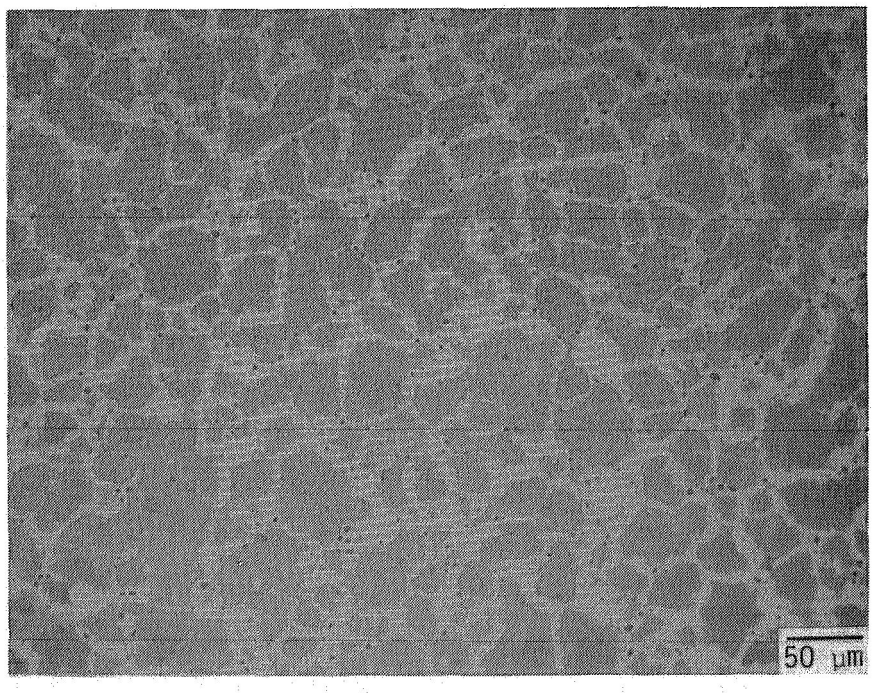

(b) Exposed 1000 hr/1000°C, etched 50 sec.

Figure 5. Microstructures of Nilsen MS Mg-PSZ before and after 1000 hr/1000°C exposure.

ORIGINAL PAGE IS
OF POOR QUALITY

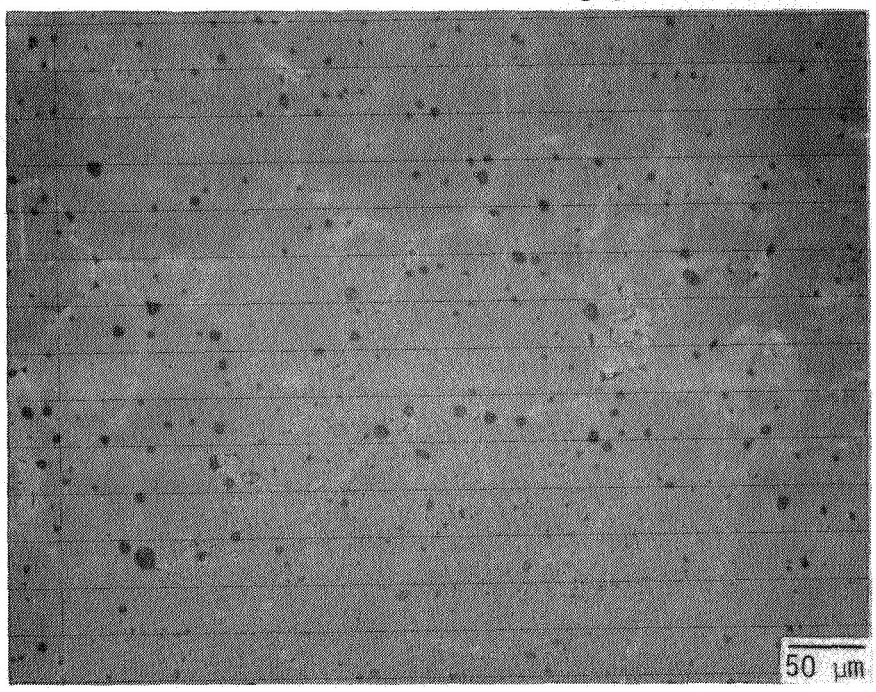

(a) Unexposed, etched 1.5 min.

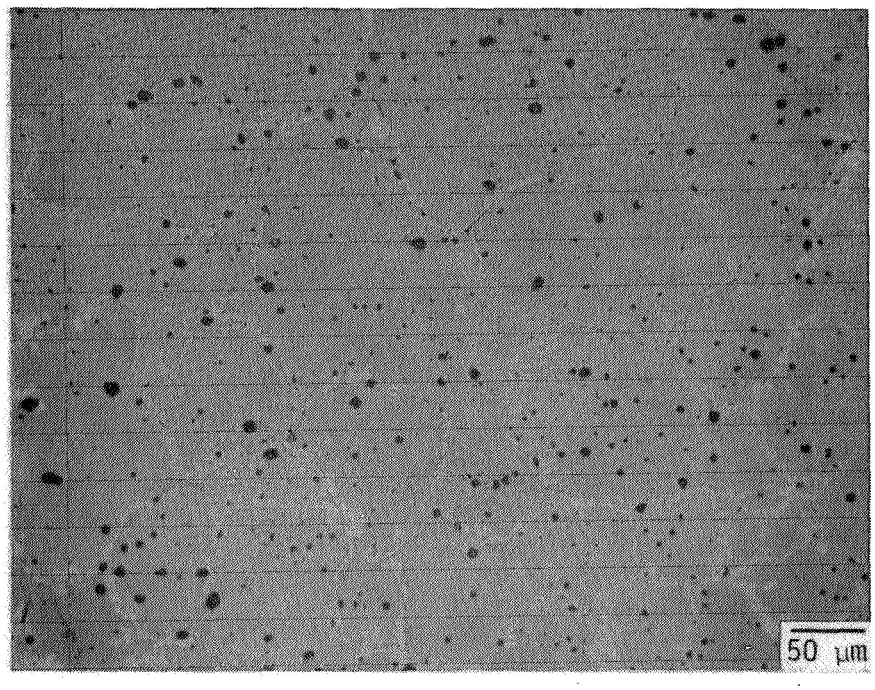

(b) Exposed 1000 hr/1000°C, etched 1 min.

Figure 6. Microstructures of Feldmuhle ZN-40 Mg-PSZ before and after 1000 hr/1000°C exposure.

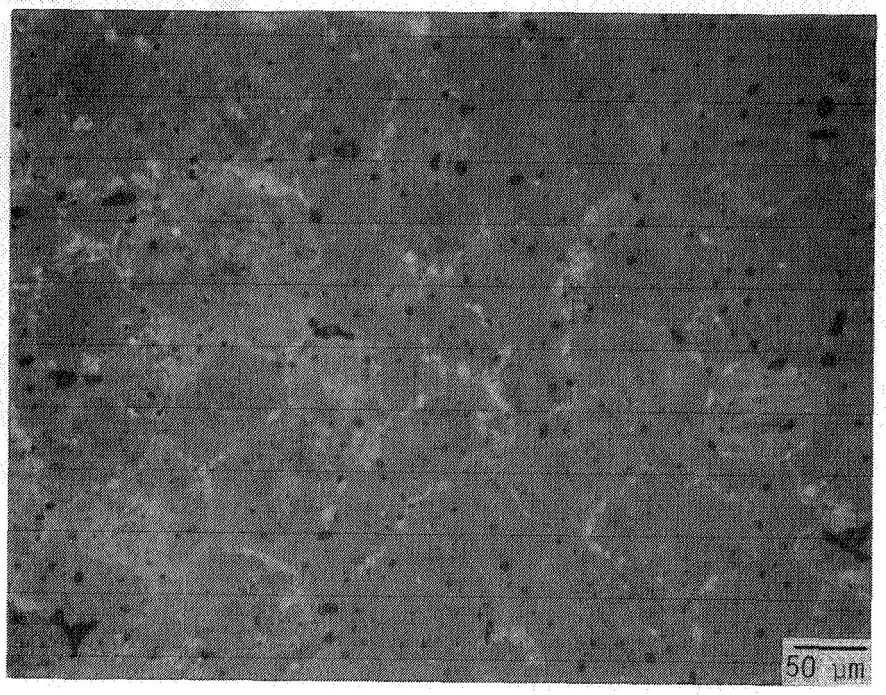

(a) Unexposed, etched 1.25 min.

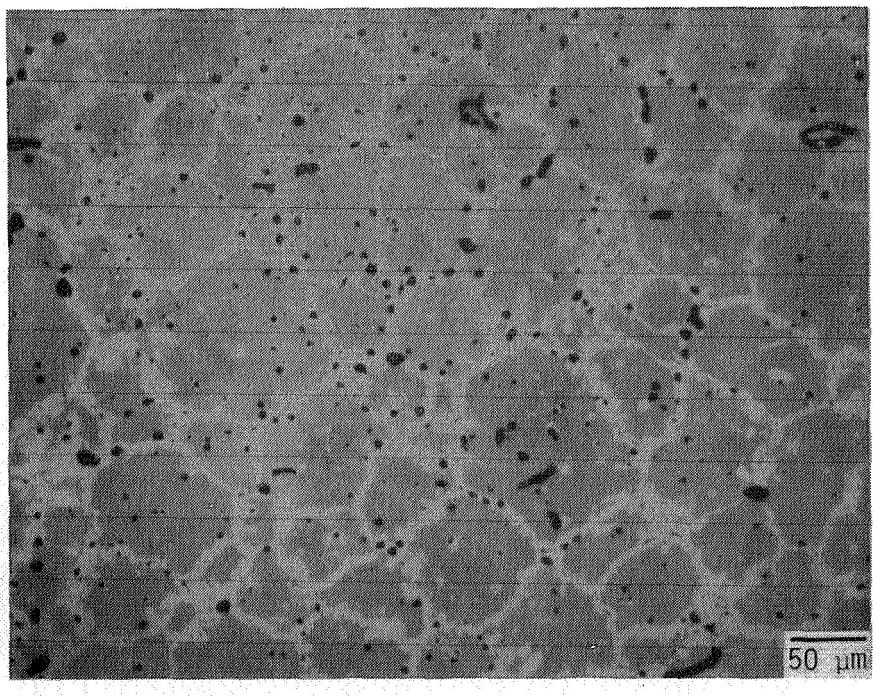

(b) Exposed 1000 hr/1000°C, etched 1.5 min.

Figure 7. Microstructures of Coors Mg-PSZ before and after 1000 hr/1000°C thermal exposure.

ORIGINAL PAGE IS
OF POOR QUALITY

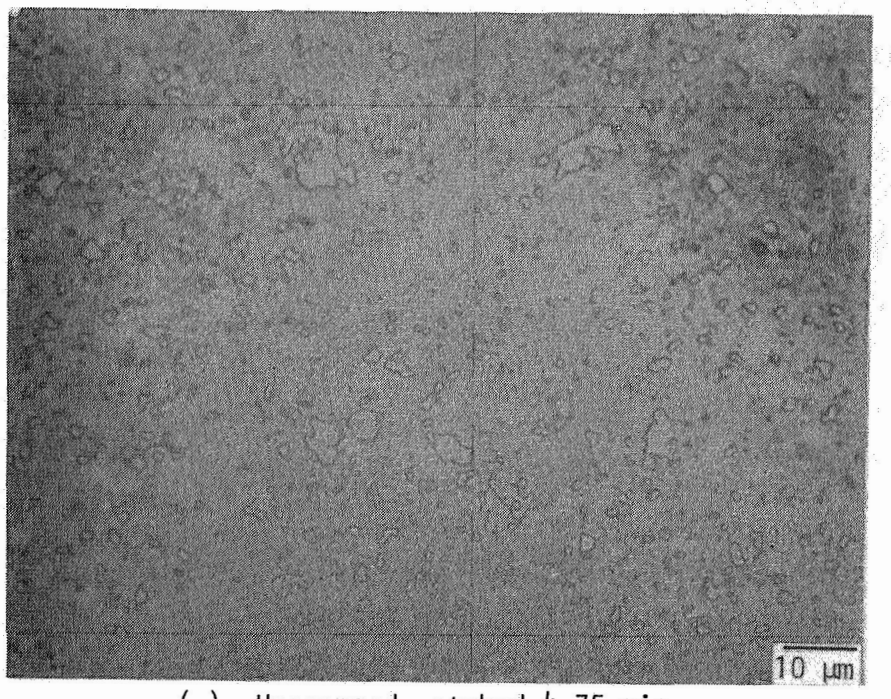

(a) Unexposed, etched 4.75 min.

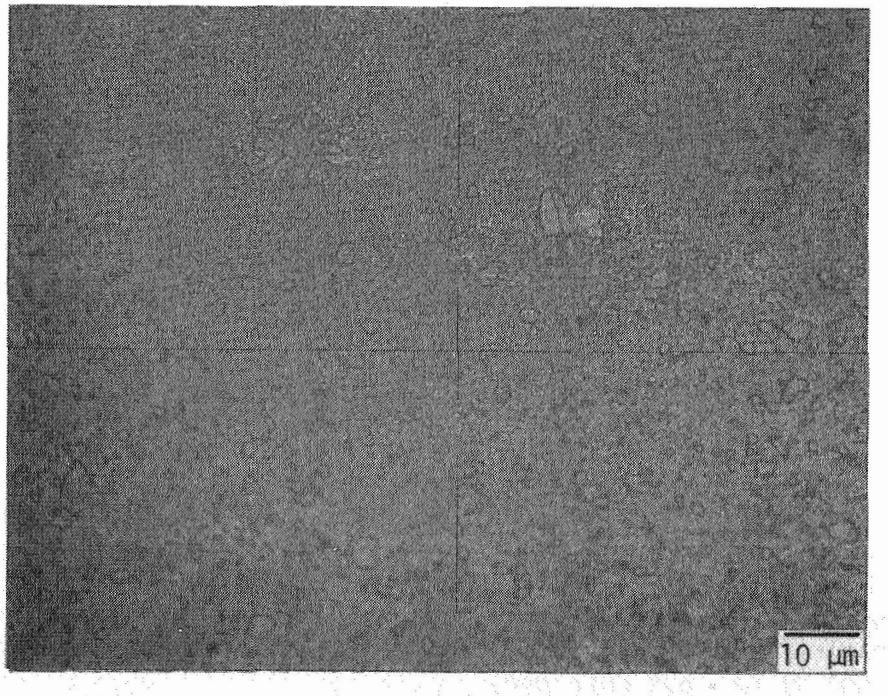

(b) Exposed 1000 hr/1000°C, etched 5.75 min.

Figure 8. Microstructures of NGK Z-191 Y-TZP before and after 1000 hr/1000°C thermal exposure.

the microstructure, as observed at 1000X, has not markedly changed. This correlates with the excellent phase retention for NGK Y-TZP discussed in the previous section.

3.3 SPECTROGRAPHIC ANALYSIS

Spectrographic analysis of the four materials was performed at AMMRC. Results are given in Table 4. The reported cation impurity concentrations fall within the range expected for these zirconias. The calculated weight percent major dopant (stabilizer) for each material is as follows: Nilsen MS, 3.35 MgO; Feldmuhle ZN-40, 3.07 MgO; Coors, 2.95 MgO; and NGK Z-191, 5.08 Y_2O_3. Thus, the magnesia-stabilized materials investigated on this program are more accurately referred to as 3% MgO-PSZ. Likewise, the yttria-stabilized zirconia is a 5% Y_2O_3-TZP. For the NGK material, if all the Si in the structure were present as SiO_2, the SiO_2 content would be 1.1%. Similarly, if all the Al impurity were present as Al_2O_3, the amount would be 0.8%. It will be shown later in the sections on creep and static fatigue, that the high intergranular silica content results in excessive deformation for NGK Z-191 ZrO_2 at elevated temperature.

TABLE 4. SPECTROGRAPHIC ANALYSIS OF MAJOR IMPURITIES IN UNEXPOSED ZIRCONIA CERAMICS[a]

Material	Analysis, Weight Percent[b]									
	Mg	Al	Si	Ca	Ti	Cr	Fe	Zn	Y	Zr
Coors Mg-PSZ	1.78	0.04	0	0.02	0.07	0.13	0.30	0.21	0.18	bal
Feldmuhle ZN-40	1.85	0.05	0.02	0.08	0.04	0.30	0.45	0.10	0.12	bal
Nilsen MS Mg-PSZ	2.02	b	0	0	0.05	0.14	0.44	0.05	b	bal
NGK Z-191 Y-TZP	b	0.43	0.52	0	0.03	0.01	0.16	0.17	4.00	bal

[a]Performed at AMMRC (courtesy of Dr. L. Schioler) by emission spectrometry (ICAP source). Results of X-ray fluorescence indicate approximately similar concentration of Hf in all four samples (a quantitative indication of the hafnia content was not obtained).

[b]Indicates presence of element in concentration of less than 0.01 weight percent.

3.4 DENSITY

The sample-to-sample density distribution for each of the zirconia materials evaluated on this program is presented in Figures 9-13. A summary tabulation is provided in Table 5, where open porosity and surface finish information is included. Note that the TZP material (NGK Z-191 Y-PSZ) is higher density than the Mg-PSZ materials.

Figure 14 illustrates the change in density after 1000 hr/1000°C exposure. The Mg-PSZ materials exhibited ~2% decrease in density, whereas the density of the TZP material survived the exposure virtually unchanged. This evidence of the superior stability of TZP correlates with its phase and microstructural retention presented above. The density decrease for Mg-PSZ is the result of the transformation of tetragonal to monoclinic (the density of cubic, tetragonal, and monoclinic forms of zirconia being 6.27, 6.10, and 5.56 g cm^{-3}, respectively). The reflected light microscopy and X-ray diffraction data confirmed the presence of the predominant monoclinic phase in Mg-PSZ after 1000 hr/1000°C exposure.

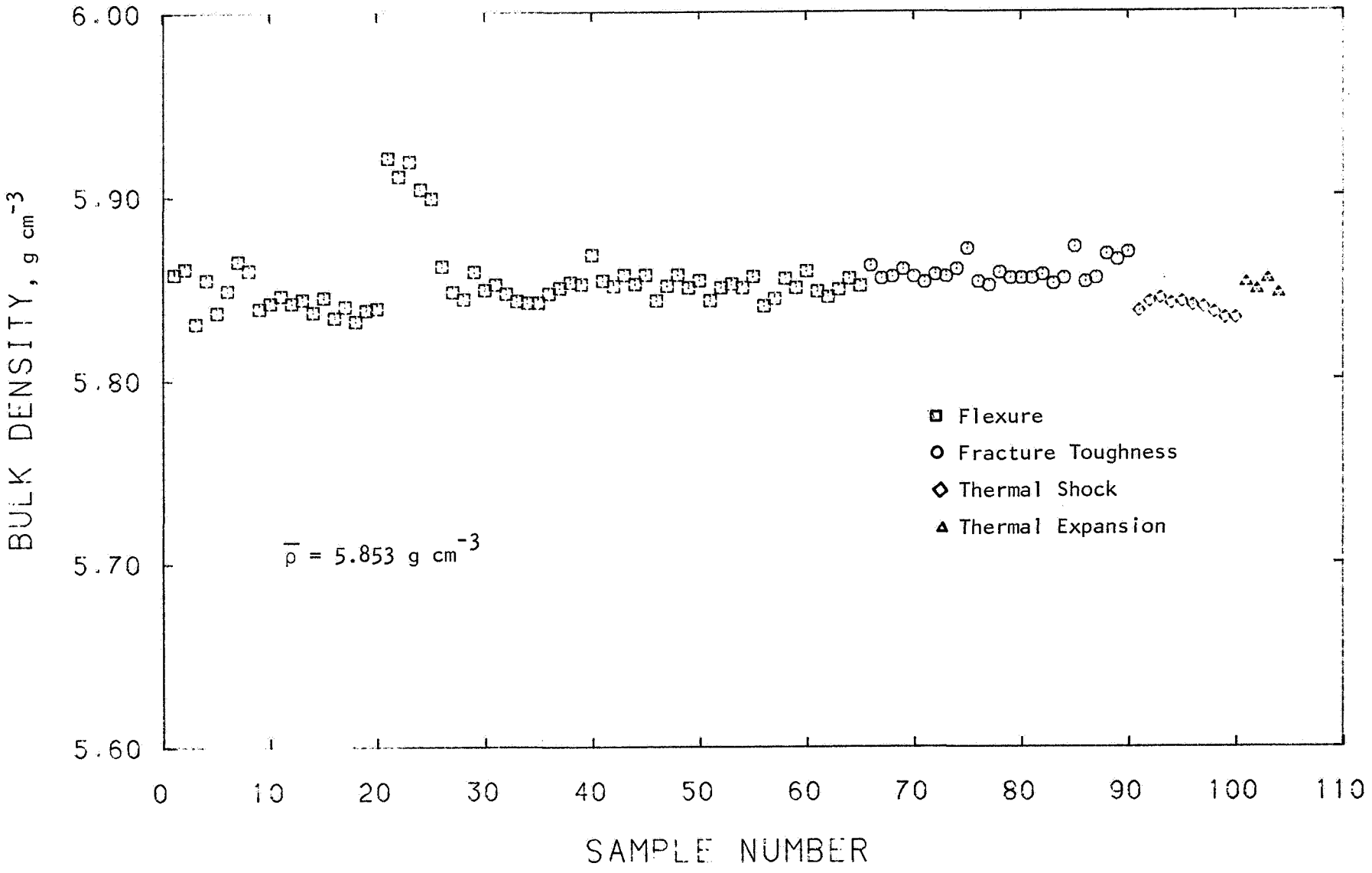

Figure 9. Density of NGK Z-191 Y-TZP.

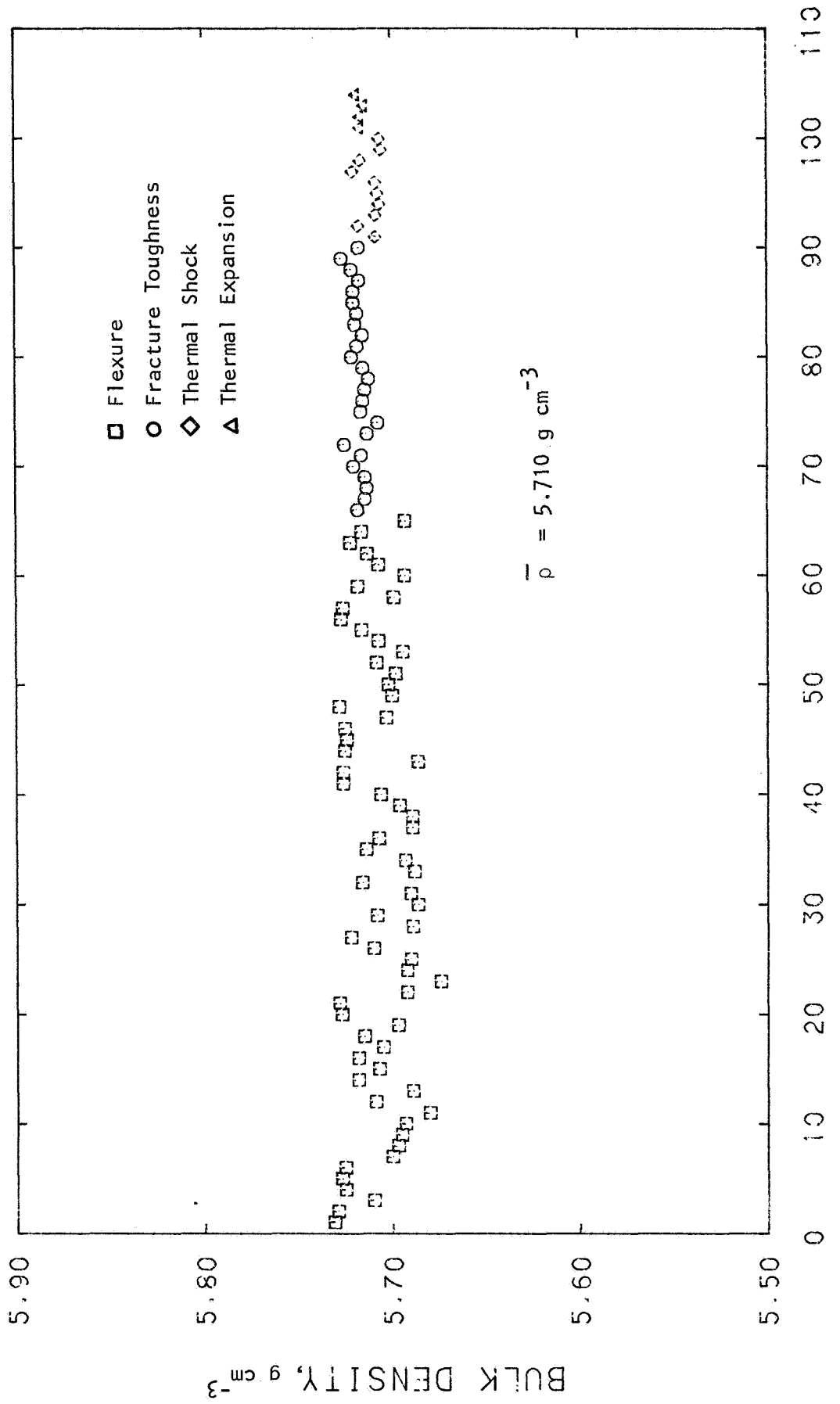

Figure 10. Density of Nilsen MS Mg-PSZ.

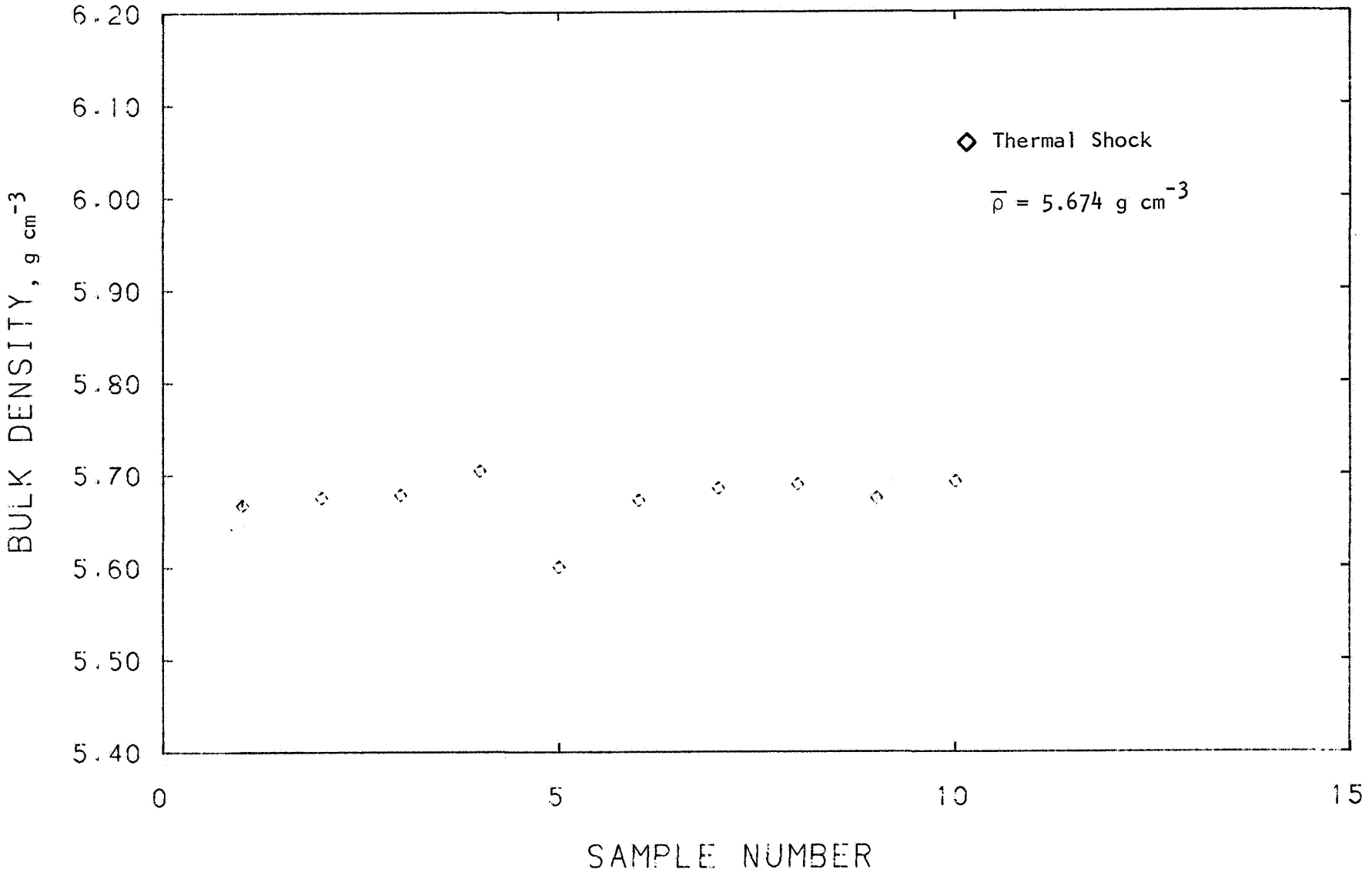

Figure 11. Density of Nilsen TS Mg-PSZ.

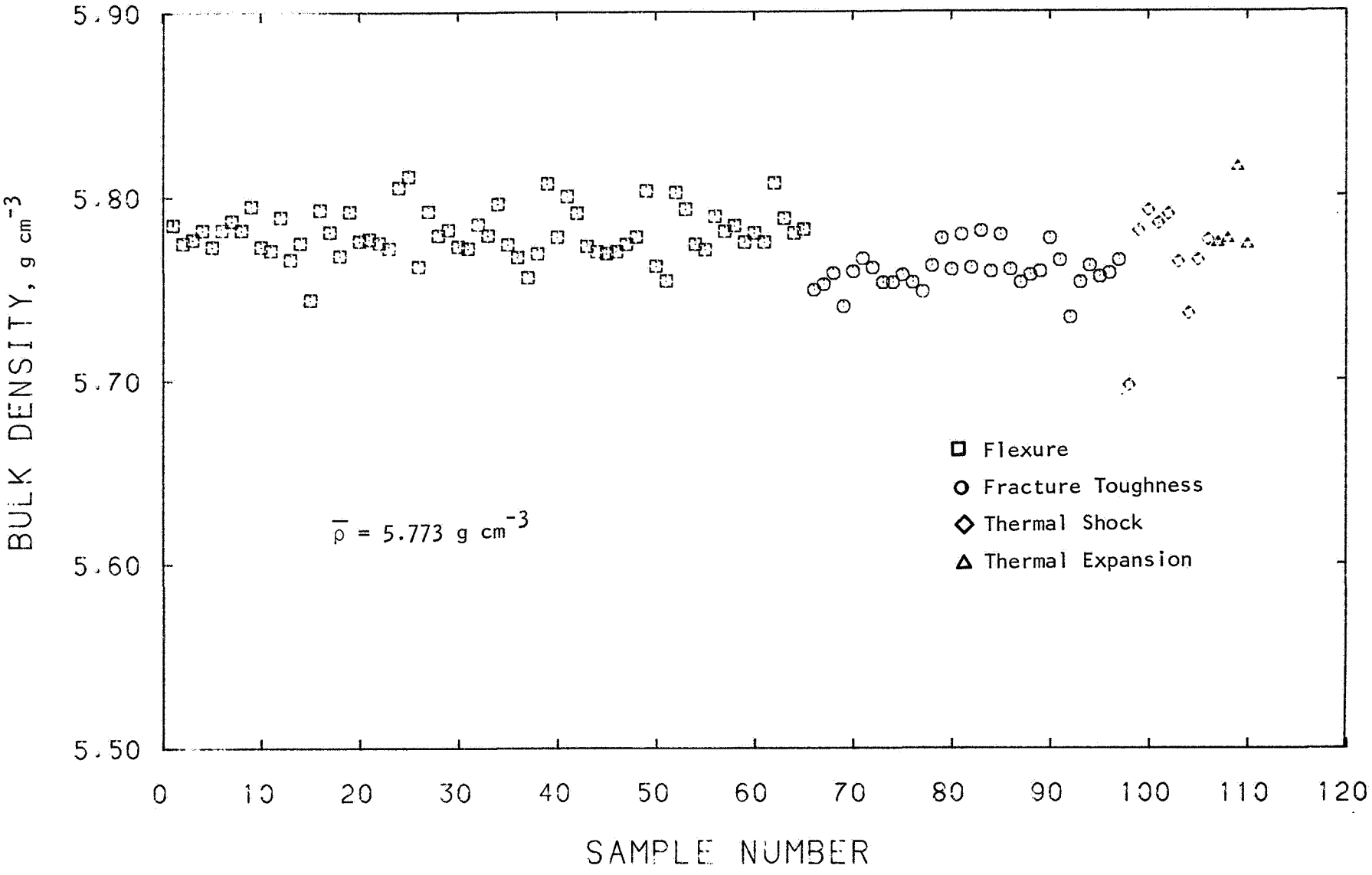

Figure 12. Density of Feldmuhle ZN-40 Mg-PSZ.

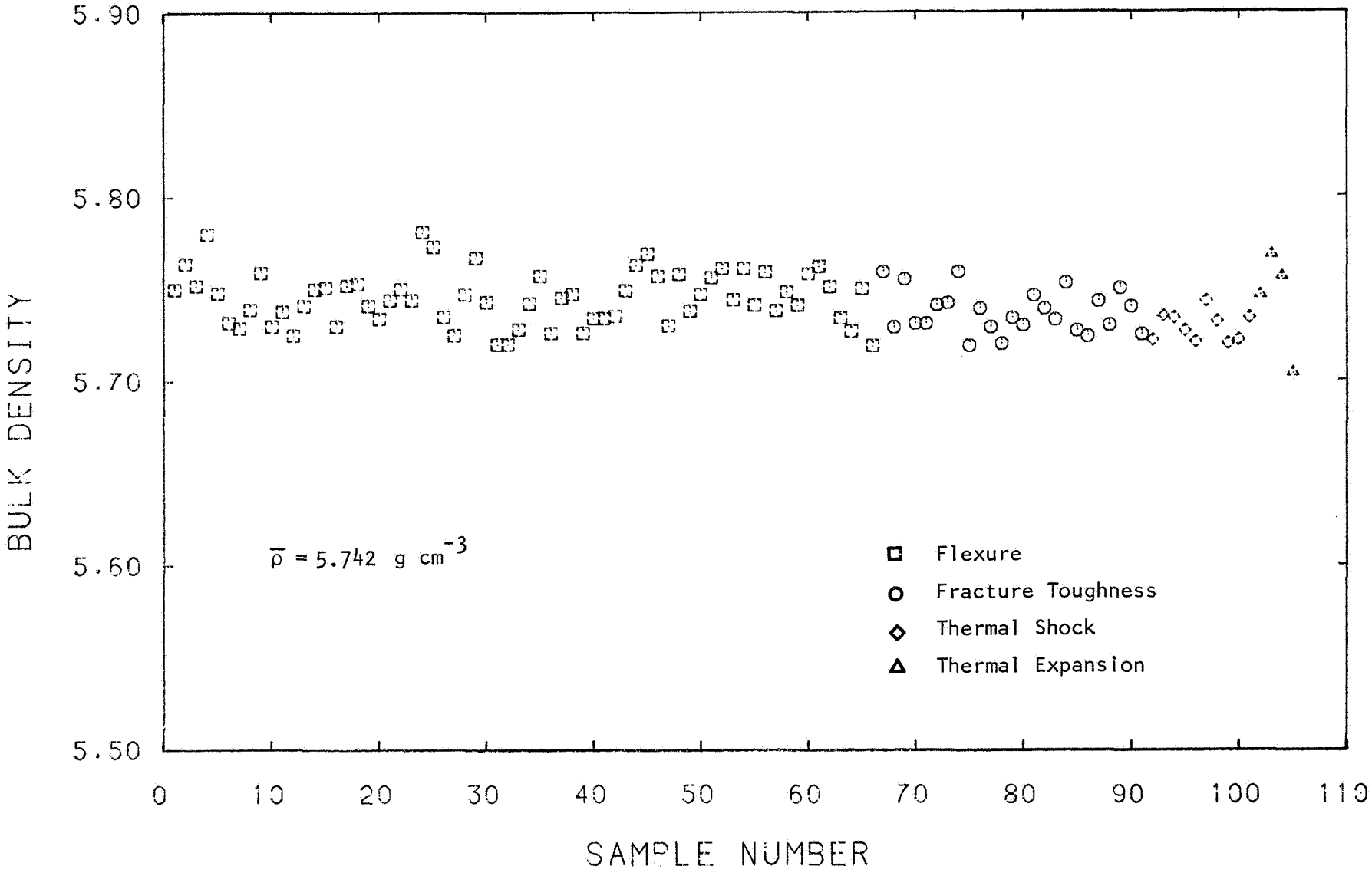

Figure 13. Density of Coors 3% Mg-PSZ.

TABLE 5. DENSITY OF TRANSFORMATION-TOUGHENED ZIRCONIA

Material	Bulk Density, g cm^{-3}					Open Porosity, %	Surface Finish µin. (rms)
	Mean	Maximum	Minimum	n[a]	S.D.[b]		
Nilsen:							
• MS Grade Mg-PSZ	5.710	5.731	5.674	104	0.013	0	11
• TS Grade Mg-PSZ	5.674	5.704	5.600	10	--	0-0.01	14
Feldmuhle ZN-40 Mg-PSZ	5.773	5.815	5.697	110	0.018	0-0.02	50
Coors Mg-PSZ	5.742	5.781	5.704	105	0.015	0.03	7-32
NGK Z-191 Y-TZP	5.853	5.921	5.831	104	0.016	0-0.02	16

[a]Number of samples.

[b]Standard deviation.

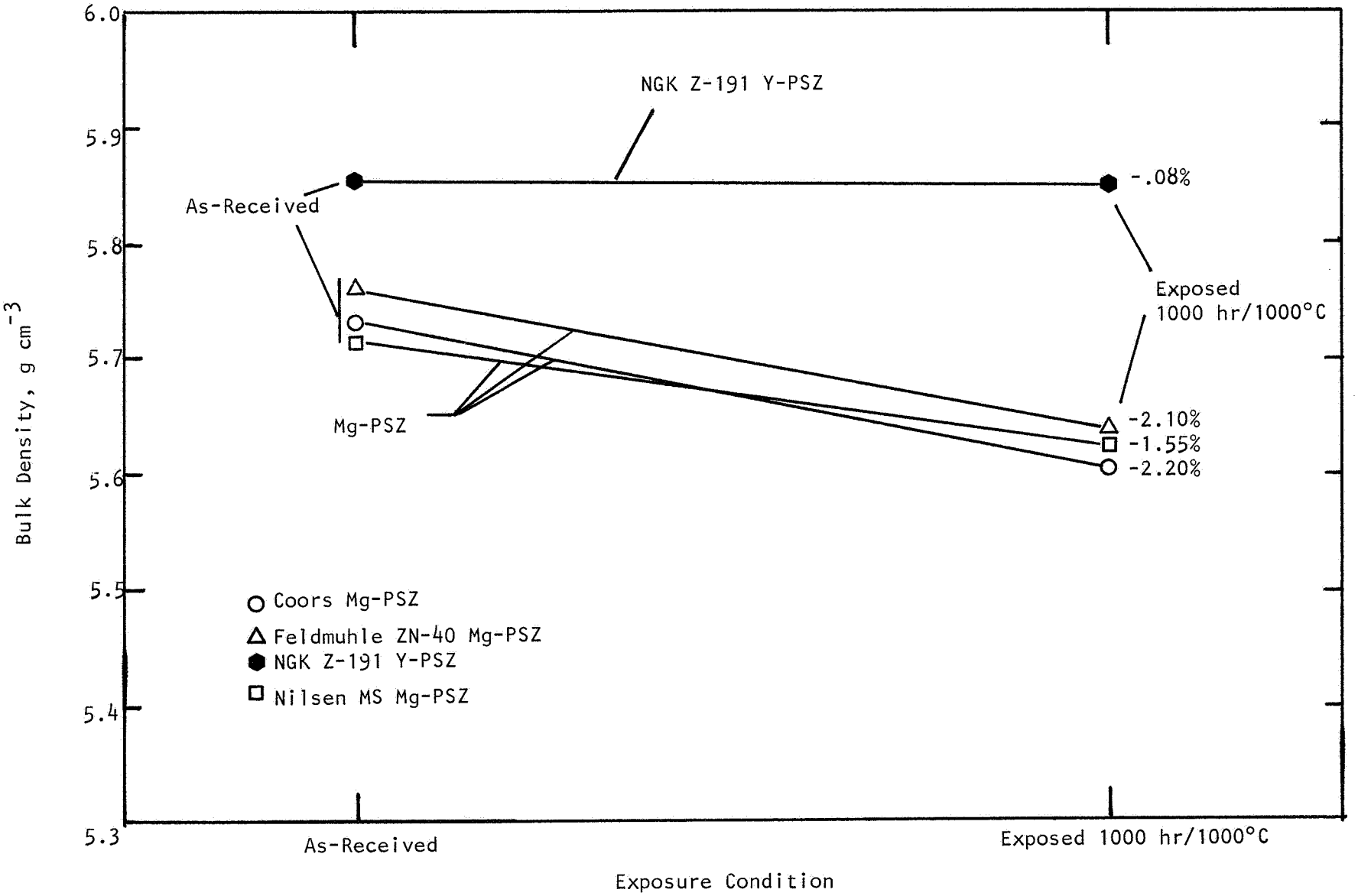

Figure 14. Density changes with overaging in transformation-toughened zirconia.

4. FLEXURAL STRENGTH

The flexural strength was determined in the quarter 4-point configuration on test samples that were of nominal dimensions 1/8 x 1/4 x 2 1/4 in. The upper and lower spans were 0.875 and 1.750 in., respectively, and the crosshead deformation rate was 0.02 ipm. It is important to recognize that the test sample population was small--from 5 to 8--and therefore only rough estimates of Weibull moduli can be made.

4.1 STRENGTH AT ROOM TEMPERATURE

The fast fracture bend strength results for the four transformation-toughened zirconia materials are presented in Figure 15.* NGK Z-191 TZP (Y_2O_3-stabilized) is the strongest material tested, having a room-temperature 4-point bend strength of ~130 ksi. This is a result of its small grain size (~2 μm vs. ~50 μm for the other materials). The strongest MgO-stabilized material was Nilsen MS Mg-PSZ, with a room-temperature strength of ~92 ksi. Also note in Figure 15 that these two materials exhibited the highest Weibull moduli. The Weibull modulus is a measure of the dispersion of the strength data. The NGK and Nilsen materials exhibited Weibull moduli of 19.4 and 24.7, respectively. These values were determined by a linear least-squares regression technique, using the sample population of eight. These values of m, the Weibull modulus, are high for ceramics, and indicate the high degree of process control being achieved for these materials. In contrast, the Weibull moduli for Feldmuhle ZN-40 Mg-PSZ and Coors Mg-PSZ were 10.5 and 6.6, respectively. These materials exhibit properties considerably more variable. It is concluded that the NGK and Nilsen materials are more processing-mature, as indicated by higher strength and higher Weibull moduli. Note that high Weibull modulus is expected to be achieved with high toughness ceramics. High toughness means greater flaw tolerance. This is seen from the Griffith

*Detailed results are tabulated in the Appendix, which includes strength, failure strain, elastic modulus, and fracture origins.

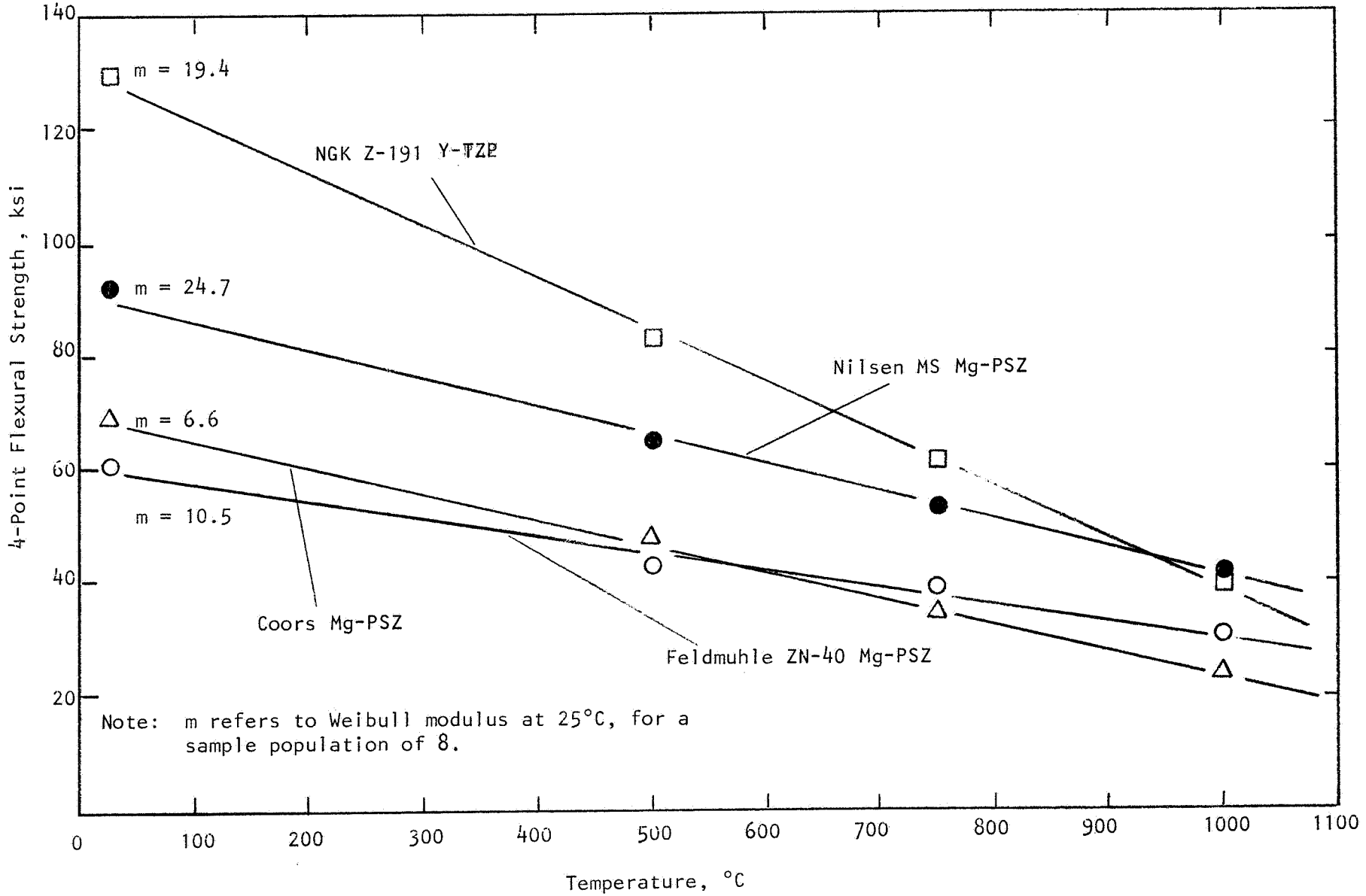

Figure 15. Baseline (unexposed) flexural strength of zirconia.

relation, where strength is proportional to the toughness and inversely proportional to the square root of the flaw size. The strength-allowable flaw size relation, illustrating the benefit of high toughness, is shown in Figure 16.

4.2 STRENGTH AT ELEVATED TEMPERATURE

At elevated temperature, Figure 15 illustrates that the flexure strength of all four materials, Y-TZP as well as Mg-PSZ, decreases linearly with temperature in the range 25°-1000°C. This strength reduction is not an intergranular effect as it is in covalently bonded ceramics such as silicon nitride which require oxide sintering aids that result in deformable glassy grain boundary films. Rather, linear strength reduction with temperature for transformation-toughened zirconia is interpreted to be the result of the metastable tetragonal phase (which is responsible for high fracture toughness) becoming increasingly stable as the test temperature is raised. The high degree of metastability of the tetragonal phase is what causes high toughness via the stress-induced martensitic phase transformation that occurs in the tensile stress field ahead of the advancing crack tip. Since the tetragonal phase is stable from above approximately 1100°C, it follows that as the test temperature of the bend test approaches 1100°C, this phase is less metastable (i.e., more stable), contributes to toughening less, and results in lower strength. Note that XRD results (refer to Table 3) for the fast fracture tests showed no change in phase assemblage as a function of temperature. The tetragonal phase is still present as the test temperature is raised, but it is more stable and thus contributes to toughening and strength retention to a lesser degree.

This effect of increased stability of the tetragonal phase with increasing temperature and thus loss of properties is inherent to transformation-toughened zirconia. Note in Figure 15 that the amount of fast fracture strength decrease with temperature is, in general, directly proportional to the original room-temperature strength of the material. That is, the higher the strength at 25°C, the greater the strength loss at elevated temperature. For instance, the strength loss from 25° to 750°C for the NGK material is 54% and that of the Feldmuhle material is 36%. This temperature effect is related to the initial state of the metastable tetragonal particles. Over the 25°-

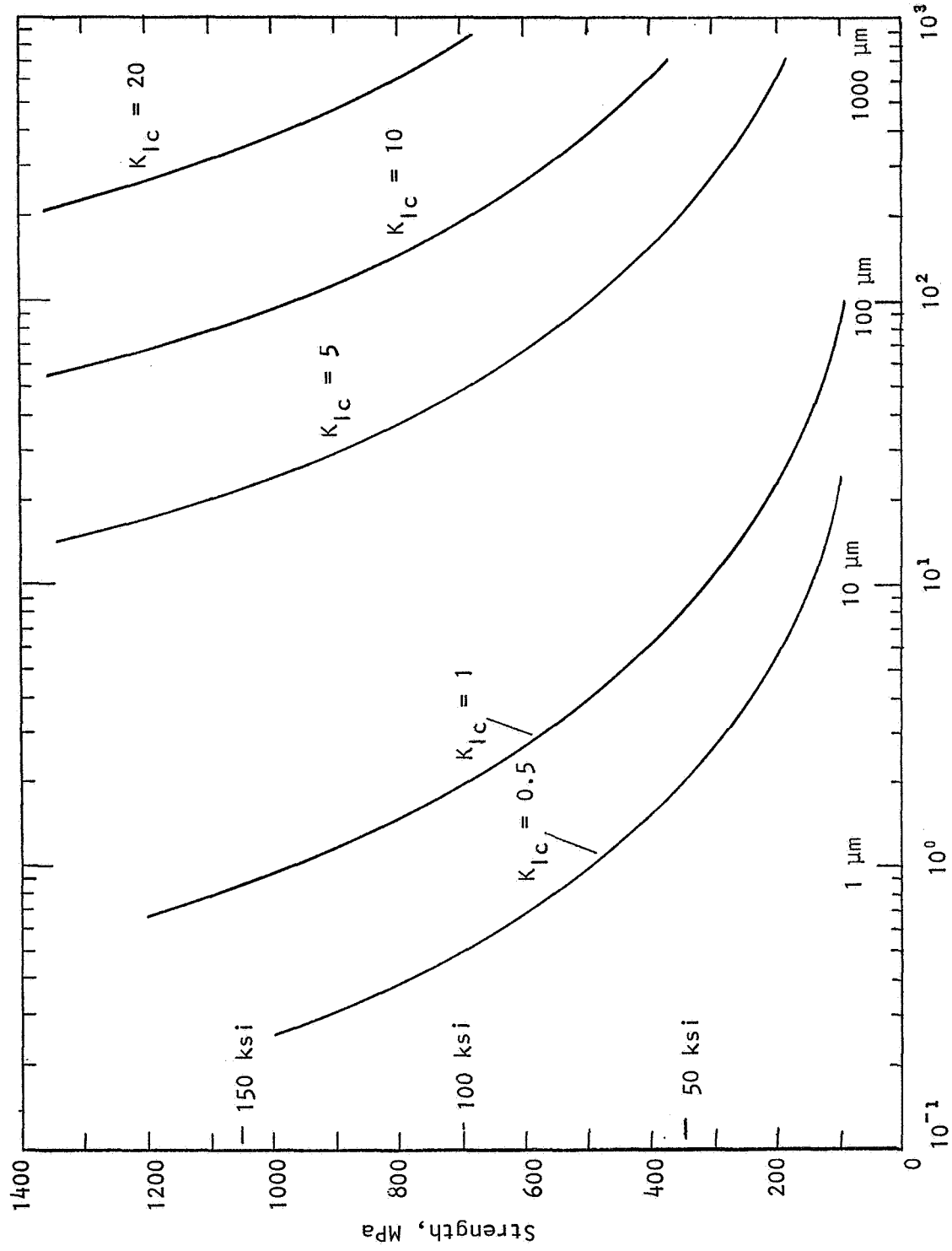

Figure 16. Strength-flaw size relation, showing effect of fracture toughness.

1000°C range, the fast-fracture strength reduction is 50-70%. The properties are controlled by the degree of metastability of the tetragonal phase. Therefore, low temperature use becomes a necessary intrinsic limitation for transformation-toughened zirconia materials.

4.3 STRENGTH AFTER 1000 HR/1000°C STATIC THERMAL EXPOSURE

The fast fracture results are not to be confused with overaging phenomenon in TT-ZrO_2, which involves tetragonal-to-monoclinic phase transformation, and resultant loss in strength. Overaging can occur in the absence of stress. It basically involves phase transformation that occurs as the tetragonal phase converts to monoclinic after prolonged time at elevated temperature. Physically, the simplest interpretation is precipitate or particle growth in size to the critical diameter where the matrix can no longer constrain the particle in its metastable tetragonal condition, resulting in transformation to the monoclinic state. For instance, Figure 17 illustrates the reduction in room-temperature strength experienced by the four candidate zirconia materials after they had been exposed in the unstressed state in static laboratory air for 1000 hr at 1000°C. Note that Y-PSZ (i.e., NGK Z-191 TZP) is much more stable with respect to overaging. In the current tests, only 7% of the strength was lost for that Y-TZP after 1000 hr/1000°C exposure. The Mg-PSZ materials experienced 30-70% strength reductions. X-ray diffraction analyses presented in Table 3 confirm that this is an overaging phenomenon for Mg-PSZ, and confirm the excellent strength retention of Y-TZP. Table 3a shows that after 1000 hr/1000°C exposure, the NGK Z-191 Y-TZP had the same tetragonal content (99-100%) as it had originally. The reflected light micrograph of NGK Z-191 after 1000 hr/1000°C exposure lends further support to this evidence of stability of Y-TZP. The microstructure looks virtually unchanged after exposure, as seen in Figure 8.

In contrast is the behavior of Mg-PSZ. Note in Table 3b that for the post 1000 hr/1000°C exposure Nilsen MS Mg-PSZ, for instance, both tetragonal and cubic contents decreased by about a factor of three, with corresponding increase in monoclinic to a level an order of magnitude greater than was present in unexposed material. This is more than simple overaging, where tetragonal converts to monoclinic. The additional conversion of cubic to monoclinic suggests that decomposition and/or destabilization are also

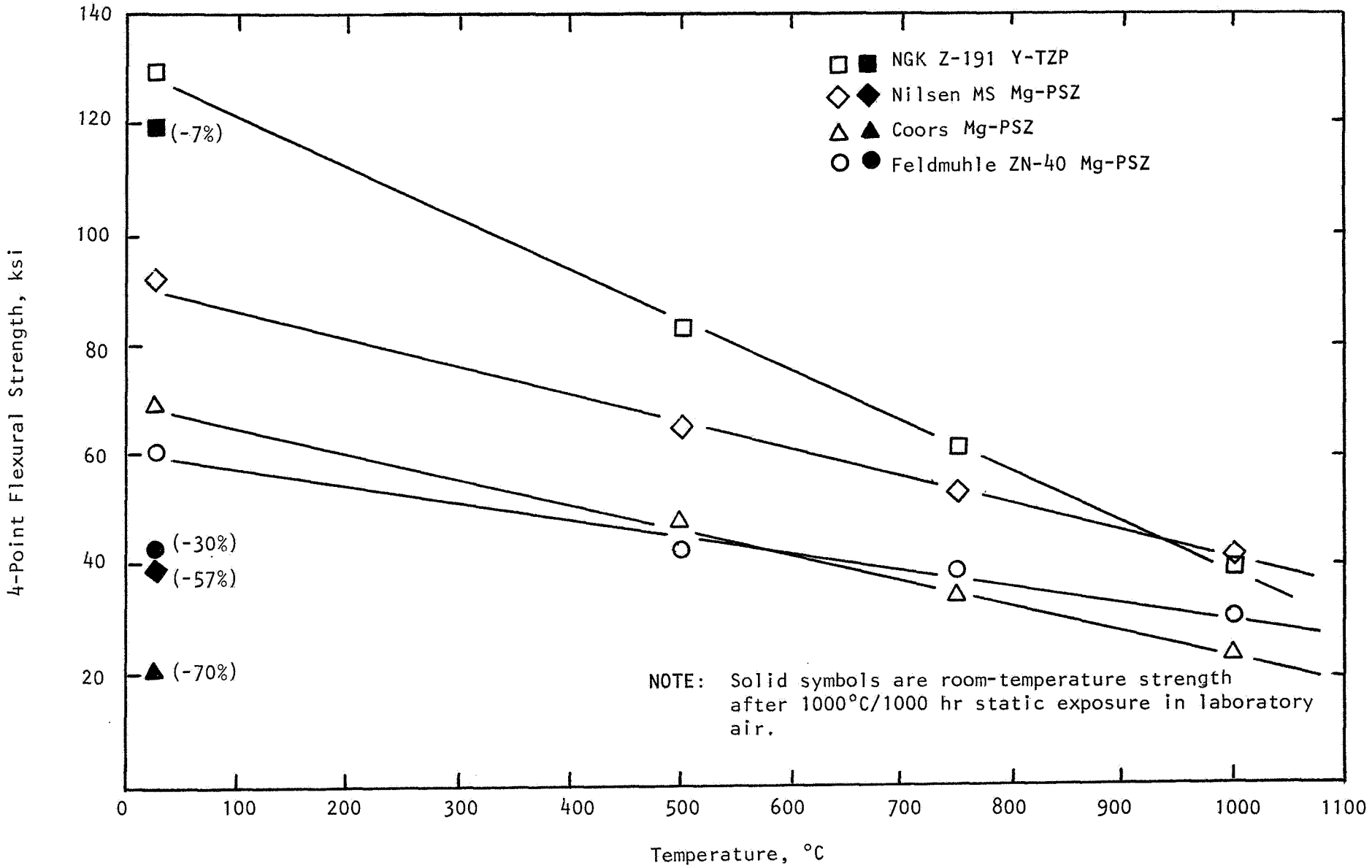

Figure 17. Flexural strength of zirconia as a function of temperature and after 1000 hr/1000°C exposure.

involved. The reflected light micrograph in Figure 5 confirms the degradation of Nilsen MS Mg-PSZ after the extended exposure at 1000°C. The lightest phase in the micrograph is monoclinic zirconia. Therefore, it is evident that a monoclinic-rich grain boundary phase has developed during the 1000 hr/1000°C thermal exposure. Similar comments hold for the other Mg-PSZ materials investigated on this program. Note, however, that Feldmuhle ZN-40 Mg-PSZ degraded to a lesser extent than did Nilsen and Coors materials. Figure 17 illustrates that Feldmuhle ZN-40 exhibited only a 30% strength reduction after 1000 hr/1000°C exposure. This correlates with the post-exposure microstructure shown in Figure 6. Note that the monoclinic grain boundary phase is not as pronounced as for the Nilsen and Coors materials (the microstructures of which were shown in Figures 5 and 7, respectively). X-ray diffraction results also illustrate the greater stability of Feldmuhle ZN-40. Table 3c illustrates that while no tetragonal remained after exposure (indicative of overaging, $t \rightarrow m$), the cubic content did not decrease as much as the other Mg-PSZ materials. This indicates greater resistance to decomposition or destabilization. Therefore, a correlation exists among strength retention, microstructural appearance, and phase assemblage. Clearly, overaging phenomena together with decomposition and/or destabilization occur simultaneously and in varying degrees in Mg-PSZ materials.

Once Mg-PSZ is in an overaged condition, no further strength reductions with temperature occur. For instance, Figure 18 presents the 1000°C bend strength of exposed (overaged) materials. In general, no temperature effect is observed. The strength at 1000°C of the overaged Mg-PSZ is roughly equivalent to its residual room-temperature strength.

SEM fractography was conducted on all tested samples. Representative results are presented in Figures 19-23 for NGK Z-191 Y-TZP, Figures 24-28 for Nilsen MS Mg-PSZ, Figures 29-33 for Feldmuhle ZN-40 Mg-PSZ, and Figures 34-38 for Coors Mg-PSZ. In general, fracture origins in these transformation-toughened zirconia materials were pores and pore clusters, 20 to 100 μm in size. Occasionally, a large grain was the fracture origin. Grain facets were judged to be the fracture origins in several cases.

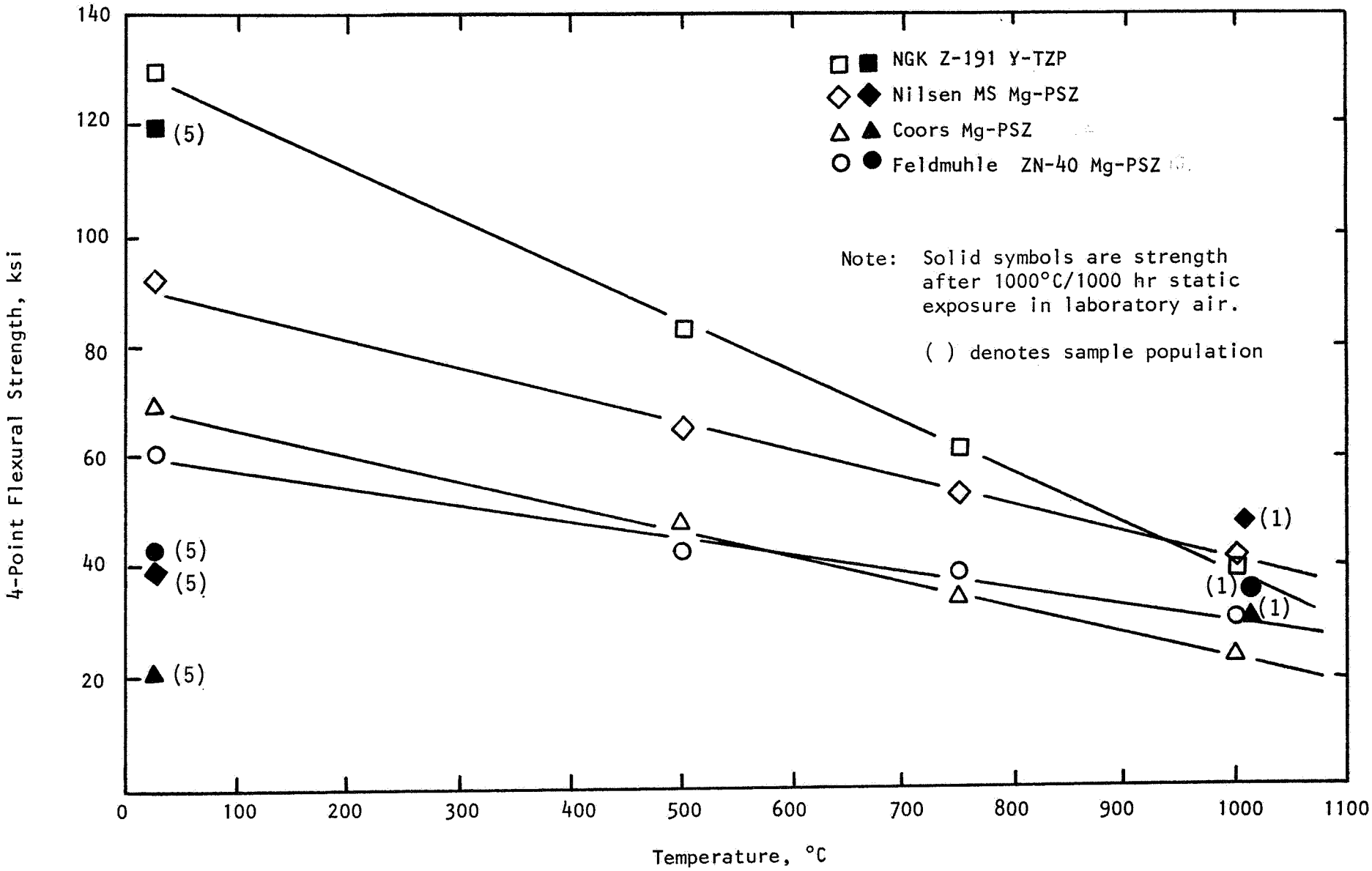

Figure 18. Flexural strength of zirconia as a function of temperature after 1000 hr/1000°C exposure.

ORIGINAL PAGE IS
OF POOR QUALITY

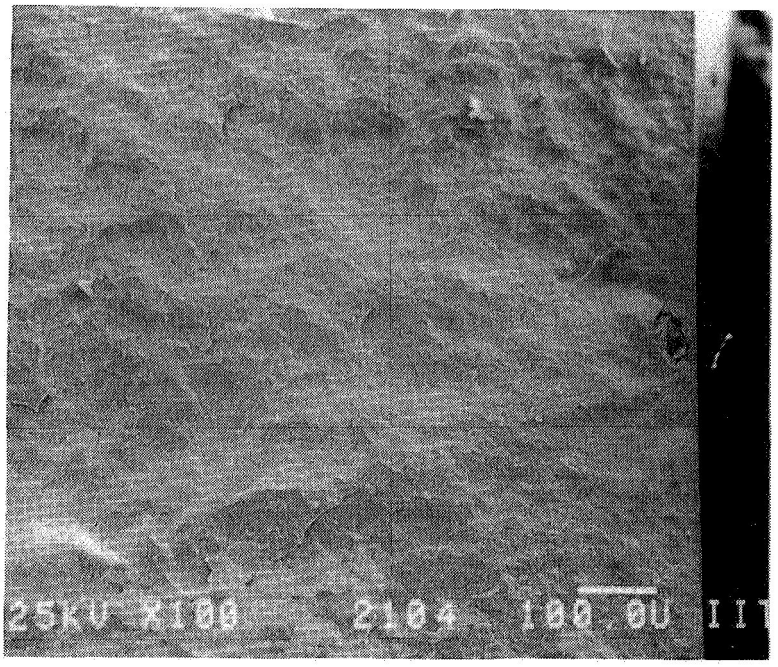

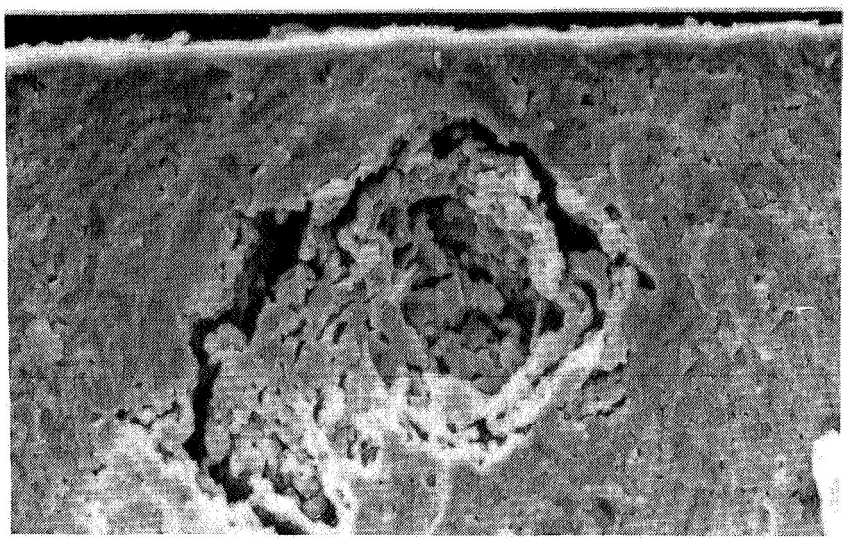

(a) Sample containing a subsurface pore fracture origin (NG1F4).

Figure 19. Fracture surfaces of NGK Z-191 Y-TZP tested at 25°C.

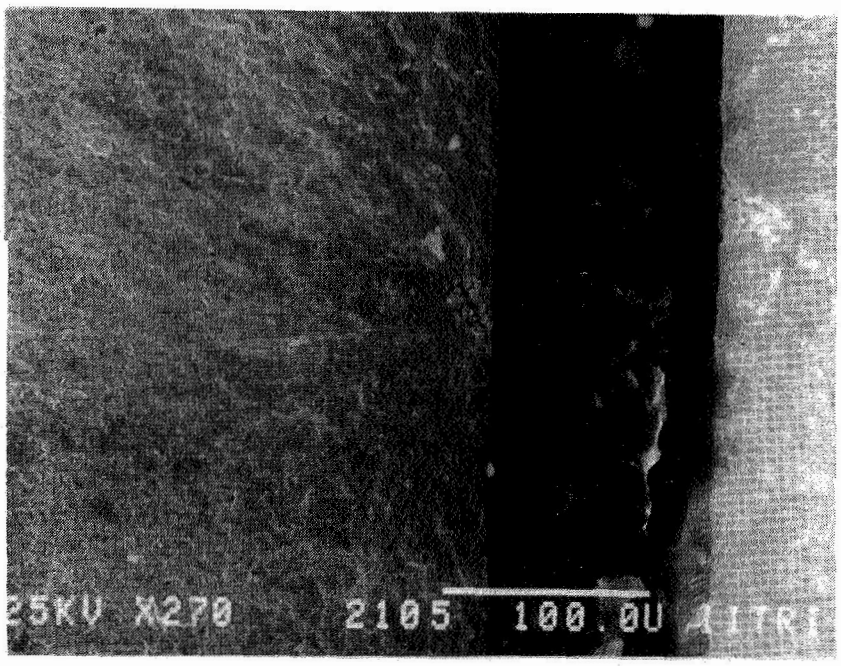

(b) Sample (tensile surfaces together) showing an open pore fracture origin (NG1F5).

Figure 19. (cont.)

ORIGINAL PAGE IS
OF POOR QUALITY

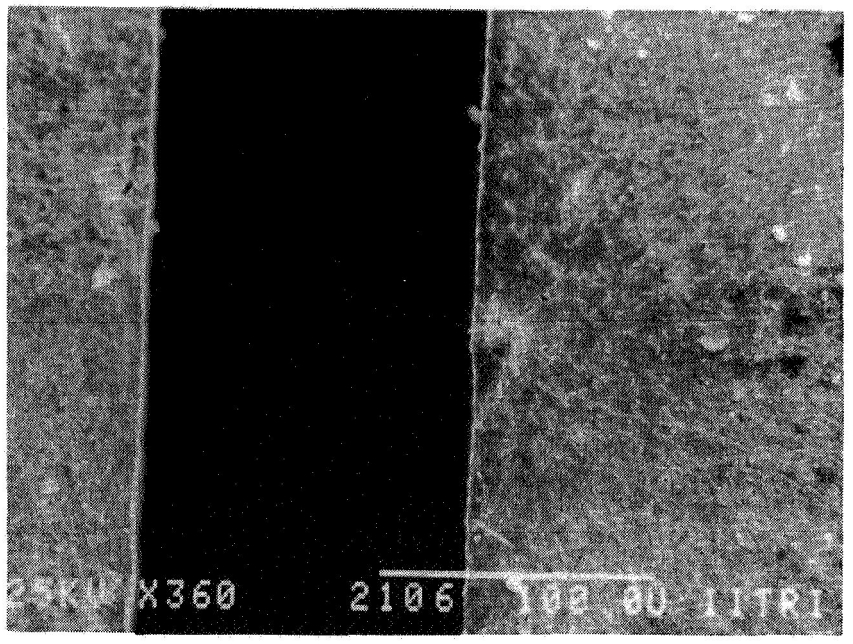

(a) Sample which failed due to a subsurface pore cluster (NG1F6).

Figure 20. Fracture surfaces of NGK Z-191 Y-TZP tested at 500°C.

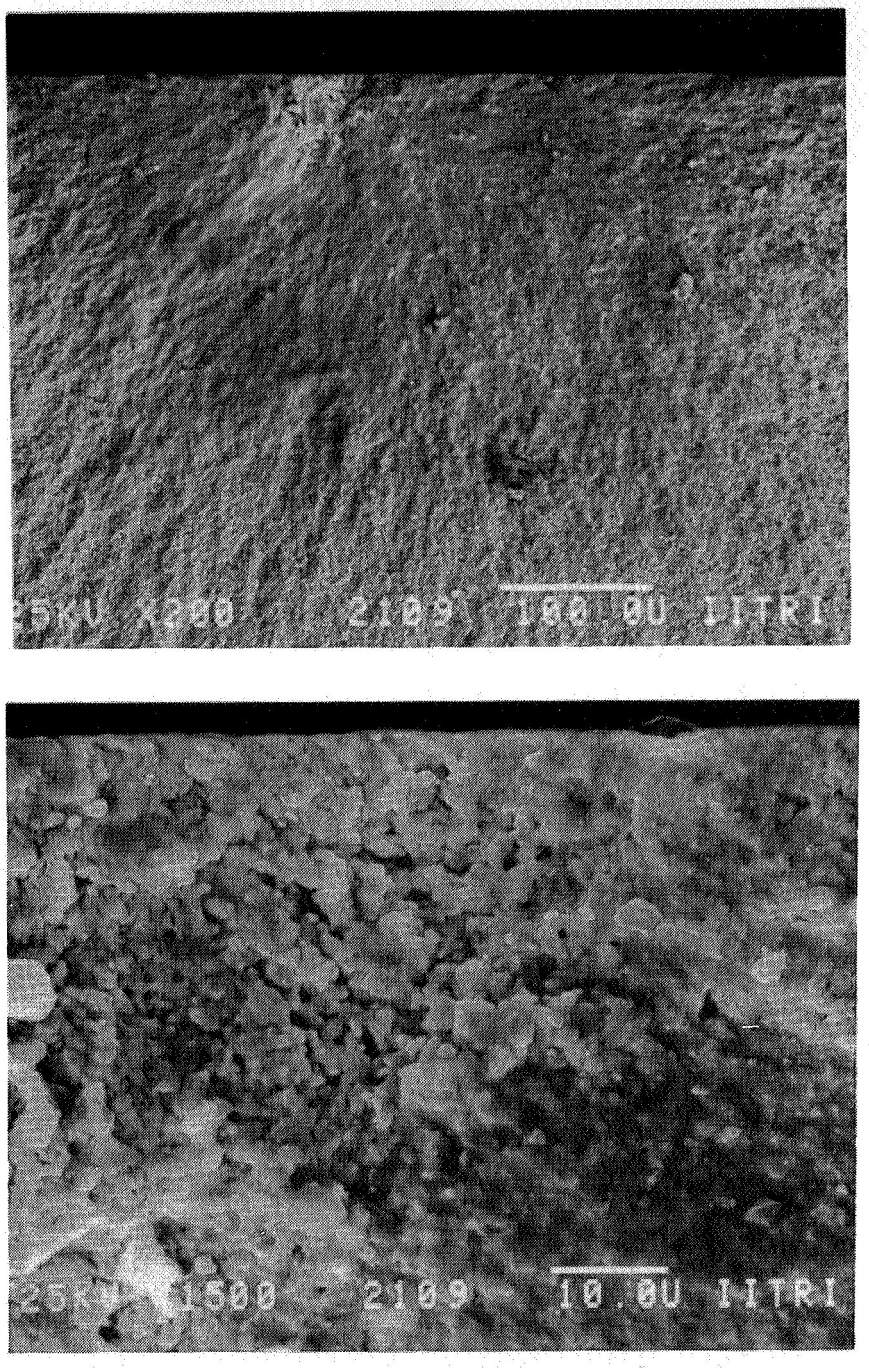

(b) The mirror region contains a subsurface pore cluster (NG1F9).

Figure 20. (cont.)

ORIGINAL PAGE IS
OF POOR QUALITY

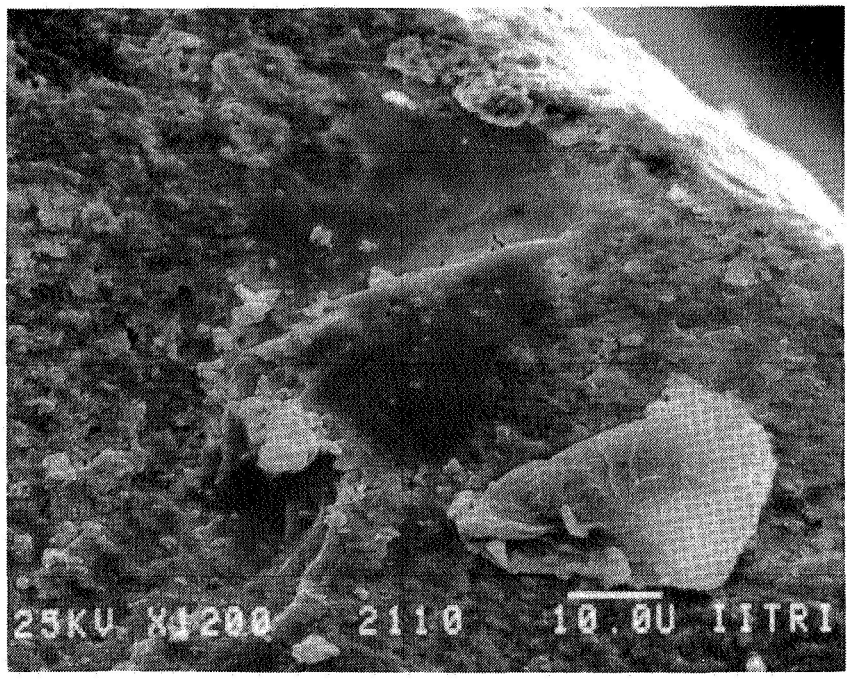

(c) Fracture origin is a large grain located at the bevel (NG1F10).

Figure 20. (cont.)

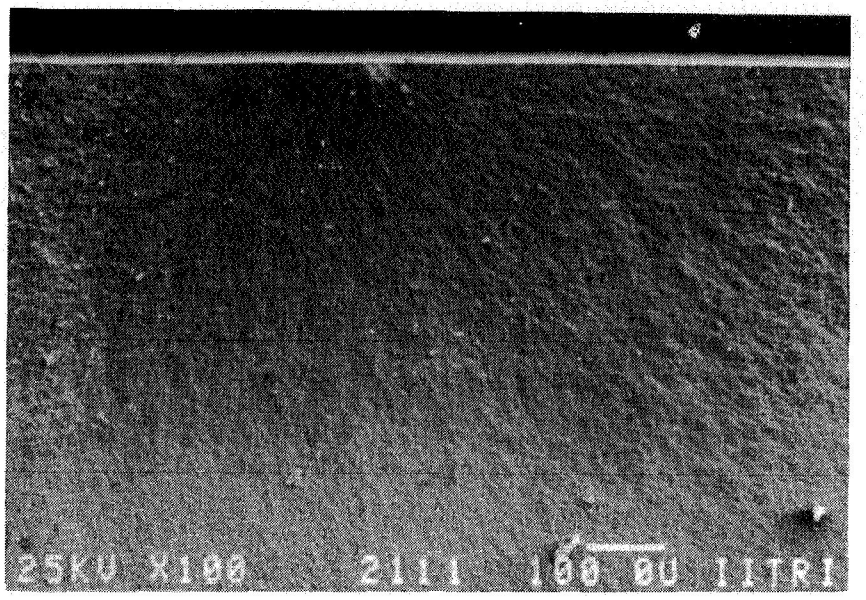

(a) Wide, flat mirror with a porous region fracture origin (NG1F11).

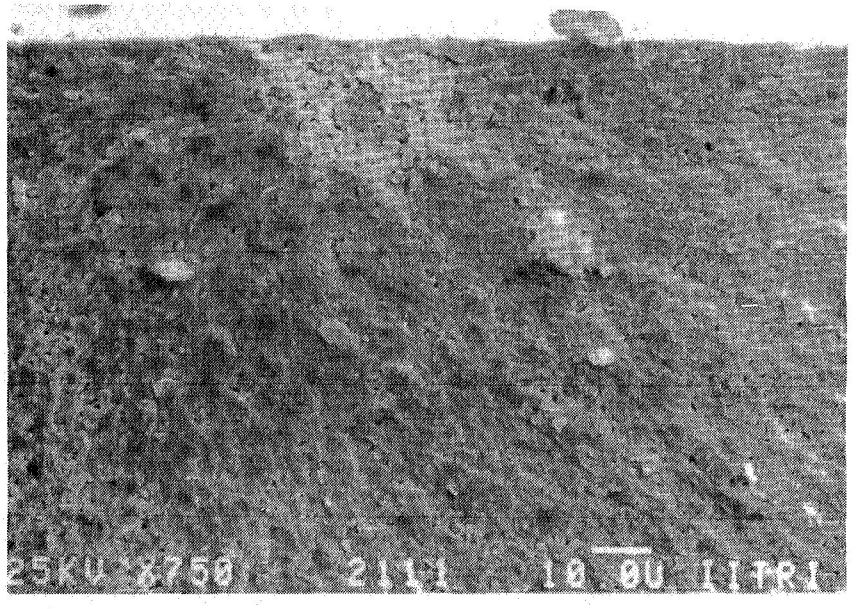

(b) Higher magnification view of sample NG1F11 pore cluster fracture origin.

Figure 21. Fracture surfaces of NGK Z-191 Y-TZP tested at 750°C.

ORIGINAL PAGE IS
OF POOR QUALITY

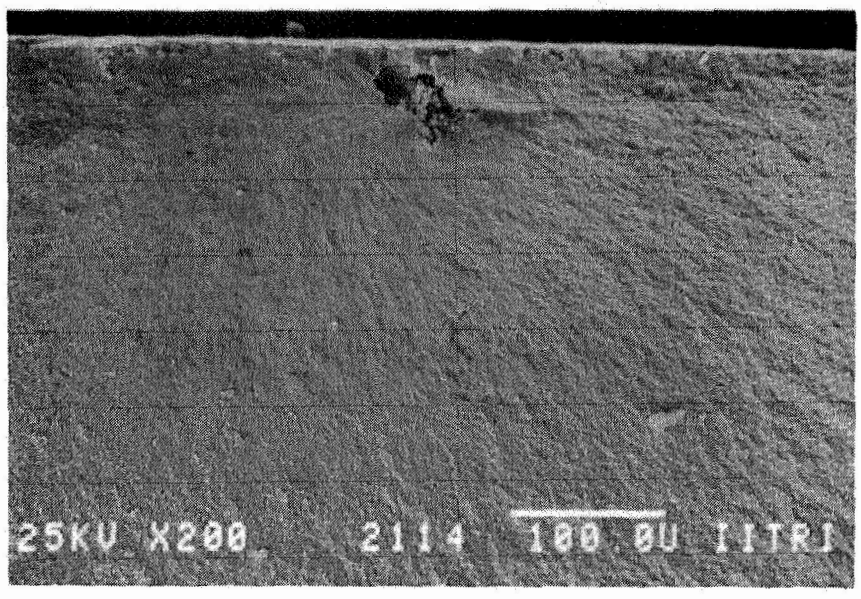

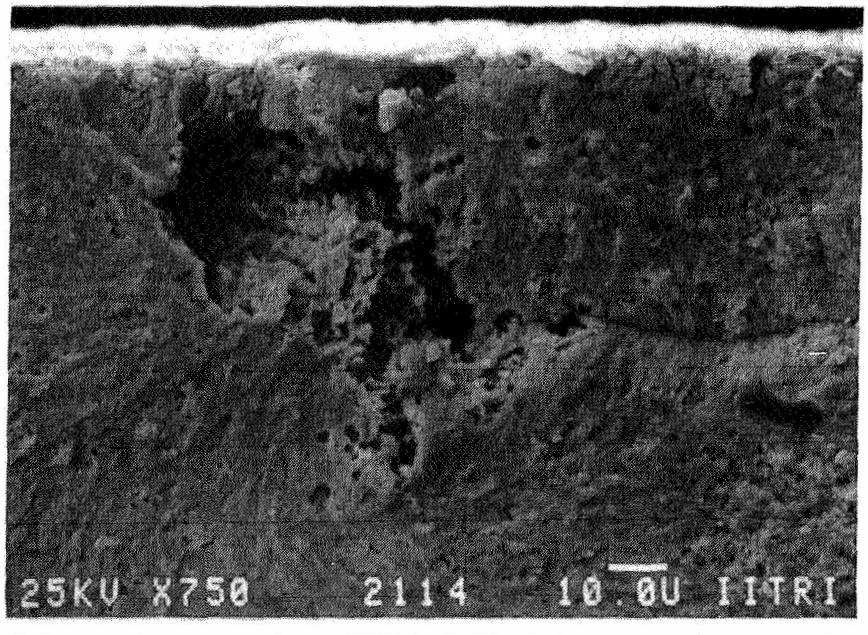

(c) Sample tested at 750°C failed due to a large subsurface pore fracture origin (NG1F14).

Figure 21. (cont.)

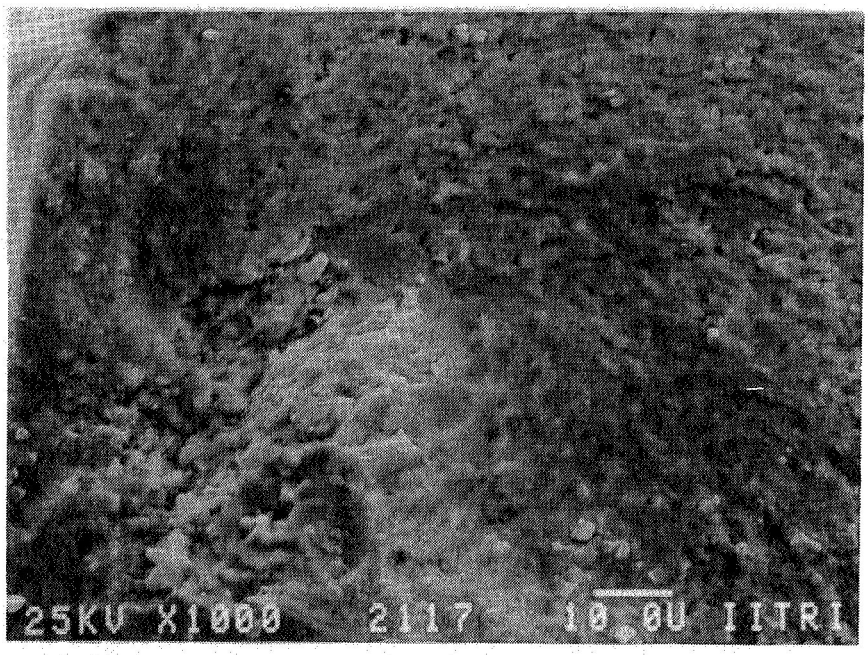

(a) Two views of the subsurface pore fracture origin within sample tested at 1000°C (tensile surfaces left, NG1F17).

Figure 22. Fracture surfaces of NGK Z-191 Y-TZP tested at 1000°C.

ORIGINAL PAGE IS
OF POOR QUALITY

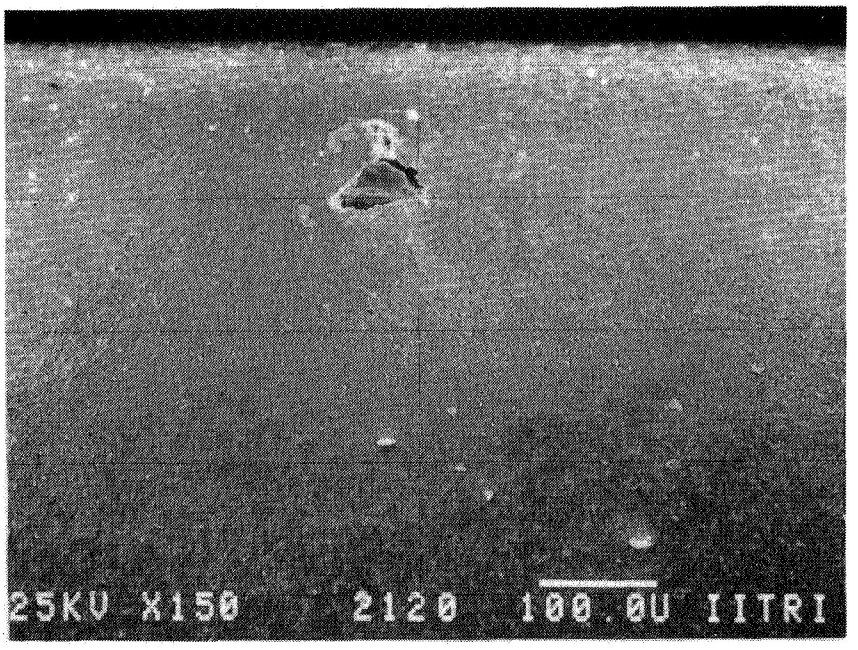

(b) Mirror region of a sample which contained a pore as the fracture origin (NG1F20).

Figure 22. (cont.)

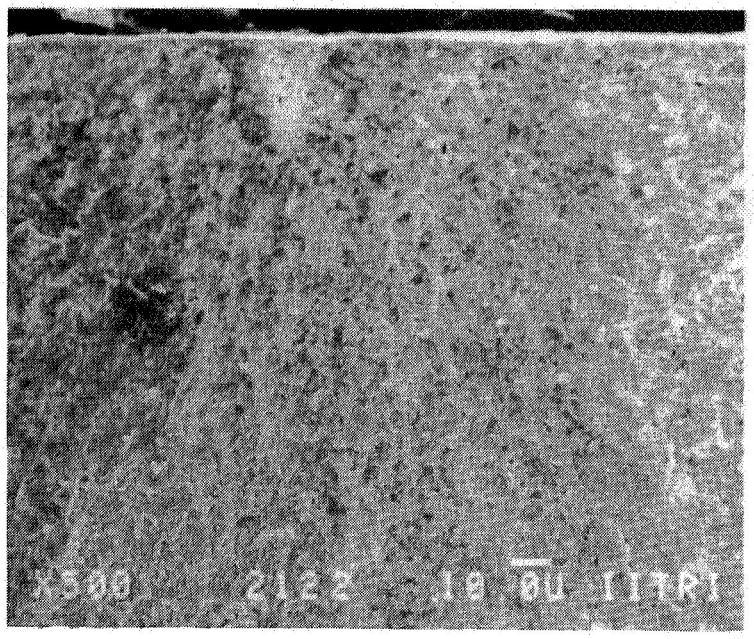

(a) Mirror region showing a fairly flat fracture surface (NG1F22).

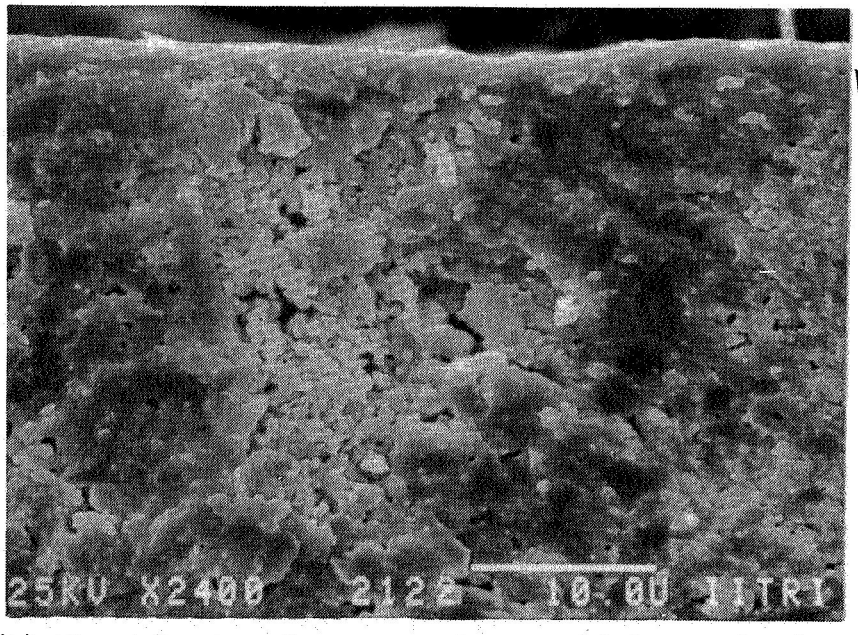

(b) View of subsurface pore cluster which was the fracture origin (NG1F22).

Figure 23. Fracture surfaces of NGK Z-191 Y-TZP tested at 25°C after 1000 hr/1000°C exposure.

ORIGINAL PAGE IS
OF POOR QUALITY

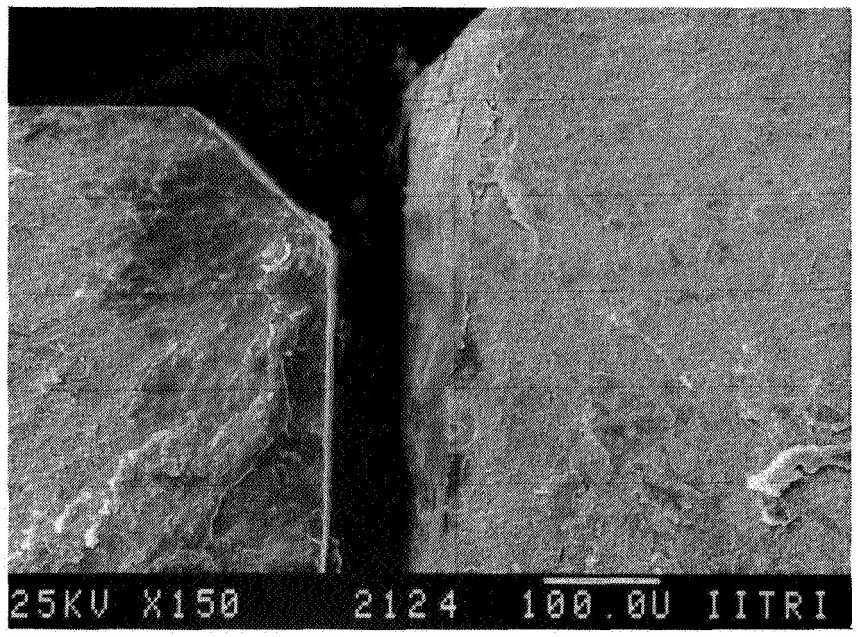

(c) Sample NG1F24 which contained a corner mirror region.

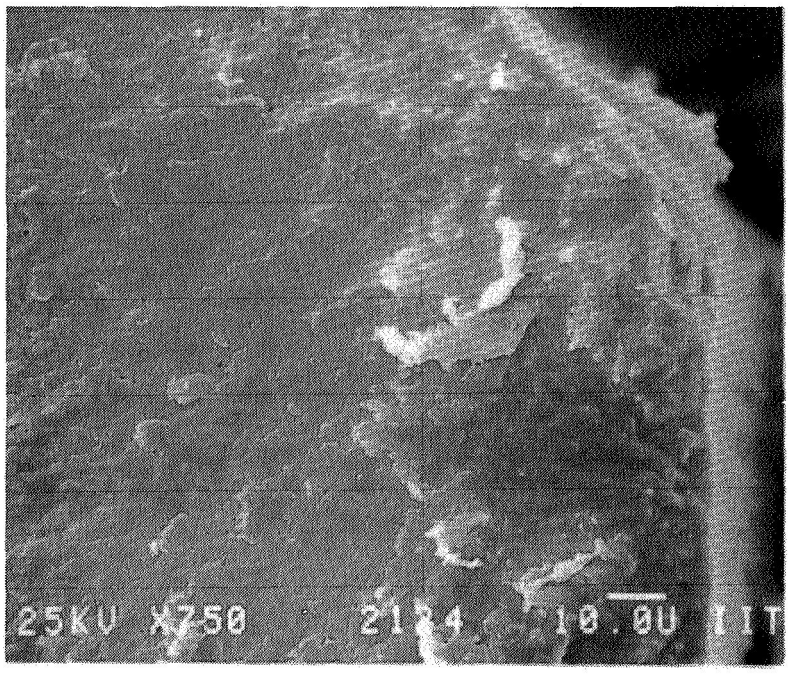

(d) Origin in quarter-round mirror of above sample was a pore at the tensile surface near the bevel (NG1F24).

Figure 23. (cont.)

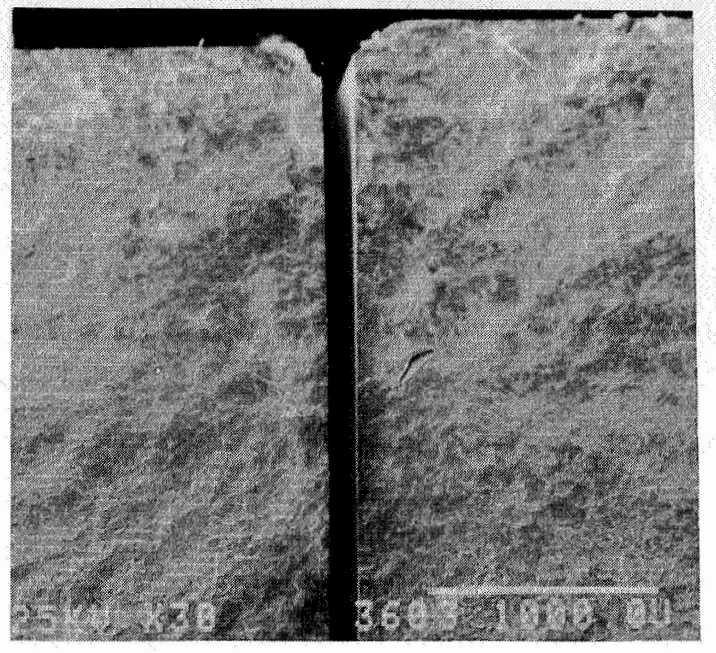

(a)

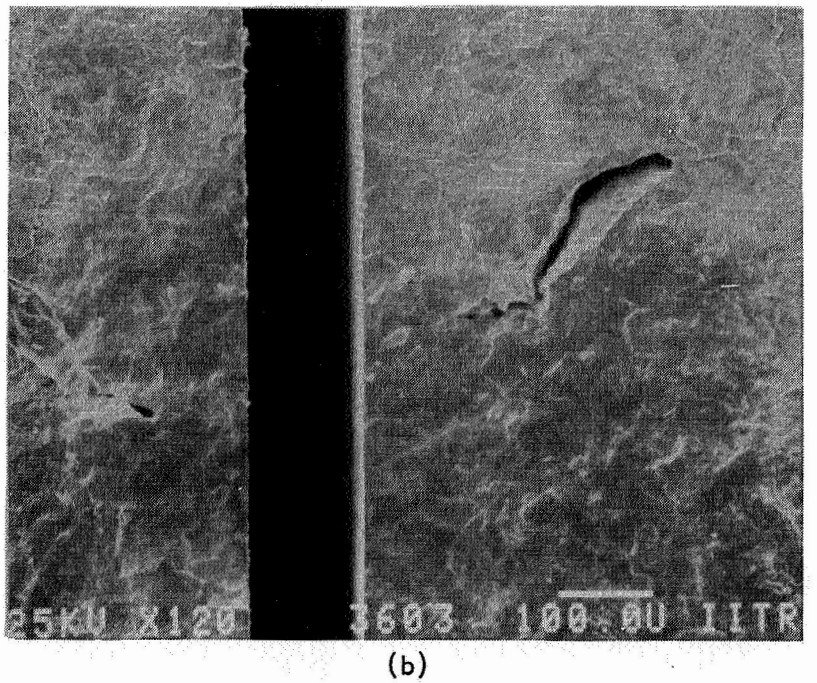

(b)

Figure 24. Fracture surfaces of Nilsen MS-grade Mg-PSZ tested at 25°C. The sample (NV1F3) contained a subsurface pore as the fracture origin.

ORIGINAL PAGE IS
OF POOR QUALITY

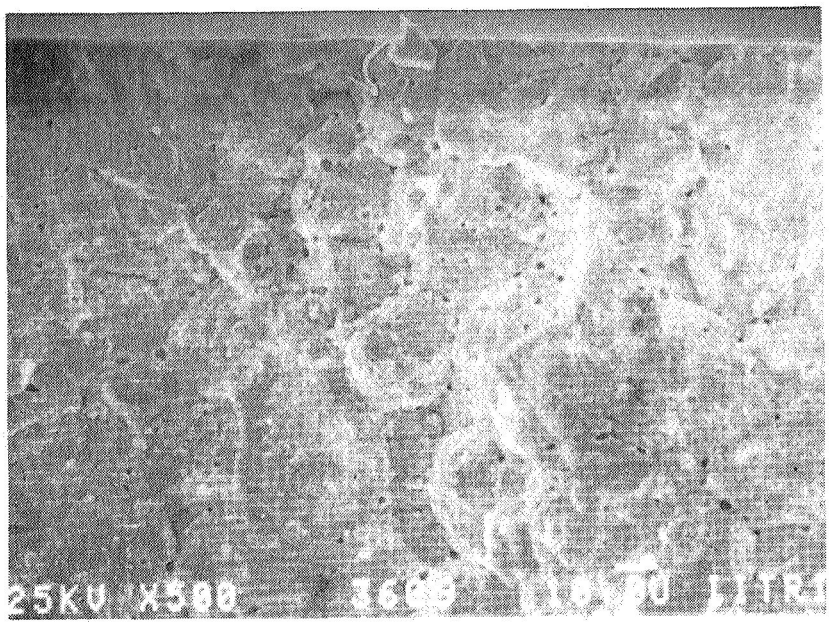

(a)

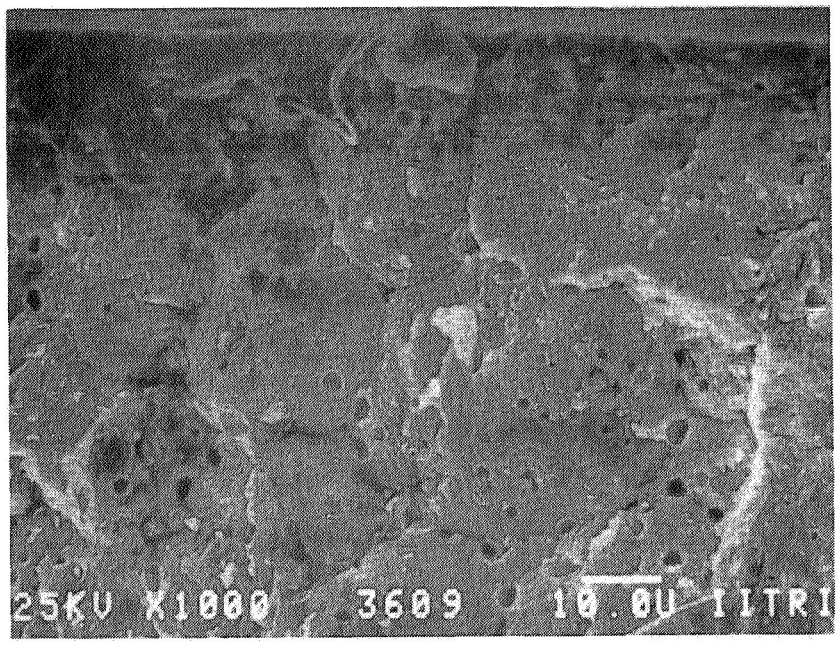

(b)

Figure 25. Fracture surfaces of Nilsen MS Mg-PSZ sample NV1F9 tested at 500°C. The sample contained a poorly sintered region, indicated by intragranular fracture, which was the fracture origin. Note the inter- and intragranular porosity and the grain facets.

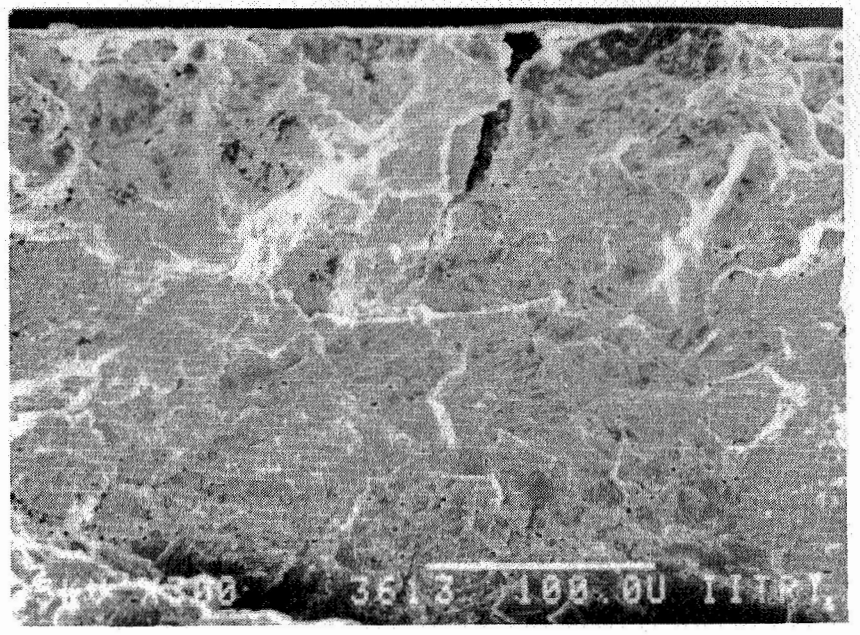

(a)

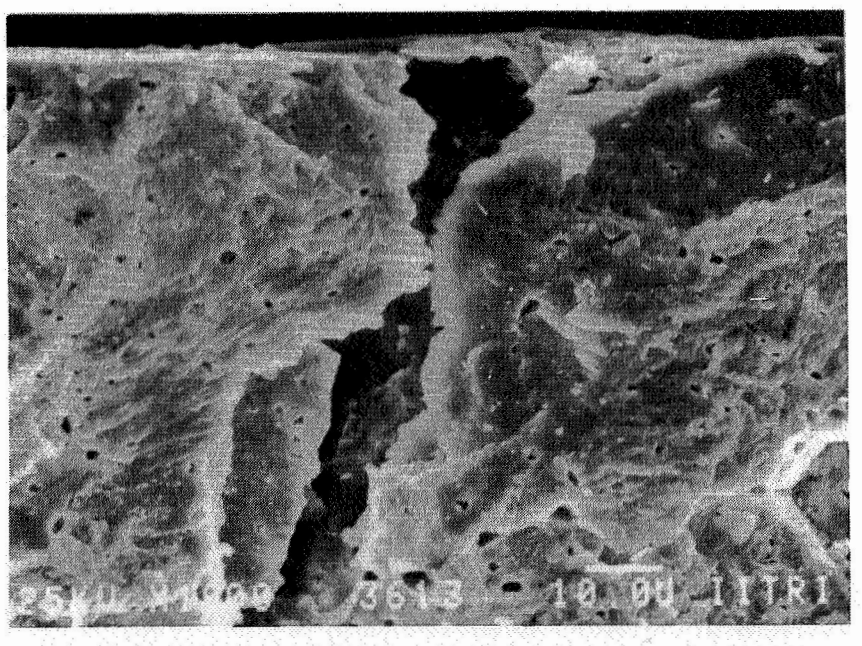

(b) Enlarged view of the surface connected pore fracture origin.

Figure 26. Fracture surfaces of Nilsen MS Mg-PSZ tested at 750°C showing porosity as the fracture origin (NV1F13).

ORIGINAL PAGE IS
OF POOR QUALITY

(a) Sample NV1F16.

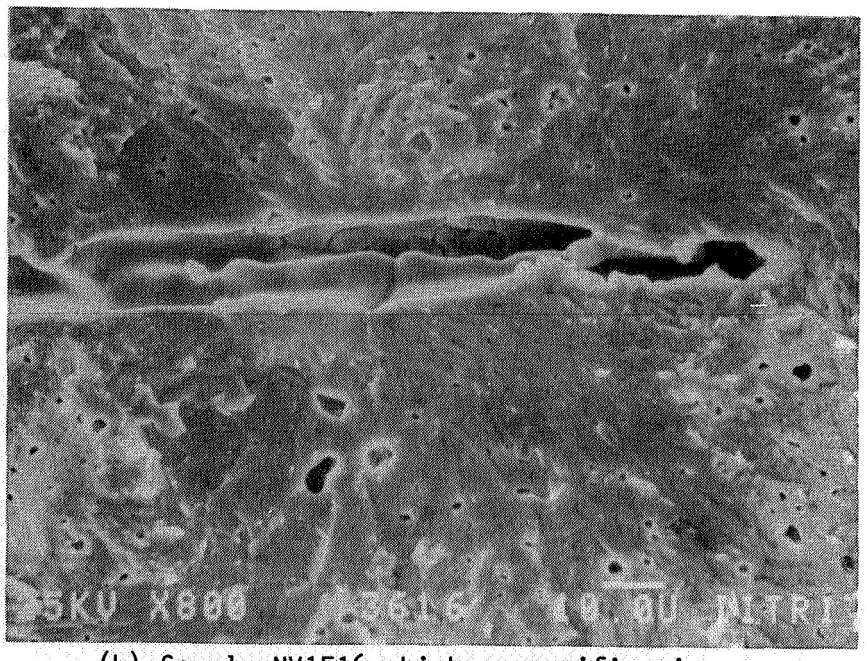

(b) Sample NV1F16, higher magnification.

Figure 27. Fracture surfaces of Nilsen MS Mg-PSZ tested at 1000°C showing pore cluster fracture origins.

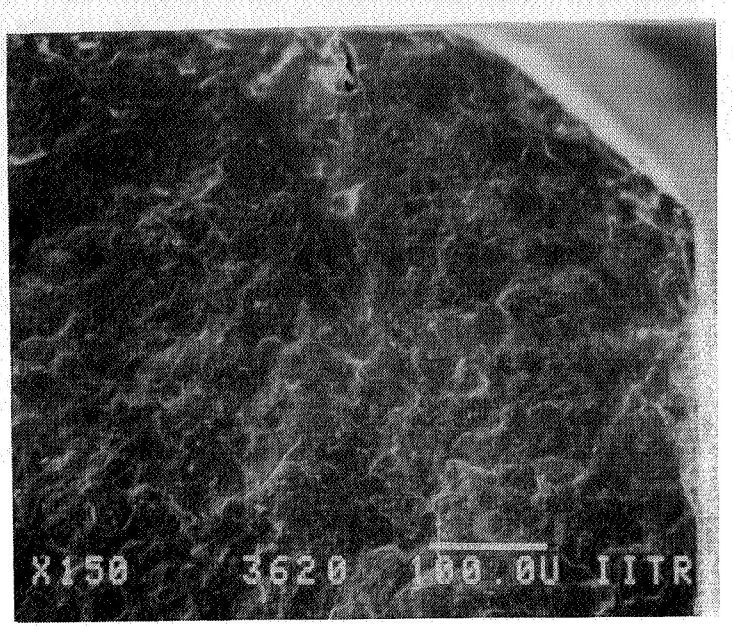

(c) Sample NV1F20.

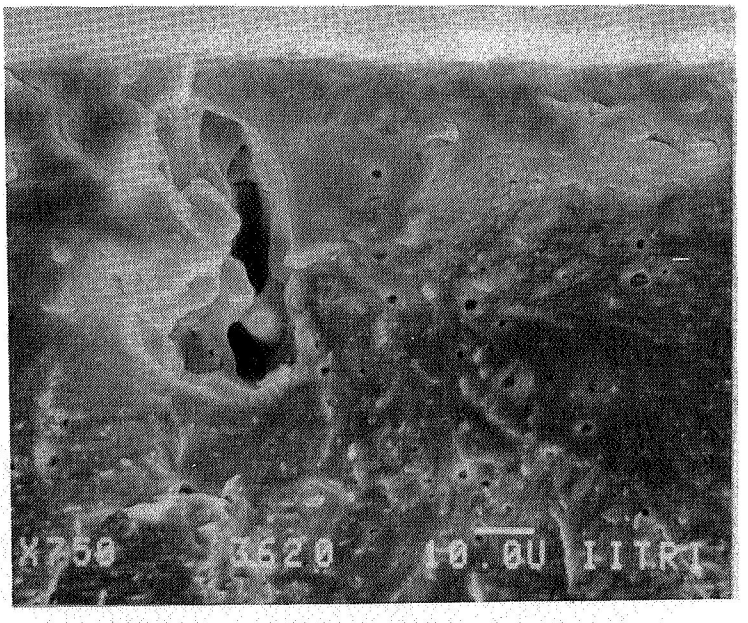

(d) Sample NV1F20, enlarged view.

Figure 27. (cont.)

ORIGINAL PAGE IS
OF POOR QUALITY

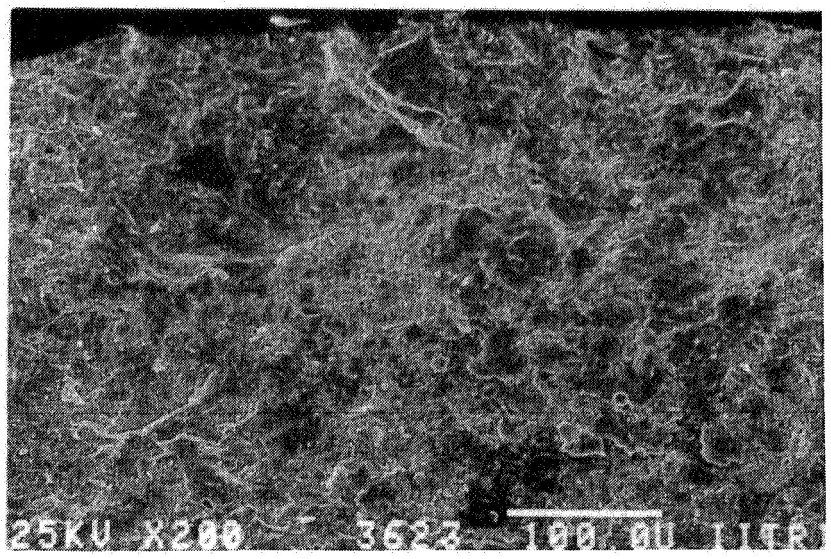

(a) Sample NV1F23.

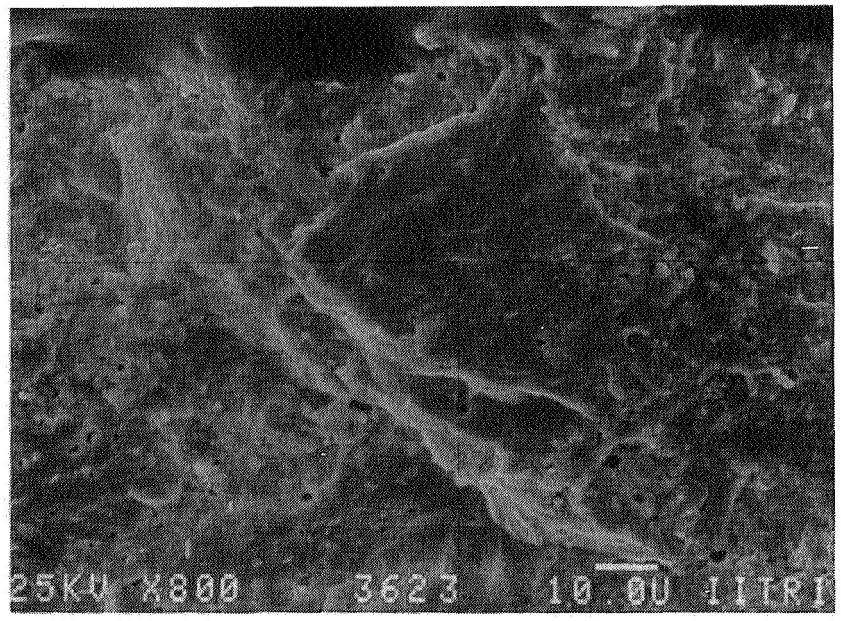

(b) Higher magnification view of the large grain fracture origin (NV1F23).

Figure 28. Fracture surfaces of Nilsen MS Mg-PSZ tested at 25°C after 1000 hr/1000°C exposure.

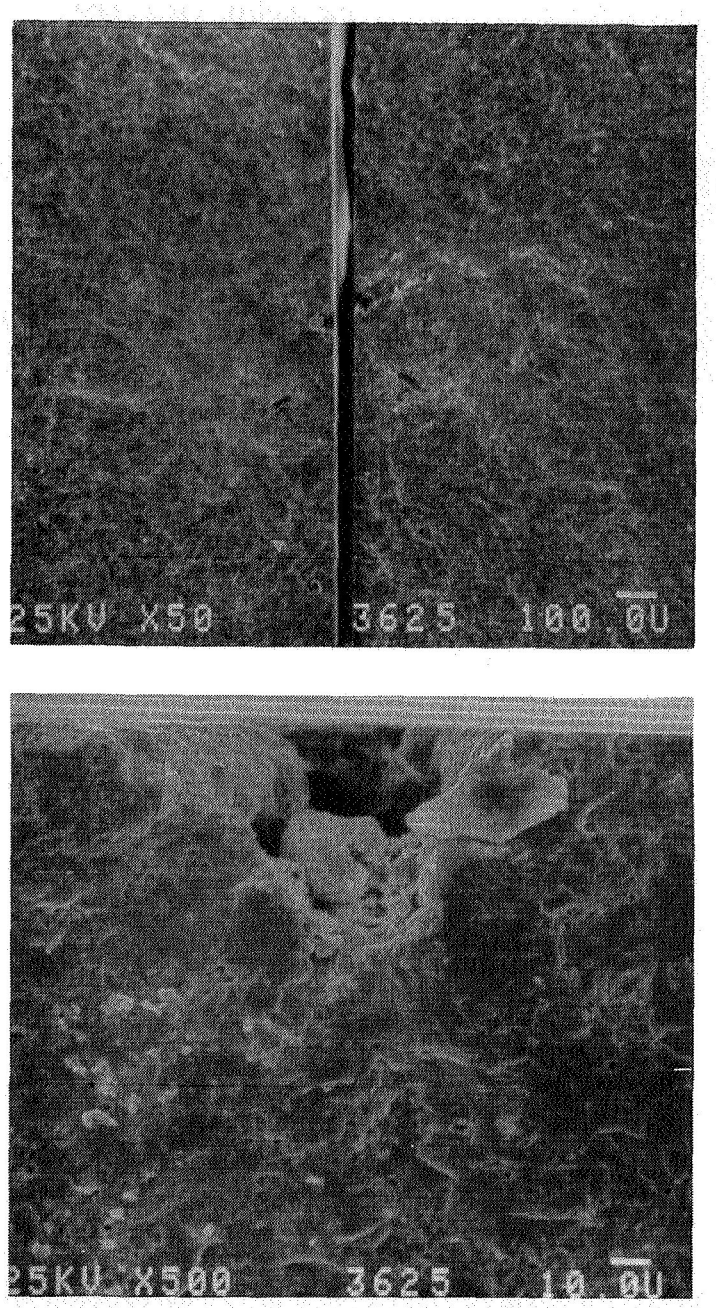

(c) Two views of a sample which contained an open pore at the tensile surface which was the fracture origin (NV1F25).

Figure 28. (cont.)

ORIGINAL PAGE IS
OF POOR QUALITY

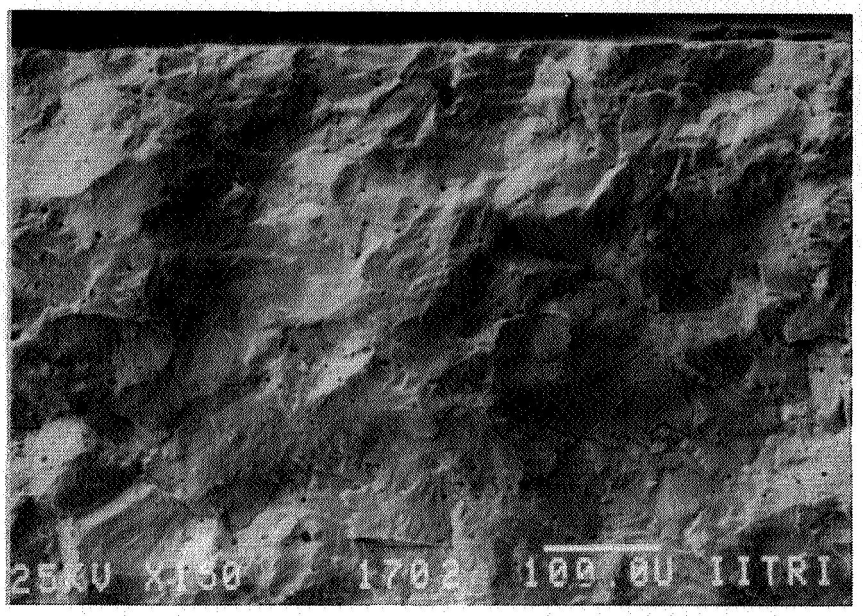

(a) Sample failed at a subsurface pore (KF1F2).

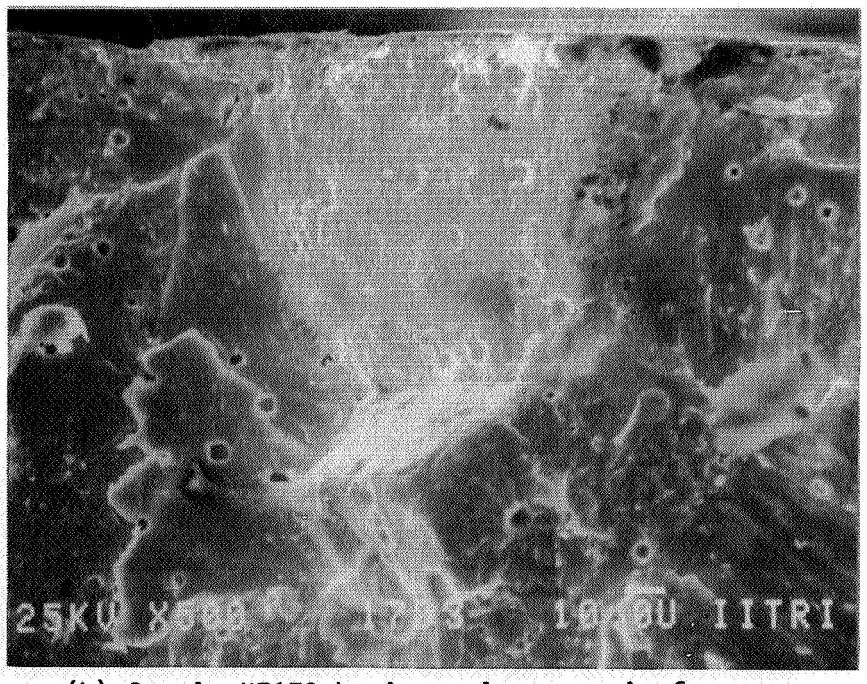

(b) Sample KF1F3 having a large grain fracture origin.

Figure 29. Fracture surfaces of Feldmuhle ZN-40 Mg-PSZ tested at 25°C.

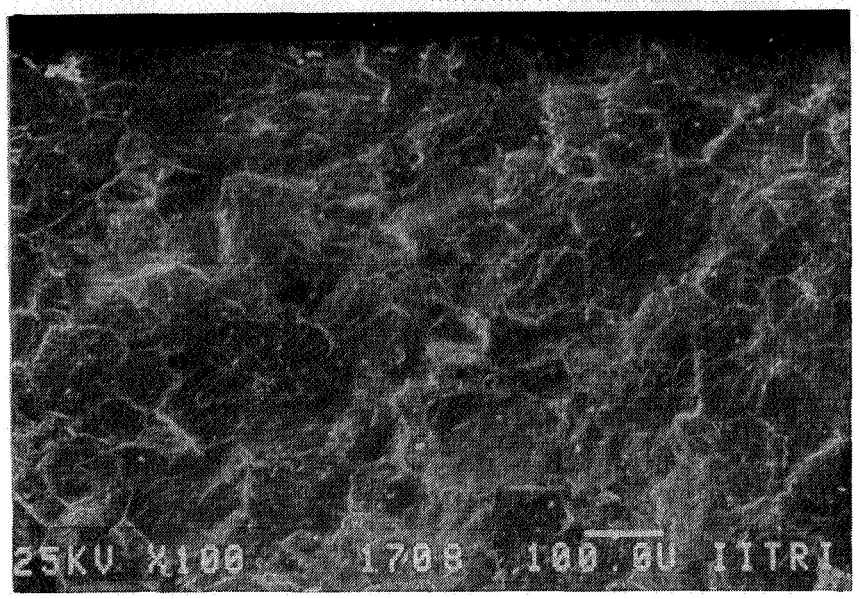

(a) Sample KF1F8 contained a subsurface porous region as the fracture origin.

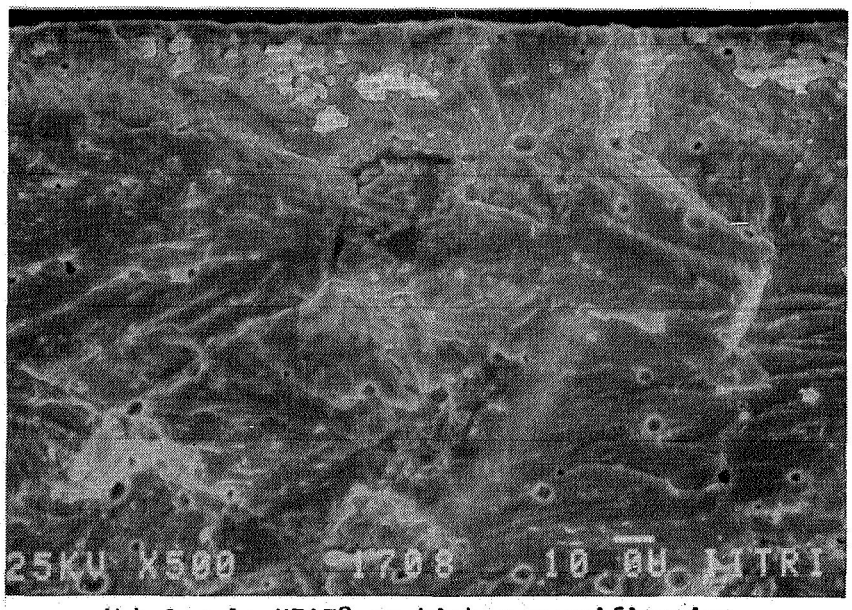

(b) Sample KF1F8 at higher magnification.

Figure 30. Fracture surfaces of Feldmuhle ZN-40 Mg-PSZ tested at 500°C.

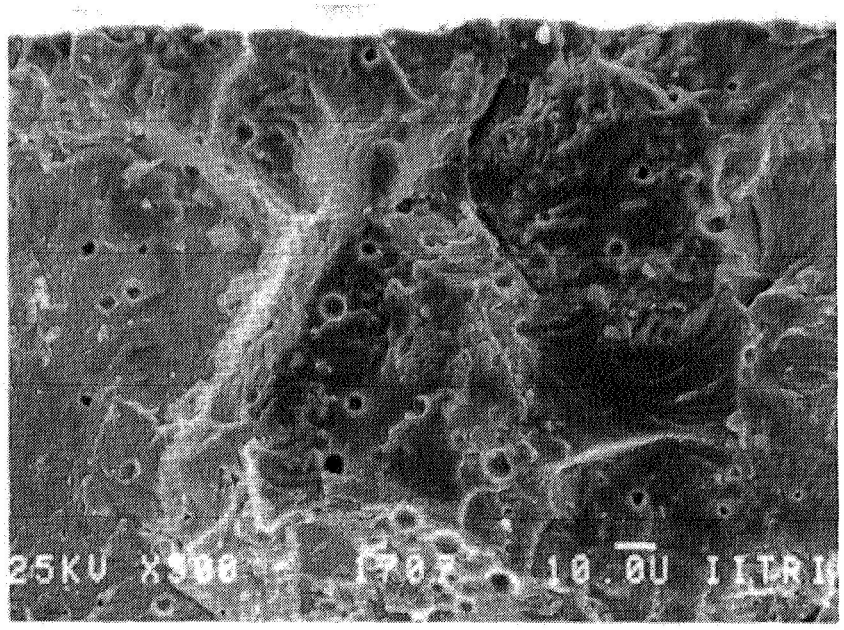

(c) Sample KF1F7, which also had a poorly sintered porous region as its fracture origin. Note porosity and grain facets.

Figure 30. (cont.)

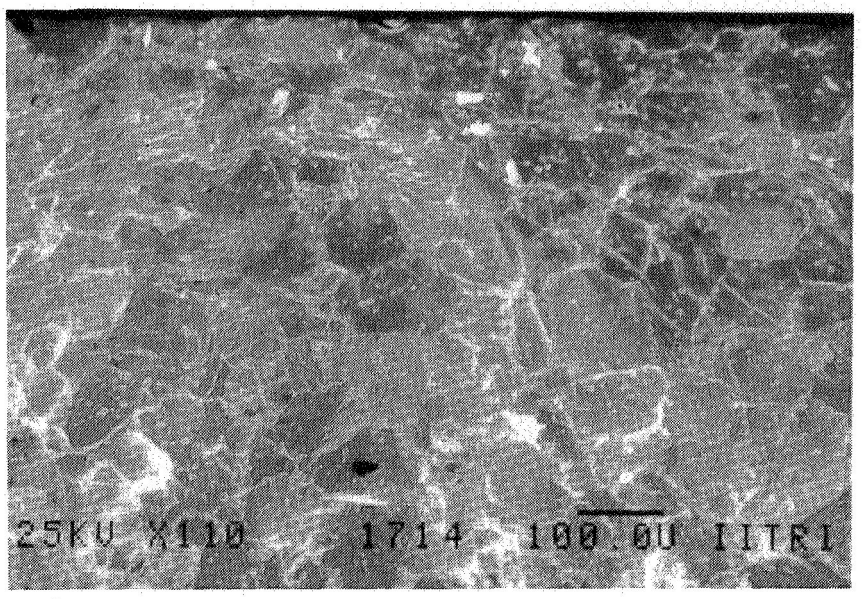

(a) Sample having an open pore on the tensile surface as the fracture origin (KF1F14).

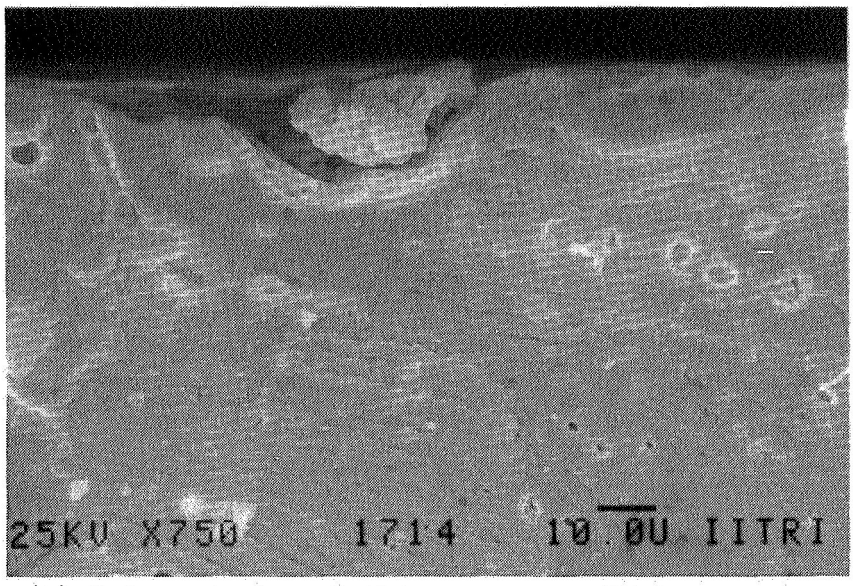

(b) Enlarged view of the open pore within a grain at the tensile surface, which was the origin (KF1F14).

Figure 31. Fracture surfaces of Feldmuhle ZN-40 Mg-PSZ tested at 750°C.

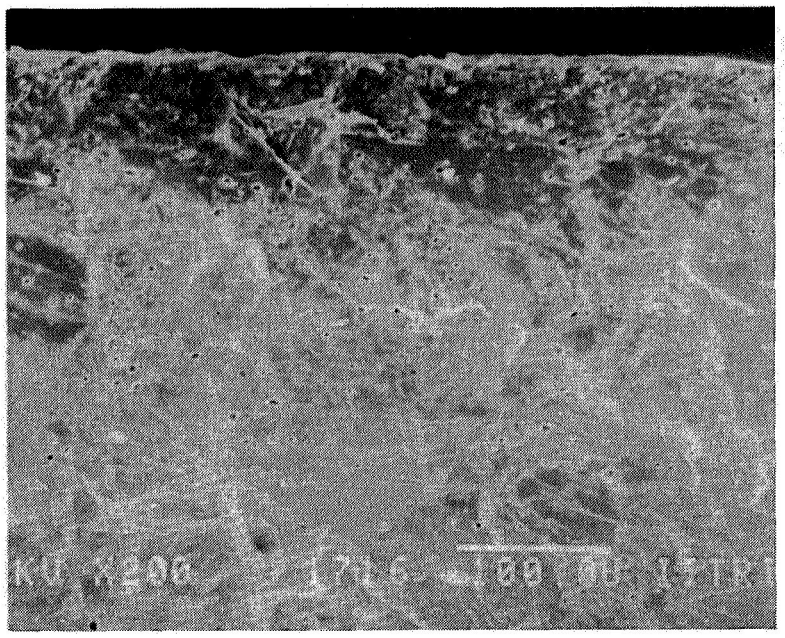

(a) Low magnification view of the mirror showing the region where the poorly bonded grains fracture origin spalled off (KF1F16).

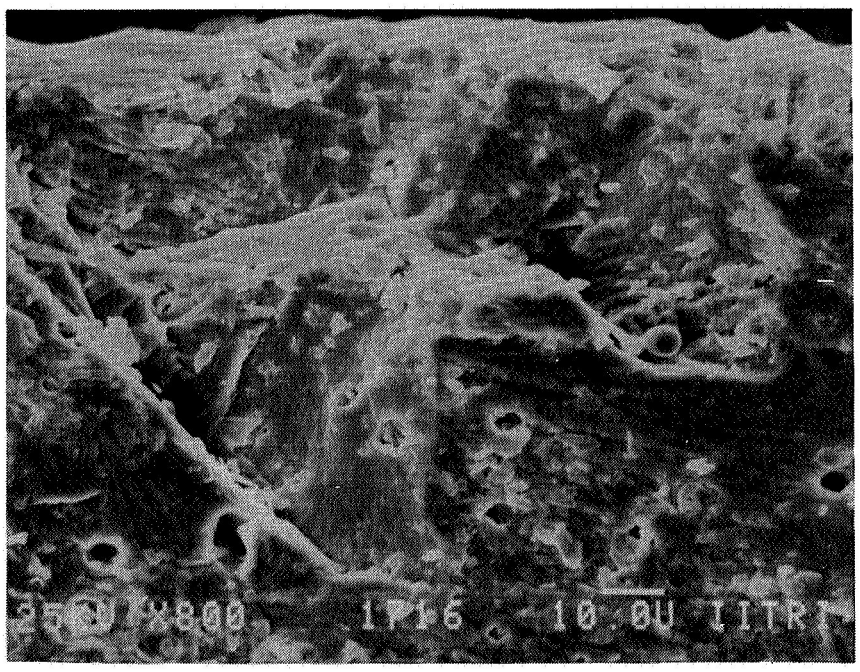

(b) Higher magnification view of above sample showing where grains had not sintered (KF1F16).

Figure 32. Fracture surfaces of Feldmuhle ZN-40 Mg-PSZ tested at 1000°C.

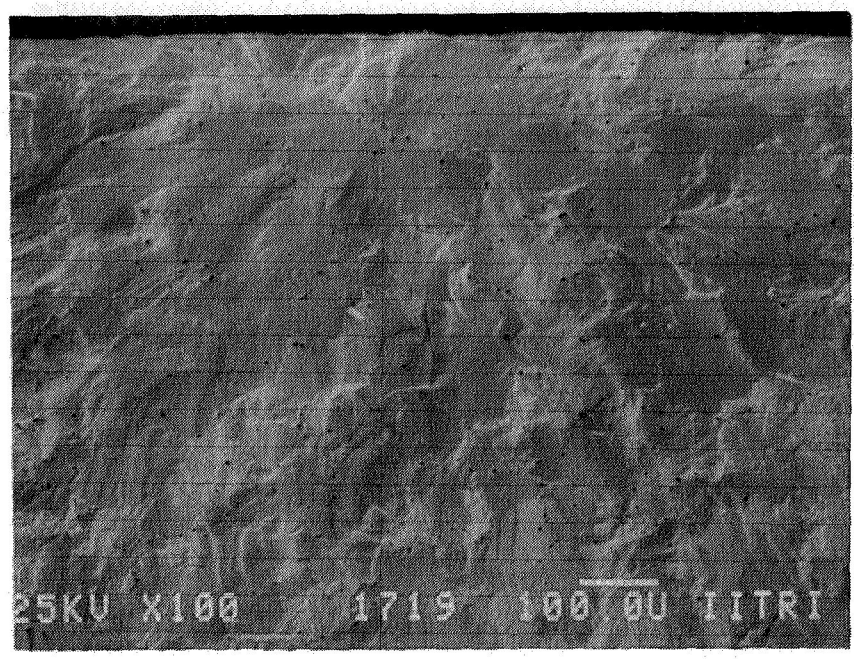

(c) Wide flat mirror region containing a slit-shaped region (perpendicular to the tensile surface) where grains were poorly bonded (KF1F19).

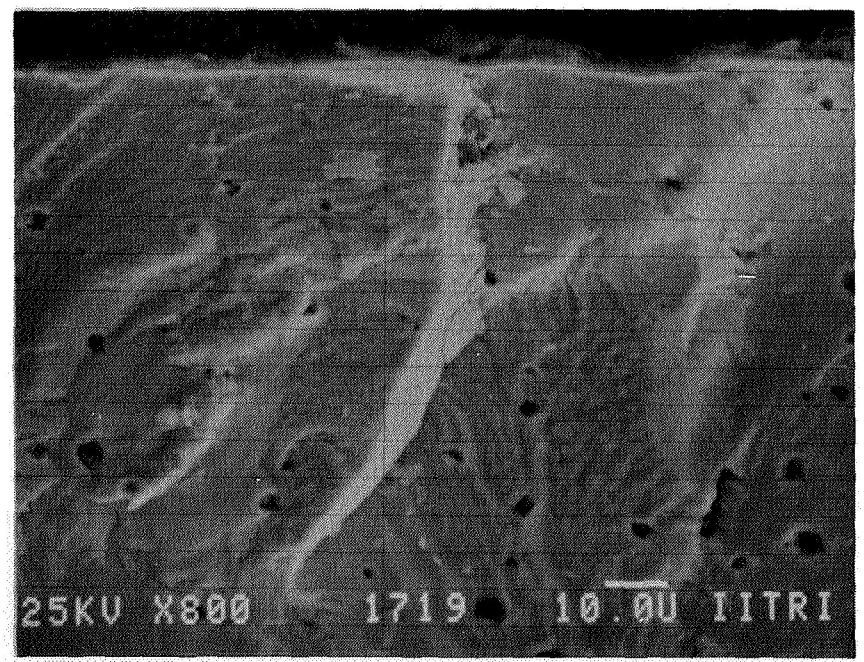

(d) View of the unbonded edge of a grain which was the fracture origin (KF1F19).

Figure 32. (cont.)

ORIGINAL PAGE IS
OF POOR QUALITY

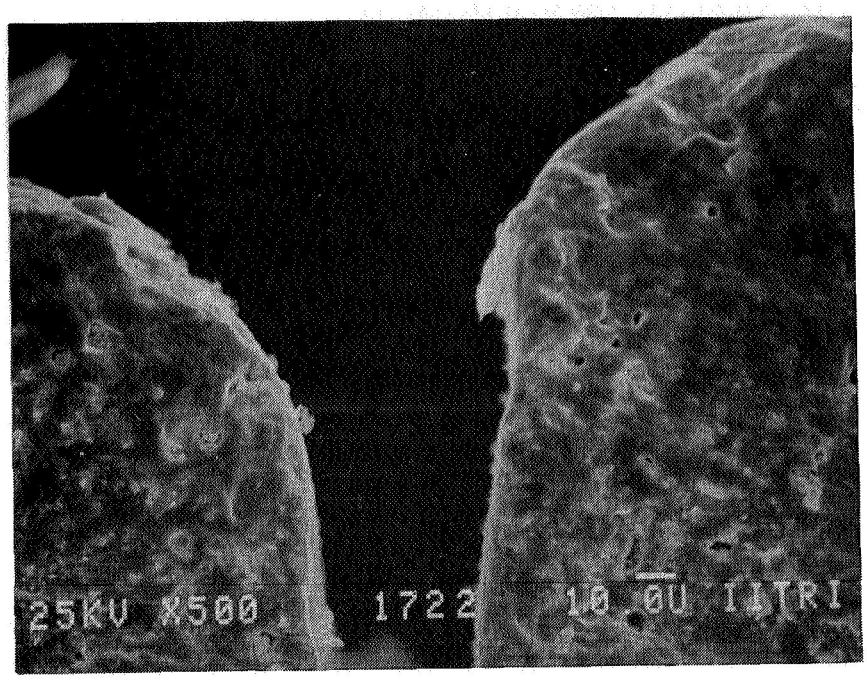

(a) Sample which contained a pore cluster at the bevel as the fracture origin (KF1F22).

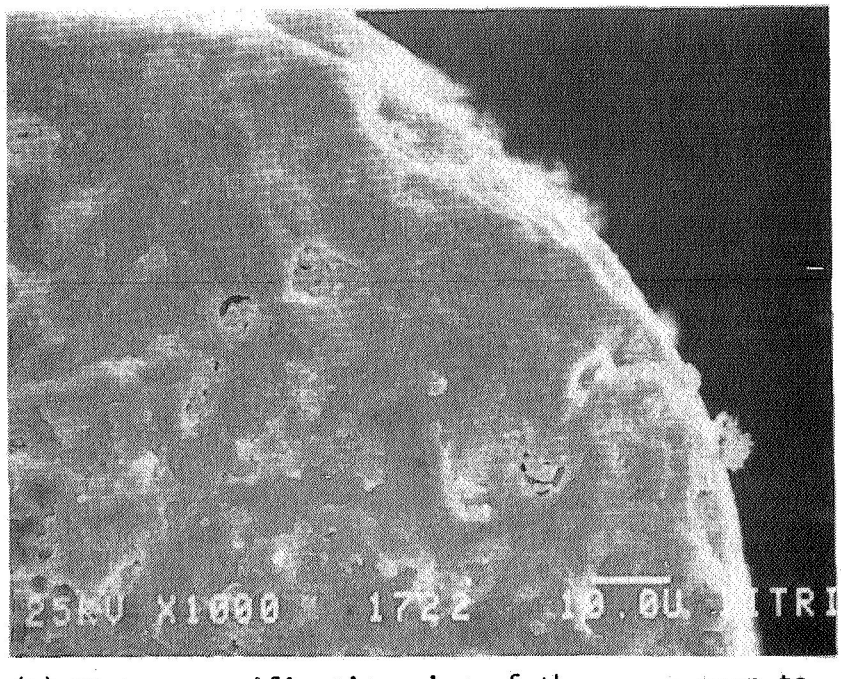

(b) Higher magnification view of the pores open to the surface at the bevel (KF1F22).

Figure 33. Fracture surfaces of Feldmuhle ZN-40 Mg-PSZ at 25°C after 1000 hr/1000°C exposure.

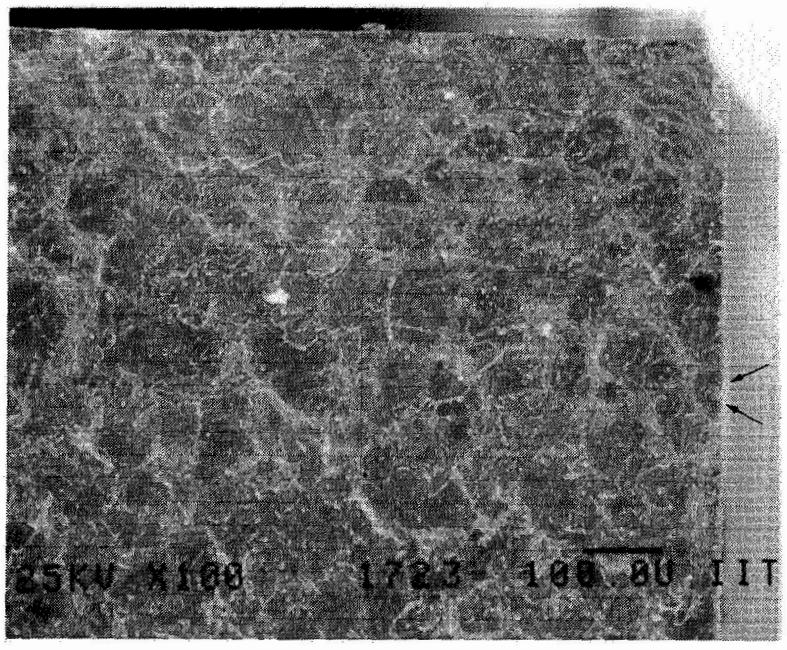

(c) Sample KF1F23 which had a small mirror region.

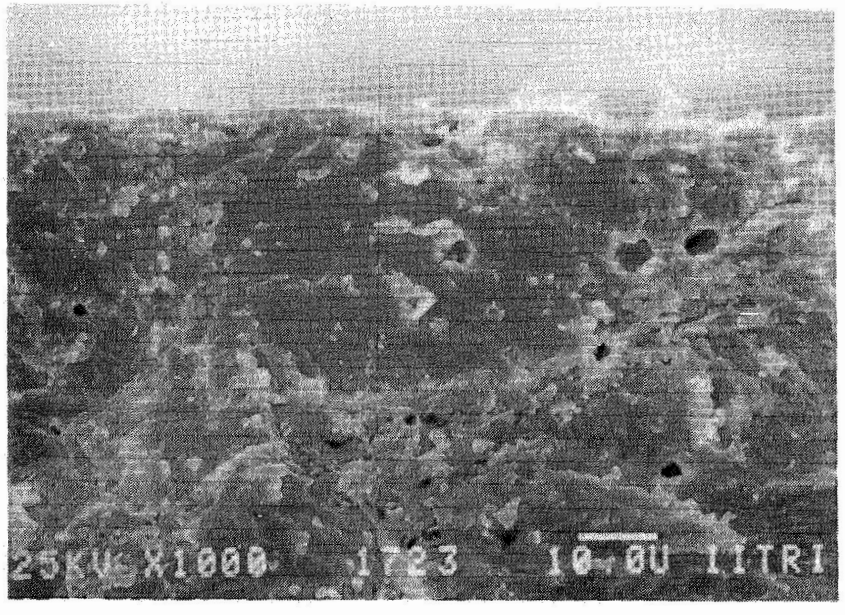

(d)

Figure 33. (cont.)

ORIGINAL PAGE IS
OF POOR QUALITY

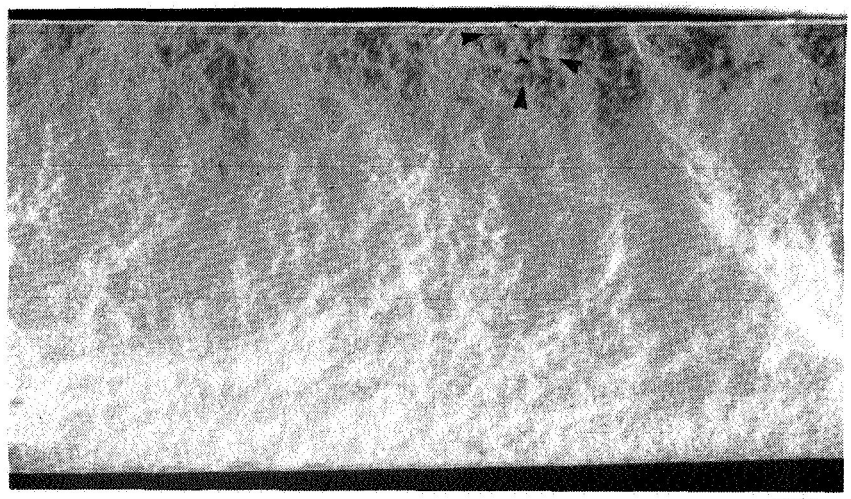

20X

(a) Low magnification photograph indicating the fracture origin and lack of typical fracture surface features (CB1F3).

Tensile surface

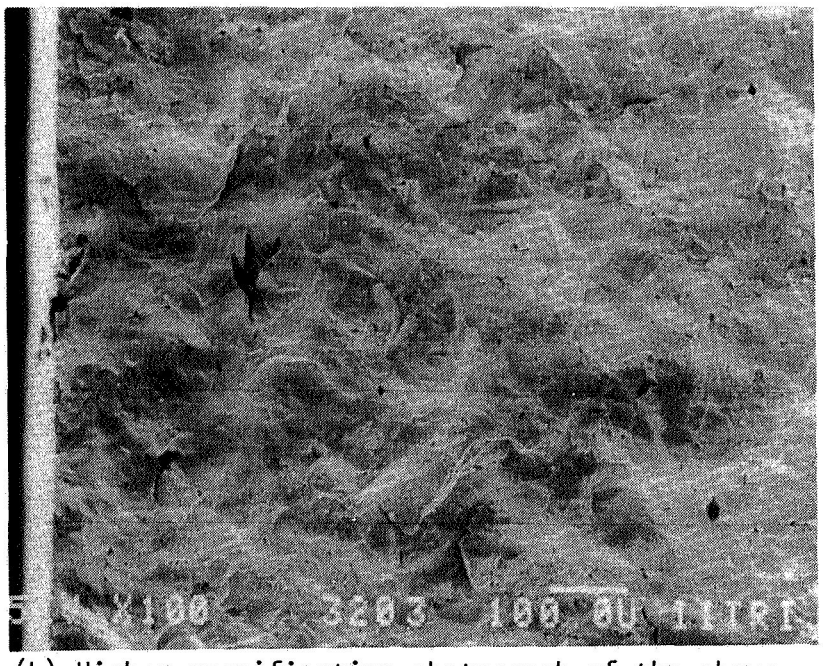

(b) Higher magnification photograph of the above sample showing the subsurface fracture origin (CB1F3).

Figure 34. Fracture surfaces of Coors (3% MgO) Mg-PSZ representative of typical pore fracture origins for samples tested at 25°C.

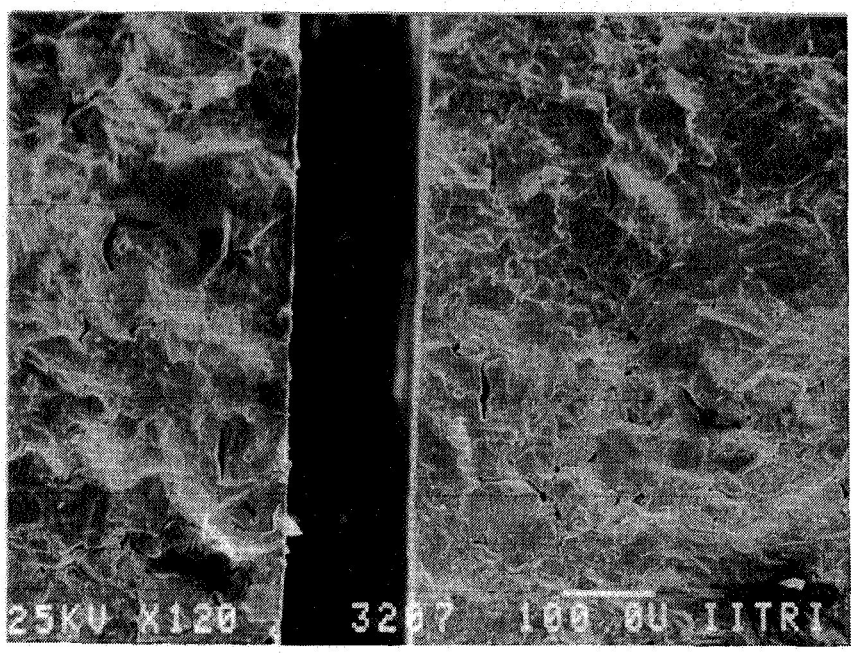

Figure 35. SEM micrograph of Coors Mg-PSZ showing a fracture surface having an undetermined fracture origin (sample CB1F7 tested in 4-point flexure at 500°C).

ORIGINAL PAGE IS
OF POOR QUALITY

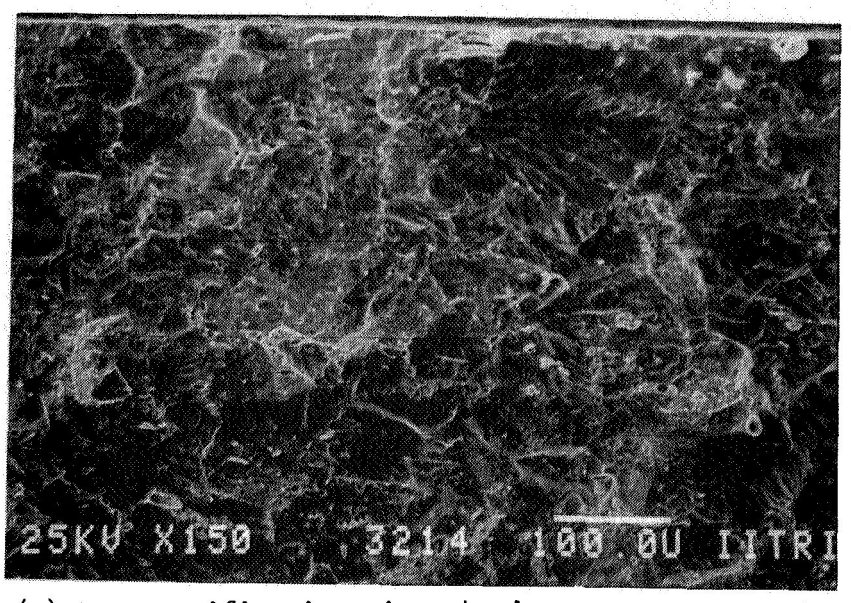

(a) Low magnification view showing an open pore at the tensile surface, which was the fracture origin (CB1F14).

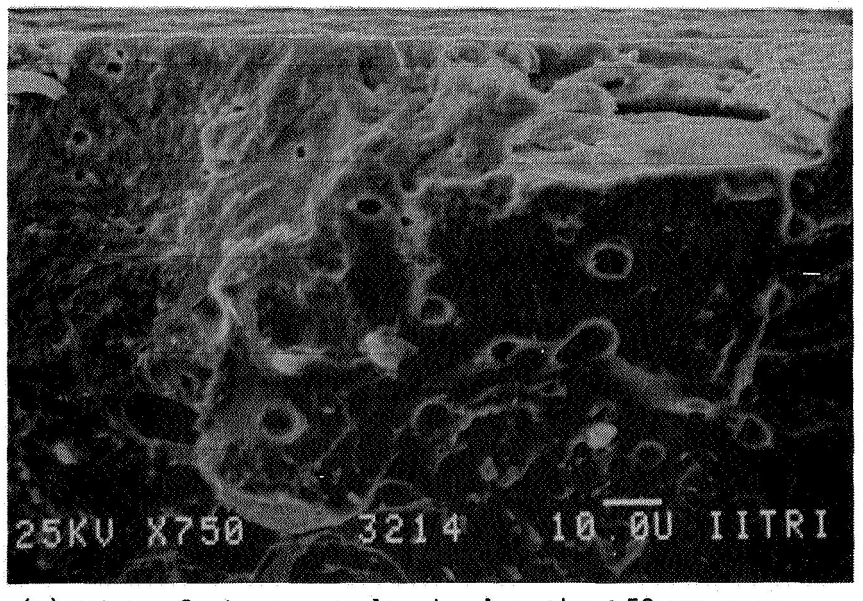

(b) View of above sample showing the ∿50 μm open pore (at right) which was the fracture origin (CB1F14).

Figure 36. Fracture surfaces of Coors Mg-PSZ tested at 750°C.

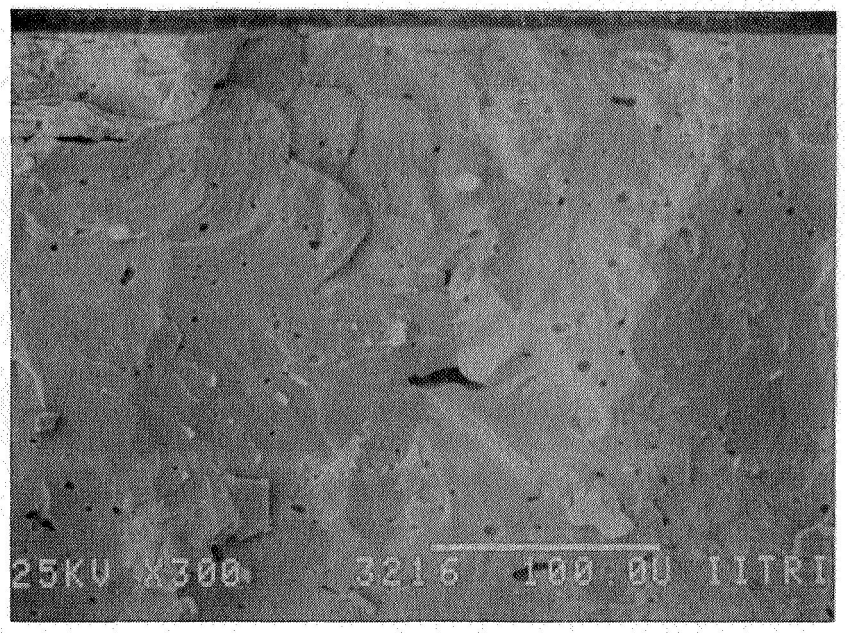

(a) Sample containing a region of poorly sintered grains at the tensile surface which became the fracture origin (CB1F16).

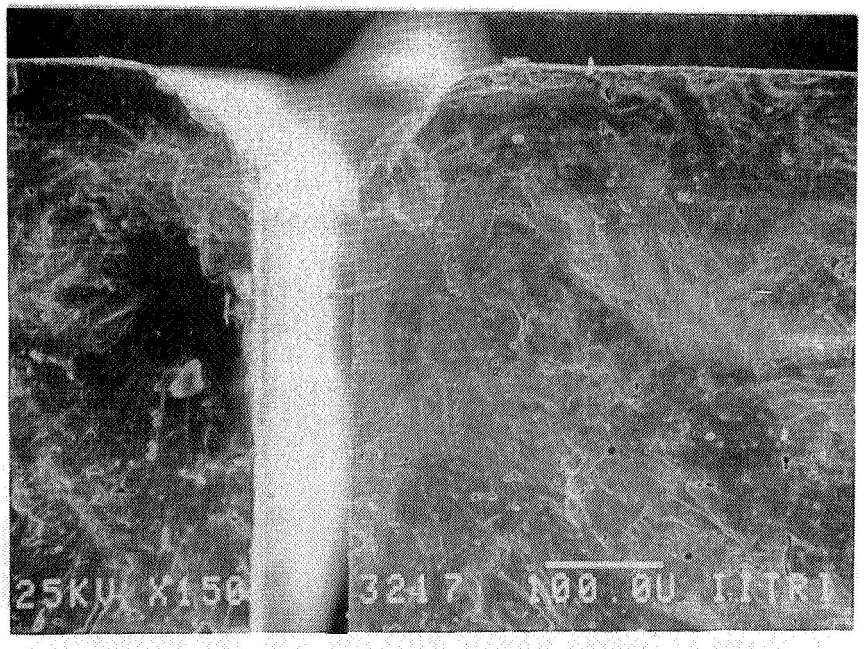

(b) This sample had an open pore at the bevel which acted as the fracture origin (CB1F17).

Figure 37. Fracture surfaces of Coors Mg-PSZ tested in 4-point flexure at 1000°C.

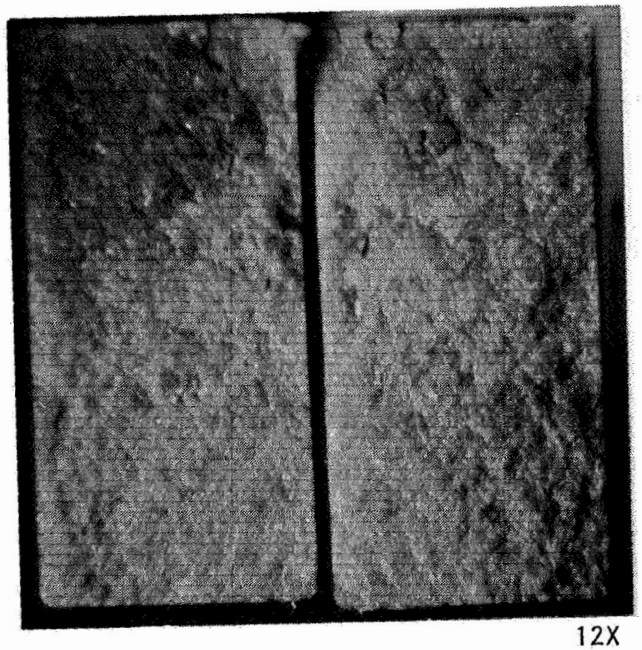

12X

(a)

ORIGINAL PAGE IS
OF POOR QUALITY

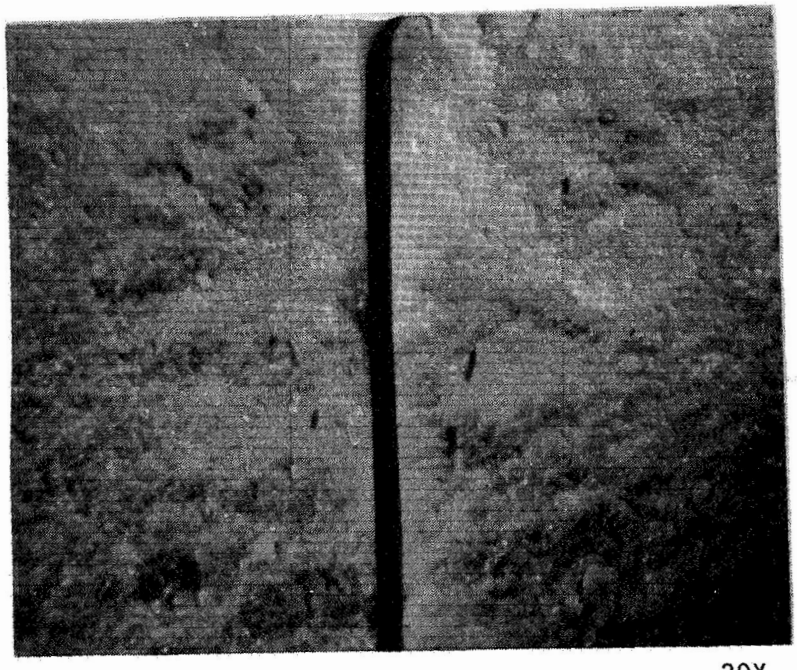

20X

(b)

Figure 38. Optical micrographs of Coors Mg-PSZ tested in 4-point flexure at 25°C after 1000 hr/1000°C static air exposure. Failure due to porosity as shown.

4.4 SUMMARY OF ZIRCONIA STRENGTH

It is often informative to present strength data in a Weibull format, where the failure probability is plotted as a function of stress. The analysis used followed Johnson,[11] where a two-parameter distribution was employed with n/N + 1 probability ranking, and the Weibull modulus was determined from a linear least-squares analysis. The results for each of the four zirconia materials evaluated on this program are provided in Figures 39-42, where all test conditions are included. These curves illustrate how the Weibull distribution shifts with temperature and overaging. Figures 43-47 are arranged so that the four materials can be directly compared for each test condition.

The bend strength data for the four transformation-toughened zirconia materials are summarized in tabular form in Table 6. To summarize, all transformation-toughened zirconia materials exhibit significant strength decrease with temperature. Yttria-stabilized TZP, however, exhibits a much more stable microstructure and phase assemblage with respect to extended elevated temperature overaging.

TABLE 6. SUMMARY OF ZIRCONIA STRENGTH DATA

	4-Point Flexural Strength,[a] psi			
	As-Received		After 1000 hr/ 1000°C Exposure	
Material	25°C[b]	1000°C[c]	25°C[c]	1000°C[d]
NGK Z-191 Y-TZP	129,090	40,320	119,840	5,790[e]
Nilsen MS Mg-PSZ	92,450	41,600	39,350	46,870
Feldmuhle ZN-40 Mg-PSZ	61,830	30,860	43,210	36,060
Coors Mg-PSZ	69,880	23,740	21,140	31,740

[a] 1/8 x 1/4 x 2 1/4 in. specimen; upper and lower spans 0.875 and 1.750 in., respectively.

[b] Sample population = 8.

[c] Sample population = 5.

[d] Sample population = 1.

[e] Sample cracked; may be anomalous, atypical, and not representative.

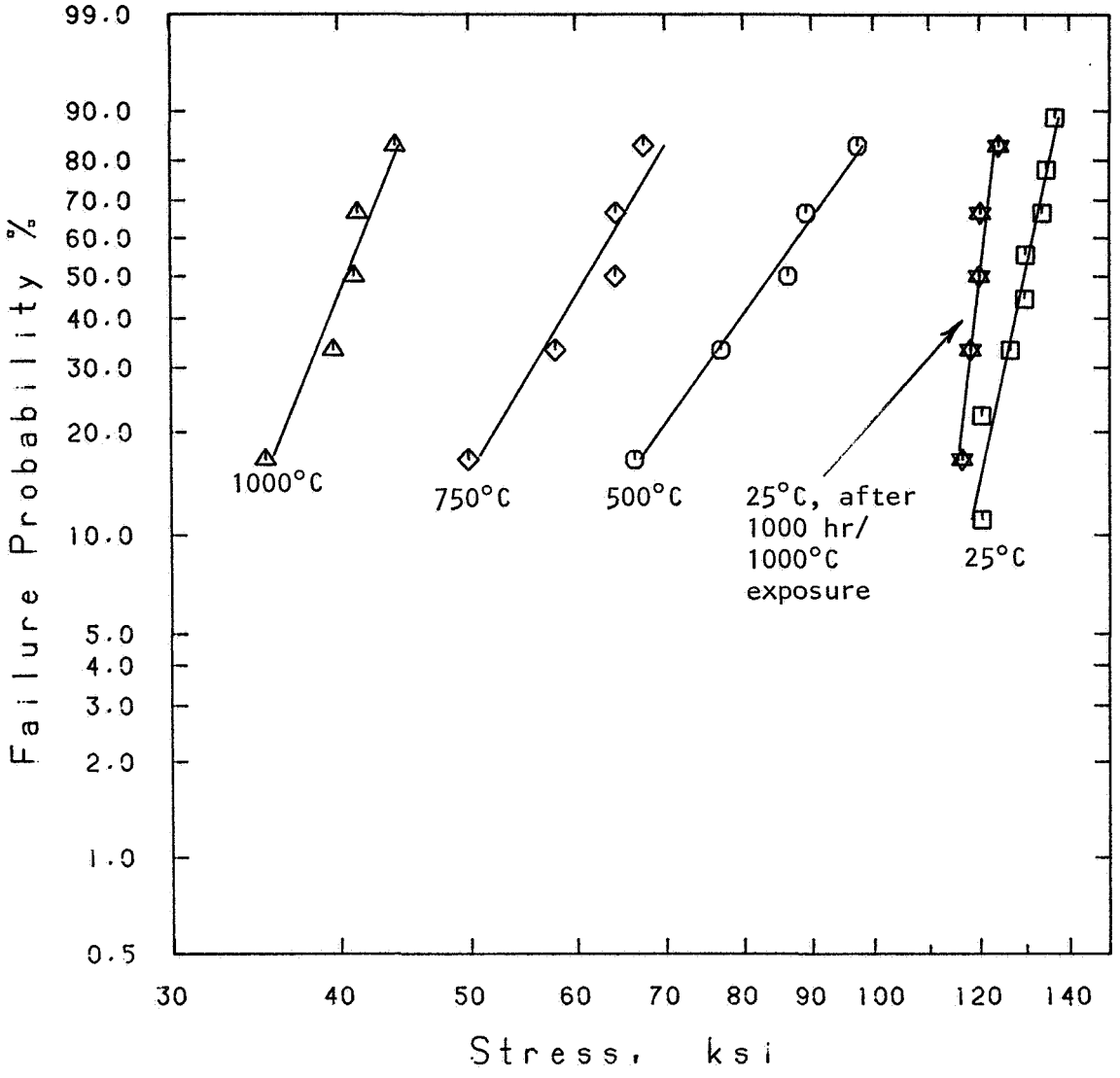

SYMBOL	TEST CONDITIONS	WEIBULL MODULUS, m	CHARACTERISTIC STRENGTH, ksi
□	25°C	19.40	132.22
○	500°C	5.94	89.31
◇	750°C	7.08	64.56
△	1000°C	10.47	42.01
✡	25°C, after exposure	35.39	121.38

Figure 39. Weibull plot for NGK Z-191 Y-TZP for five test conditions.

C-2

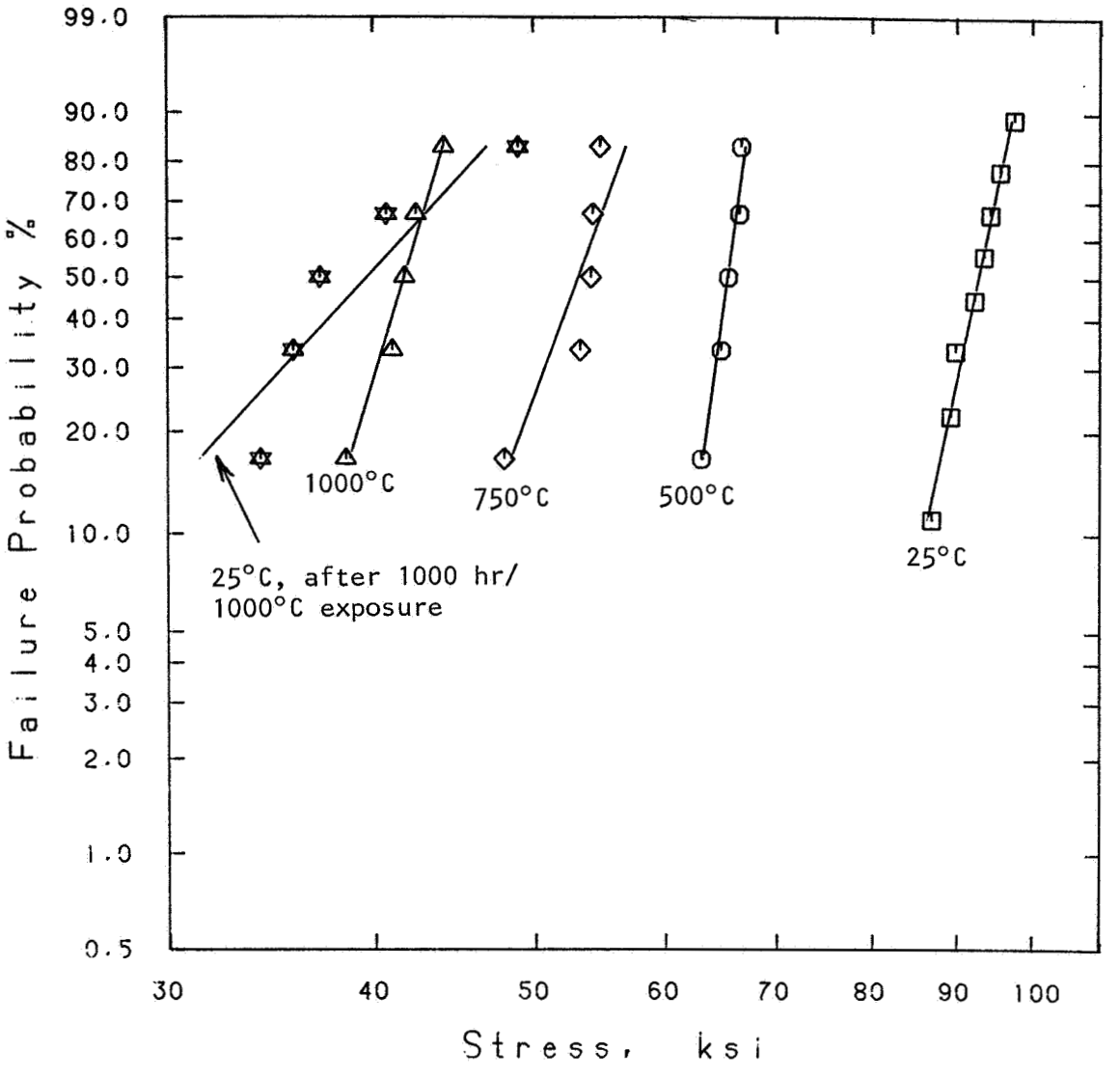

SYMBOL	TEST CONDITIONS	WEIBULL MODULUS, m	CHARACTERISTIC STRENGTH, ksi
□	25°C	24.85	94.21
○	500°C	38.50	66.20
◇	750°C	14.19	54.66
△	1000°C	17.41	42.66
✡	25°C, after exposure	5.69	42.30

Figure 40. Weibull plot for Nilsen MS Mg-PSZ for five test conditions.

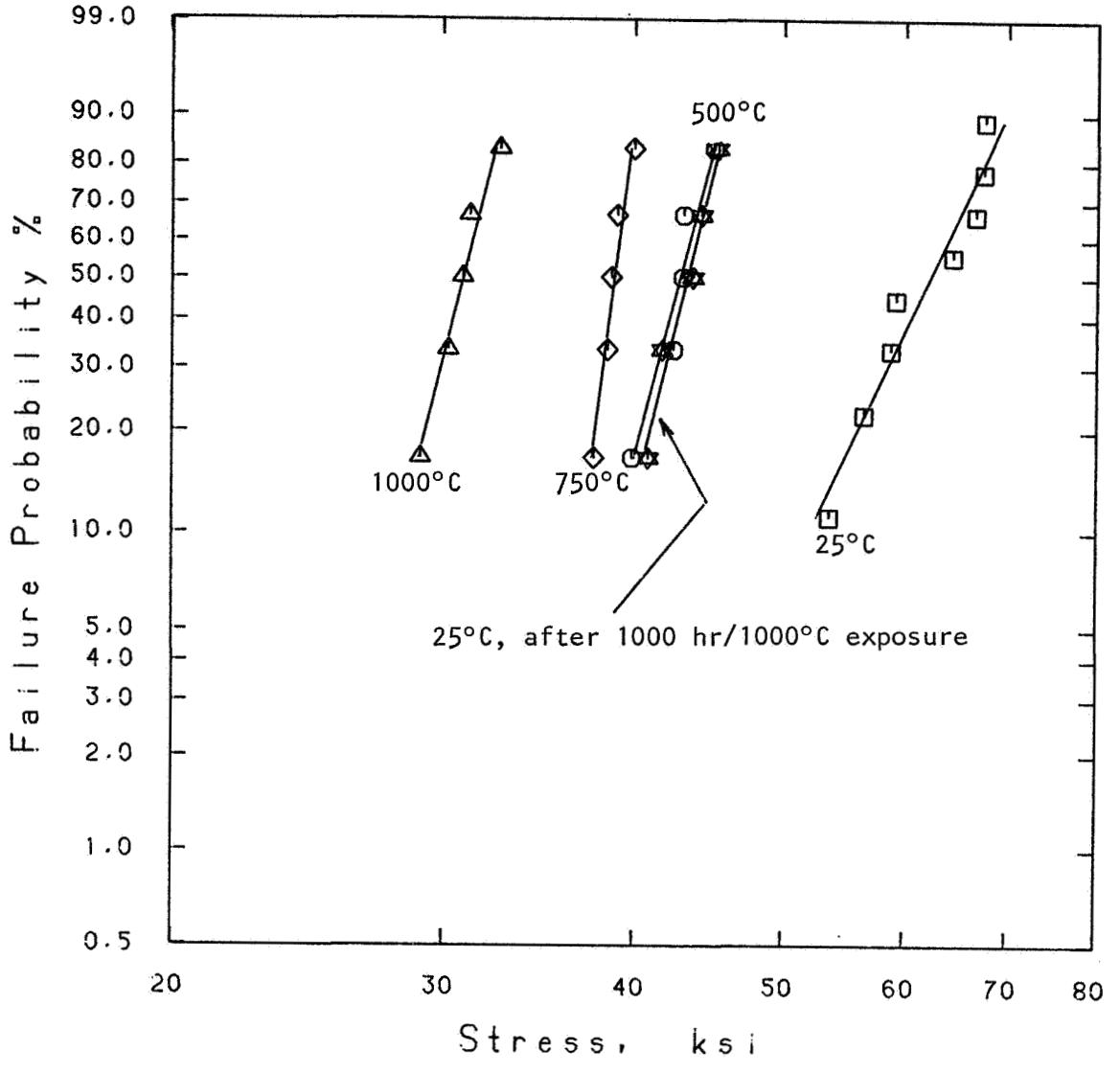

SYMBOL	TEST CONDITIONS	WEIBULL MODULUS, m	CHARACTERISTIC STRENGTH, ksi
□	25°C	10.49	64.52
○	500°C	19.43	43.74
◇	750°C	39.54	39.24
△	1000°C	20.10	31.55
✡	: 25°C, after exposure	20.59	44.15

Figure 41. Weibull plot for Feldmuhle ZN-40 Mg-PSZ for five test conditions.

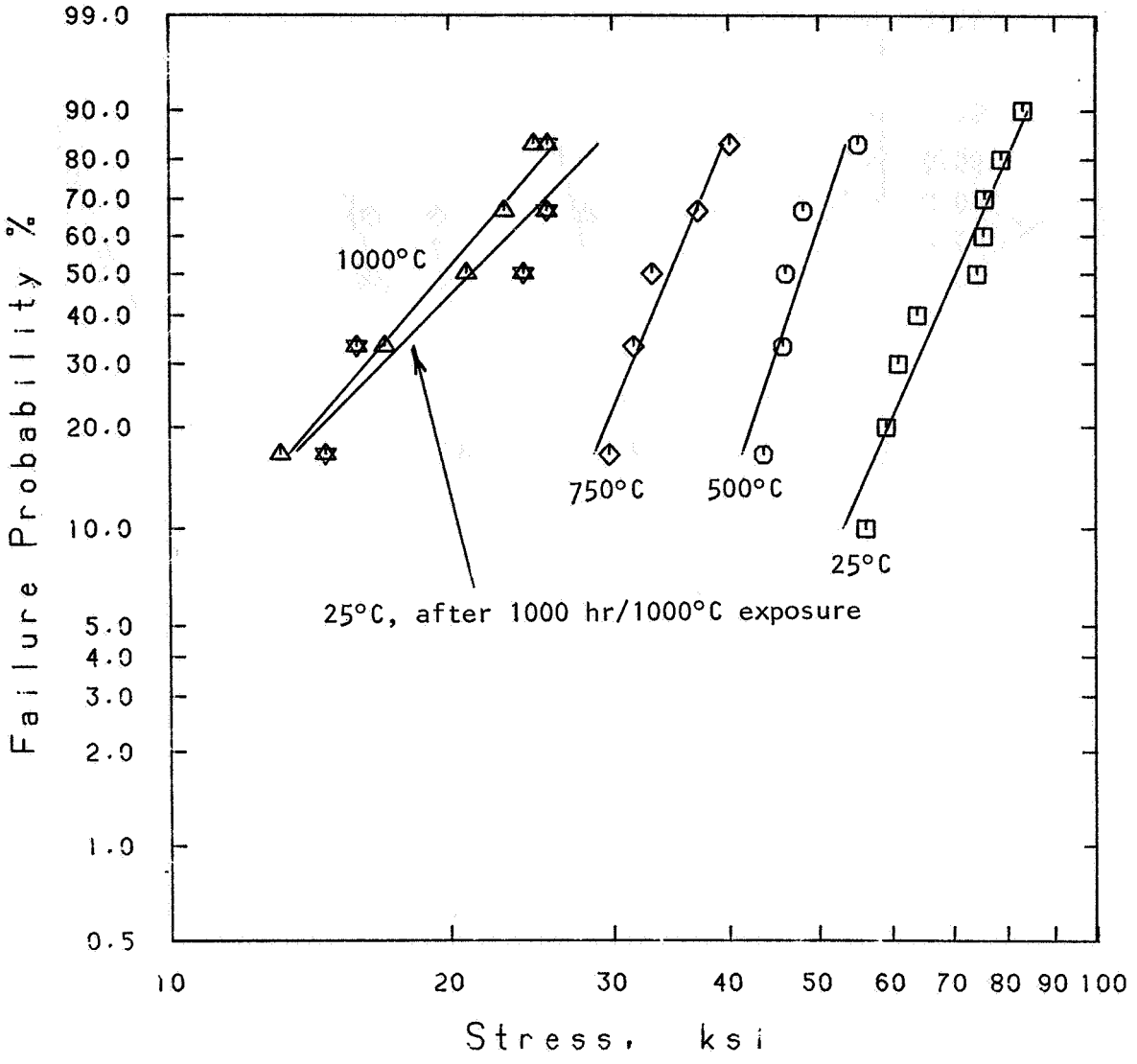

SYMBOL	TEST CONDITIONS	WEIBULL MODULUS, m	CHARACTERISTIC STRENGTH, ksi
□	25°C	6.69	74.53
○	500°C	8.79	50.27
◇	750°C	7.09	36.49
△	1000°C	3.44	22.00
✡	25°C, after exposure	3.01	23.93

Figure 42. Weibull plot for Coors Mg-PSZ for five test conditions.

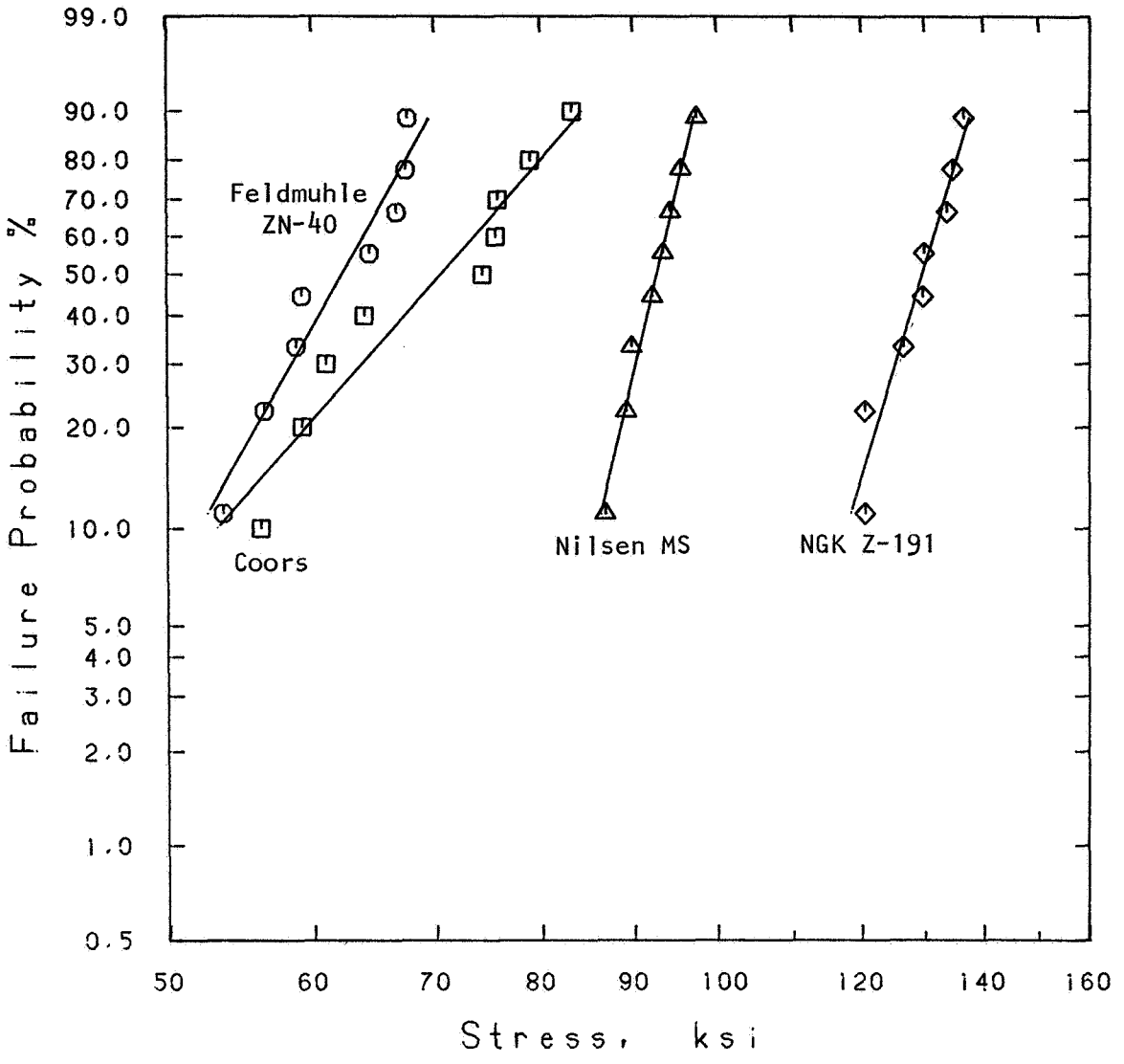

SYMBOL	MATERIAL	WEIBULL MODULUS, m	CHARACTERISTIC STRENGTH, ksi
□	Coors Mg-PSZ	6.69	74.53
○	Feldmuhle ZN-40 Mg-PSZ	10.49	64.52
◇	NGK Z-191 Y-TZP	19.40	132.22
△	Nilsen MS Mg-PSZ	24.85	94.21

Figure 43. Weibull plot for candidate zirconia materials at 25°C.

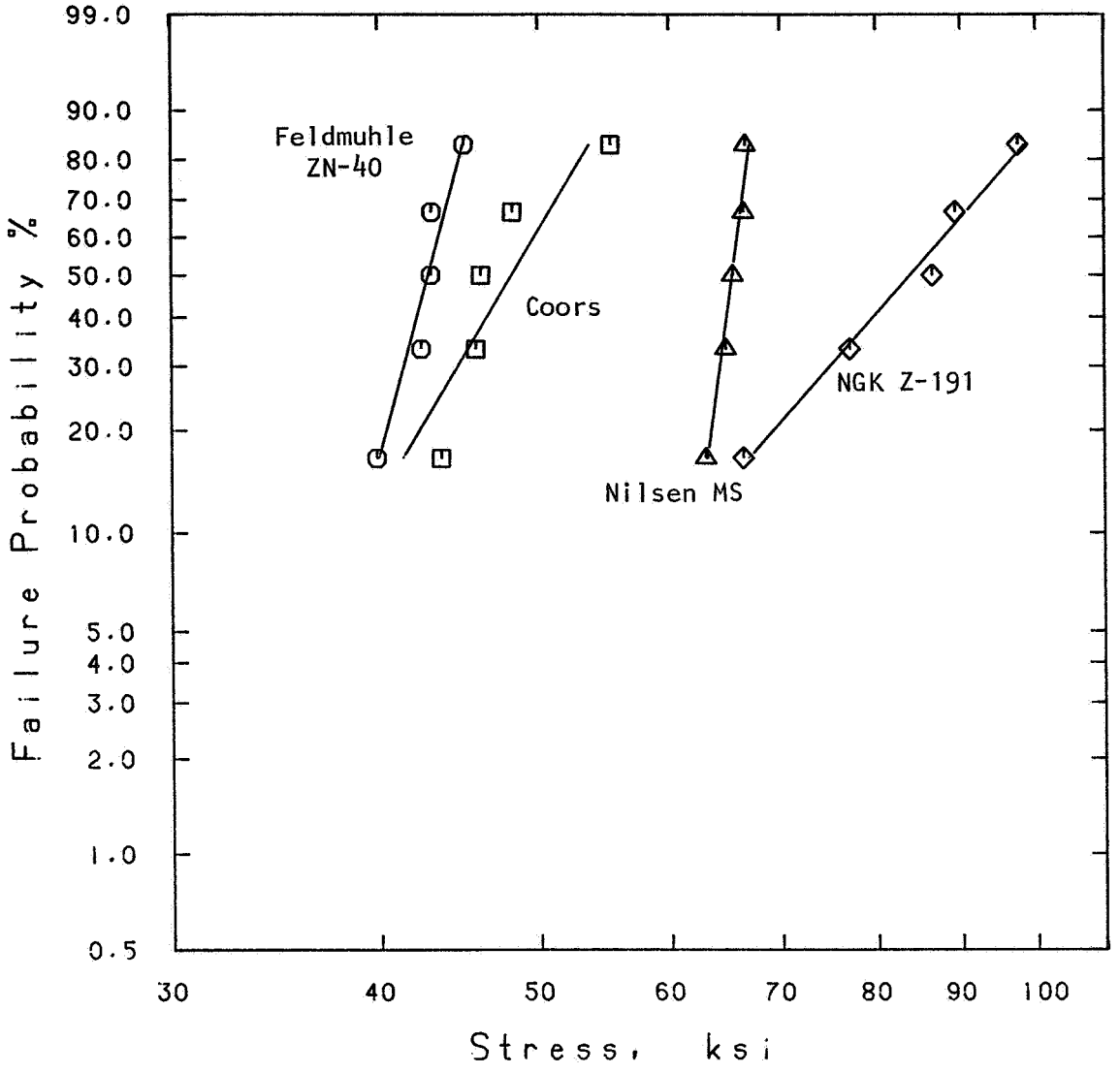

SYMBOL	MATERIAL	WEIBULL MODULUS, m	CHARACTERISTIC STRENGTH, ksi
□	Coors Mg-PSZ	8.79	50.27
○	Feldmuhle ZN-40 Mg-PSZ	19.43	43.74
◇	NGK Z-191 Y-TZP	5.94	89.31
△	Nilsen MS Mg-PSZ	38.50	66.20

Figure 44. Weibull plot for candidate zirconia materials at 500°C.

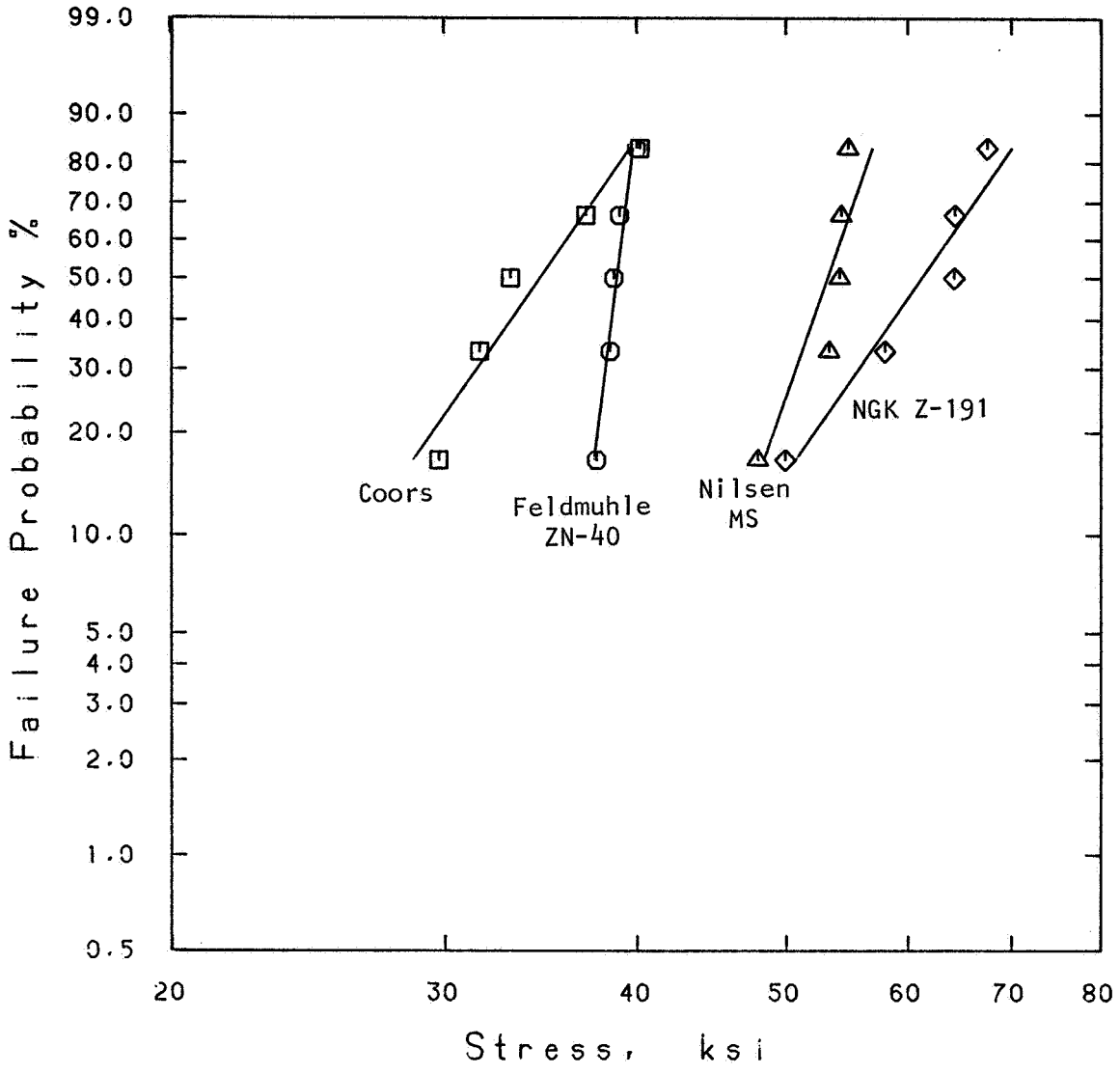

SYMBOL	MATERIAL	WEIBULL MODULUS, m	CHARACTERISTIC STRENGTH, ksi
□	Coors Mg-PSZ	7.09	36.49
○	Feldmuhle ZN-40 Mg-PSZ	39.54	39.24
◇	NGK Z-191 Y-TZP	7.08	64.56
△	Nilsen MS Mg-PSZ	14.19	54.66

Figure 45. Weibull plot for candidate zirconia materials at 750°C.

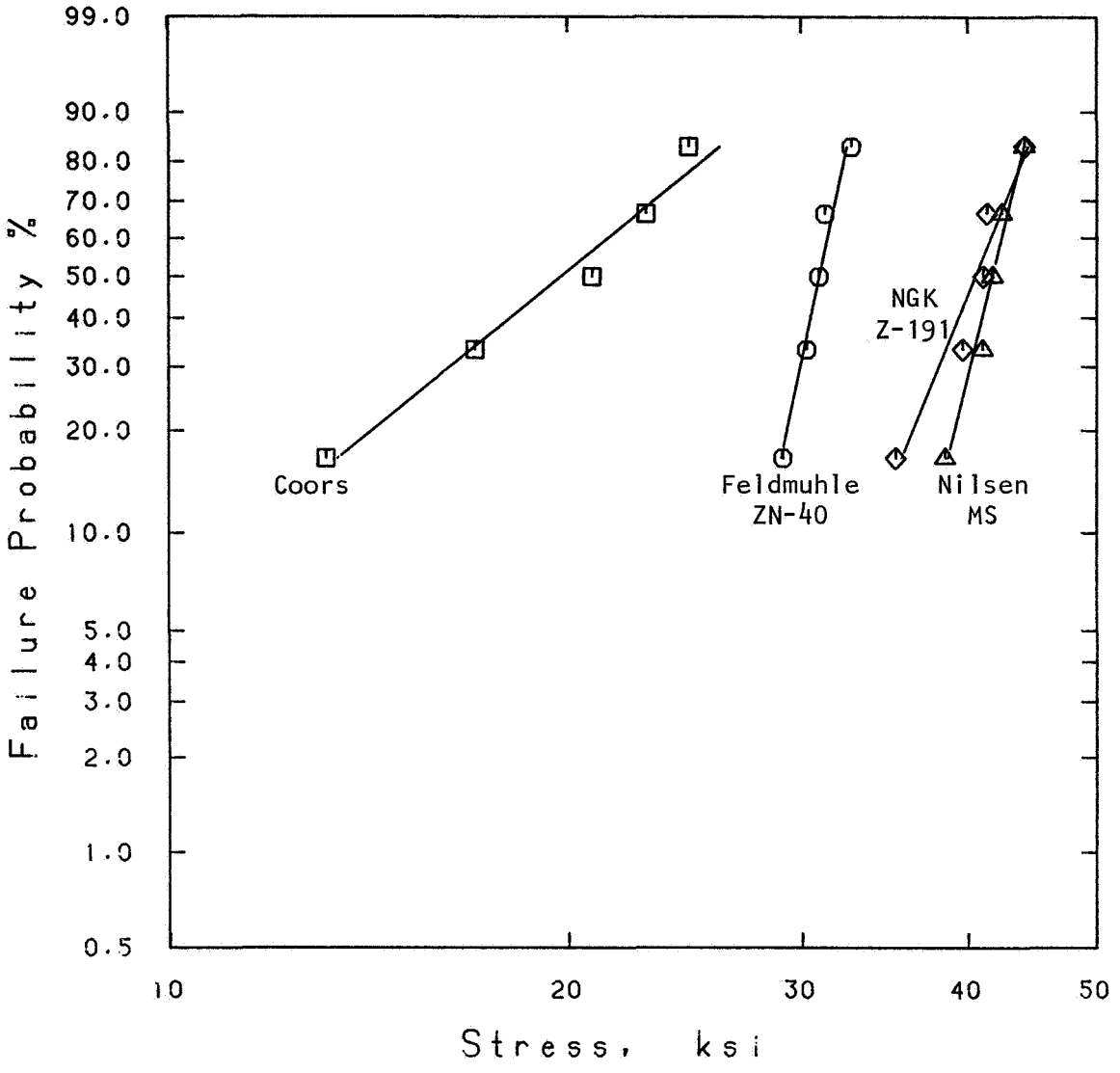

SYMBOL	MATERIAL	WEIBULL MODULUS, m	CHARACTERISTIC STRENGTH, ksi
□	Coors Mg-PSZ	3.44	22.00
○	Feldmuhle ZN-40 Mg-PSZ	20.10	31.55
◇	NGK Z-191 Y-TZP	10.47	42.01
△	Nilsen MS Mg-PSZ	17.41	42.66

Figure 46. Weibull plot for candidate zirconia materials at 1000°C.

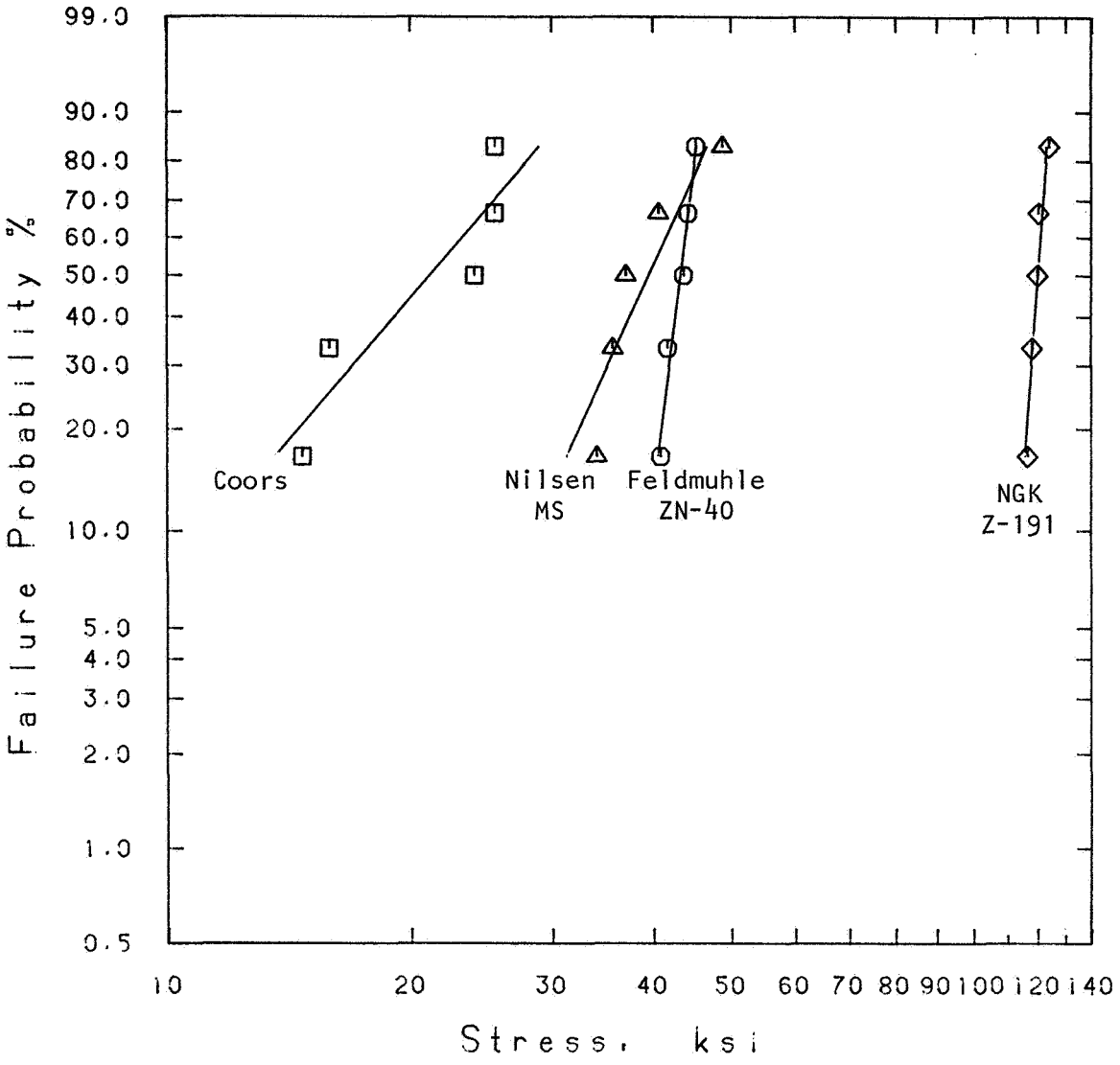

SYMBOL	MATERIAL	WEIBULL MODULUS, m	CHARACTERISTIC STRENGTH, ksi
□	Coors Mg-PSZ	3.01	23.93
○	Feldmuhle ZN-40 Mg-PSZ	20.59	44.15
◇	NGK Z-191 Y-TZP	35.39	121.38
△	Nilsen MS Mg-PSZ	5.69	42.30

Figure 47. Weibull plot for candidate zirconia materials at 25°C, after 1000 hr/1000°C exposure.

5. ELASTIC MODULUS/STRESS-STRAIN BEHAVIOR

The dynamic elastic modulus was measured by a flexural resonant frequency technique from 25° to 1000°C. The static or relaxed modulus was determined by measuring the outer fiber tensile strain during flexural strength testing. Resistance strain gages were used to measure deformation at 25°C. At elevated temperature, a precision electromechanical instrument was employed, where deformation was recorded at three positions on the sample tensile face within the region of pure bending (i.e., within the upper span length) as shown in Figure 48. This was accomplished by extending SiC rods from an LVDT coil and core up through the furnace to the sample. In this manner, the outer fiber tensile strain was directly recorded, without the need to employ potentially inaccurate methods of subtracting out the fixture/load rod deformations. The continuous stress-strain curves obtained are very helpful in assessing material behavior.

5.1 AMBIENT TEMPERATURE ELASTIC MODULUS

Results at ambient room temperature are provided in Tables 7 and 8. It is observed that the dynamic elastic moduli are approximately 5-7% higher than the static relaxed elastic moduli (~29.4 vs. 27.7 x 10^6 psi on the average). This is common for many ceramic materials and is related to plasticity effects. The deformation is very small in the dynamic test, and large in the static test. The elastic moduli of the four as-received zirconia materials evaluated agreed to within 3%.

Note that the room-temperature elastic moduli did not change appreciably after 1000 hr/1000°C exposure. The NGK Y-TZP modulus was the same before and after exposure. This was expected since the strength, microstructure, and phase assemblage were not affected either. Nilsen and Feldmuhle Mg-PSZ materials were shown above to be appreciably overaged and decomposed/destabilized after the 1000 hr/1000°C exposure, and their strength, phase assemblage, and microstructure significantly degraded. Table 7 illustrates, however, that the elastic modulus of these Mg-PSZ materials changed by only 2 to 3%, at most, after the 1000 hr/1000°C exposure.

PRECEDING PAGE BLANK NOT FILMED

PAGE 88 INTENTIONALLY BLANK

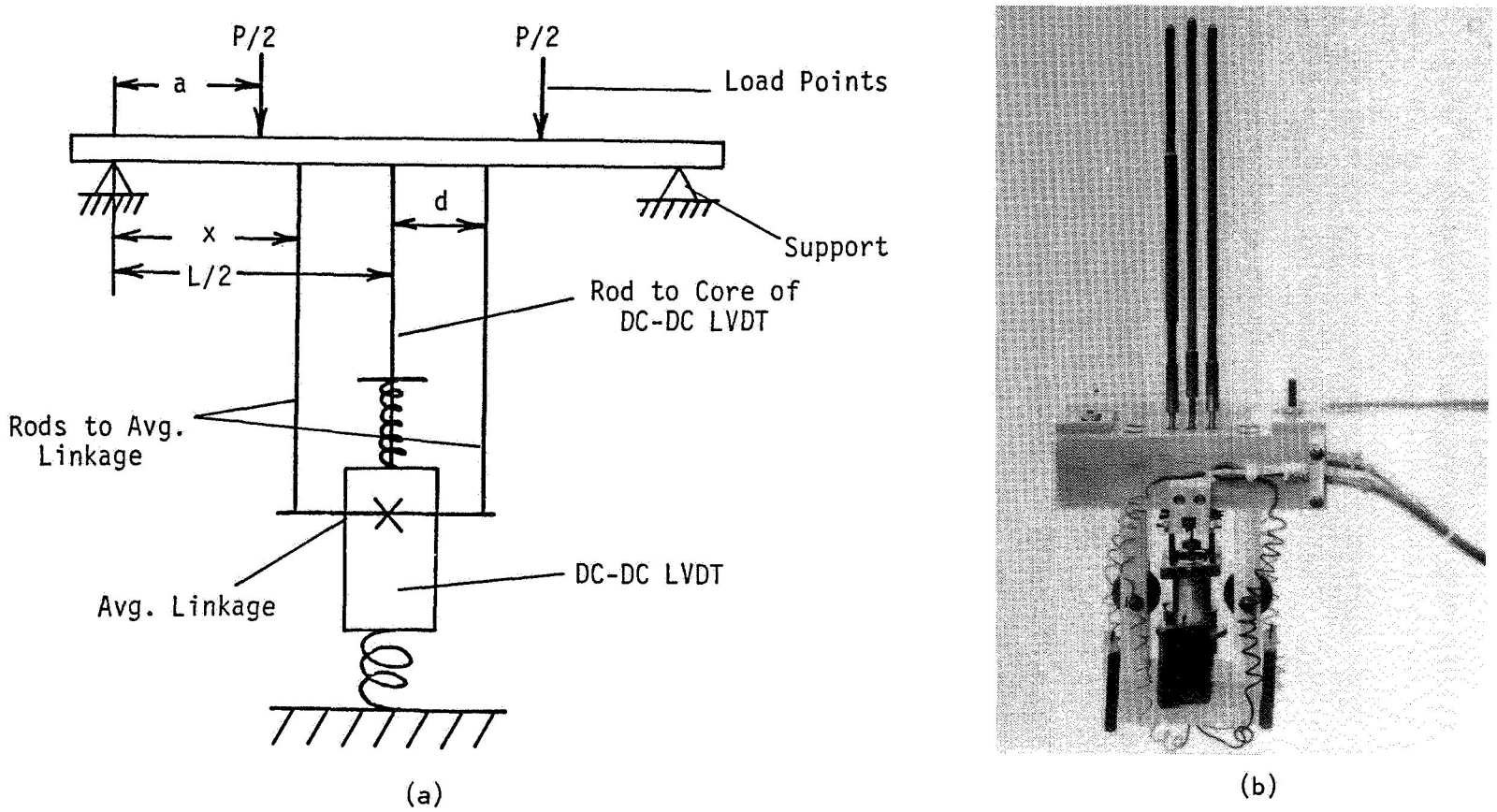

Figure 48. Schematic and photograph of 3-point deflectometer assembly for measurement of flexural deformation.

TABLE 7. ROOM TEMPERATURE ELASTIC MODULUS OF ZIRCONIA

Material	Young's Elastic Modulus, 10^6 psi			
	As-Received		After 1000 hr/ 1000°C Exposure	
	Relaxed[a]	Dynamic[b]	Relaxed[a]	Dynamic[b]
NGK Z-191 Y-TZP	27.4	28.9	27.5	28.9
Nilsen MS Mg-PSZ	27.2	29.3	27.1	30.2
Feldmuhle ZN-40 Mg-PSZ	28.0	29.8	27.2	29.2
Coors Mg-PSZ	28.0	29.5	18.3-27.0	--

[a]Determined with resistance strain gages during flexural strength test.
[b]Flexural resonant frequency method.

The Coors Mg-PSZ, however, was more severely affected. It was shown previously that this material exhibited an average strength decrease of 70% due to the exposure (Figure 17 and Table 6). Table 7 shows the range of room-temperature elastic moduli obtained for Coors Mg-PSZ after exposure. Appendix Table A20 illustrates that the strength degradation was not as uniform as for the other materials. Roughly half the exposed Coors samples tested exhibited a 64% strength decrease, and a 6% elastic modulus decrease. The other half were more severely affected, showing strength and elastic modulus degradation of 80% and 33%, respectively. Note that X-ray results (Table 3d) illustrated that the Coors material degraded the most also (with respect to phase content). After exposure the phase composition was 80% monoclinic. It is surmised that the Coors Mg-PSZ is more microcracked than the other Mg-PSZ materials. The behavior of the Nilsen material illustrated that elastic modulus is rather insensitive to overaging phenomena. The 33% decrease in elastic modulus for the overaged Coors Mg-PSZ then could only be explained by much more extensive microcracking which accompanied the transformation to monoclinic. This would also explain the larger strength decrease for the exposed Coors material. Also, note in Table 8 that significant amplitude-frequency peak broadening precluded accurate dynamic elastic modulus measurement for the exposed Coors Mg-PSZ. Extensive microcracking would explain this also.

TABLE 8. DYNAMIC ELASTIC MODULUS OF ZIRCONIA

Sample No.[b]	Dynamic Young's Modulus,[a] 10^6 psi	
	As-Received	After 1000 hr/1000°C Static Exposure
	A. Nilsen MS Mg-PSZ	
1	29.2	30.3
2	29.2	30.0
3	29.1	30.3
4	29.4	30.0
5	29.4	30.2
Avg	29.3	Avg 30.2
	B. Nilsen TS Mg-PSZ	
1	29.2	29.6
2	29.2	29.2
3	28.9	31.0
4	29.3	29.8
5	28.7	29.9
Avg	29.1	Avg 29.9
	C. Feldmuhle ZN-40 Mg-PSZ	
1	29.2	29.6
2	29.9	29.6
3	30.0	29.2
4	29.9	28.0
5	-	29.6
Avg	29.8	Avg 29.2
	D. Coors Mg-PSZ	
1	29.3	c
2	29.7	c
3	29.8	c
4	29.5	c
5	29.4	c
Avg	29.5	

TABLE 8. (cont.)

Sample No.[b]	Dynamic Young's Modulus,[a] 10^6 psi As-Received	After 1000 hr/1000°C Static Exposure
	E. NGK Z-191 Y-TZP	
1	28.7	28.9
2	28.9	28.9
3	28.9	29.1
4	29.0	28.9
5	28.8	28.9
	Avg 28.9	Avg 28.9

[a]Determined at 25°C by flexural resonant frequency method.

[b]Note that as-received, as-exposed data were obtained on five different sample sets from each material lot.

[c]Dynamic amplitude-frequency peak broadened too greatly to permit measurement of resonant frequency from which to compute the dynamic modulus. However, static measurements (i.e., bend test) indicate the elastic modulus decreased substantially. Values ranged from 17-27 x 10^6 psi.

5.2 ELEVATED TEMPERATURE ELASTIC MODULUS

Elevated temperature elastic modulus measurements were conveniently made using the dynamic flexural resonant frequency method. The technique involved suspending a rectangular bar sample (0.090 x 0.25 x 2.500 in.) in a furnace, and measuring the flexural resonant frequency as the furnace temperature was increased. The use of flame de-sized Nippon Carbon Nicalon® SiC yarn to suspend the sample as well as to transmit input and output mechanical vibrations made this extremely amenable to high temperature measurement. The amorphous SiC yarn can readily be used in air atmosphere (a distinct advantage over previously used graphite yarn) and is easily coupled to test samples yielding a minimum of system resonances (often a problem with previously used platinum-rhodium wire).

The measured dynamic elastic modulus as a function of temperature to 1000°C for each of the four ZrO_2 materials is presented in Figure 49-52. The individual data points are given, illustrating specific regions of the thermal cycle (i.e., upon heating or cooling, replicate runs, etc.). In general, the elastic modulus of zirconia decreased from a value of approximately 29.5 x 10^6 psi at 25°C, to values around 23 x 10^6 psi at 1000°C. Note in Figure 49 the excellent agreement with literature data[12] for Y-PSZ. Figure 53 presents the modulus-temperature relation for each of the zirconia materials investigated. Note that the three Mg-stabilized materials exhibit similar behavior. The slightly lower elastic modulus for the NGK Y-stabilized material is most probably explained by the significant silica-rich intergranular regions in this material, the elastic modulus of silica being about a third of that for zirconia (refer to spectrographic analysis results presented in Table 4).

For the most mature Mg- and Y-PSZ materials (i.e., Nilsen and NGK), the elevated temperature dynamic elastic modulus was measured after 1000 hr/1000°C exposure. The results are presented in Figures 54 and 55. As previously stated, the extended exposure has little effect on elastic modulus (a 2-3% effect at most). Any decreases in modulus could be attributed to increased microcracking and increased monoclinic content (lower density) upon overaging/destabilization. Any increases in modulus could conceivably be caused by crystallization of a glass phase, for instance. The apparent minimum in the Mg-PSZ curve shown in Figure 55 is not explainable. It is not known whether

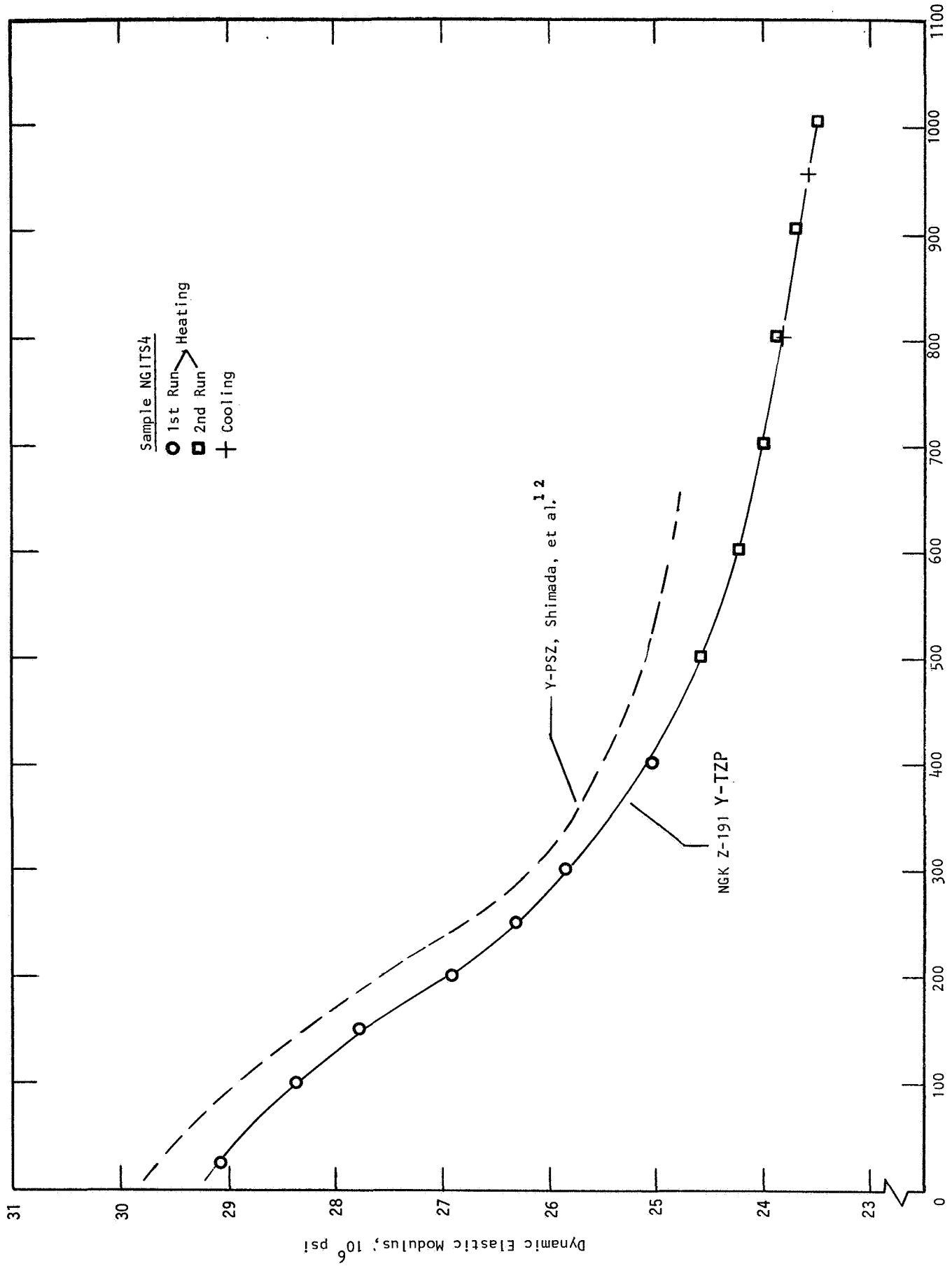

Figure 49. Dynamic elastic modulus as a function of temperature of NGK Z-191 Y-PSZ.

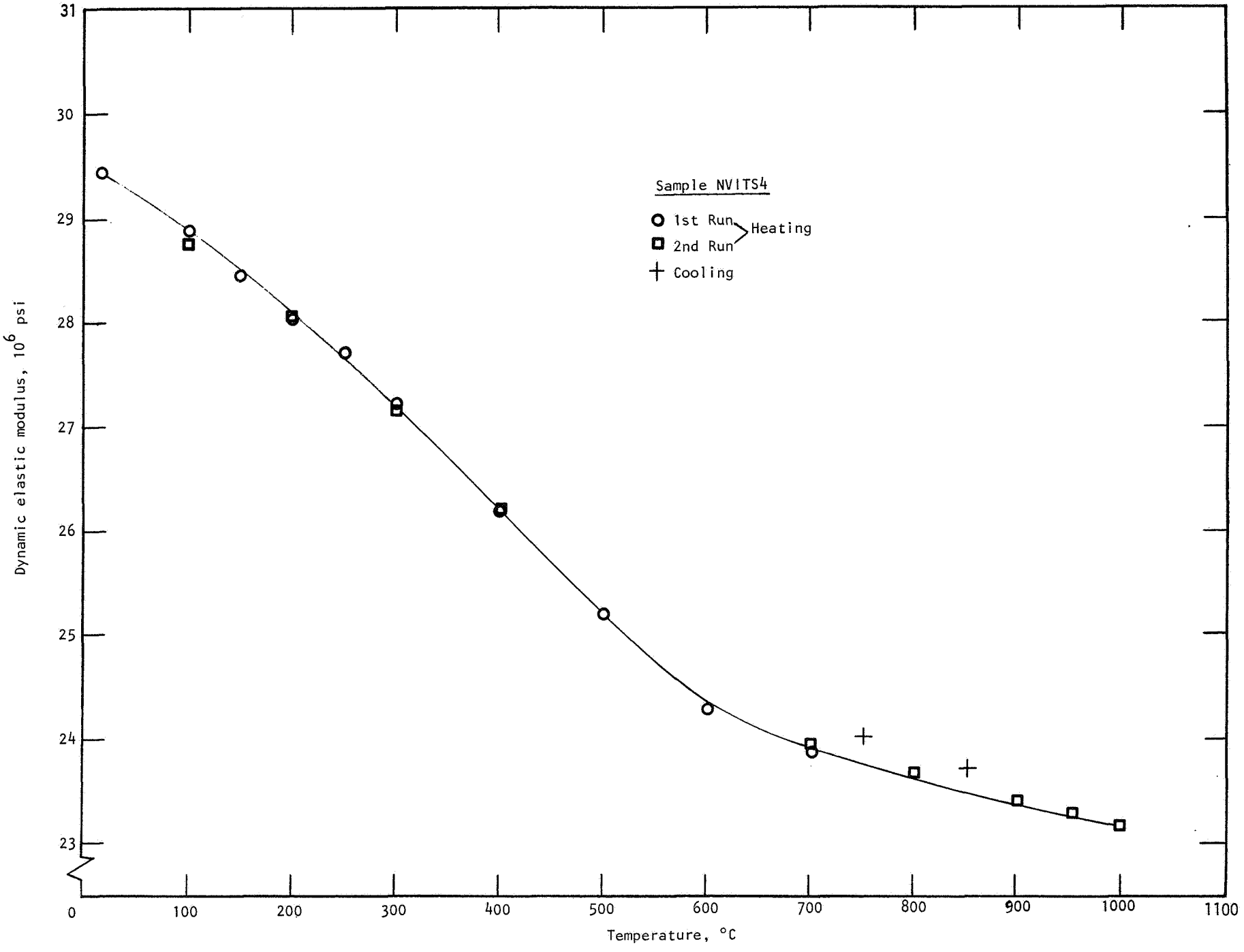
Sample NVITS4
1st Run
2nd Run
Heating
Cooling
Dynamic elastic modulus, 10^6 psi
Temperature, °C
31
30
29
28
27
26
25
24
23
0
100
200
300
400
500
600
700
800
900
1000
1100

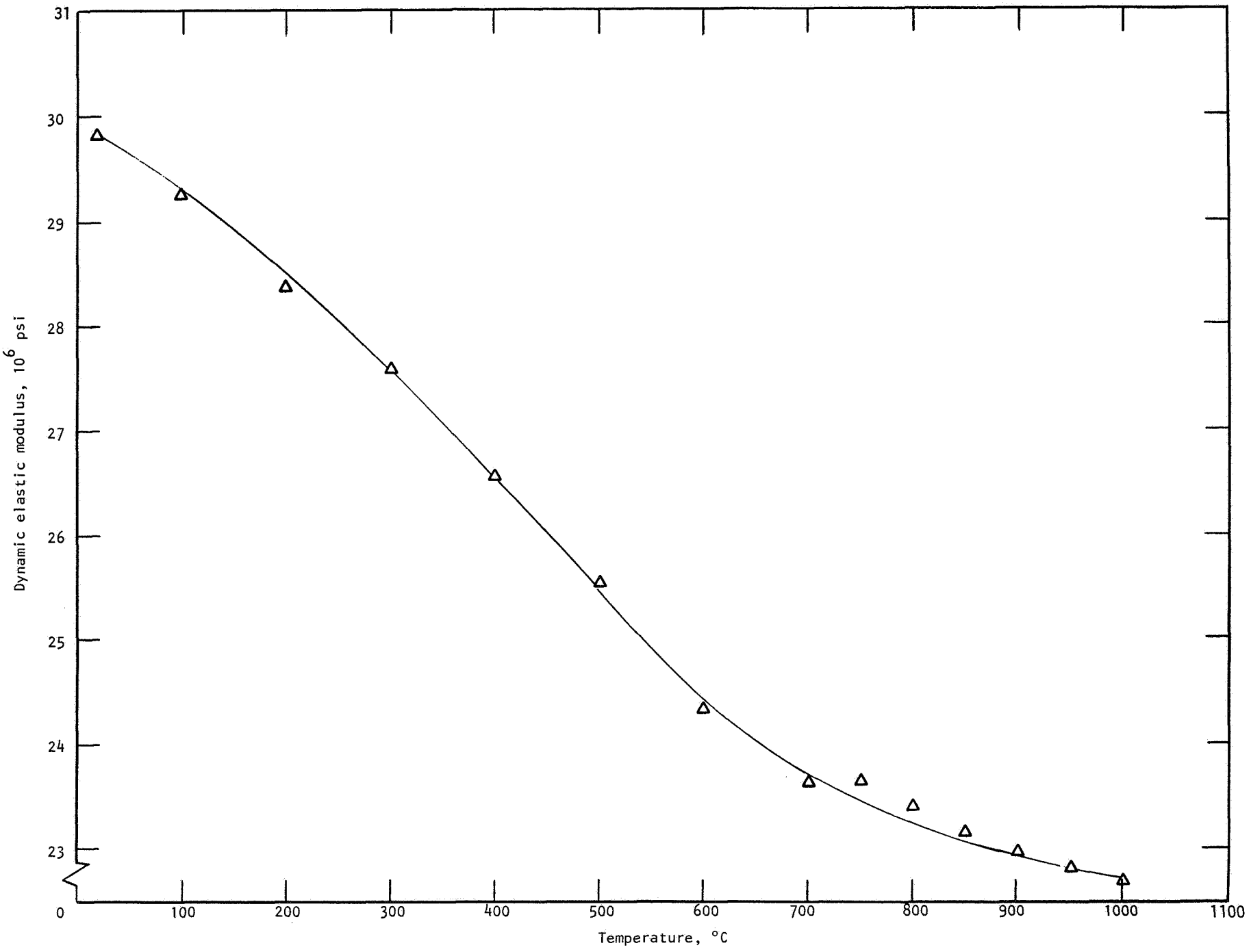

Figure 51. Dynamic elastic modulus as a function of temperature for Feldmuhle ZN-40 Mg-PSZ.

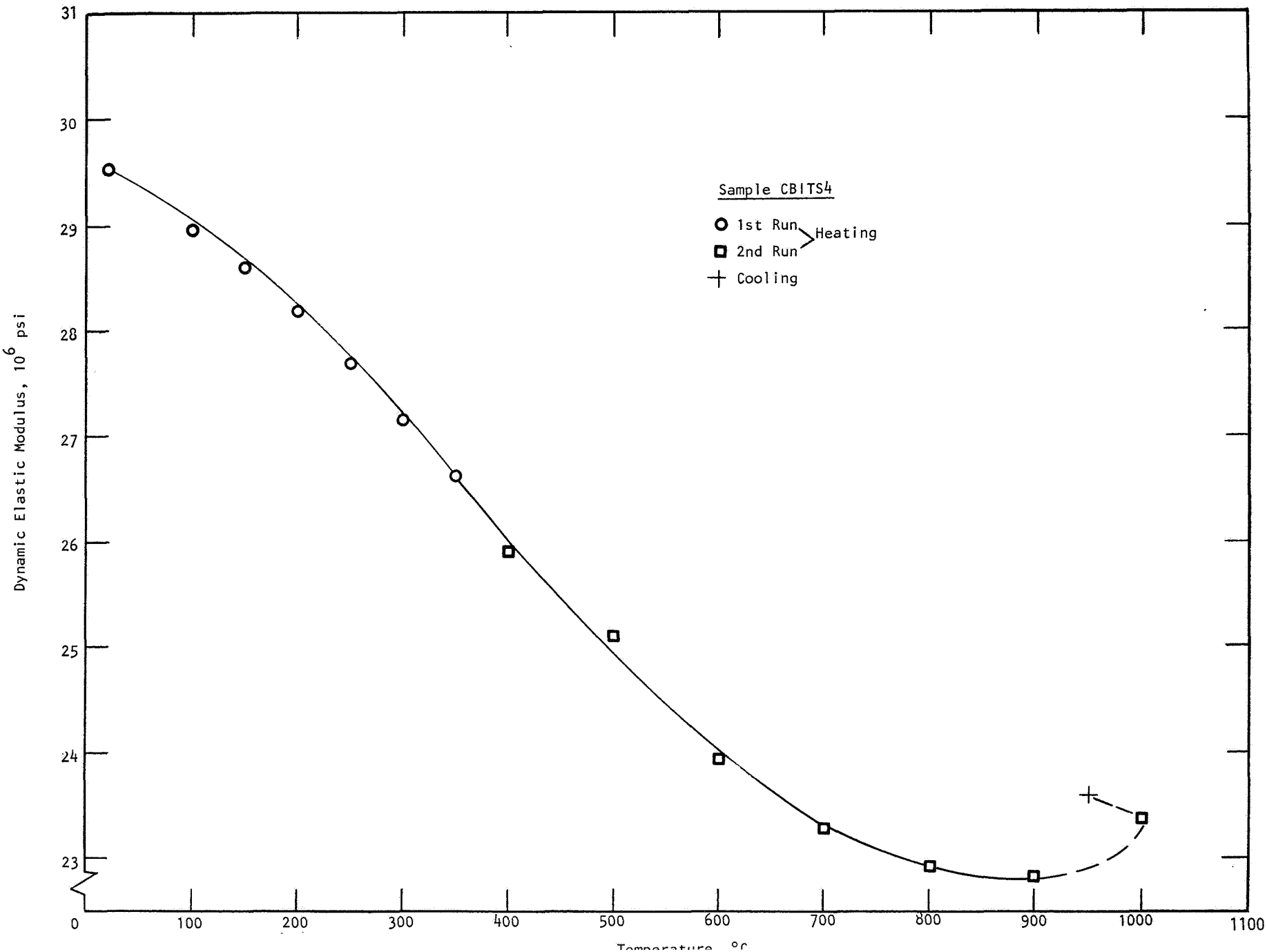
Sample CBITS4
1st Run
2nd Run
Heating
Cooling
Dynamic Elastic Modulus, 10^6 psi
Temperature, °C
31
30
29
28
27
26
25
24
23
0
100
200
300
400
500
600
700
800
900
1000
1100

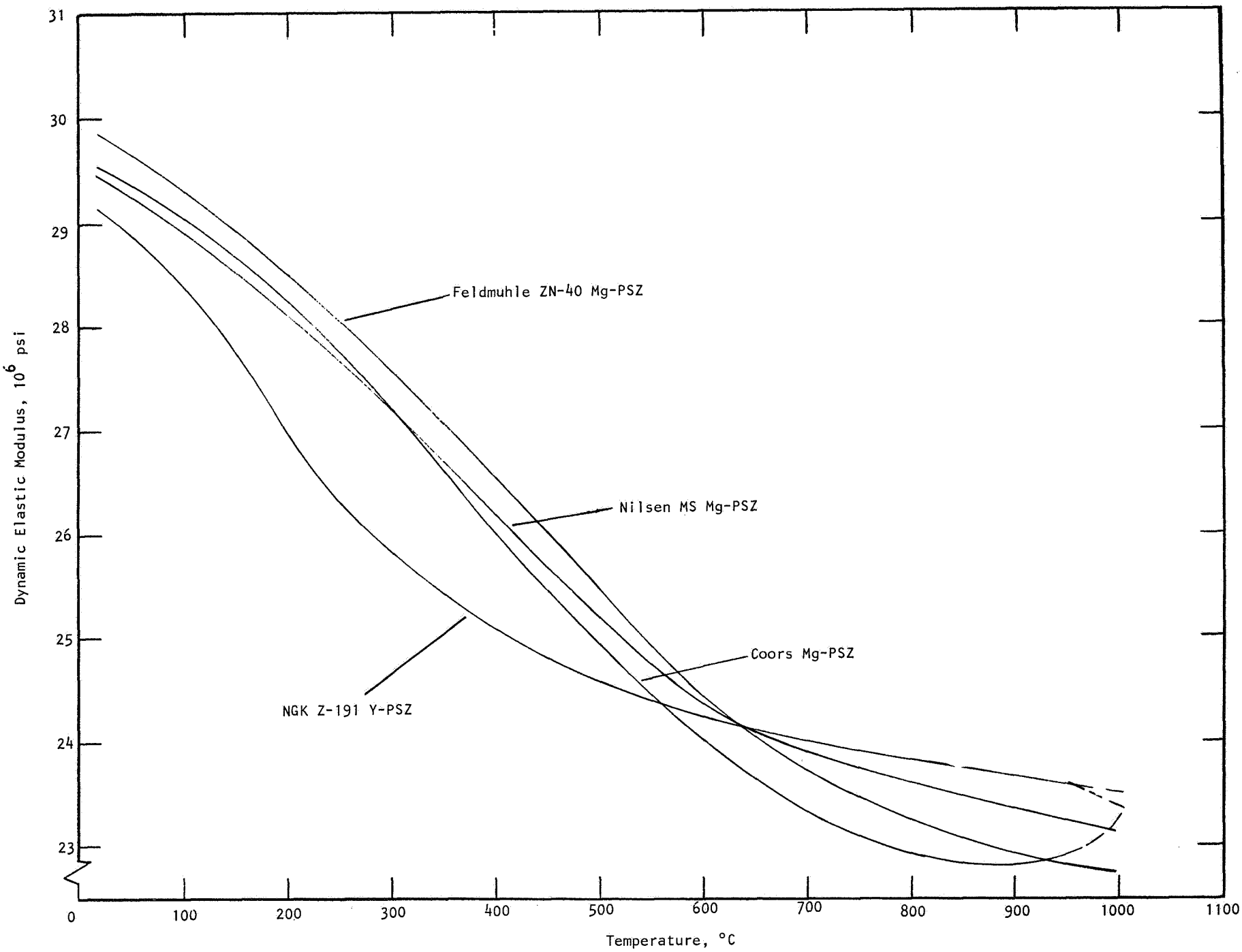

Figure 53. *Dynamic elastic modulus of Mg- and Y-PSZ materials.*

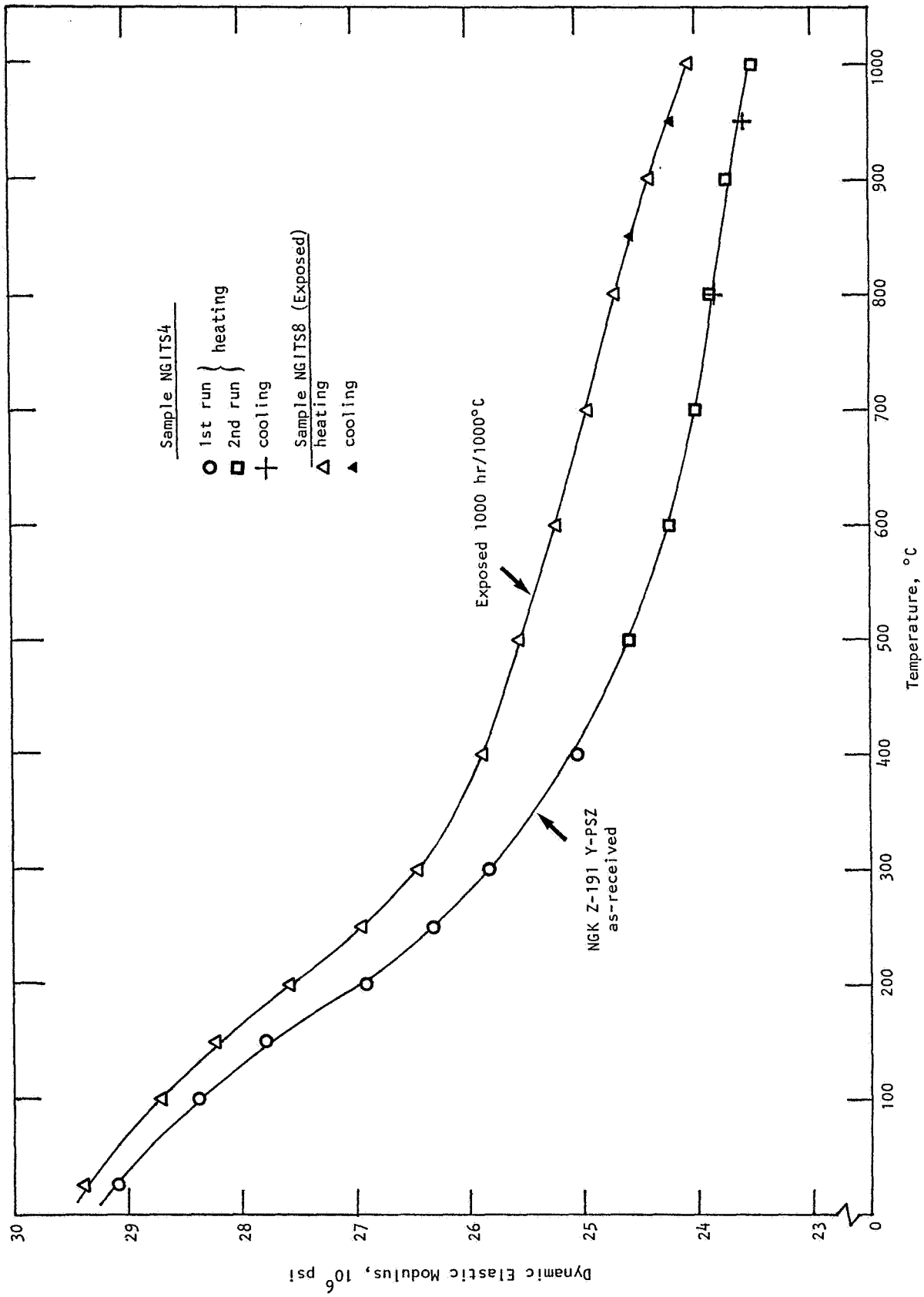

Figure 54. Dynamic elastic modulus as a function of temperature of NGK Z-191 Y-TZP before and after 1000 hr/1000°C exposure.

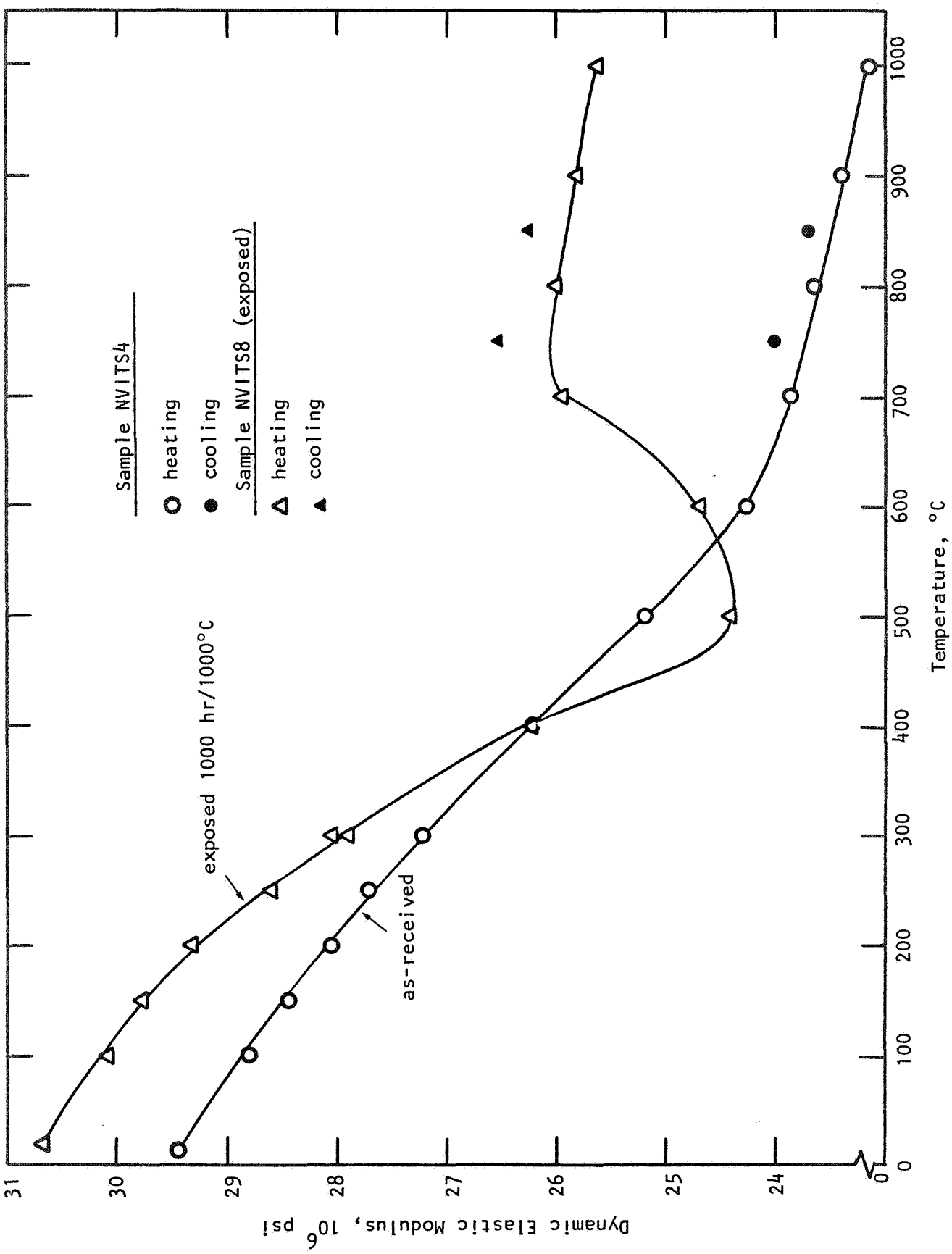

Figure 55. Dynamic elastic modulus as a function of temperature of Nilsen MS-grade Mg-PSZ before and after 1000 hr/1000°C exposure.

or not this minimum is reproducible. Note that the exposed and unexposed modulus-temperature curves in Figures 54 and 55 was obtained on different samples for each material (i.e., the same sample was not measured over the 25°-1000°C range both before and after exposure).

5.3 STRESS-STRAIN BEHAVIOR

It is extremely informative to observe the stress-strain behavior of these transformation-toughened zirconia materials. This was measured during fast-fracture flexure testing from 25° to 1000°C, and is provided for each zirconia in Figures 56-59. Feldmuhle ZN-40 Mg-PSZ, Coors Mg-PSZ, and NGK Z-191 Y-TZP materials all exhibited linear stress-strain behavior at all temperatures from 25° to 1000°C. This illustrates the absence of glassy grain boundary phases in these materials. This is significant for the NGK material, since it has ~1% intergranular silica phase, which is detrimental from a creep resistance standpoint (to be discussed in Section 8).

Nilsen MS Mg-PSZ, however, exhibited nonlinear stress-strain behavior at 25°C, and linear stress-strain behavior at all elevated temperatures (Figure 57). This is interesting, and is related to the particular condition of the tetragonal phase, and how close to transformation the precipitates are. For instance, for the Nilsen material (Figure 57) the strength and toughness at the elevated temperatures (>500°C) are reduced enough that the high stress levels required for transformation are not attained. Therefore, the elevated temperature stress-strain curves remain linear.

After 1000 hr/1000°C exposure, Figures 60-63 compare the residual ambient temperature stress-strain curves. Note in Figure 60 that for NGK Z-191 TZP, these curves are almost superimposed. This is consistent with the superior stability of this material as previously discussed. Note in Figure 63 that the Coors material exhibits a nonlinear stress-strain curve after the 1000 hr/1000°C exposure. This is consistent with the mounting evidence of extensive microcracking in this material after exposure.

The failure strains for each material as a function of test temperature are provided in Figure 64. The materials with the highest strength, i.e., NGK Z-191 Y-TZP and Nilsen MS Mg-PSZ, have the highest failure strains. The

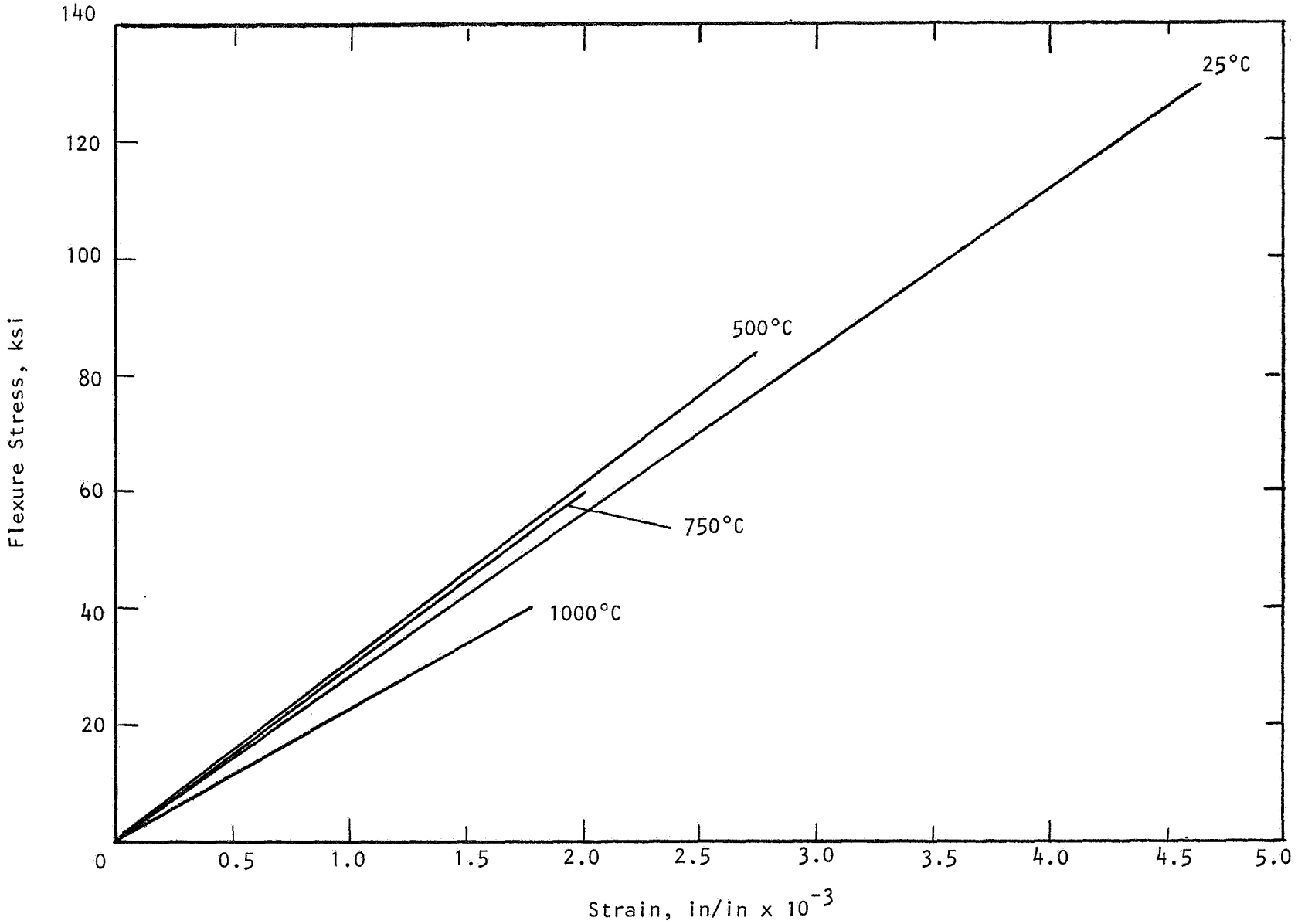

Figure 56. Representative flexural stress-strain behavior of NGK Z-191 Y-TZP.

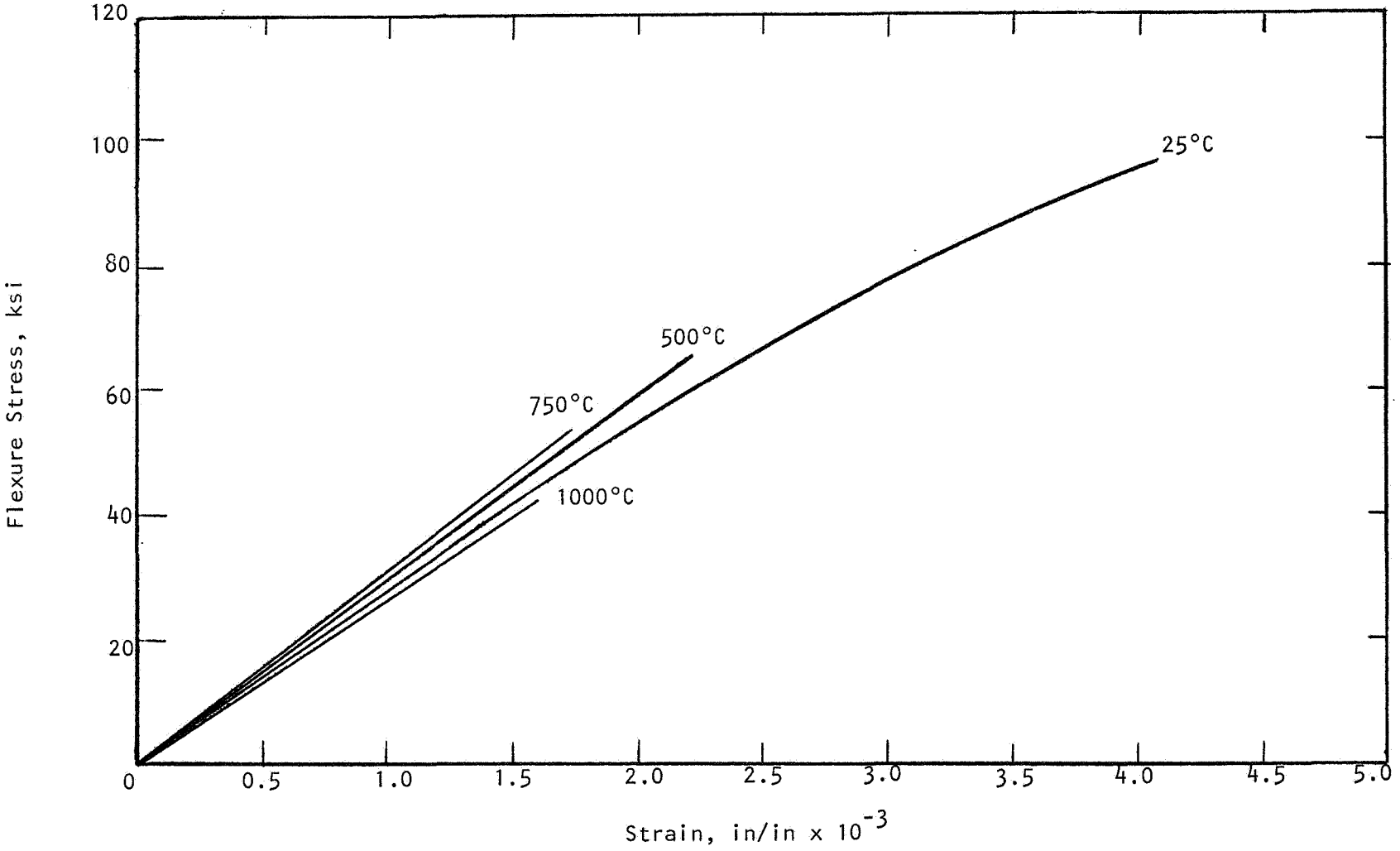

Figure 57. Representative flexural stress-strain behavior of Nilsen MS ***Mg-PSZ.***

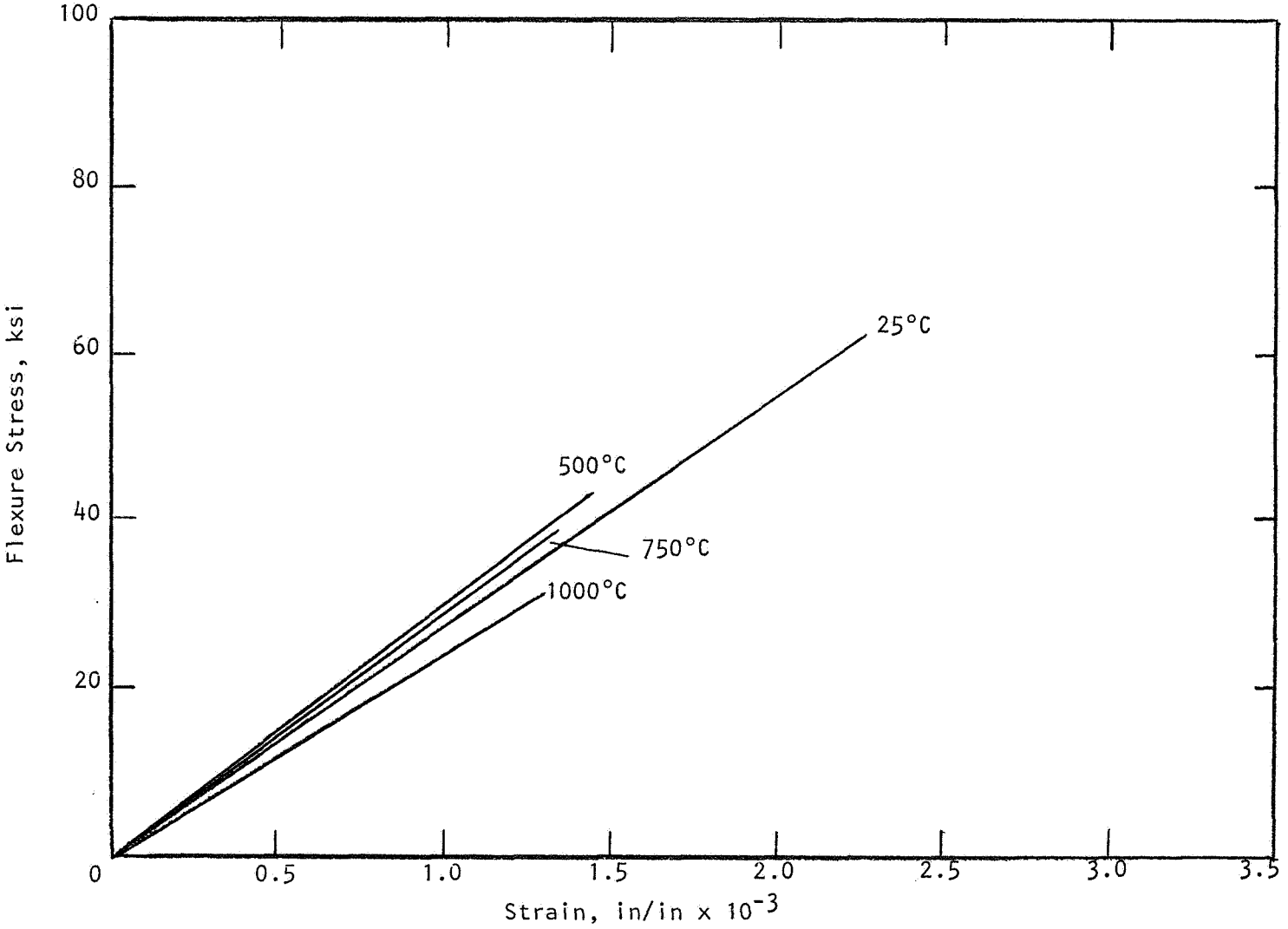

Figure 58. Representative flexural stress-strain behavior of Feldmuhle ZN-40 Mg-PSZ.

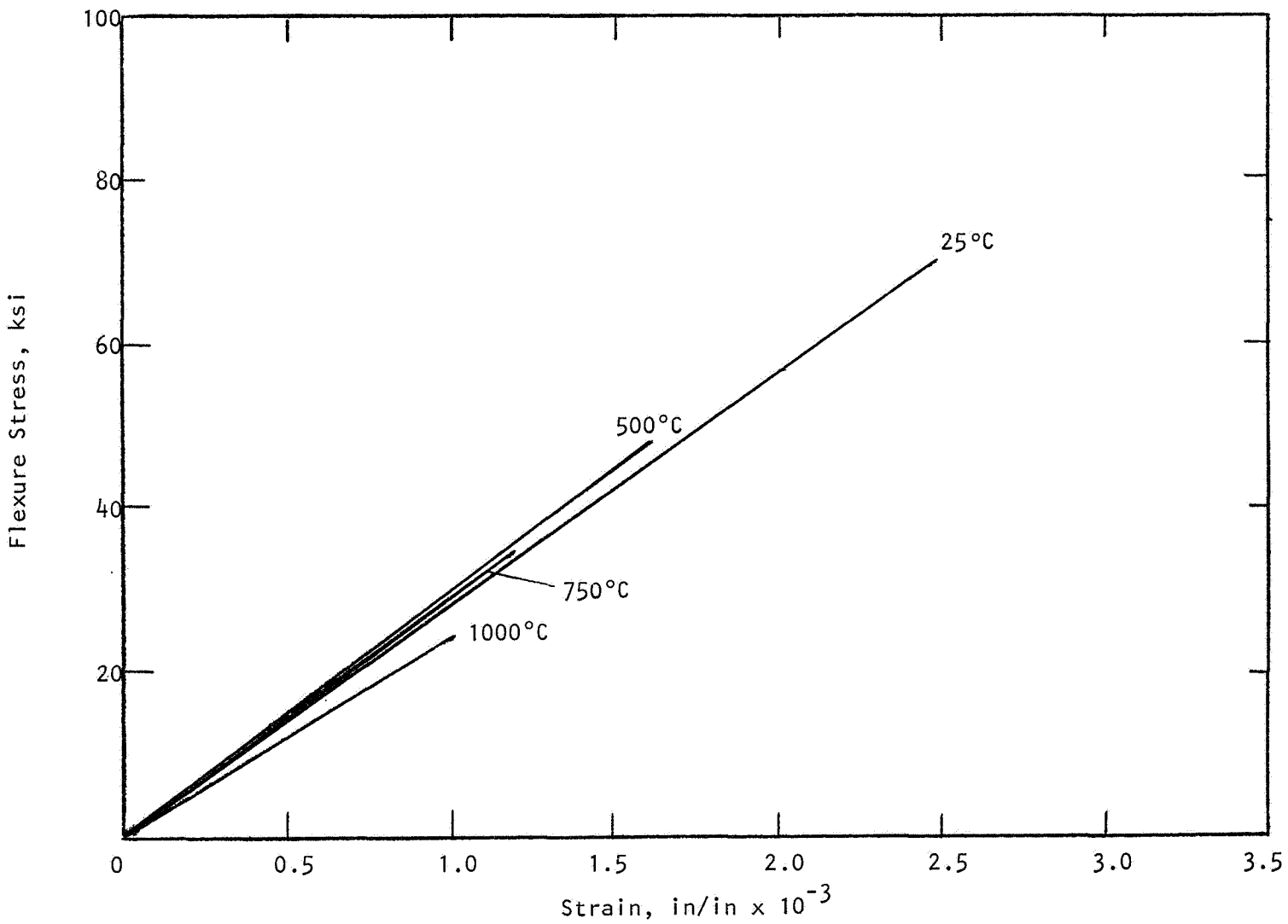

Figure 59. Representative flexural stress-strain behavior of Coors Mg-PSZ.

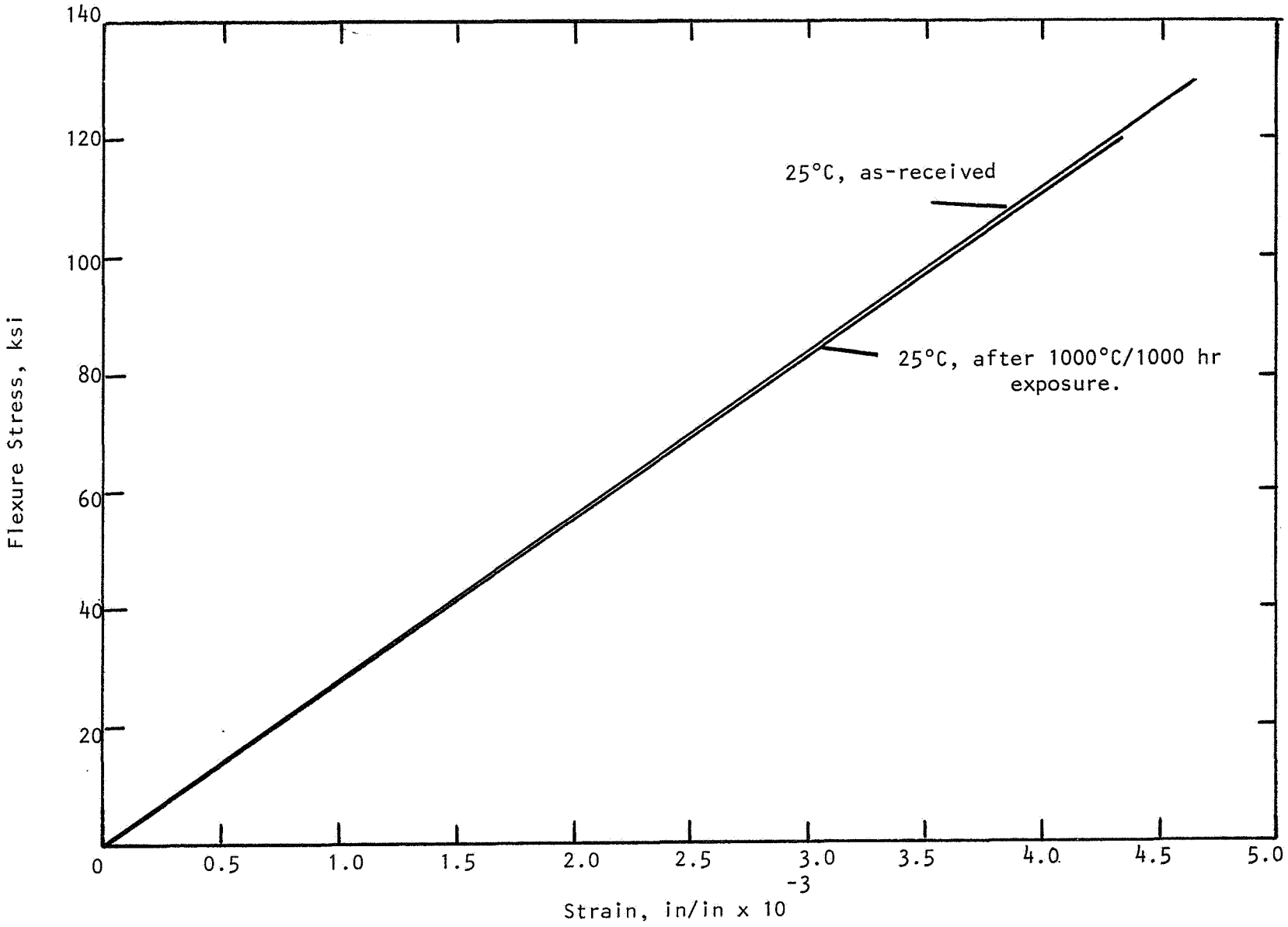

Figure 60. Flexural stress-strain behavior of NGK Z-191 Y-TZP at 25°C, before and after 1000°C/1000 hr static exposure.

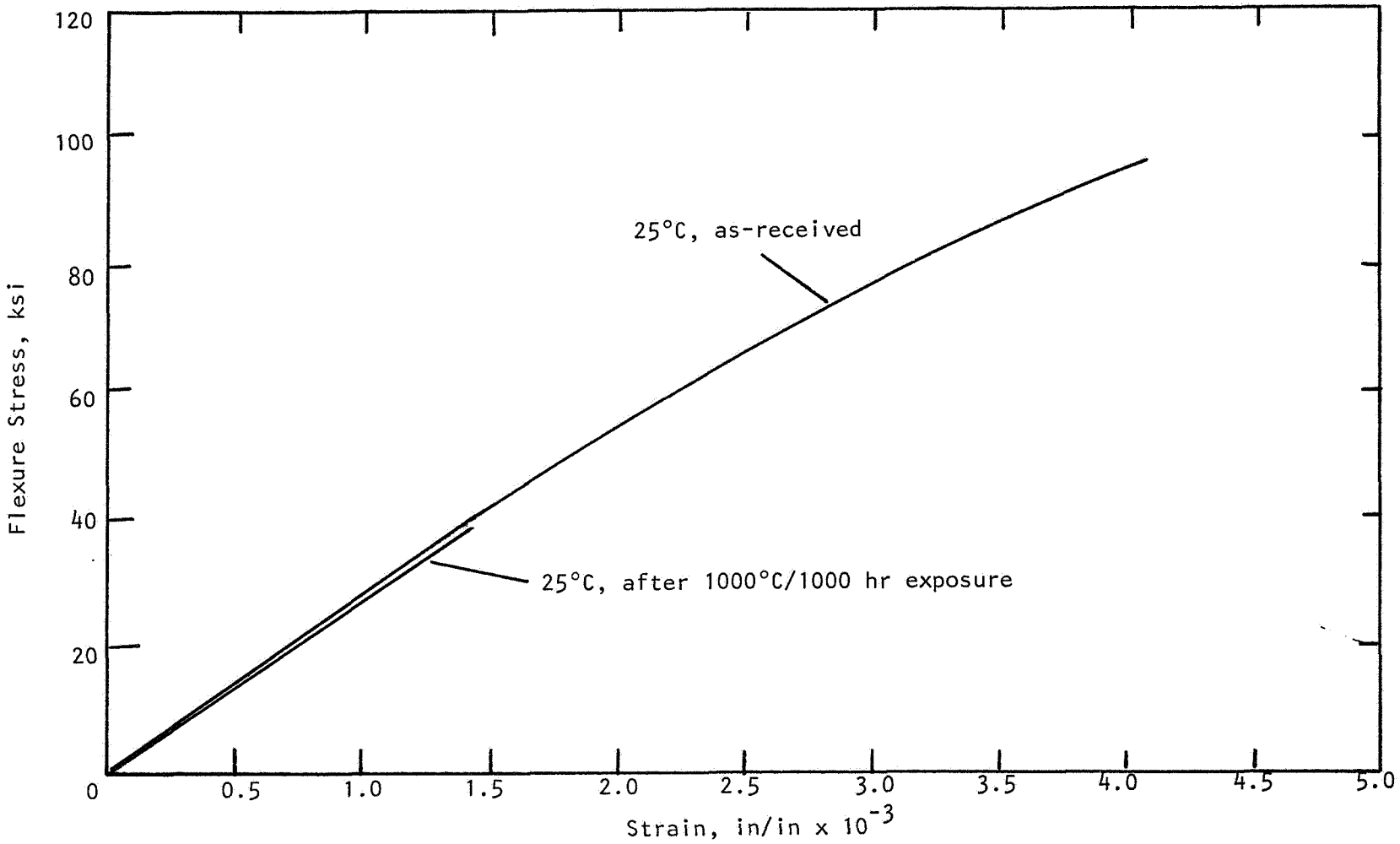

Figure 61. Flexural stress-strain behavior of Nilsen MS ***Mg-PSZ at 25°C,*** *before and after 1000 hr/1000°C static exposure.*

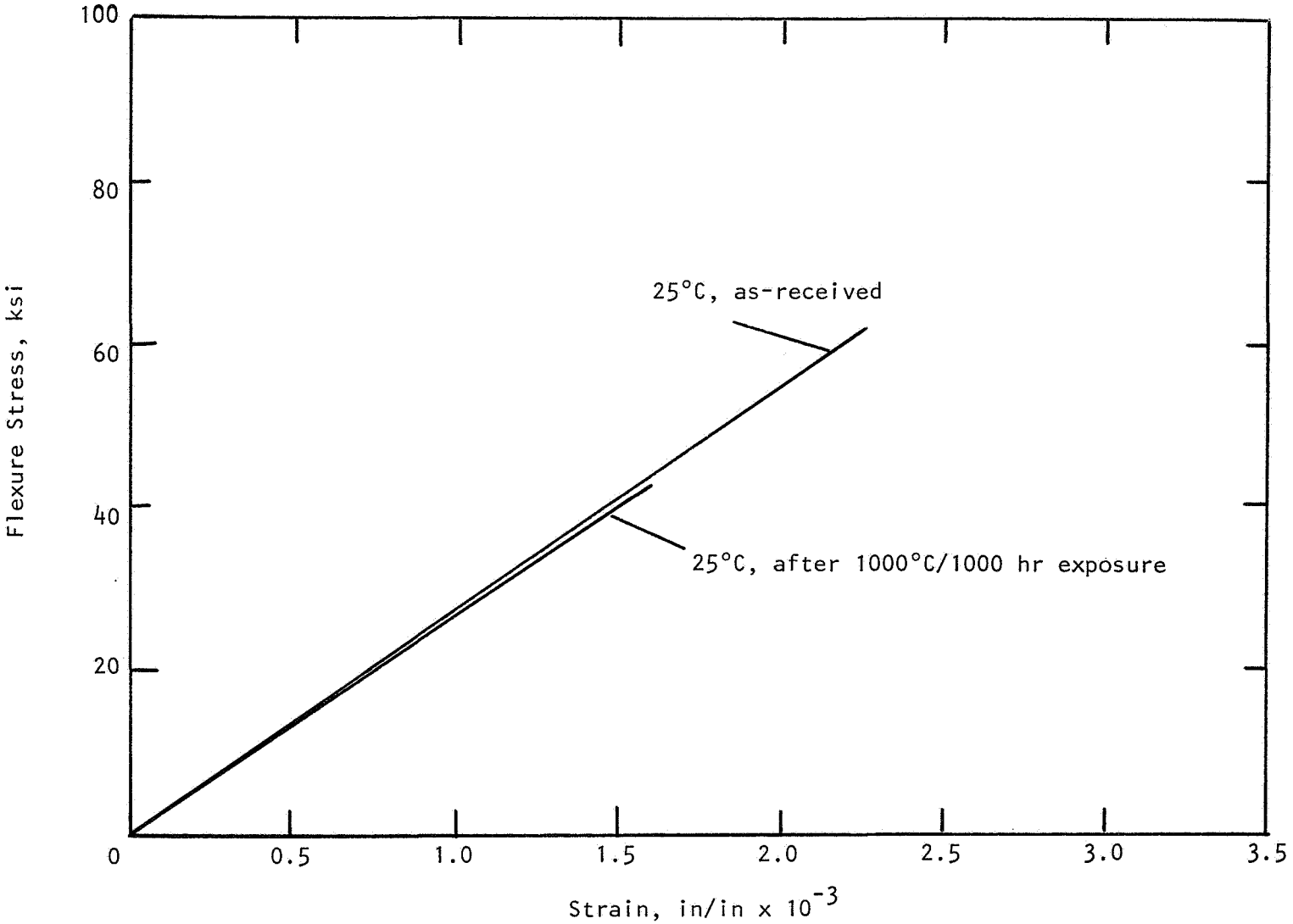

Figure 62. Flexural stress-strain behavior of Feldmuhle ZN-40 Mg-PSZ at 25°C, before and after 1000°C/1000 hr static exposure.

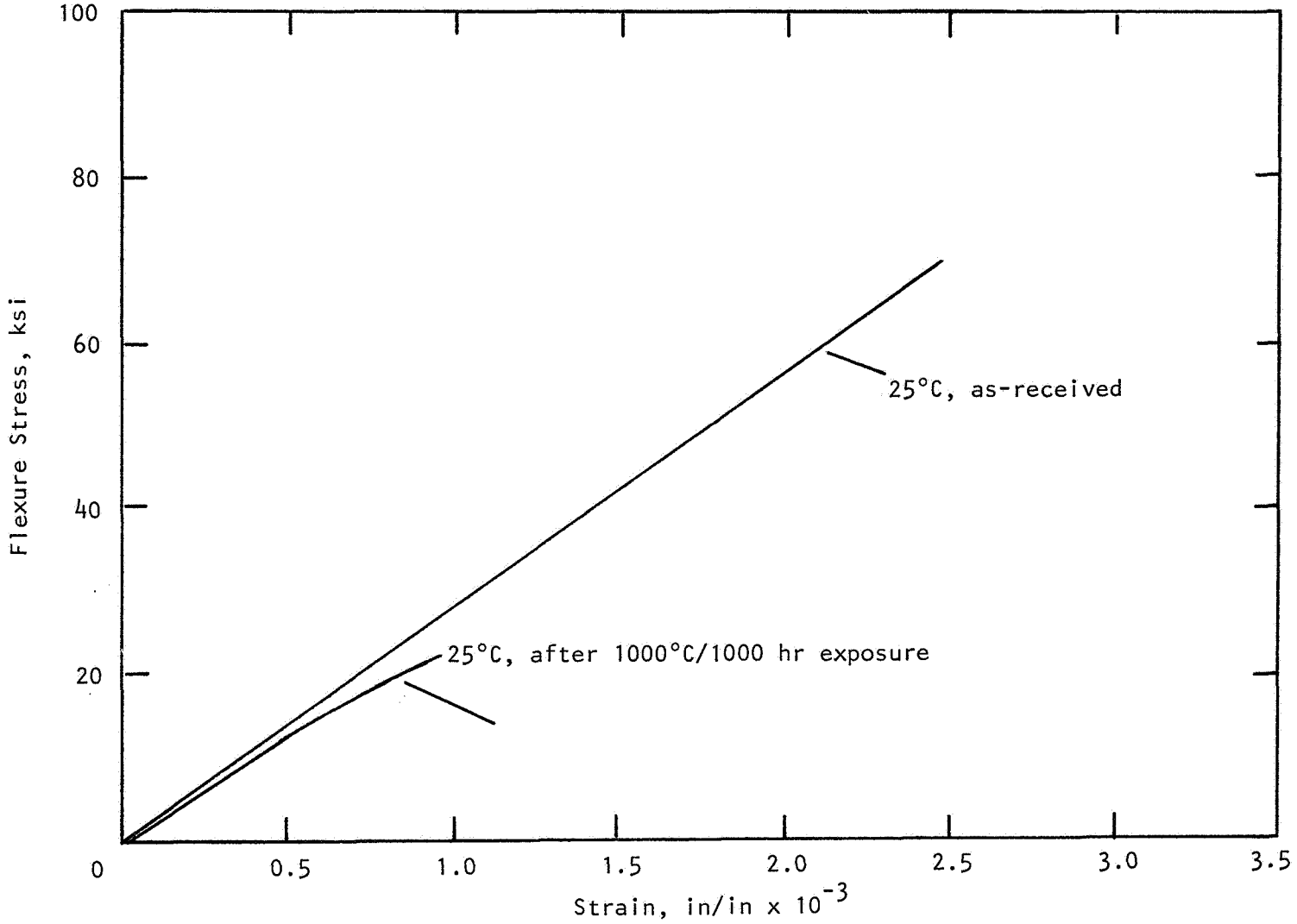

Figure 63. Flexural stress-strain behavior of Coors Mg-PSZ at 25°C, before and after 1000 hr/1000°C static exposure.

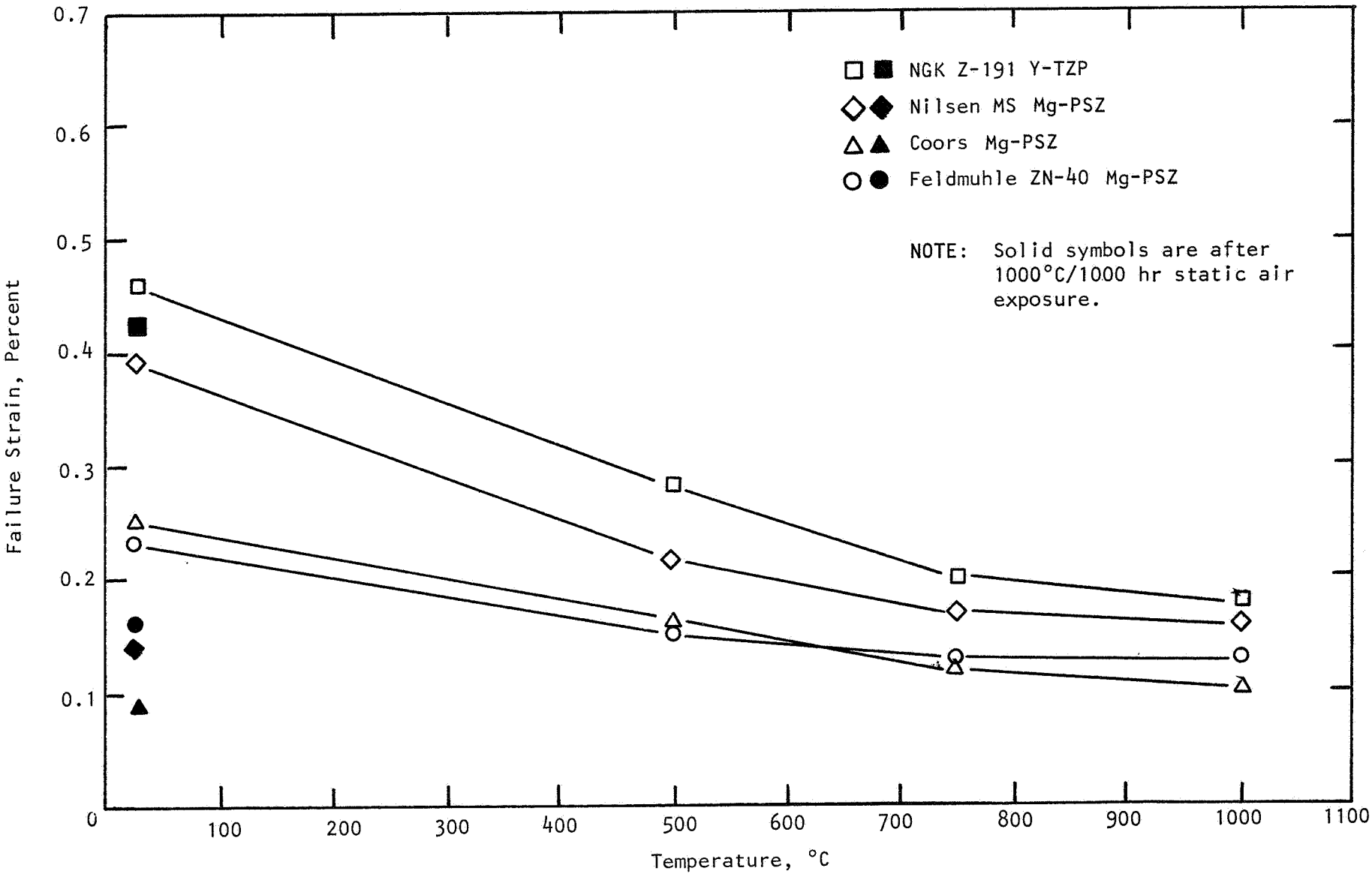

Figure 64. Failure strain of zirconia, before and after long-term exposure at 1000°C.

decrease in failure strain with temperature exhibited by all materials follows the strength reduction as a function of temperature.

The mechanical properties (strength, failure strain, and elastic modulus) for all zirconia materials evaluated, both as-received and after 1000 hr/1000°C exposure, are summarized in Table 9. The elastic modulus generally decreases from ~29.5 x 10^6 psi at 25°C to nominally 23 x 10^6 psi at 1000°C. After 1000 hr/1000°C thermal exposure, the dynamic elastic modulus only changed ~2-4% for both Y-TZP and Mg-PSZ (Nilsen) materials. The elastic modulus is a property related to interatomic bonding and is a function of temperature only; it is not affected by the relative amounts of cubic, tetragonal, and monoclinic phases in the structure. This holds true unless very significant microcracking accompanies the phase changes during exposure. The developmental Coors material was found to exhibit as much as a 30% modulus decrease due to this effect.

TABLE 9. ROOM TEMPERATURE MECHANICAL PROPERTIES OF ZIRCONIA BEFORE AND AFTER 1000°C/1000 HR STATIC AIR EXPOSURE

Material	Density, g cm^{-3}	Properties As-Received			Properties After 1000°C/1000 hr Exposure		
		Flexural Strength, psi	Failure Strain, %	Elastic Modulus, 10^6 psi	Flexural Strength,[a] psi	Failure Strain, %	Elastic Modulus, 10^6 psi
Nilsen MS Mg-PSZ	5.710	92,450	0.39	27.2	39,350 (-57%)	0.15	27.1
Feldmuhle ZN-40 Mg-PSZ	5.773	61,830	0.23	28.0	43,210 (-30%)	0.16	27.2
Coors Mg-PSZ	5.742	69,880	0.25	28.0	21,140 (-70%)	0.09	23.2
NGK Z-191 Y-TZP	5.853	129,090	0.46	27.4	119,840 (-7%)	0.43	27.5

[a]Numbers in parentheses indicate percentage change.

6. FRACTURE TOUGHNESS

Fracture toughness values, K_c, were determined using a modified indentation-strength method. The objective was to observe the relative change in toughness of each material as a function of temperature and long-term static air exposure (1000 hr/1000°C).

The indentation-strength method of Chantikul et al.[13] was chosen for this work, where strength is related to material toughness by the equation:

$$K_c = n_v^R (E/H)^{1/8} (\sigma P^{1/3})^{3/4}$$

where: n_v^R is a dimensionless constant
E/H is the ratio of elastic modulus to hardness, GPa/GPa
σ is the indentation flexure strength, MPa
P is the indentation contact load, MN

Initial measurements were necessary to determine the proper indentation load, P, to be used for both fine grain Y-TZP and coarse grain Mg-PSZ materials. To determine the proper indentation load, samples having indentation loads of 5 to 20 kgf (4.9×10^{-5} to 1.96×10^{-4} MN) were tested in 4-point flexure at ambient temperature and at 1000°C. It was found that some Coors and Feldmuhle Mg-PSZ samples failed at natural flaws instead of at the indentations, thereby invalidating them for the toughness measurement. It was therefore decided to test the materials in the 3-point configuration in order to assure failure at the indentation. An indentation load of 20 kgf (1.96×10^{-4} MN) was chosen as the one which would assure a controlled flaw large enough (relative to grain size and natural flaws) to be the fracture origin.

Indentations were made using a Vicker's Hardness test machine. They were made at room temperature, in ~40% relative humidity, just prior to flexure testing. The indentation load duration was 15 sec. The indentation axes were oriented parallel to the sample length and width. The samples were not post-indentation annealed, nor was any oil placed on the indentations, since at elevated temperature those treatments would be ineffectual. Table 10

PAGE 114 INTENTIONALLY BLANK

PRECEDING PAGE BLANK NOT FILMED

TABLE 10. PARAMETERS FOR K_c CALCULATION

Samples

- 1/4 x 1/8 x 2 1/4 in. flexure bars
- As-received, as-machined surfaces

Material	Avg. Surface Finish, Microinches (RMS)
Coors 3% MgO-PSZ	32
Feldmuhle ZN-40 Mg-PSZ	52
Nilsen MS-grade Mg-PSZ	11
NGK Z-191 Y-TZP	15

Controlled Flaw

- One Vicker's indentation at center of tensile surface
- Indentation load = 20 kgf = 196 N
- No post-indentation anneal
- Indentations not covered with immersion oil

Flexure Testing

- 3-point configuration
- Lower span 1.75 in.
- All testing in air
- Relative humidity = 35-45%
- One break per sample
- Fracture surfaces of all samples examined for valid failure
- Crosshead deformation rate = 0.02 ipm

K_c Calculation

- $K_c = \eta_v^R (E/H)^{1/8} (\sigma P^{1/3})^{3/4}$ [1,2]
- η_v^R = 0.59 assumed
- E/H considered equal to 20 for all test conditions
- Fracture surfaces of all samples examined for valid failure

summarizes the test and calculation parameters. Table 11 indicates mean values of indentation diagonals, a. For Mg-stabilized materials, the value is approximately twice the average cubic grain size. For the NGK Y-TZP, this value is that of a flaw approximately an order of magnitude larger than the average grain size. In general, the post-exposure room temperature average value of this parameter (a) fell within one standard deviation of the average unexposed value of a.

The material toughness was calculated according to the equation above. Two assumptions were made in order to perform the calculations. First, the constant η_v^R was assumed to be 0.59, based upon the reference work[13,14] and work done by Schioler.[15,16] Second, the ratio of elastic modulus to hardness was assumed constant over the range of temperature and exposures. Schioler[15,16] found the maximum error to be ±5% when the specific ratio for each material was used and compared to the assumed E/H value of 20.* Lawn's[17] comment on the choice of 20 for E/H was that variations of $10 \leq E/H \leq 50$ adds no more than ±10% error in K_c measurement. This is true primarily because E/H is raised to a small power (1/8) in the equation to determine K_c.

TABLE 11. AVERAGE VICKER'S INDENTATION SIZE FOR INDENTATIONS MADE AT ROOM TEMPERATURE (Load = 20 kgf = 196 N)

Material	Indentation Diagonal (a), μm[a]	
	Unexposed	1000 hr/1000°C
NGK Z-191 Y-TZP	101.0 (7.2)	104.8 (2.2)
Coors Mg-PSZ	130.6 (15.0)	157[b]
Nilsen MS Mg-PSZ	127.4 (10.6)	136.0 (4.8)
Feldmuhle ZN-40 Mg-PSZ	115.8 (16.5)	103.3 (8.4)

[a]Numbers in parentheses represent the standard deviation, in micrometers.

[b]One sample only.

*For unexposed material at room temperature, E/H values ranged from 16.6 for Nilsen MS-grade Mg-PSZ, 17.5 for NGK Z-191 Y-PSZ, 21.6 for Nilsen TS-grade Mg-PSZ, 22.1 for Coors Mg-PSZ, and 23.1 for Feldmuhle ZN-40 Mg-PSZ.

Tabular results of fracture toughness as a function of temperature and exposure (for 1000 hr/1000°C) are presented in Tables 12a through 12e. The information is plotted as both indented strength and toughness versus temperature in Figures 65 and 66. An overall summary is provided in Table 13. It is observed that the room-temperature fracture toughness of the three as-received Mg-PSZ materials agreed within 8%, with an average of 10.6 MPa·$m^{1/2}$. The TZP material, NGK Z-191, exhibited a toughness approximately 25% lower than the Mg-PSZ materials, i.e., 7.9 MPa·$m^{1/2}$. This illustrates a basic difference in the microstructures of Mg- and Y-PSZ materials, with regard to the state of the metastable tetragonal phase and the operable toughening mechanisms.

At 1000°C, the fracture toughness was more than 50% lower than the room temperature toughness. The toughness degradation as a function of temperature almost exactly paralleled fast fracture strength reduction (fracture toughness decrease of 63% for Coors, 54% for Feldmuhle, 54% for Nilsen, and 70% for NGK Z-191). Therefore, for both strength and toughness over the 25°-1000°C temperature range, there is a 50-65% decrease for Mg-PSZ. Over the same temperature range, the NGK TZP material exhibits a 70% decrease in both strength and fracture toughness. The tetragonal particles that comprise TZP exhibit more sensitivity to temperature than do the constrained tetragonal precipitates in Mg-PSZ. With regard to ambient temperature strength, there is a large benefit to low temperature strength resulting from the fine grain size of TZP. Note that the room temperature strength of NGK Z-191 is 40% higher than the strongest Mg-PSZ (Nilsen), and yet its fracture toughness is 30% lower. Note also that whereas the strength reduction with temperature was linear for both Mg- and Y-PSZ, the toughness-temperature relation was not linear. This may be due to the influence of the modulus-temperature relation, and possibly residual stress effects in indented samples as the temperature is raised.

After 1000 hr/1000°C exposure, the trend for fracture toughness reduction was about the same or slightly less pronounced than for the strength reduction. Table 13 illustrates that, consistent with its microstructural and phase stability, NGK Z-191 exhibited only a 6% reduction in toughness after the 1000 hr/1000°C exposure. This agrees precisely with its related strength reduction (only 7%). Likewise, Nilsen and Feldmuhle Mg-PSZ materials exhibited about the same level of toughness decrease (i.e., 46% and 34%, respectively) as they had for strength decrease after the exposure (i.e., 57% and

TABLE 12a. FRACTURE TOUGHNESS OF UNEXPOSED ZIRCONIA MATERIALS DETERMINED BY THE INDENTATION-STRENGTH METHOD AT ROOM TEMPERATURE (P = 196 N)

Sample	Indented 3-Point Flexure Strength psi	MPa	K_c, MPa·m$^{1/2}$
		Coors Mg-PSZ	
CB1F40	71,120	490.5	Fracture not at indentation
CB1F41	67,290	464.1	10.2
CB1F42	42,140	290.6	Fracture not at indentation
CB1F43	66,670	459.8	10.1
CB1F44	75,590	521.3	11.1
Mean	69,850	481.7	10.4
		Feldmuhle ZN-40 Mg-PSZ	
KF1F40	68,140	470.0	10.3
KF1F41	60,780	419.1	9.4
KF1F42	63,570	438.4	9.7
KF1F43	64,700	446.2	9.9
KF1F44	61,840	426.5	9.5
Mean	63,810	440.1	9.8
		Nilsen MS Mg-PSZ	
NV1F40	76,790	529.5	11.2
NV1F41	81,470	561.8	11.7
NV1F42	81,720	563.6	11.7
NV1F43	81,570	562.5	11.7
NV1F44	78,940	544.4	11.4
Mean	80,100	552.4	11.6
		NGK Z-191 Y-TZP	
NG1F42	45,940	316.8	7.6
NG1F43	50,120	345.6	8.1
NG1F44	45,940	316.8	7.6
NG1F45	49,880	344.0	8.1
NG1F46	47,910	330.4	7.9
Mean	47,950	330.7	7.9

TABLE 12b. FRACTURE TOUGHNESS OF UNEXPOSED ZIRCONIA MATERIALS DETERMINED BY THE INDENTATION-STRENGTH METHOD AT 500°C (P = 196 N)

Sample	Indented 3-Point Flexure Strength psi	MPa	K_c, MPa·m$^{1/2}$
		Coors Mg-PSZ	
CB1F45	30,730	212.0	5.6
CB1F46	41,740	287.8	Fracture not at indentation
CB1F47	40,460	279.0	6.9
CB1F48	37,870	261.2	6.6
CB1F49	34,610	238.7	6.2
Mean	35,920	247.7	6.3
		Feldmuhle ZN-40 Mg-PSZ	
KF1F45	35,200	242.8	6.2
KF1F46	35,340	243.7	6.3
KF1F47	39,350	271.4	6.8
KF1F48	35,460	244.6	6.3
KF1F49	32,880	226.8	5.9
Mean	35,650	245.8	6.3
		Nilsen MS Mg-PSZ	
NV1F45	61,480	424.0	9.5
NV1F46	64,210	442.8	9.8
NV1F47	59,220	408.4	9.2
NV1F48	57,230	394.7	9.0
NV1F49	64,870	447.3	9.9
Mean	61,400	423.5	9.5
		NGK Z-191 Y-TZP	
NG1F47	36,160	249.4	6.4
NG1F48	39,240	270.6	6.8
NG1F49	35,040	241.7	6.2
Mean	36,820	253.9	6.5

TABLE 12c. FRACTURE TOUGHNESS OF UNEXPOSED ZIRCONIA MATERIALS DETERMINED BY THE INDENTATION-STRENGTH METHOD AT 750°C (P = 196 N)

Sample	Indented 3-Point Flexure Strength psi	MPa	K_c, MPa·m$^{1/2}$
		Coors Mg-PSZ	
CB1F50	20,700	142.8	4.2
CB1F51	19,790	136.5	4.1
CB1F52	25,150	173.4	4.9
CB1F53	23,320	160.8	4.6
CB1F54	20,300	139.9	4.1
Mean	21,850	150.0	4.4
		Feldmuhle ZN-40 Mg-PSZ	
KF1F50	18,970	130.8	3.9
KF1F51	24,620	169.8	4.8
KF1F52	22,520	155.3	4.5
KF1F53	17,660	121.8	3.7
KF1F54	18,190	125.4	3.8
Mean	20,390	140.6	4.1
		Nilsen MS Mg-PSZ	
NV1F50	22,930	158.1	4.5
NV1F51	27,730	191.3	5.2
NV1F52	22,610	155.9	4.5
NV1F53	28,210	194.6	5.3
NV1F54	26,420	182.2	5.0
Mean	25,580	176.4	4.9
		NGK Z-191 Y-TZP	
NG1F50	8930	61.6	2.2
NG1F51	8930	61.6	2.2
Mean	8930	61.6	2.2

TABLE 12d. FRACTURE TOUGHNESS OF UNEXPOSED ZIRCONIA MATERIALS DETERMINED BY THE INDENTATION-STRENGTH METHOD AT 1000°C (P = 196 N)

Sample	Indented 3-Point Flexure Strength, psi	Indented 3-Point Flexure Strength, MPa	K_c, MPa·m$^{1/2}$
		Coors Mg-PSZ	
CB1F55	21,580	148.8	4.3
CB1F56	17,410	120.1	3.7
CB1F57	10,670	73.6	Fracture not at indentation
CB1F58	17,940	123.7	3.8
CB1F59	19,020	131.2	Fracture not at indentation
Mean (3)	18,970	130.9	3.9
		Feldmuhle ZN-40 Mg-PSZ	
KF1F55	11,170	77.1	Fracture not at indentation
KF1F56	20,130	138.8	4.1
KF1F57	6,430	44.4	Fracture not at indentation
KF1F58	25,830	178.2	5.0
KF1F59	10,630	73.3	Fracture not at indentation
Mean (2)	22,980	158.5	4.5
		Nilsen MS Mg-PSZ	
NV1F55	33,620	231.9	6.0
NV1F56	31,680	218.4	5.8
NV1F57	20,250	139.6	4.1
NV1F58	22,980	158.5	4.5
NV1F59	31,740	218.9	5.8
Mean	28,050	193.5	5.3
		NGK Z-191 Y-TZP	
NG1F52	10,580	73.0	2.5
NG1F53	10,190	70.2	2.5
NG1F54	10,580	73.0	2.5
NG1F55	8,800	60.7	2.2
NG1F56	9,460	65.2	2.3
Mean	9,920	68.4	2.4

TABLE 12e. FRACTURE TOUGHNESS OF ZIRCONIA MATERIALS EXPOSED 1000 hr/1000°C IN STATIC AIR DETERMINED BY THE INDENTATION-STRENGTH METHOD AT ROOM TEMPERATURE (P = 196 N)

Sample	Indented 3-Point Flexure Strength		K_c, MPa·m$^{1/2}$
	psi	MPa	
	Coors Mg-PSZ		
CB1F38	Sample failed while being indented		
CB1F39	28,320	195.7	Fracture not at indentation
CB1F60	40,260	277.8	Fracture not at indentation
CB1F61	41,530	286.4	7.1
Mean	36,700	253.3	7.1
	Feldmuhle ZN-40 Mg-PSZ		
KF1F60	38,010	262.1	6.6
KF1F61	32,730	225.7	5.9
KF1F62	Sample failed while being indented		
KF1F63	40,840	281.7	7.0
Mean	37,190	256.5	6.5
	Nilsen MS Mg-PSZ		
NV1F60	36,530	251.9	6.4
NV1F61	34,050	234.8	6.1
NV1F62	35,260	243.2	6.3
NV1F63	37,100	255.8	6.5
Mean	35,730	246.4	6.3
	NGK Z-191 Y-TZP		
NG1F57	43,310	298.7	7.3
NG1F58	43,120	297.4	7.3
NG1F59	43,970	303.2	7.4
NG1F60	43,730	301.6	7.4
NG1F61	45,080	310.9	7.5
Mean	43,840	302.4	7.4

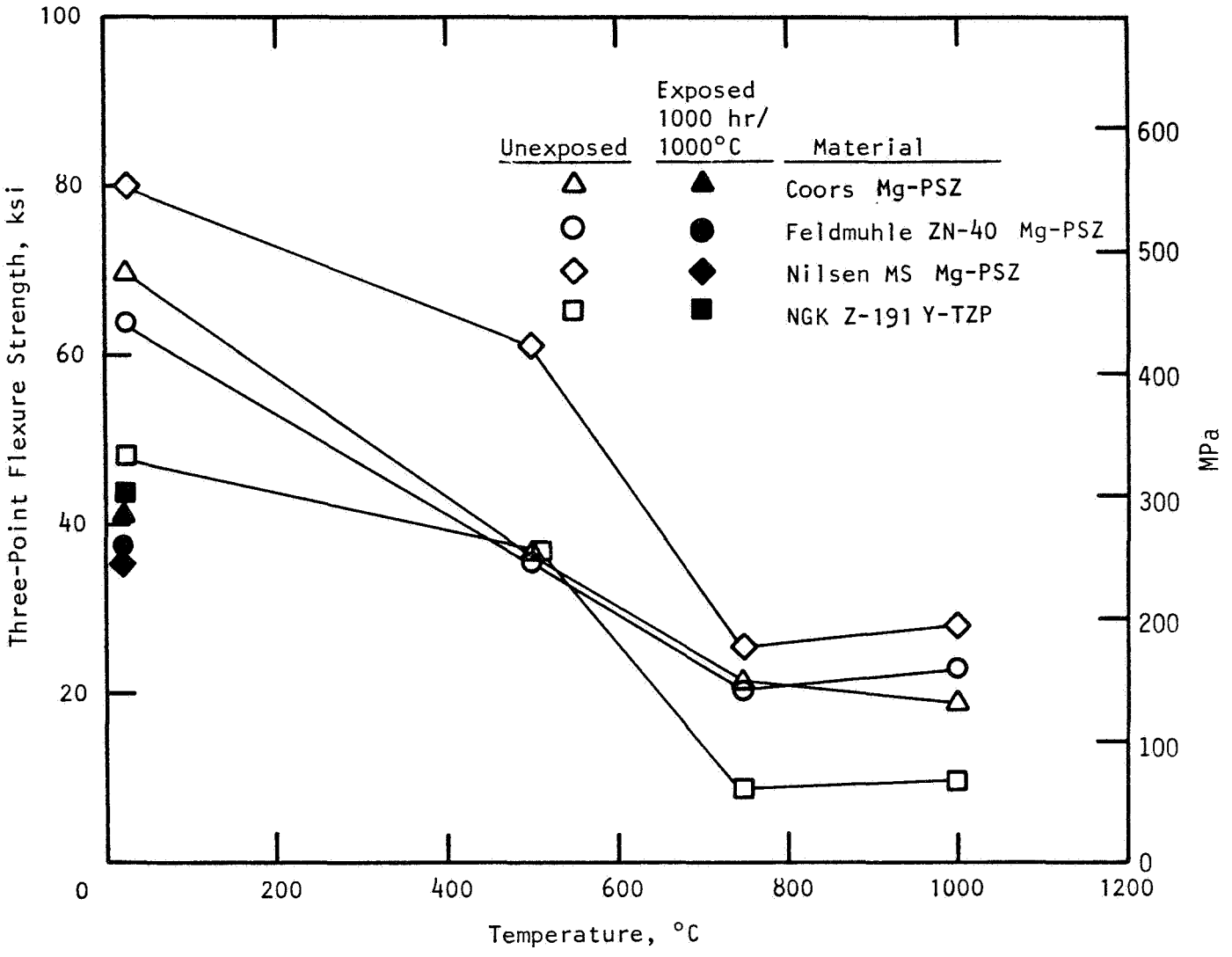

Figure 65. Three-point flexure strength of controlled flaw zirconia materials (Vickers indentation P = 196N).

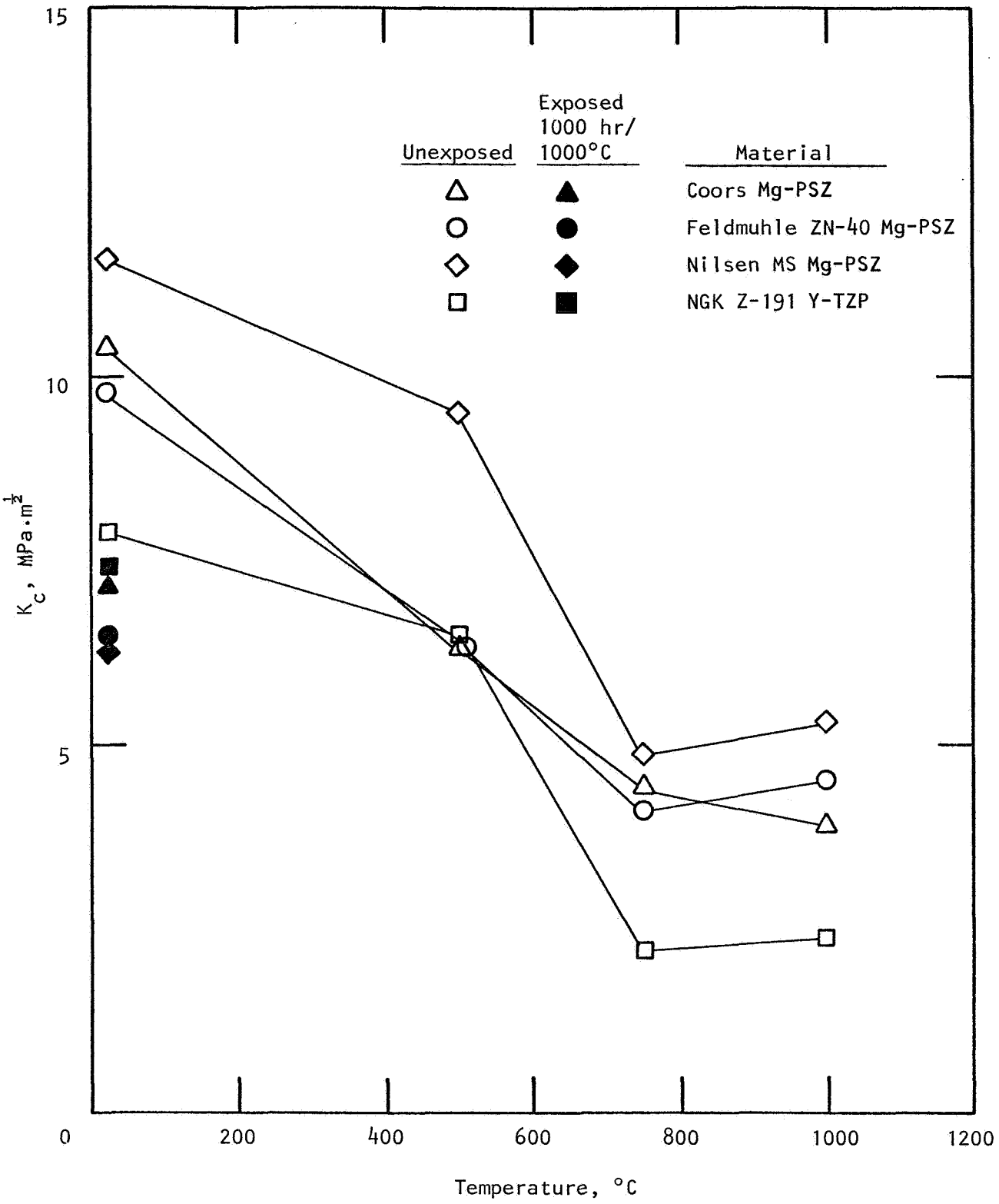

Figure 66. Fracture toughness of zirconia materials determined by the indentation-strength method at various temperatures (Vickers indentation P = 196N).

TABLE 13. SUMMARY OF FRACTURE TOUGHNESS[a] RESULTS

Material	Fracture Toughness: K_c, MPa·m$^{1/2}$				
	As-Received				At 25°C, After 1000 hr/1000°C Exposure[b]
	25°C	500°C	750°C	1000°C	
NGK Z-191 Y-TZP	7.9	6.5	2.2	2.4	7.4 (-6%)
Nilsen MS Mg-PSZ	11.6	9.5	4.9	5.3	6.3 (-46%)
Feldmuhle ZN-40 Mg-PSZ	9.8	6.3	4.1	4.5	6.5 (-34%)
Coors Mg-PSZ	10.4	6.3	4.4	3.9	7.1 (-32%)

[a]Indentation-strength method.

[b]Numbers in parentheses indicate change from the as-received condition.

30%, respectively). Interestingly, the Coors Mg-PSZ only exhibited a 32% toughness degradation after the 1000 hr/1000°C exposure, but had previously been shown to yield as much as an 80% strength reduction and a 30% elastic modulus decrease. Previous discussion showed that extensive microcracking, following conversion of 80% of the microstructure to the monoclinic phase in the Coors Mg-PSZ, would explain the large residual strength and elastic modulus decrease. Likewise, a significant network of microcracks could add resistance to crack propagation, and serve to reduce the amount of toughness degradation following the 1000 hr/1000°C exposure. This might explain the better than expected post-exposure toughness for the Coors material.

In general, fracture toughness in transformation-toughened zirconia is strongly dependent on temperature for the same reasons that strength is. Yttria-doped TZP materials exhibit lower toughness values, and may be a bit more temperature sensitive, but they are much more stable with respect to long-term overaging and other phase change effects (e.g., destabilization/decomposition) than are Mg-PSZ materials.

7. THERMAL EXPANSION

Thermal expansion is the most important material property, along with elastic modulus, for design calculations from a thermal stress (as opposed to a structural loading) standpoint. This is especially true for zirconia since its low thermal diffusivity and conductivity can result in large temperature gradients. Thermal expansion was measured using an automatic recording single pushrod dilatometer (Netzsch) over the range 25°-1000°C.

Thermal expansion in transformation-toughened zirconia is not greatly affected by the choice of stabilizer used--both Mg-PSZ and Y-TZP have basically similar coefficients of thermal expansion, with some minor variations. This is observed for the results of as-received materials, which are presented in Table 14, where the percent linear expansion is tabulated for 500°, 750°,

TABLE 14. THERMAL EXPANSION OF ZIRCONIA (AS-RECEIVED CONDITION)[a]

Material	Percent Linear Expansion 500°C	750°C	1000°C	Mean Coefficient of Thermal Expansion (20°-1000°C), 10^{-6}/°C
Nilsen MS Mg-PSZ	0.425	0.690	0.965	9.85
	0.450	0.705	0.975	9.95
NGK Z-191 Y-TZP	0.480	0.760	1.050	10.71
	0.475	0.750	1.035	10.56
Feldmuhle ZN-40 Mg-PSZ	0.465	0.730	1.030	10.51
	0.470	0.740	1.045	10.66
Coors Mg-PSZ	0.465	0.740	1.045	10.66
	0.465	0.685	0.965	9.85
Nilsen TS Mg-PSZ[b]	0.404	0.575	0.817	8.34

[a]Data for two samples each material; heating rate: 1°C min^{-1} for 20°-200°C, and 5°C min^{-1} for 200°-1000°C; cooling rate: ~5°C min^{-1}. Data for heating cycle.

[b]Note only one sample replicate; material was included in program only to assess thermal shock behavior.

and 1000°C. Additionally, the mean coefficient of thermal expansion over the range 20°-1000°C was computed, and is provided in the table. Representative graphical results are provided in Figures 67-71, where the percent linear expansion is plotted continuously as a function of temperature for both heating and cooling cycles.

It is observed in Table 14 for the as-received zirconia materials from Nilsen, NGK, and Feldmuhle, the variation in thermal expansion between the two replicate samples was only 1-2%. The Coors material, however, exhibited an 8% variation between two samples. This correlates with the larger strength and modulus variations for the Coors Mg-PSZ. Figure 71 illustrates an indication of the presence of the monoclinic phase in the as-received Coors material--note the discontinuity in the heating cycle curve at roughly the A_s temperature (monoclinic to tetragonal phase transformation upon heating). The X-ray diffraction analyses provided in Table 3 showed that the Coors material has acceptably low monoclinic phase, however. The present thermal expansion results would then indicate the possibility of a large sample-to-sample variation in monoclinic content for the developmental Coors material. The lower coefficient of expansion for the second replicate sample and the discontinuity in the expansion temperature curve would tend to be the influence of a higher than normal monoclinic content. Note also that this Coors sample exhibited a permanent +0.025% length increase as indicated by post-test micrometer measurement. All other samples and materials exhibited stable expansion behavior from 20°-1000°C, with no permanent dimension changes. Therefore, the 8% variability in expansion for as-received Coors Mg-PSZ is thought to be caused by a higher than usual monoclinic content.

It is noted in Table 14 that the as-received Nilsen MS-grade Mg-PSZ is consistently 7% lower in expansion than that of the other materials--even the yttria-doped TZP material (NGK Z-191). The expansion of Nilsen MS is exactly the same as the Coors sample suspected of having higher monoclinic content. The XRD results presented in Table 3 indicates as-received Nilsen MS Mg-PSZ indeed does have higher monoclinic content than the other materials (~9% monoclinic for Nilsen vs. 4% for the other Mg-PSZ, and ~1% for TZP). The other grade of Nilsen material, TS, has ~16% lower expansion yet. That material exhibits improved thermal shock properties (to be discussed in Section 9). The reason for the lower expansion and better thermal shock resistance for the

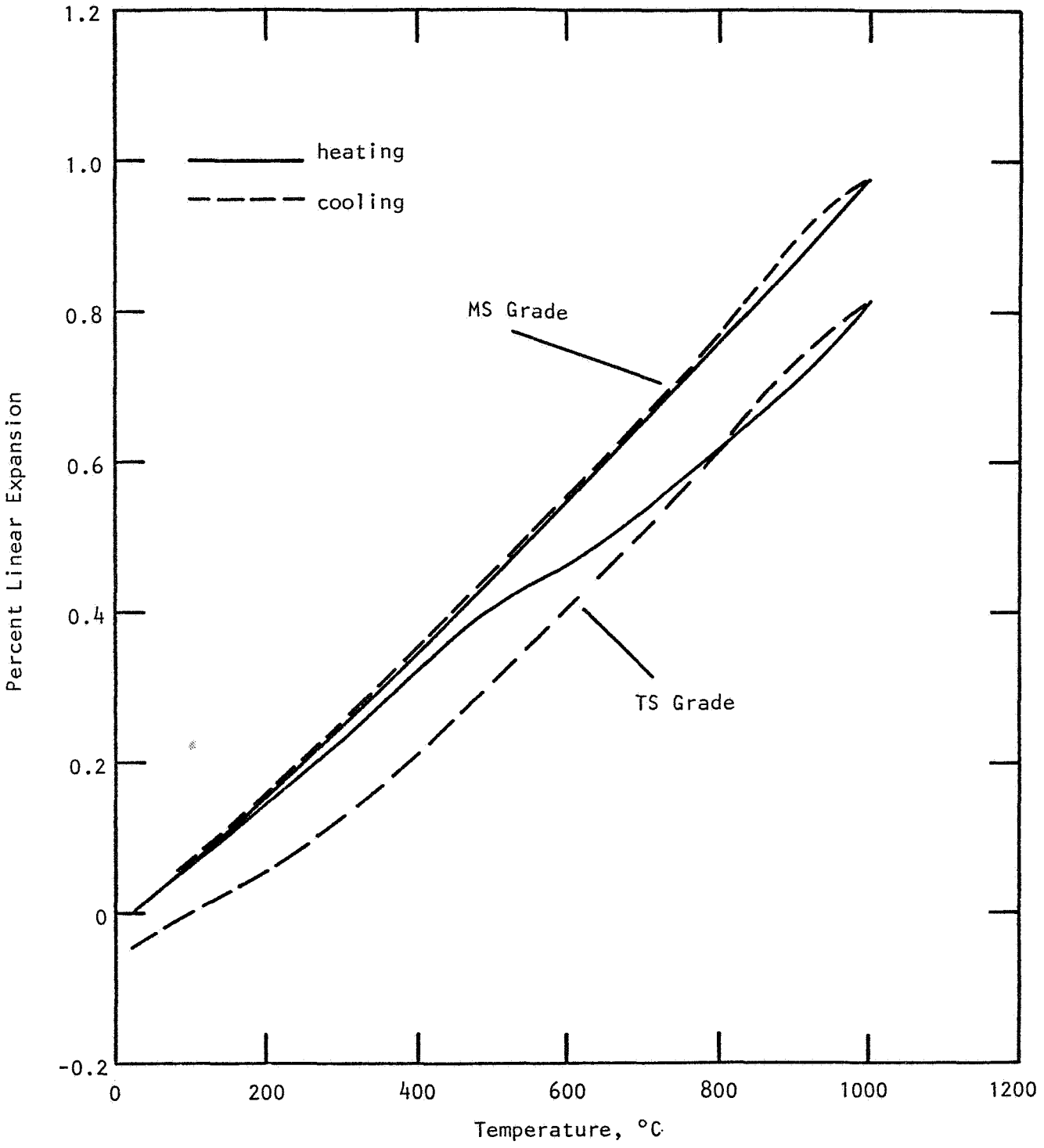

Figure 67. Thermal expansion of MS and TS grades of Nilsen Mg-PSZ (as-received condition)

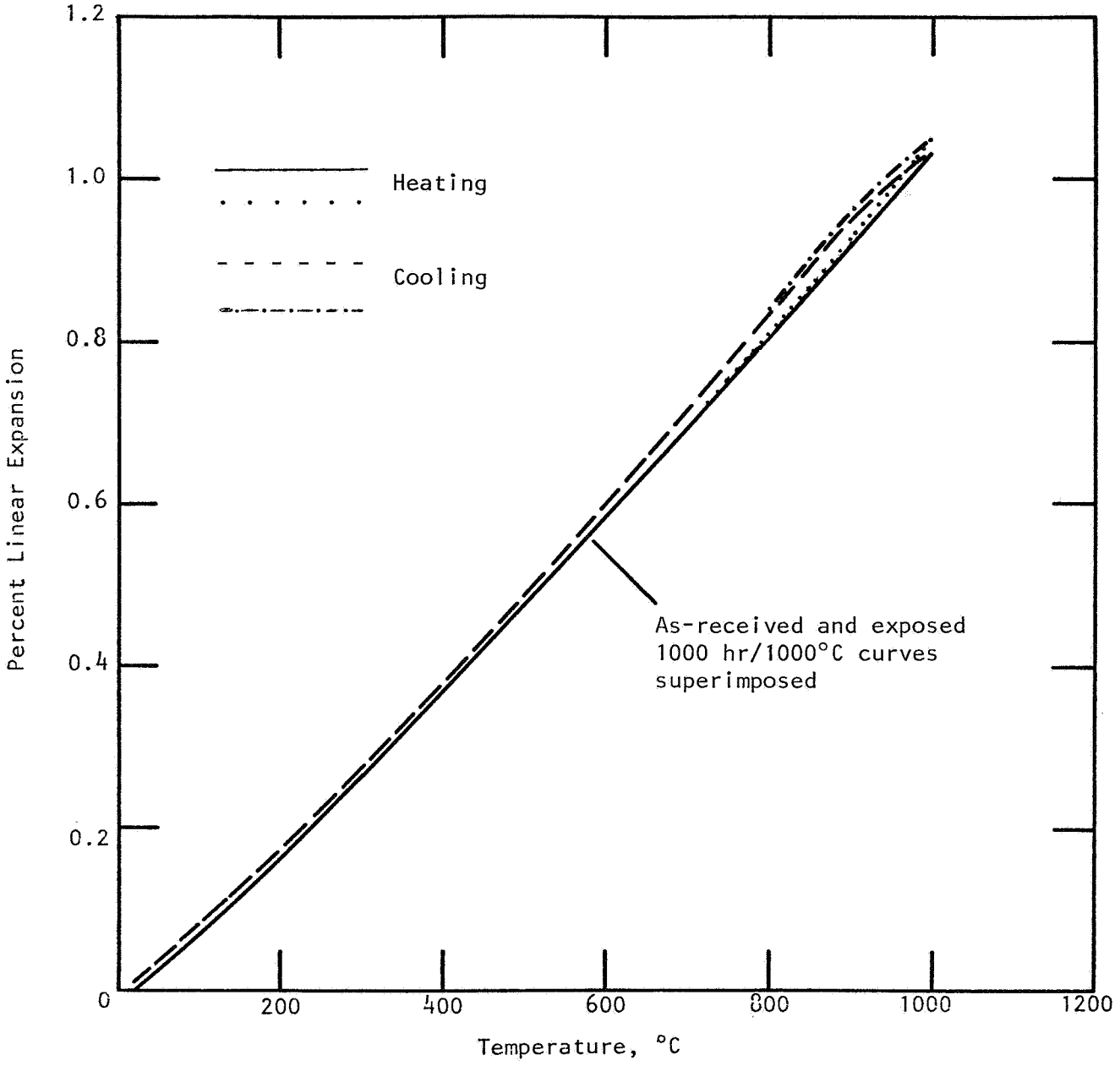

Figure 68. Thermal expansion of NGK Z-191 Y-TZP before and after 1000 hr/1000°C thermal exposure.

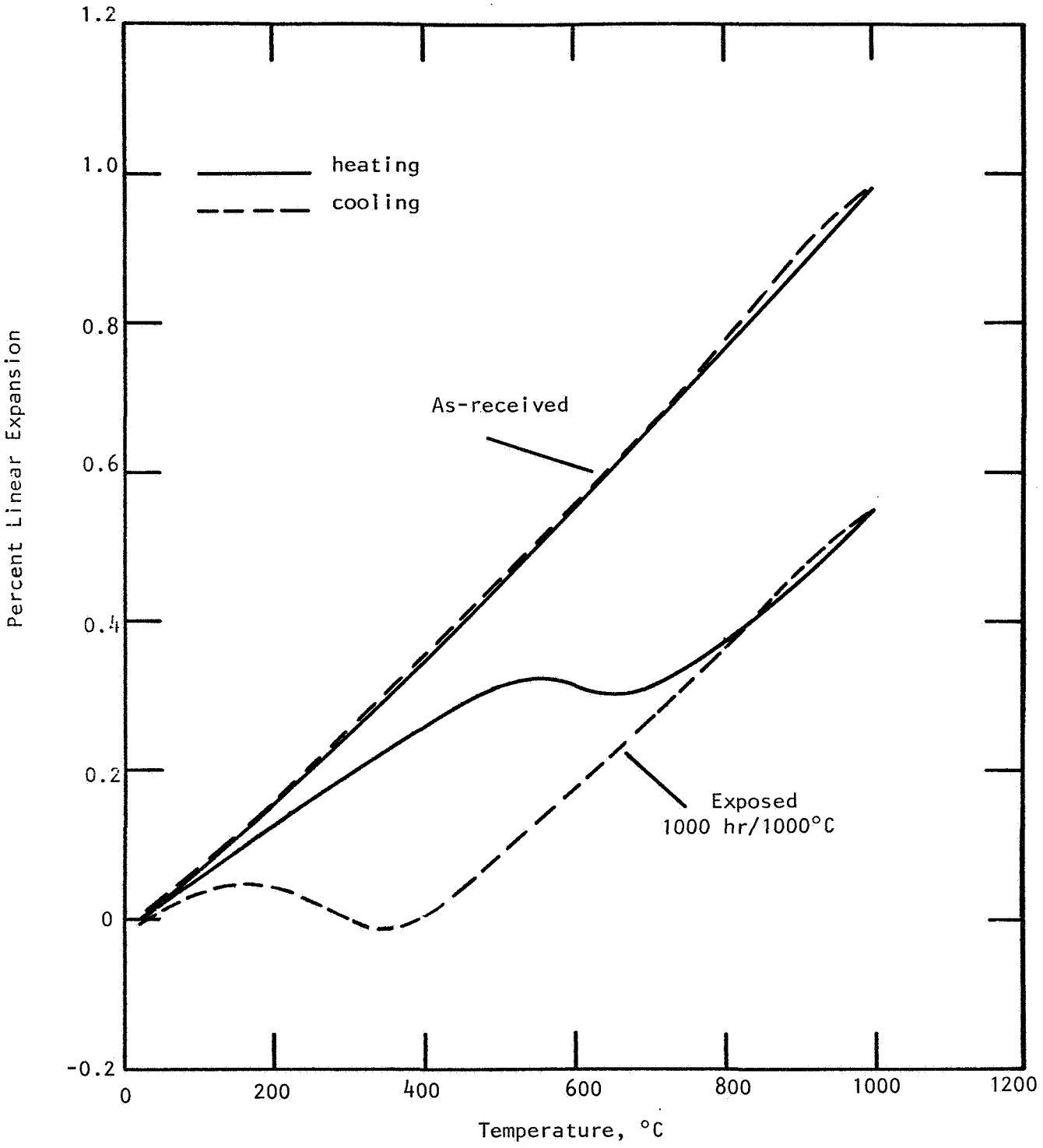

Figure 69. Thermal expansion of Nilsen MS Mg-PSZ before and after 1000 hr/1000°C thermal exposure.

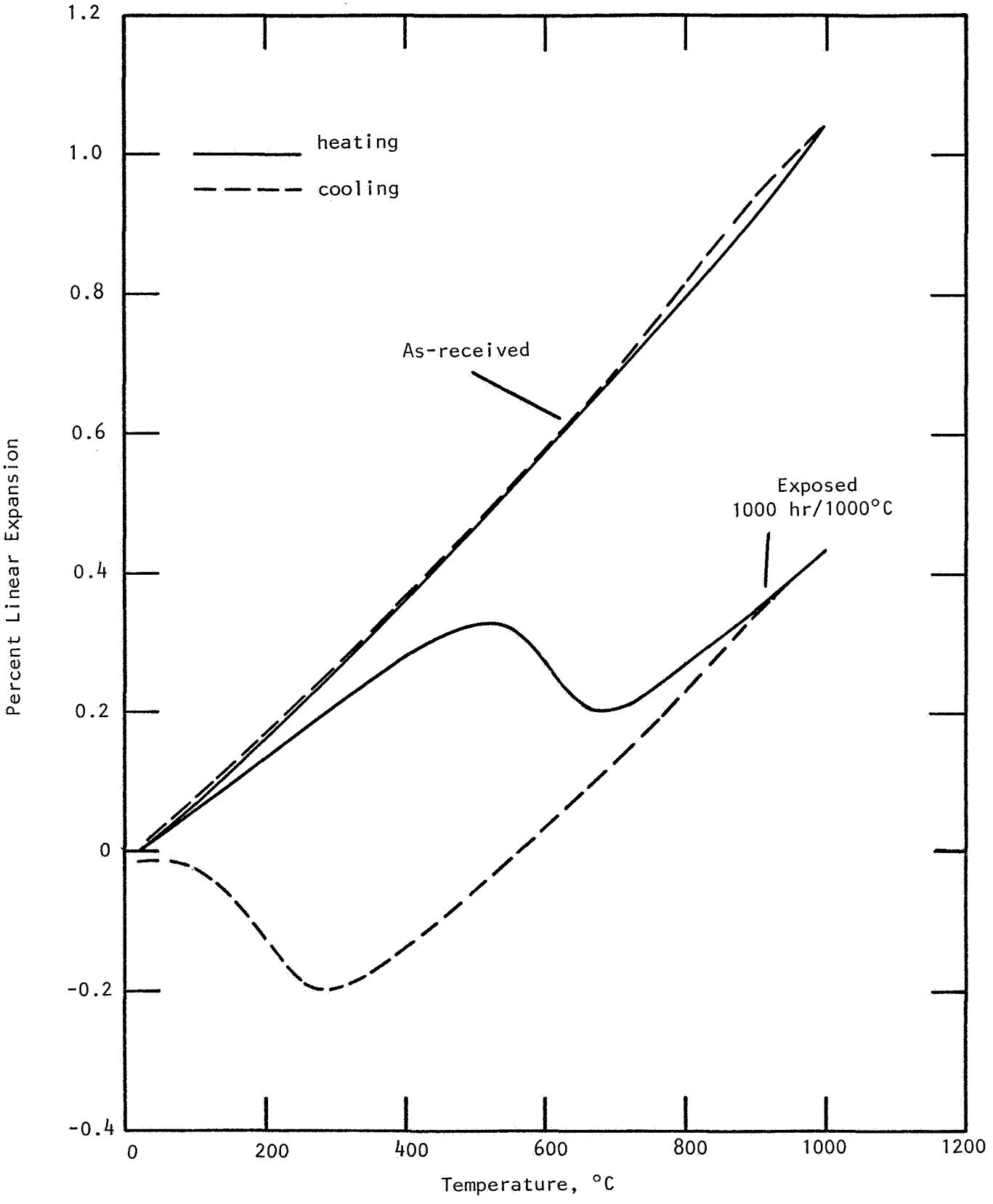

Figure 70. Thermal expansion of Feldmuhle ZN-40 Mg-PSZ before and after 1000°C/1000 hr thermal exposure.

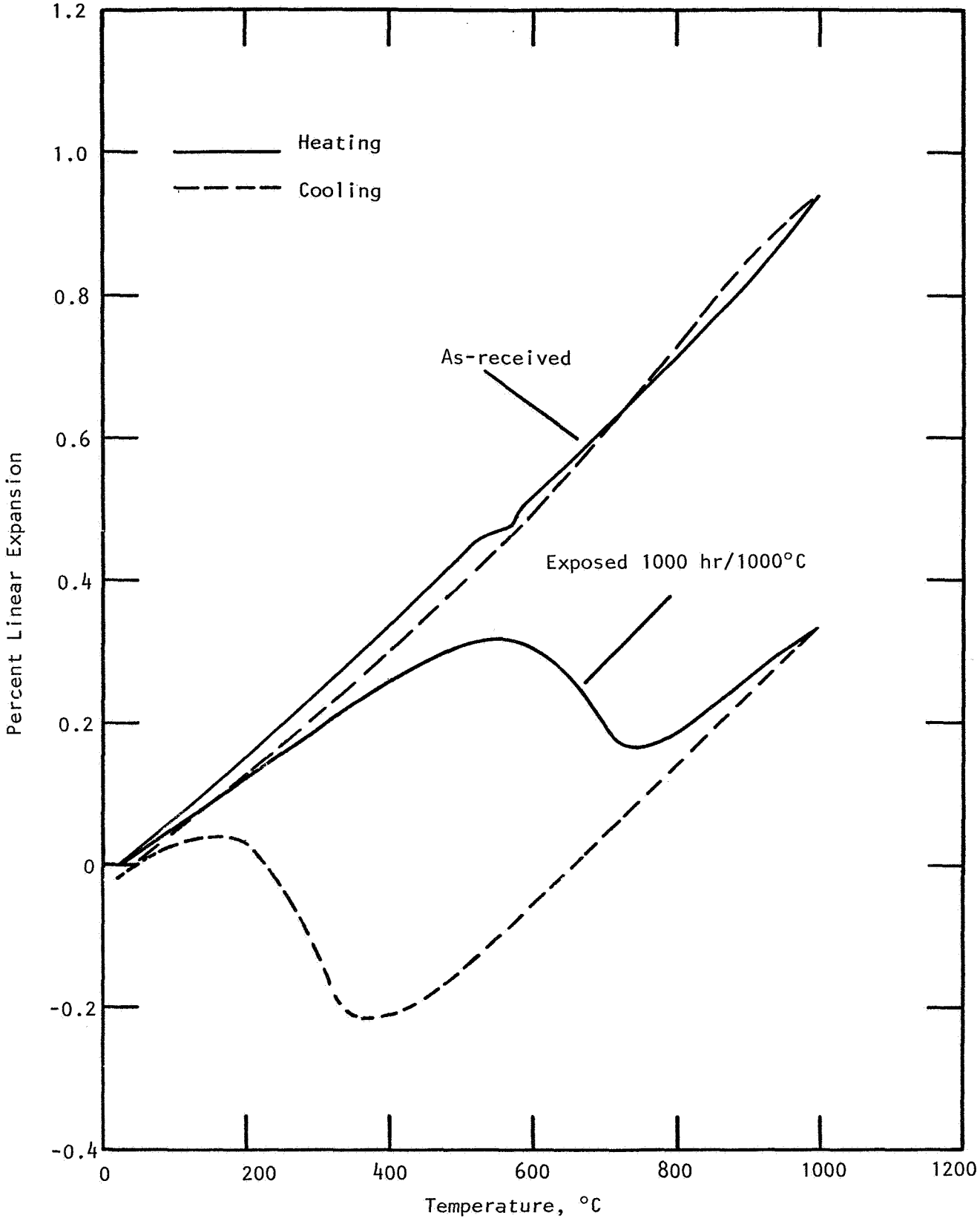

Figure 71. Thermal expansion of Coors Mg-PSZ before and after 1000 hr/1000°C thermal exposure.

TS material is thought to be its higher content of monoclinic zirconia. The clue to this is shown in the heating rate expansion curve presented in Figure 67. The inflection at ~550°C indicates a monoclinic-to-tetragonal phase change. It occurs upon heating as the monoclinic phase was there initially. Therefore, Nilsen materials have lower thermal expansion than the other materials due to slightly higher monoclinic content. This is especially true for TS-grade. XRD analysis confirms this interpretation. Nilsen TS Mg-PSZ is nominally 56% cubic, 24% tetragonal, and 20% monoclinic. Ms-grade material is 57% cubic, 37% tetragonal, and 5% monoclinic. Therefore, for TS-grade material, the cubic content is the same as an MS-PSZ, but the monoclinic content is increased at the expense of tetragonal. Thus, reduced strength and toughness for Nilsen TS Mg-PSZ would be expected.

Thermal expansion tests were also conducted on the four zirconia materials after 1000 hr/1000°C thermal exposure. Representative results are provided in Figures 68-71, where the as-received expansion curve is shown for reference. The data are summarized in tabular form in Table 15.

TABLE 15. THERMAL EXPANSION OF ZIRCONIA AFTER 1000 HR/1000°C STATIC THERMAL EXPOSURE[a]

Material	Percent Linear Expansion			Mean Coefficient of Thermal Expansion (20°-1000°C), 10^{-6}/°C
	500°C	750°C	1000°C	
Nilsen MS Mg-PSZ	--	--	0.548	5.59
	--	--	0.562	5.73
NGK Z-191 Y-TZP	0.486	0.757	1.051	10.72
	0.478	0.750	1.046	10.67
Feldmuhle ZN-40 Mg-PSZ	--	--	0.454	4.63
	--	--	0.433	4.42
Coors Mg-PSZ	--	--	0.335	3.42
	--	--	0.348	3.55

[a]Data for two samples each material; heating rate: 1°C min^{-1} for 20°-200°C, and 5°C min^{-1} for 200°-1000°C; cooling rate: ~5°C min^{-1}. Data for heating cycle.

The thermal expansion results for exposed and as-received NGK Z-191 Y-TZP are remarkably identical. The expansion-temperature curves presented in Figure 68 illustrate that data for the two conditions virtually overlap. No evidence of the monoclinic phase is evident in the expansion behavior. The originally tetragonal structure did not transform. This high degree of stability for the TZP material correlates with the strength and toughness retention after exposure and the maintenance of the original phase assemblage and microstructure. TZP is very stable for long-term elevated temperature use.

By contrast, the thermal expansion results for all of the Mg-PSZ materials illustrate clear evidence for a major tetragonal-to-monoclinic phase transformation during the 1000 hr/1000°C thermal exposure. Representative results for all three Mg-PSZ materials in the as-received and exposed conditions are shown in Figures 69-71. This overaging effect seen in the expansion data agrees with previous X-ray and microstructural evidence of major phase transformation to monoclinic and certainly explains the strength and toughness degradation due to overaging. Note that, in general, the degree of thermal expansion hysteresis for the overaged Mg-PSZ materials correlates with the quantitative XRD determination of the monoclinic content.

The indicated stability in Y-TZP and lack of stability in Mg-PSZ thermal expansion behavior is entirely consistent with the strength, XRD, and microstructural evidence for these materials discussed above. Thermal expansion is an extremely sensitive indicator of any monoclinic phase present in the structure.

8. CREEP

Creep rates were measured in 4-point bending at 1000°C in laboratory air. The stepwise method was used, with deformation continuously recorded using the 3-point electromechanical deflectometer previously described. A view of the SiC fixturing is provided in Figure 72. Samples were tested at various incremental stress levels, with enough time spent at any given level to obtain an approximately constant creep rate. Deadweight loading was employed. Testing continued for 3-4 stress steps per sample. Testing of approximately three samples in this manner permitted the steady-state stress dependence of the creep rate to be assessed for each material studied.

The results are presented graphically as the creep strain rate vs. applied stress. The results for NGK Z-191 Y-TZP shown in Figure 73 illustrate that identical behavior was obtained for as-received samples and those previously exposed for 1000 hr at 1000°C. This result correlates with the previously presented strength, thermal expansion, and microstructural evidence that the phase assemblage and microstructure of this Y-TZP are extremely stable during extended thermal exposure.

Creep results for the Mg-PSZ materials are presented in Figures 74-76. Little or no differences were observed in the creep behavior of as-received and overaged materials. Note that this is in contrast to the previously observed phase assemblage, strength, thermal expansion, fracture toughness, and microstructural changes (degradation) caused by overaging in Mg-PSZ. This implies that the mechanism of creep in zirconia is independent of the phase assemblage. Potential mechanisms of plastic deformation in ceramics include dislocation slip, deformation twinning, diffusional transport, grain boundary sliding, and microcrack nucleation (cavitation). The stress exponent ($n \sim 1$) observed for these materials suggests a diffusional mechanism.

The creep results for the four materials are compared directly in Figure 77. Note that results for the three Mg-PSZ materials are in relatively close agreement. Creep rates for the Y_2O_3-stabilized NGK Z-191 material are more than an order of magnitude higher than for the Mg-PSZ materials. Note that

PAGE 136 INTENTIONALLY BLANK PRECEDING PAGE BLANK NOT FILMED

ORIGINAL PAGE IS
OF POOR QUALITY

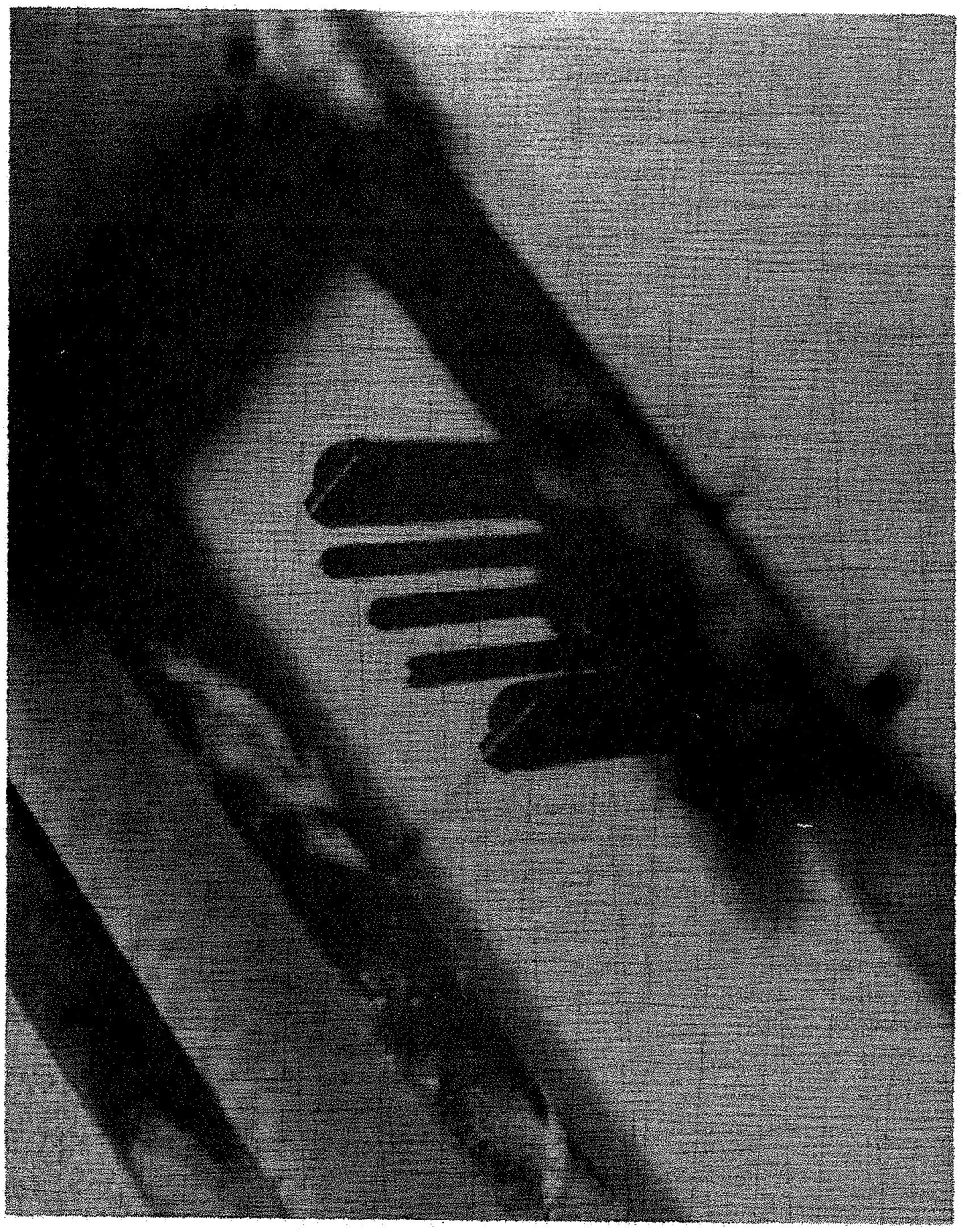

Figure 72. SiC flexural creep deflection fixturing for use at temperatures up to 1500°C in air.

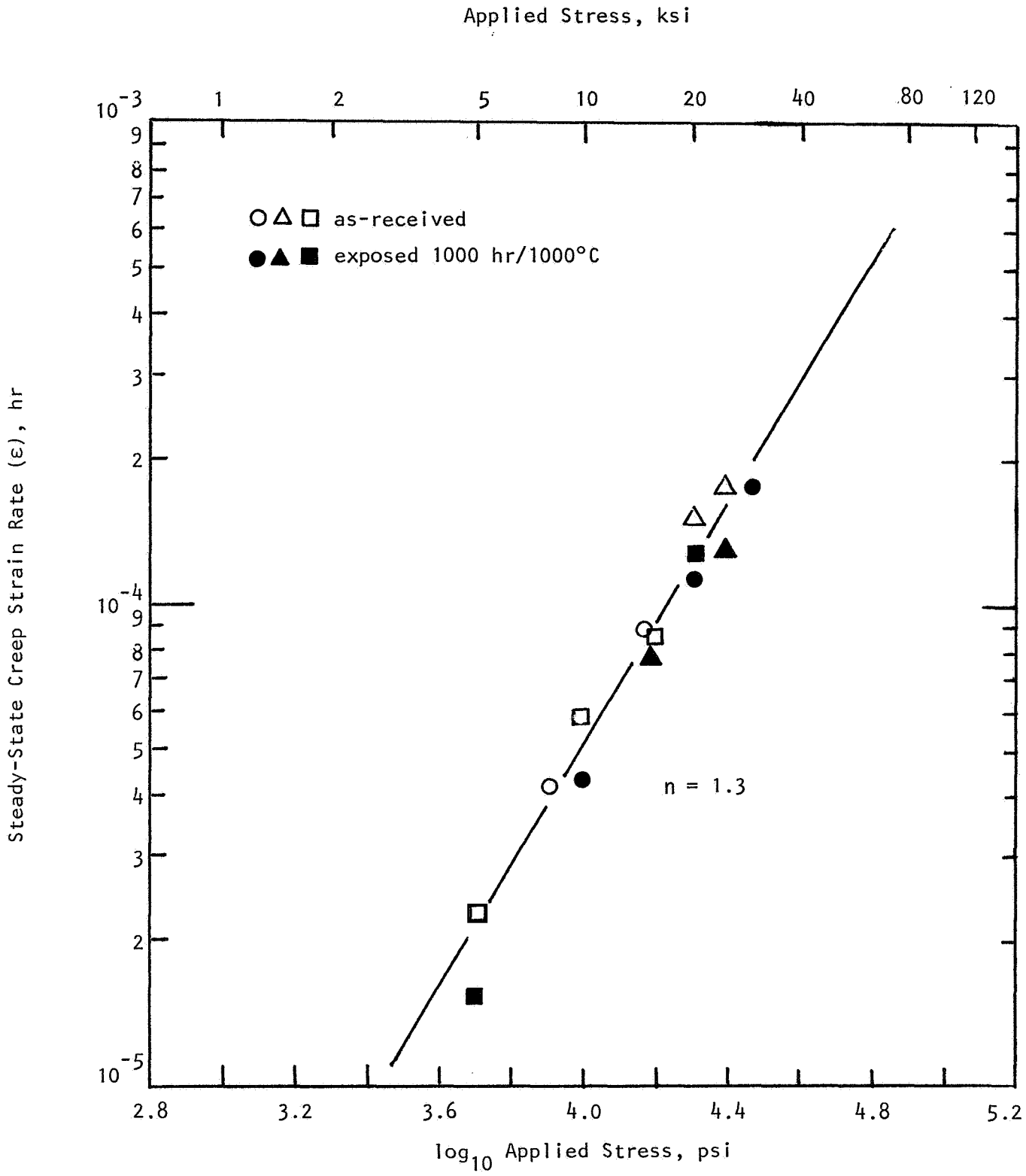

Figure 73. Flexural creep of NGK Z-191 Y-TZP at 1000°C.

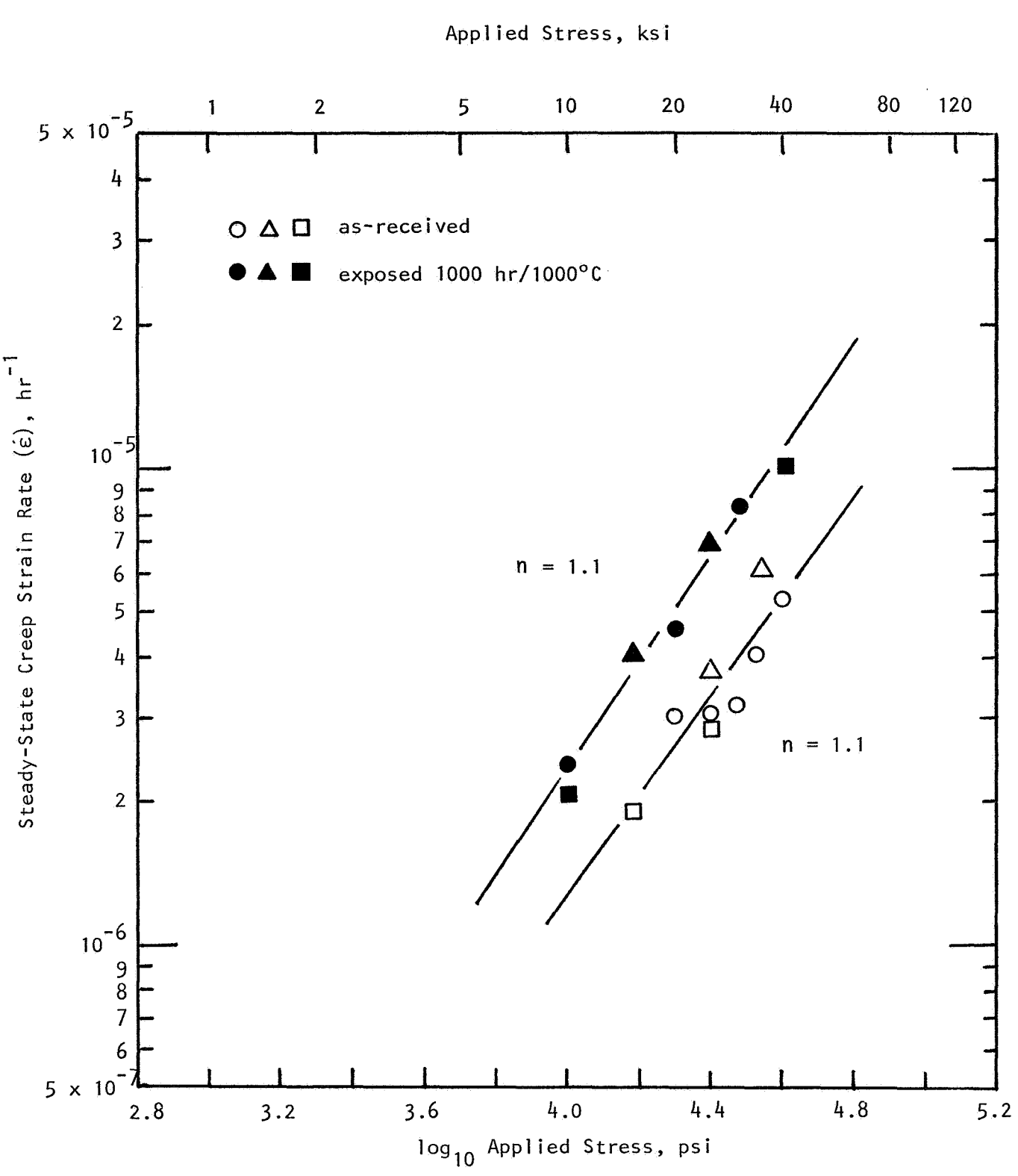

Figure 74. Flexural creep of Nilsen MS Mg-PSZ at 1000°C.

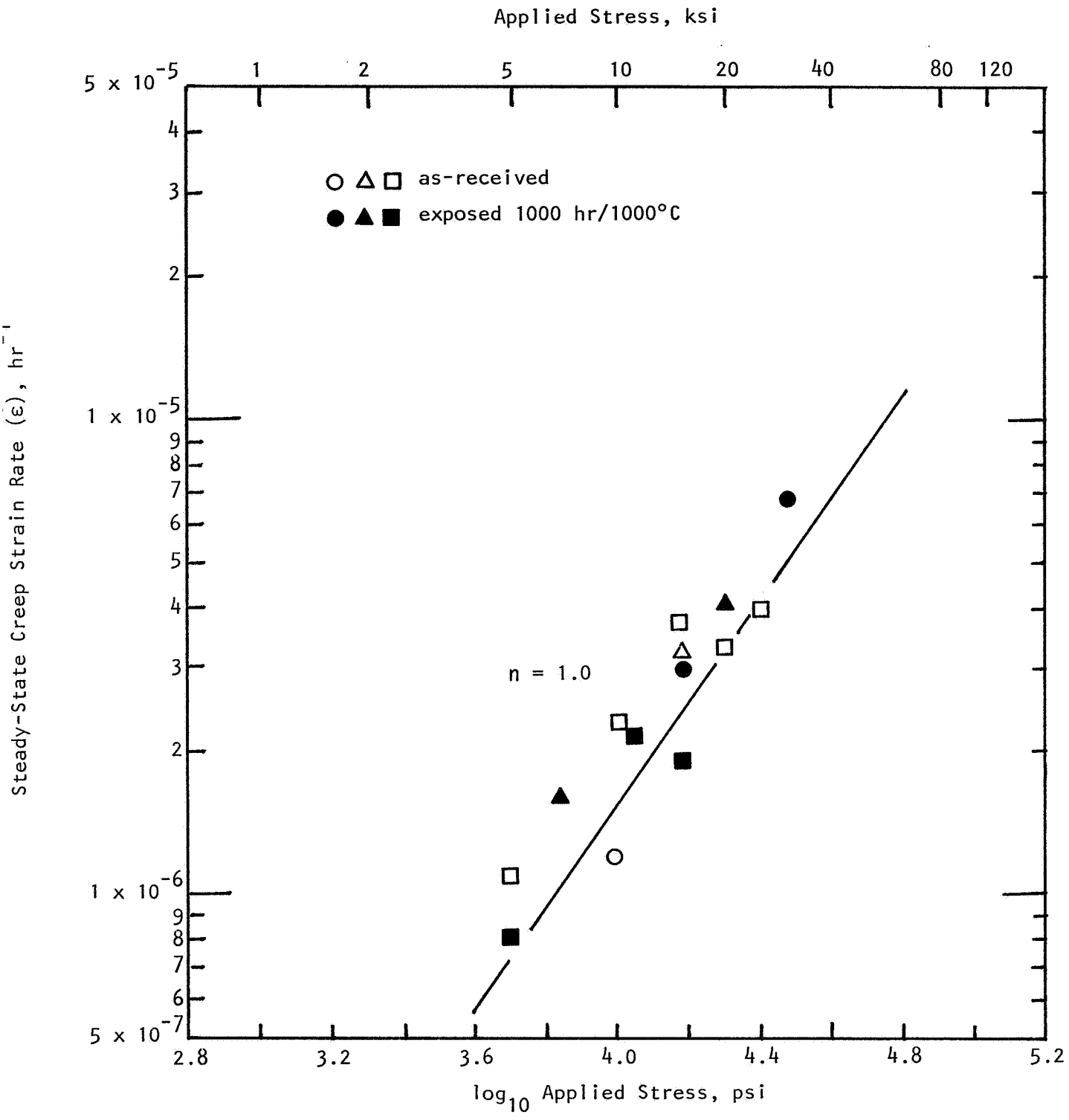

Figure 75. Flexural creep of Coors Mg-PSZ at 1000°C.

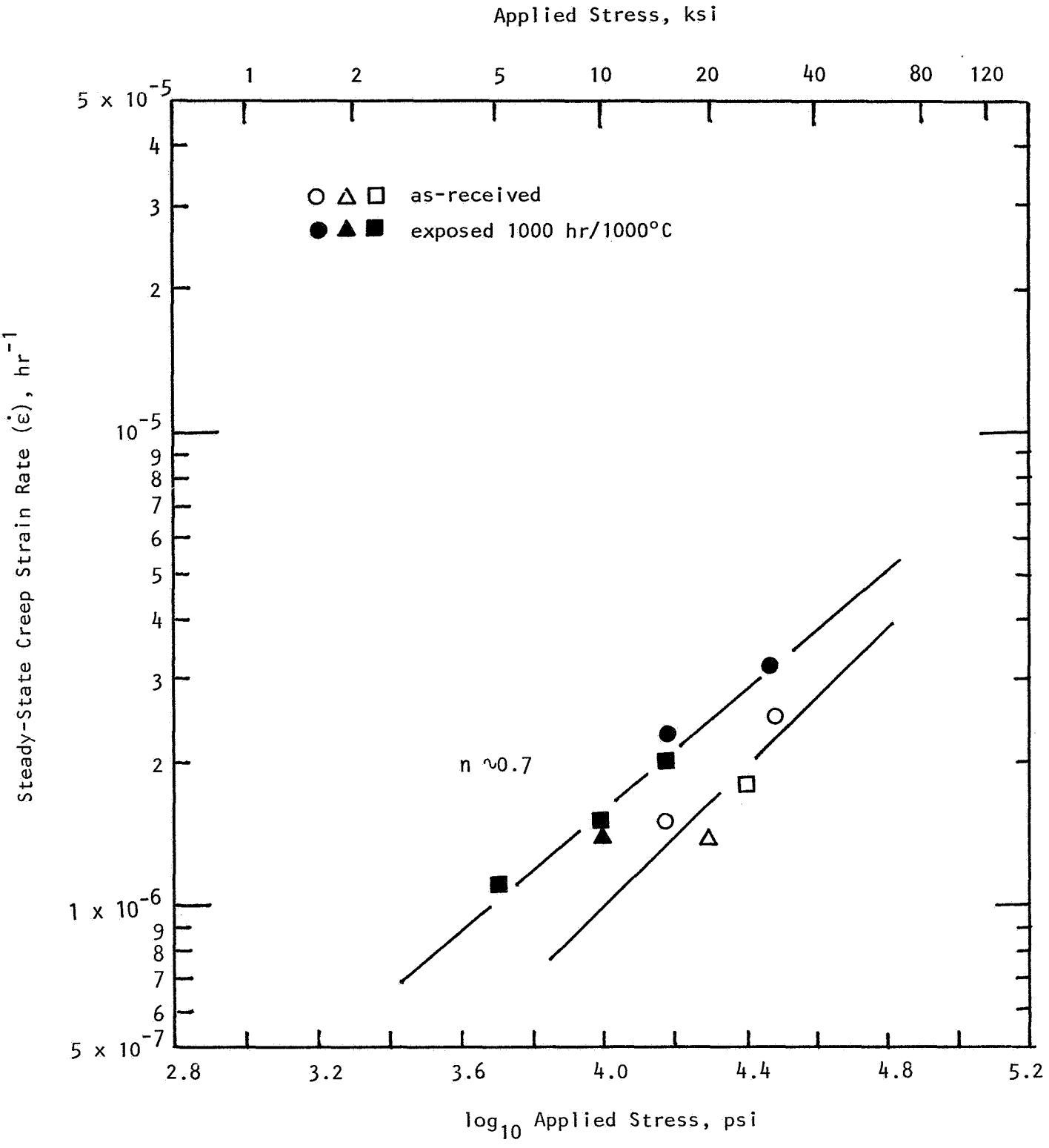

Figure 76. Flexural creep of Feldmuhle ZN-40 Mg-PSZ at 1000°C.

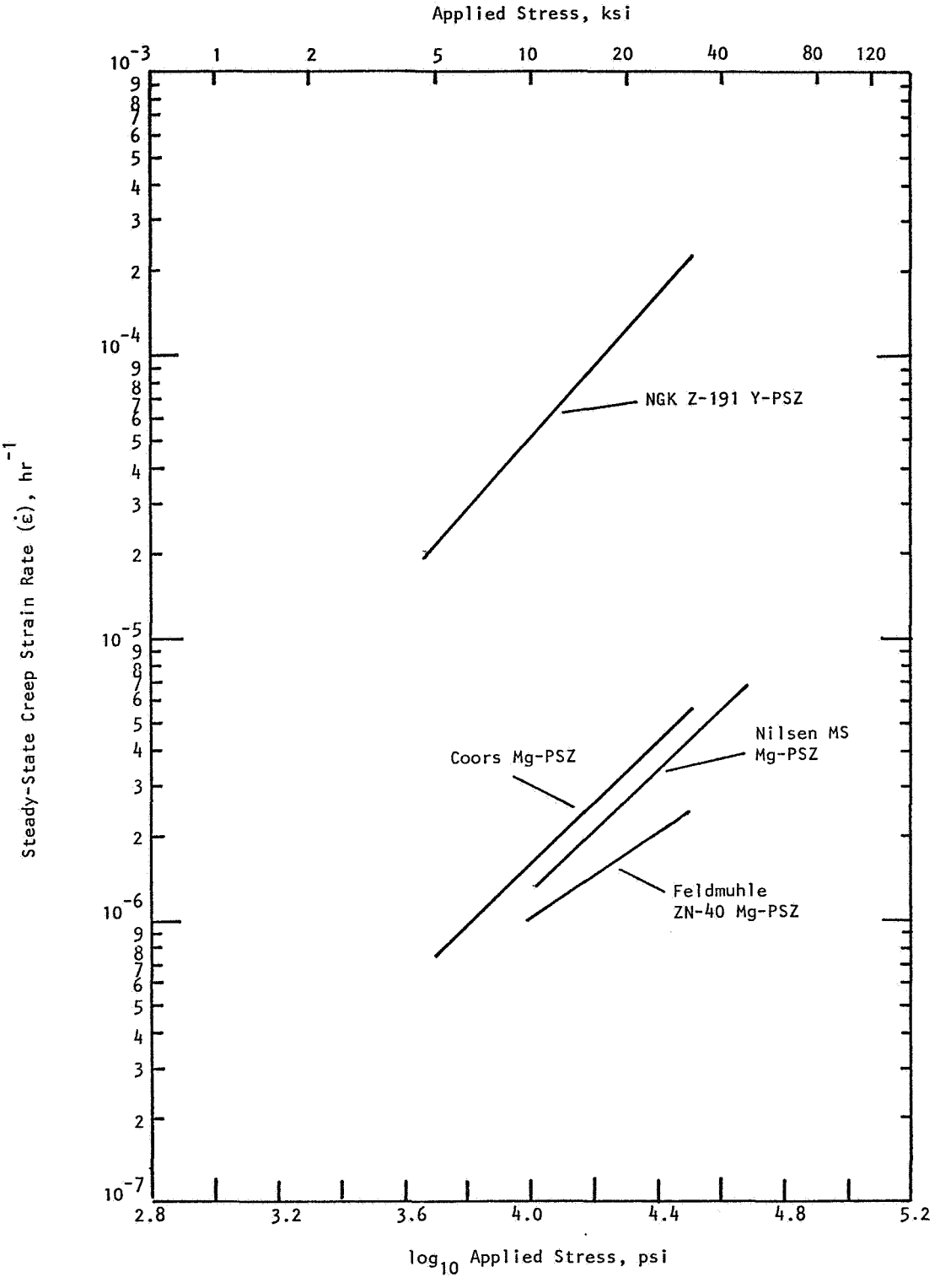

Figure 77. Flexural creep behavior of transformation-toughened zirconia at 1000°C.

the stress exponent is slightly higher also (n = 1.3, as shown in Figure 73). The reason for the higher creep rate for the NGK Z-191 material is potentially twofold: (a) it has a finer grain structure (refer to previously presented reflected light microscopy) and more grain boundary volume, and (b) it has high Si impurity (refer to the spectrographic cation impurity analysis shown in Table 4), implying a SiO_2-rich glass phase in intergranular regions. These two aspects of Y-TZP lead to low resistance to deformation at elevated temperature. The relatively large amount of intergranular glass phase leads to enhanced grain boundary diffusion as well as the possibility for activation of the additional deformation mechanism of grain boundary sliding. Note, however, that the fast-fracture stress-strain curve for NGK Z-191 (Figure 56) at 1000°C was linear. This tends to rule out grain boundary sliding as an operable mechanism. The fact that this is a long-time effect implies intergranular diffusion.

To summarize, Y-TZP is fine grain and has a significant silica-rich intergranular phase. Either one or both of these aspects of TZP result in much higher creep rates as compared to Mg-PSZ. There is evidence for a diffusional mechanism in these materials. Little or no differences were observed in the creep behavior of as-received and overaged Mg-PSZ (1000 hr/1000°C exposed) materials. This implies that the mechanism of creep in zirconia is independent of the phase assemblage.

9. INTERNAL FRICTION

Internal friction is an informative measurement to make on transformation-toughened zirconia. Zener[18] and others[19-21] have provided excellent reviews of internal friction. Hookean elastic theory implies a direct and instantaneous linear relation between low level force application and resultant deformation. However, as the rate of loading and unloading is increased, a phase lag between stress and strain appears with accompanying absorption of energy. This time-dependent elastic behavior is termed anelasticity. Internal friction may be defined as the amount of energy absorbed during deformation compared to the maximum amount of energy applied initially. As the number and extent of flaws in a body increases, the amount of energy absorbed through flaw surface friction, plastic zone dislocation motion, etc., also increases. Thus, the internal friction is an integrated effect, the measurement of the total flaw spectrum in a material. It is a particularly interesting measurement for transformation-toughened zirconia, since it is potentially sensitive to detecting instabilities relating to the tetragonal-to-monoclinic phase transformation.

Test samples were suspended from piezoelectric drive and pickup transducers as for dynamic elastic modulus measurement. The frequency range just adjacent (above and below) the fundamental resonant frequency was scanned with a Hewlett-Packard spectrum analyzer.* The Zener bandwidth[18] method involves computing the internal friction, Q^{-1}, from the measured peak width at half maximum amplitude:

$$Q^{-1} = \frac{\Delta f}{\sqrt{3}\, f}$$

where Q^{-1} = internal friction

f = resonant frequency

Δf = peak width at half amplitude

*Model No. 3580A.

The concept is illustrated in Figure 78. This method is useful for measuring the range of internal friction normally found in ceramic materials (10^{-2} to 10^{-6}). As with the dynamic elastic modulus measurement, the use of Nicalon SiC fibers to suspend the sample from points just adjacent to the flexural nodal points permitted a relatively convenient way of supporting the sample in the furnace for elevated temperature measurement.

The room-temperature resonant frequency, peak width, and computed internal friction for five zirconia materials in the as-received (i.e., unexposed) condition are presented in Table 16. Values for the four coarse-grained Mg-PSZ materials (i.e., Nilsen, Feldmuhle, and Coors) are similar, while the fine-grained material from NGK has slightly higher internal friction. This is presumably due to the greater number of surfaces/interfaces in the fine grain microstructure of the TZP material.

Figure 79 illustrates the internal friction for NGK Z-191 Y-TZP from 25° to 950°C. Note the pronounced internal friction peak at 200°C. This is precisely the same behavior shown by Shimada et al.[12] for a similar Y-PSZ, as shown in Figure 80. Wachtman and Corwin[22] discuss internal friction peaks in calcia-stabilized zirconia (PSZ and FSZ); their results are discussed in terms of the motion of oxygen vacancies. The observed internal friction peak in TZP at 200°C may or may not be related to another interesting aspect of zirconia--

TABLE 16. ROOM TEMPERATURE INTERNAL FRICTION AND RESONANT FREQUENCY[a]

Material	Resonant Frequency f, Hz	Resonant Frequency Δf, Hz	Internal Friction, $Q^{-1} \times 10^4$
Nilsen MS Mg-PSZ	3620	1.96	3.13
Nilsen TS Mg-PSZ	3598	1.89	3.03
Feldmuhle ZN-40 Mg-PSZ	3524	2.19	3.50
Coors Mg-PSZ	3533	2.28	3.73
NGK Z-191 Y-TZP	3400	3.11	5.29

[a]As-received material.

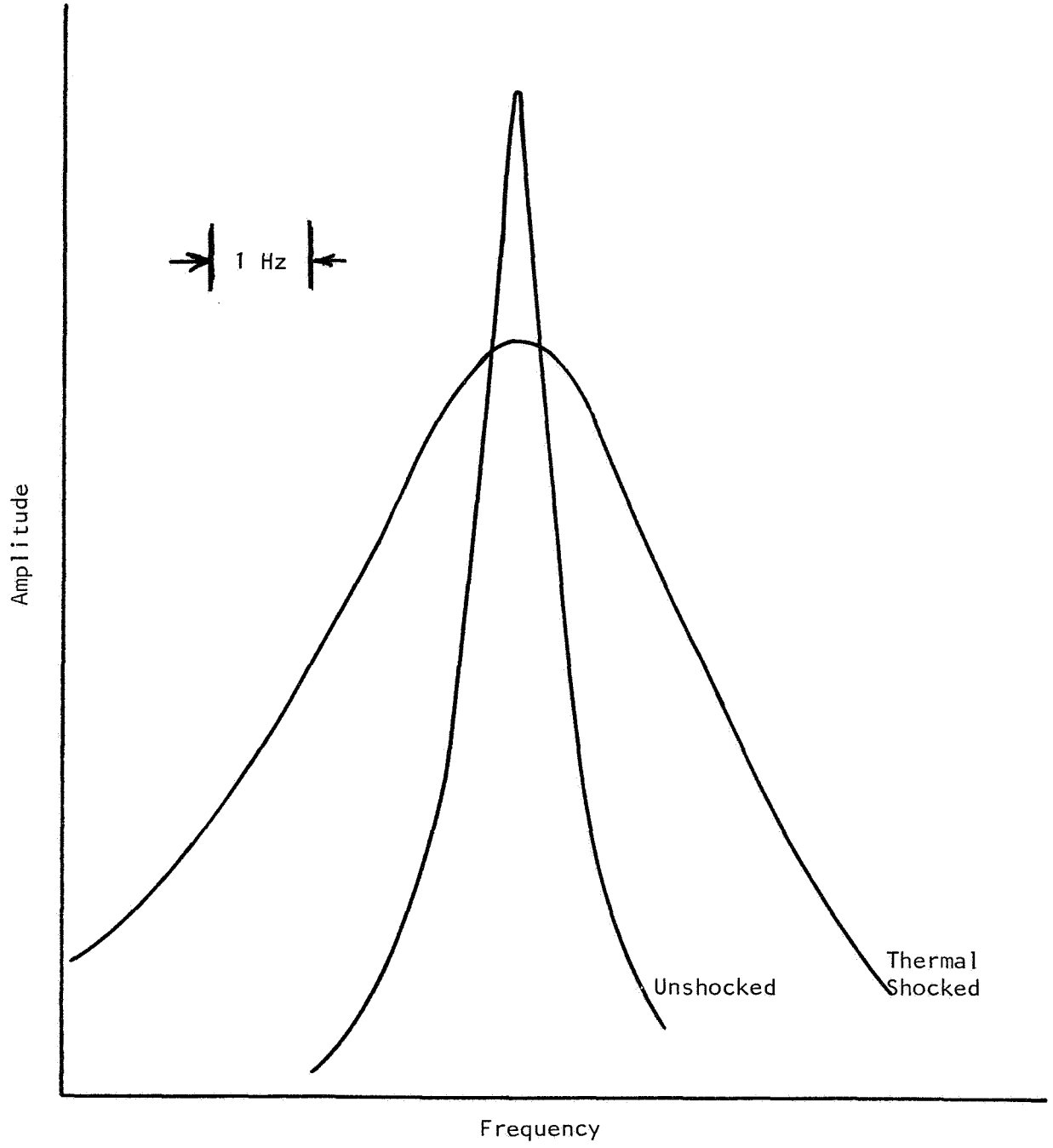

Figure 78. Typical amplitude-frequency curves of unshocked and thermal shocked ceramics for internal friction measurement.

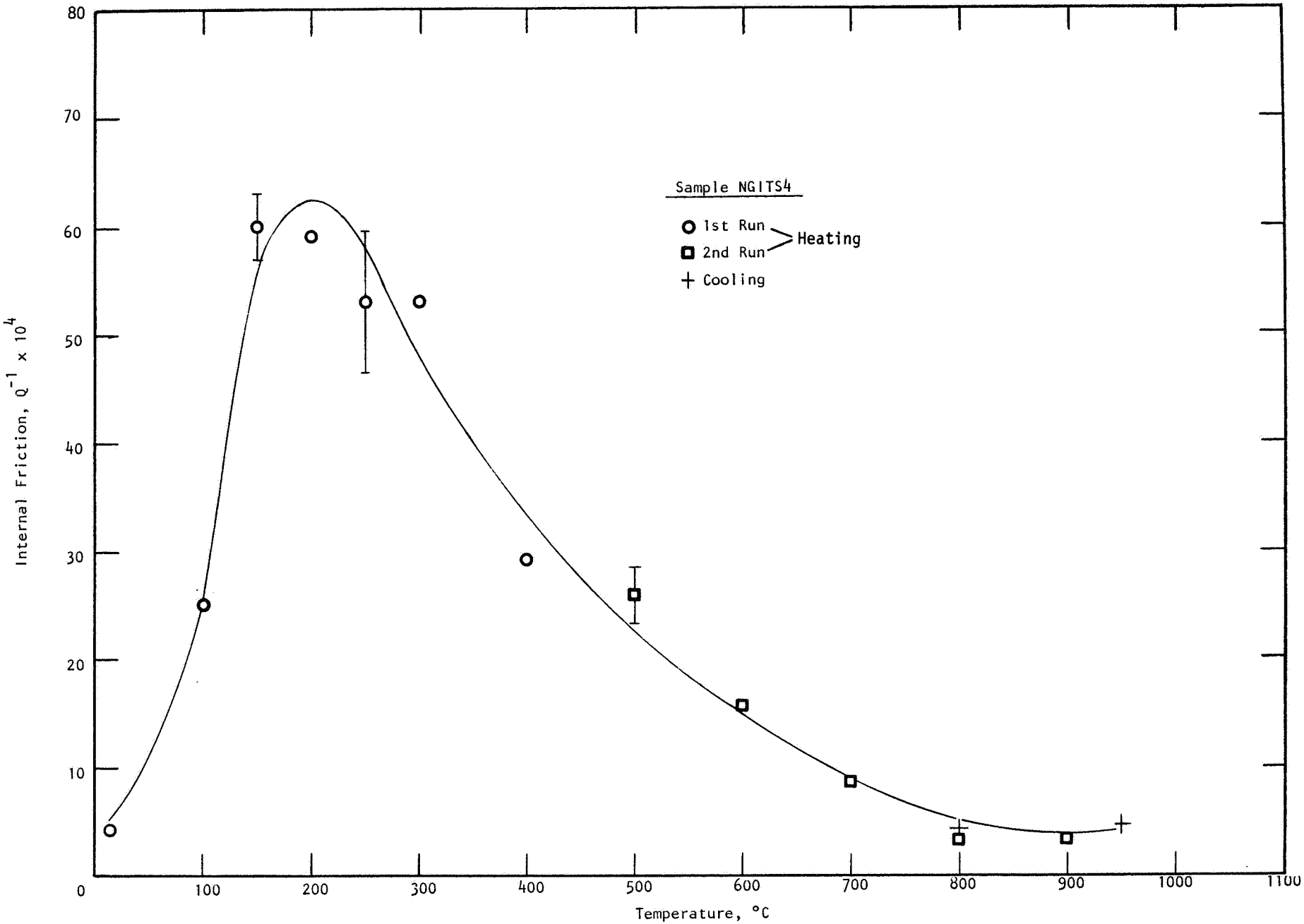

Figure 79.. Internal friction as a function of temperature for NGK Z-191 Y-TZP.

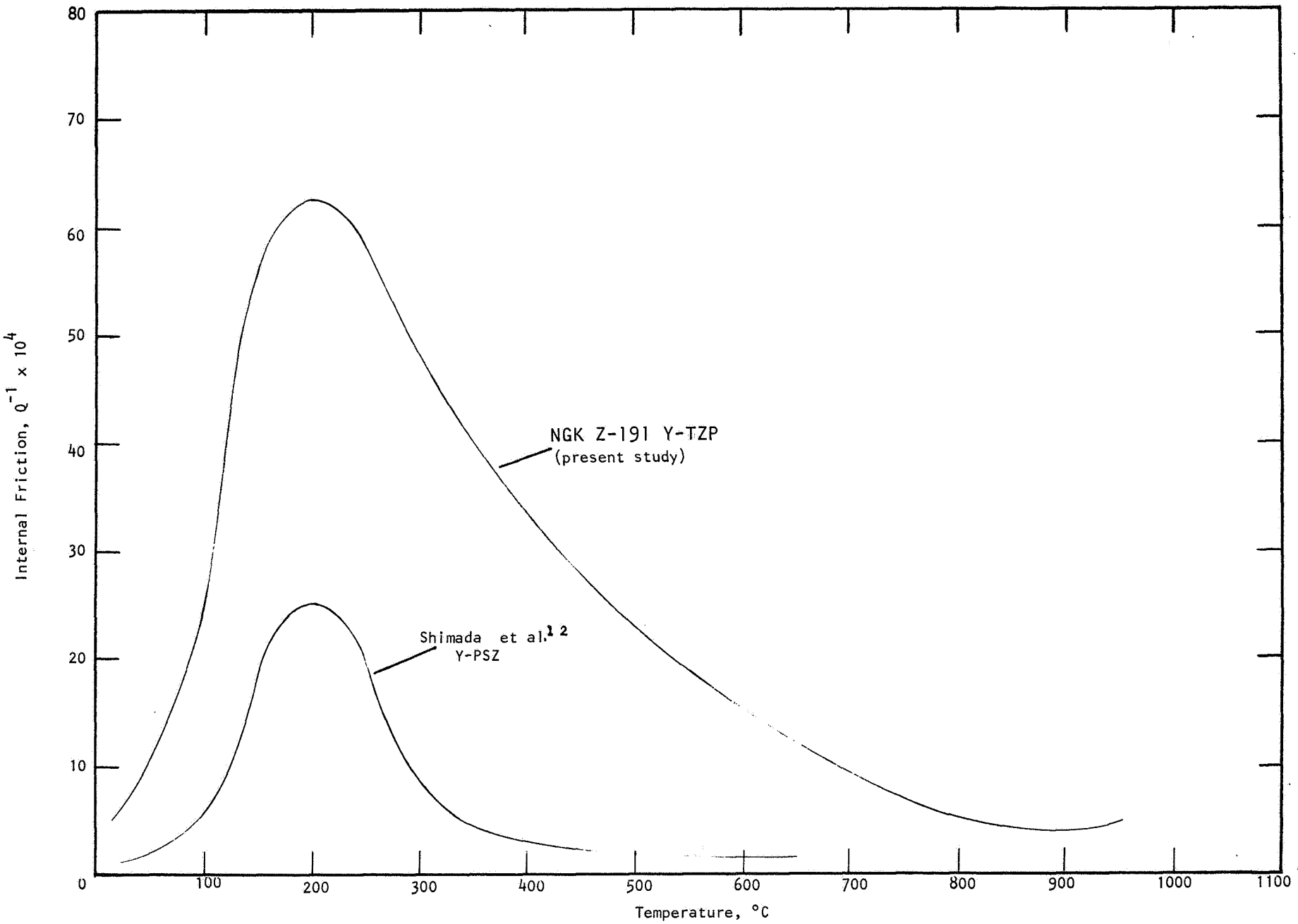

Figure 80. Internal friction as a function of temperature for Y-PSZ materials.

the deleterious effect of water vapor on some Y_2O_3-stabilized zirconia materials. NGK personnel have reported a massive strength degradation at 200°C for this form of Y-PSZ.[23,24] Lange[25] has studied this phenomenon and has discussed unpublished work that leads to the conclusion that this strength degradation at 200°C is caused by the formation of yttrium hydroxide on the surface of the tetragonal particles in Y-PSZ, which subsequently nucleates the transformation of the particles from tetragonal to monoclinic. In fact, such materials have been known to be reduced to powder form in an autoclave environment, an experiment that has apparently been performed by several researchers in the field. On the current program, the internal friction measurements were performed in a laboratory atmosphere where the relative humidity was measured to be nominally 45% RH. Strength measurement was made at 200°C (where the internal friction peak and water vapor problem occurred). The results are shown in Figure 81. It is seen that no such effect is apparent in the fast fracture results for NGK Z-191 Y-TZP. The bend strength at 200°C follows the strength-temperature trend line established previously. The potential of degradation of some forms of Y-PSZ in high water vapor environments is particularly a problem since the tetragonal particles are unprotected from the environment. X-ray diffraction results (Table 3) show that the NGK material consists of nearly 100% tetragonal grains. In fact, it is more properly referred to as a TZP (tetragonal zirconia polycrystals) instead of a TTZ (transformation-toughened zirconia). In the technical community this distinction is beginning to be made and has been in this report.

The active (metastable) tetragonal phase in MgO-stabilized transformation-toughened zirconia materials, however, is contained within large cubic ZrO_2 grains. The intragranular tetragonal zirconia is a precipitate phase that results from a thermal aging process. Therefore, the tetragonal phase that results in high fracture toughness is protected from the environment in Mg-PSZ. This may be the reason that extensive water vapor effects have not been reported for Mg-PSZ. Lange[25] asserts that the precipitate TTZ's have the additional advantage that hydroxide compounds of magnesium are not stable at 200°C (as is yttrium hydroxide in Y-PSZ), but do not form until a higher temperature is reached. The elevated temperature internal friction results for the Nilsen and Coors Mg-PSZ materials provided in Figures 82 and 83 apparently lend support to this view. The exact origin of the

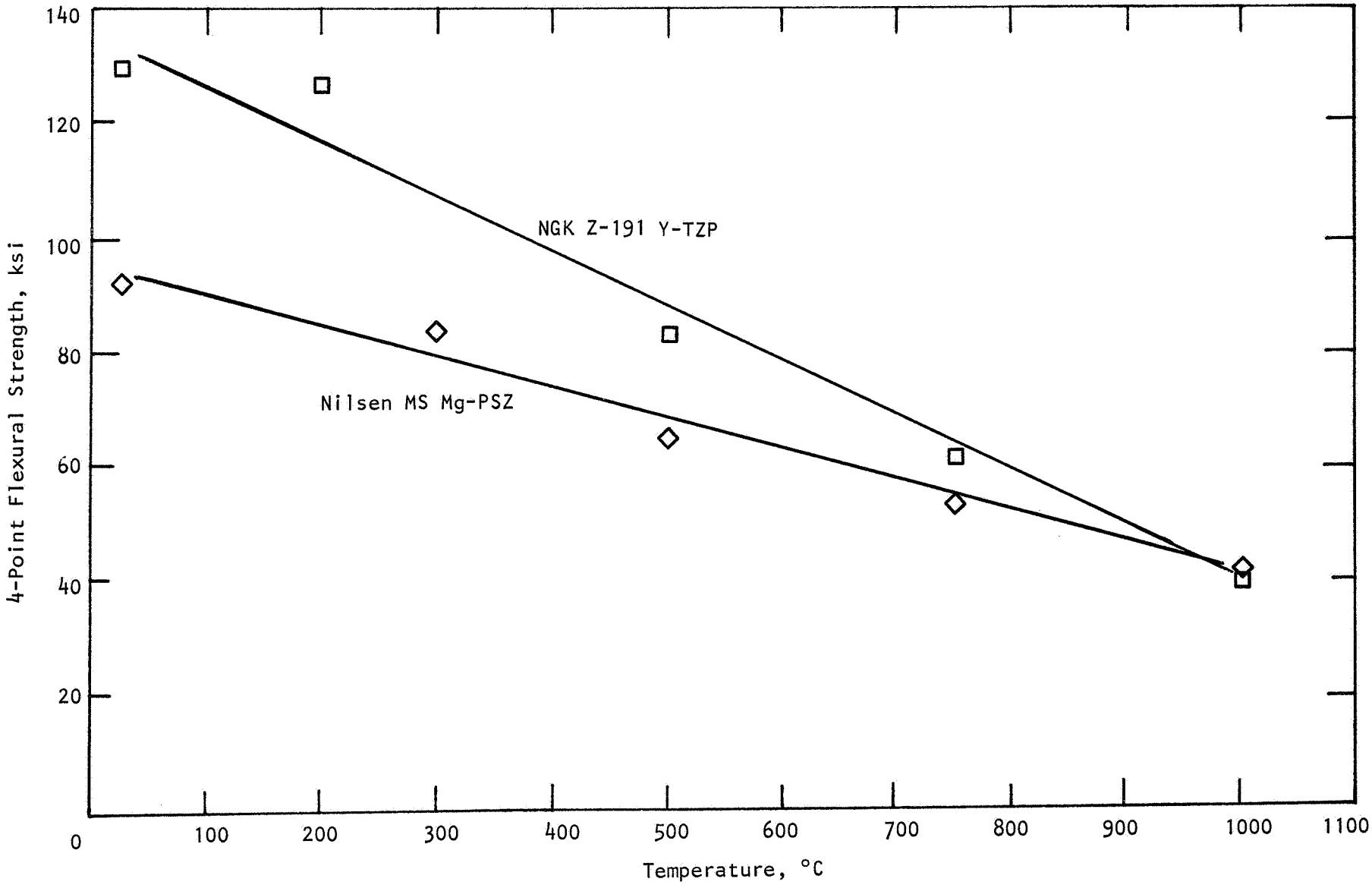

Figure 81. Flexural strength of Y-TZP and Mg-PSZ, illustrating absence of fast fracture strength degradation at temperatures (200° and 300°C) corresponding to internal friction peaks.

internal friction peaks shown is as yet unexplained, but it certainly occurs at higher temperatures than for Y-PSZ (300-600°C, as shown in Figures 82 and 83).

Both Y- and Mg-PSZ materials are compared in the internal friction summary presented in Figure 84. Peak amplitudes are high for NGK TZP, presumably due to its fine grain microstructure (many internal boundary surfaces). For the Coors Mg-PSZ material, larger internal friction may be due to more microcracking in the structure. The internal friction peaks of Mg-PSZ materials occur at substantially higher temperatures than for yttria-stabilized TZP.

Internal friction measurements were also made on material that had been exposed for 1000 hr at 1000°C. Room temperature results are presented in Table 17, which illustrates that all MgO-stabilized materials (i.e., Nilsen, Coors, and Feldmuhle) exhibited at least ~100% increases in internal friction after exposure. This correlates with the strength and toughness degradation and phase and microstructural changes for these materials after exposure discussed previously. The magnitudes of the changes in Q^{-1} and residual strength also correlate. The strength changes with exposure are shown in Table 18. Note that the Nilsen TS PSZ was added to this compilation. Comparing Tables 17 and 18, it is observed that the Coors material exhibited the largest strength reduction as a result of the static thermal exposure. It could be surmised that these thermally aged MgO-stabilized materials would be substantially microcracked. The loss of strength alone could be related to a loss in toughness through t → m transformation. However, accompanied by substantial increase in internal friction would lead to speculation of severe microcracking also. The speculation of extensive microcracking for the Coors material was discussed previously to explain its strength, elastic modulus, and fracture toughness changes with exposure.

Note, however, the behavior of Y_2O_3-stabilized NGK Z-191 ZrO_2. A negligible change in internal friction was observed after the 1000°C/1000 hr exposure, as shown in Table 17. This correlates with only a 7% reduction in strength experienced by this material as shown in Table 18, as well as the indications of stability shown by nonchanging microstructure, phase assemblage, etc. These are all indications that Y_2O_3-stabilized materials are

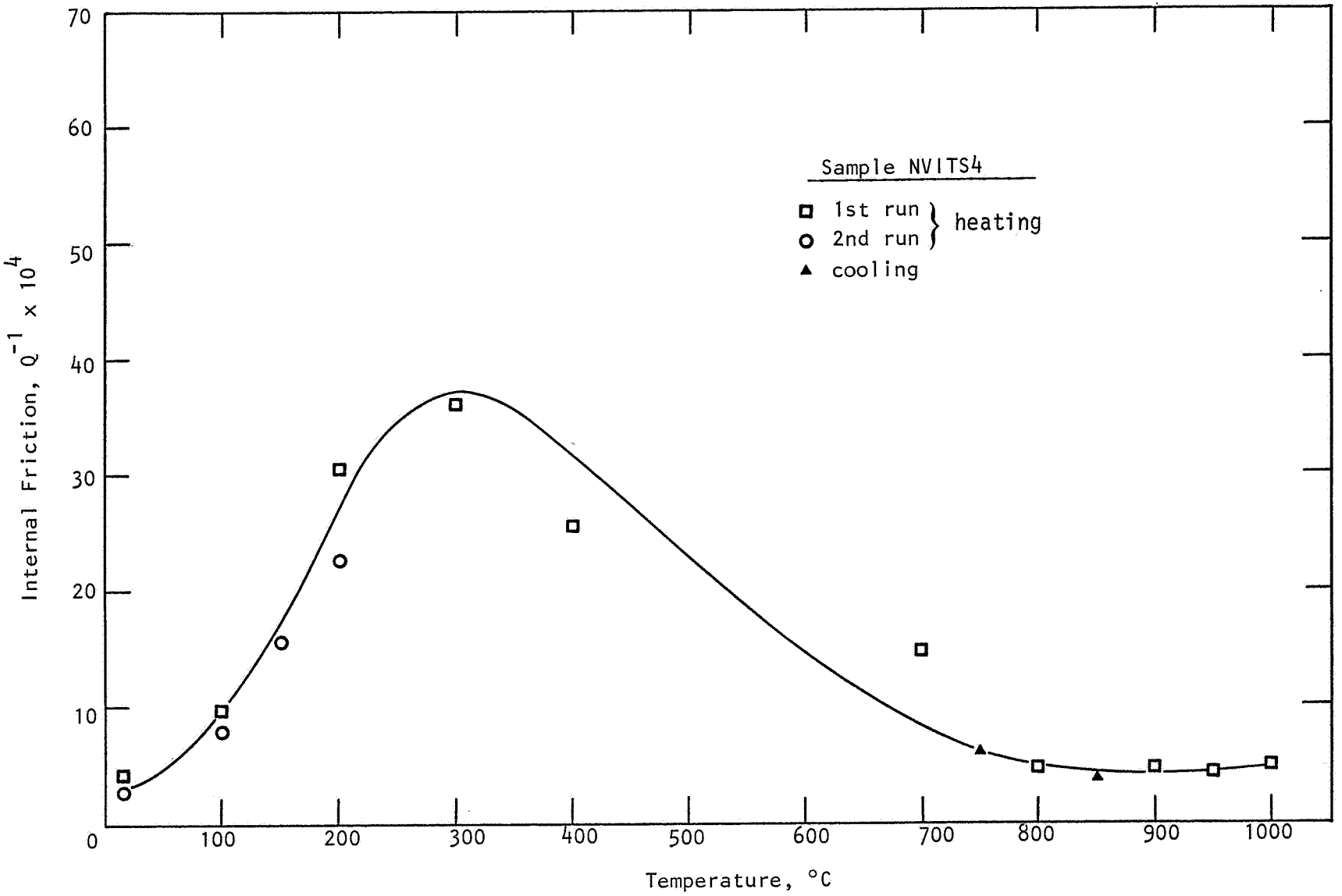

Figure 82. Internal friction as a function of temperature for Nilsen MS Mg-PSZ.

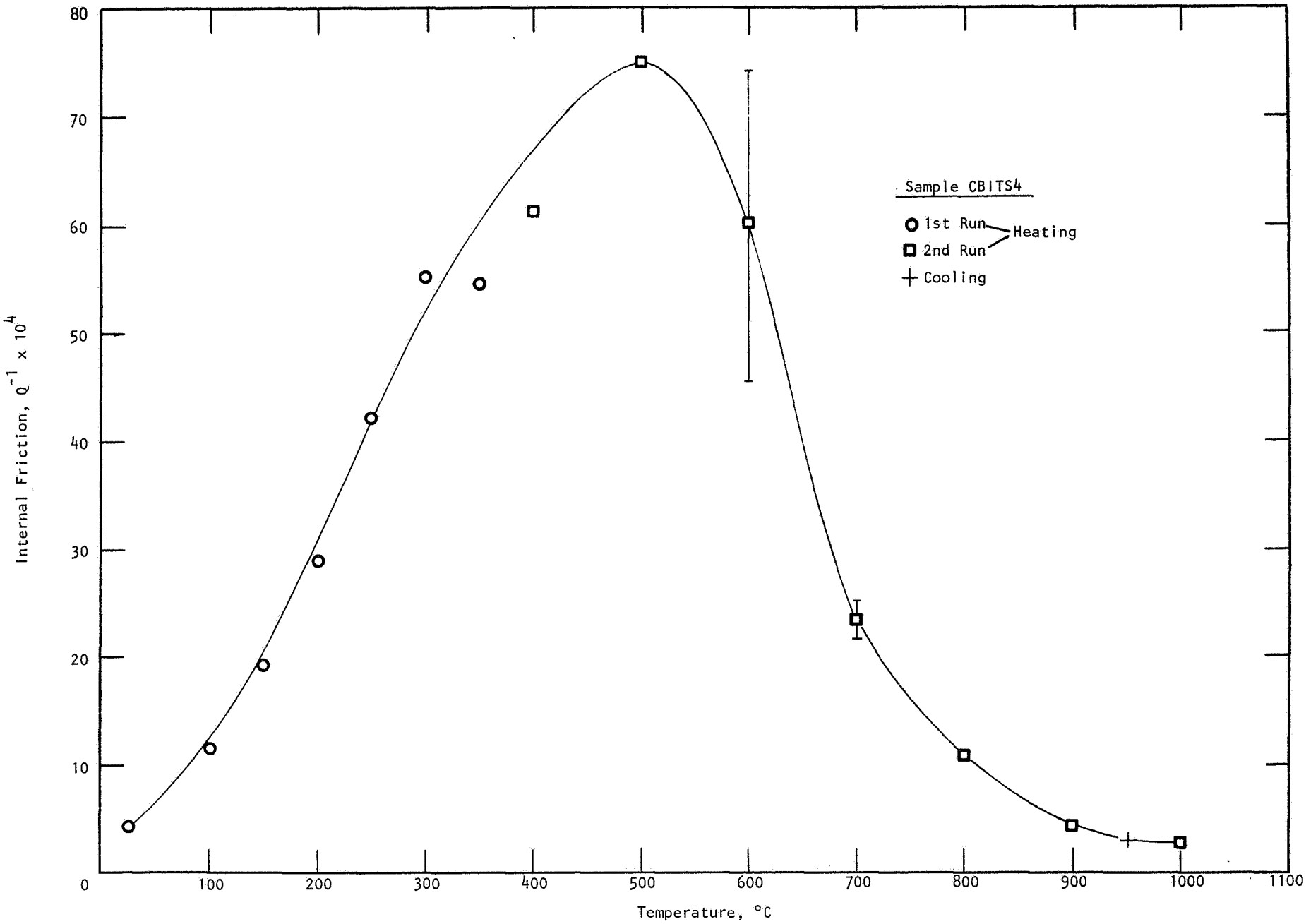

Figure 83. Internal friction as a function of temperature for Coors Mg-PSZ.

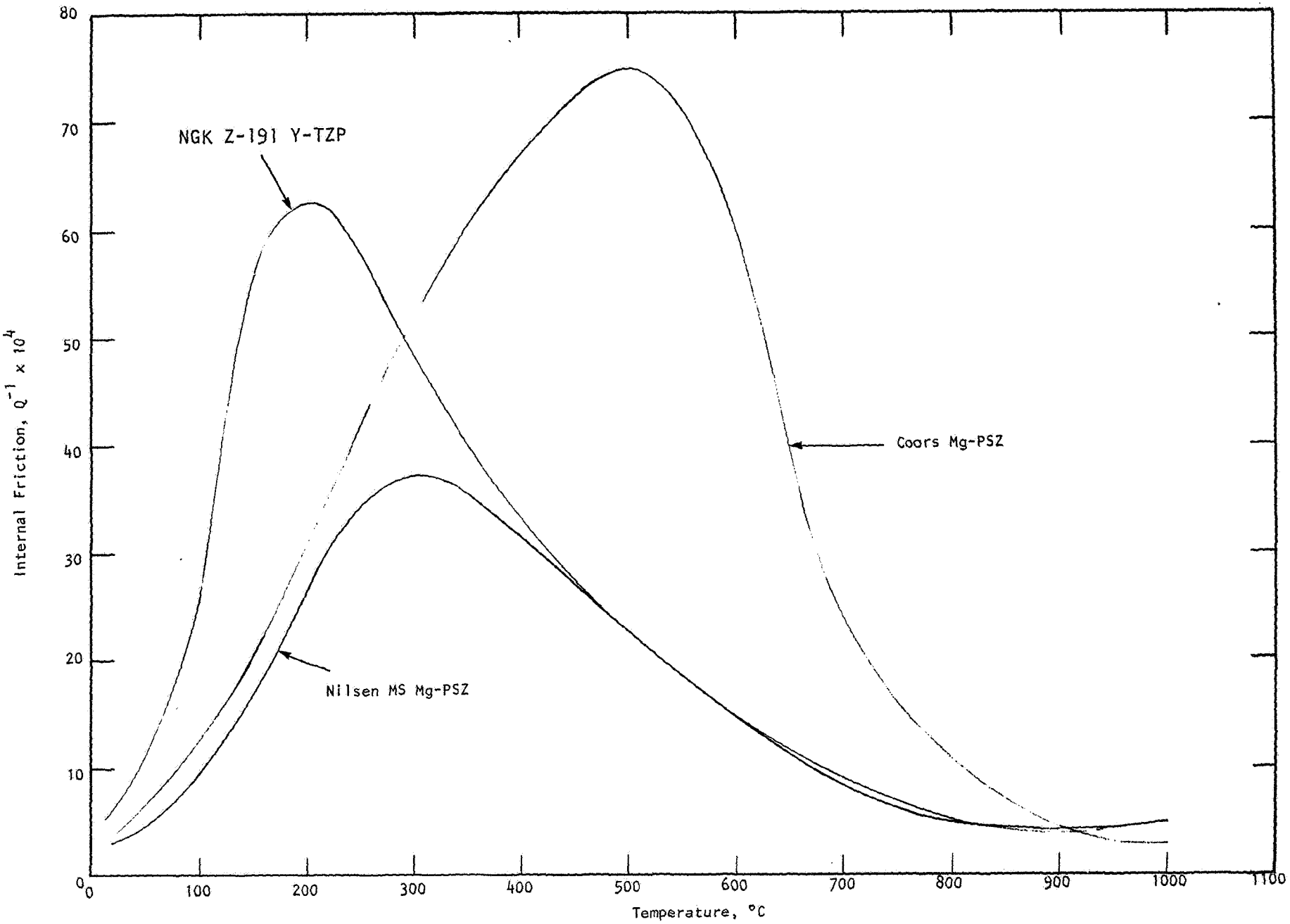

Figure 84. Internal friction as a function of temperature for transformation-toughened zirconia.

TABLE 17. INTERNAL FRICTION AND RESONANT FREQUENCY AT 25°C AFTER 1000 HR/1000°C STATIC EXPOSURE[a]

Material	Resonant Frequency f, Hz	Resonant Frequency Δf, Hz	Internal Friction,[b] $Q^{-1} \times 10^4$
Nilsen MS Mg-PSZ	3668	3.36	5.29 (+69%)
Nilsen TS Mg-PSZ	3638	3.69	5.87 (+94%)
Feldmuhle ZN-40 Mg-PSZ	3506	3.71	6.10 (+74%)
Coors Mg-PSZ	--	~16-26	~11-17 (+~300%)
NGK Z-191 Y-TZP	3410	3.03	5.14 (-3%)

[a] Prior to thermal shock experiments.

[b] Numbers in parentheses indicate change from as-received condition.

superior to MgO-stabilized materials in terms of long-term overaging phenomena.

Elevated temperature internal friction results, both before and after 1000 hr/1000°C exposure, for NGK Z-191 TZP and Nilsen MS Mg-PSZ are provided in Figures 85 and 86, respectively. The internal friction peak for the NGK material is only slightly shifted after exposure, and its amplitude is unchanged. The Mg-PSZ, however, exhibits a substantial peak amplitude increase, as well as a shift to a higher temperature after the 1000 hr/1000°C static thermal exposure.

A study of the mechanisms of internal friction in transformation-toughened zirconia is beyond the scope of this program. However, their relative peak amplitudes, temperature dependence, and relative changes with overaging and other degradation phenomena such as destabilization and/or decomposition are consistent with the phase and microstructural evidence obtained on this program for Mg- and Y-stabilized TTZ materials.

TABLE 18. ROOM-TEMPERATURE MECHANICAL PROPERTIES OF ZIRCONIA BEFORE AND AFTER 1000°C/1000 HR STATIC AIR EXPOSURE

Material	Properties As-Received			Properties After 1000°C/1000 hr Exposure		
	Flexural Strength, psi	Failure Strain, %	Elastic Modulus, 10^6 psi	Flexural Strength,[a] psi	Failure Strain, %	Elastic Modulus, 10^6 psi
Nilsen MS Mg-PSZ	92,450	0.39	27.2	39,350 (-57%)	0.15	27.1
Feldmuhle ZN-40 Mg-PSZ	61,830	0.23	28.0	43,210 (-30%)	0.16	27.2
Coors Mg-PSZ	69,880	0.25	28.0	21,140 (-70%)	0.09	23.2
NGK Z-191 Y-TZP	129,090	0.46	27.4	119,840 (-7%)	0.43	27.5
Nilsen TS Mg-PSZ	75,900	--	--	48,340 (-36%)	--	--

[a]Numbers in parentheses indicate percentage change.

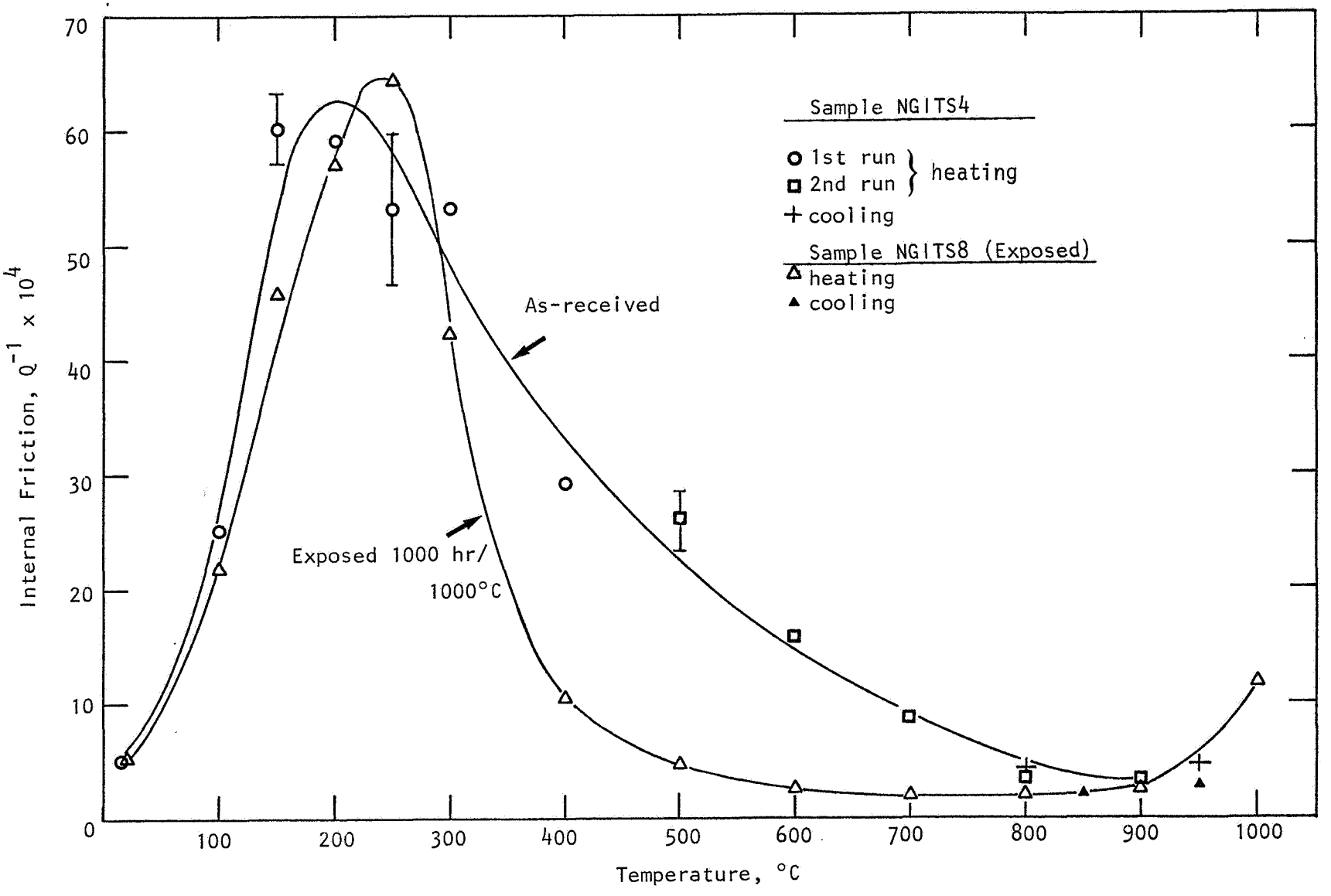

Figure 85. Internal friction as a function of temperature for NGK Z-191 Y-TZP, before and after 1000 hr/1000°C static exposure.

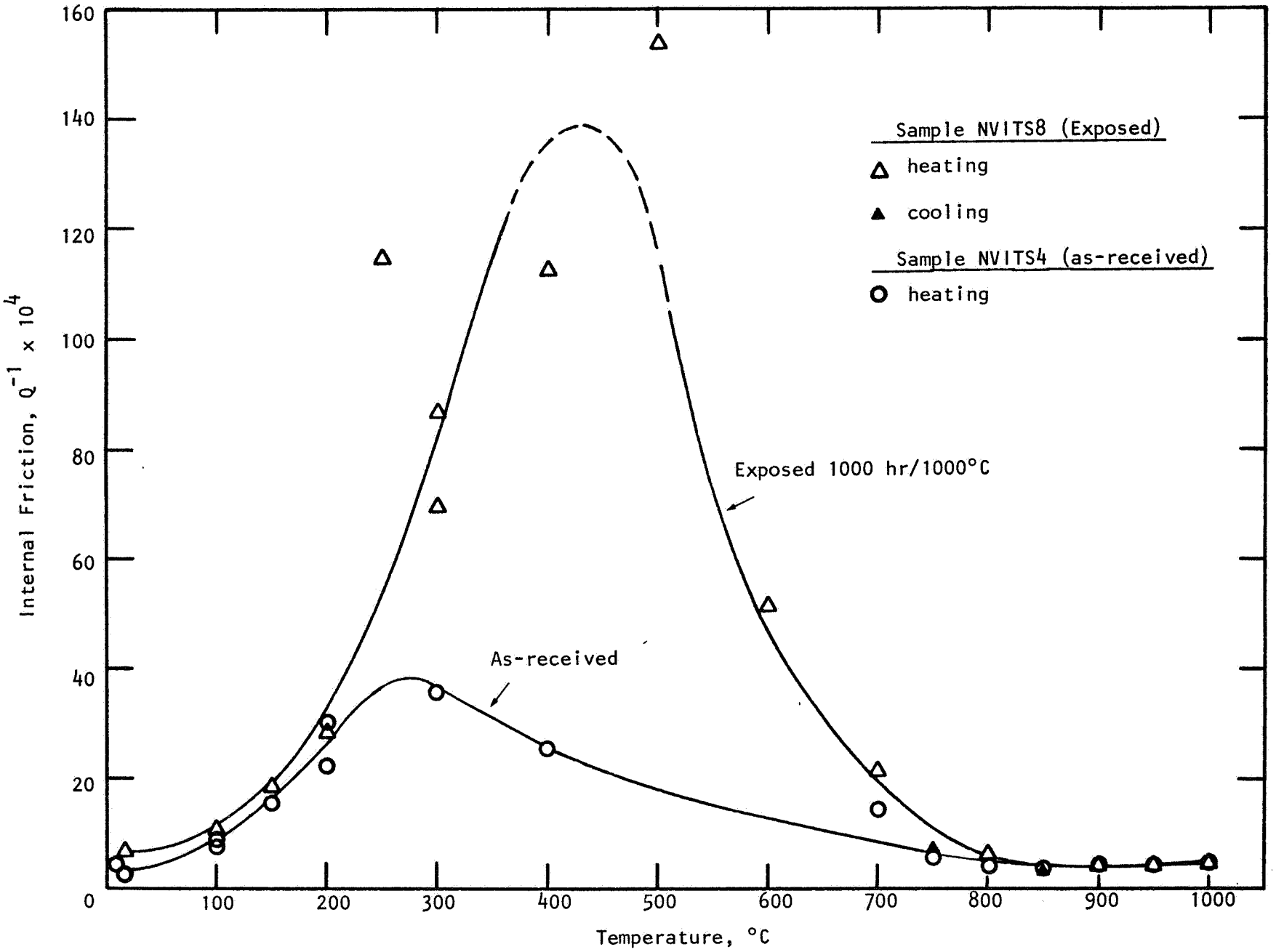

Figure 86. Internal friction as a function of temperature for Nilsen MS Mg-PSZ. before and after 1000 hr/1000°C static exposure.

10. THERMAL SHOCK

Thermal shock resistance was determined on this program by the water quench method, with the initiation of thermal shock damage being detected by internal friction measurement. This technique was chosen not in an attempt to simulate in-service engine conditions, but rather as a relative ranking of candidate materials in severe thermal downshock. In conducting this test, internal friction was measured before and after water quench from successively higher temperatures using the flexural resonant frequency Zener bandwidth method. A marked change in internal friction (specific damping capacity) or observable surface microcracking indicated the onset of thermal shock damage (i.e., thermal stress-induced crack initiation). This defined the critical quench temperature difference, ΔT_c, which was compared to analytical thermal stress resistance parameters. The parameter which is most applicable to the experimental severe water quench is $R = \sigma(1 - \mu)/\alpha E$,[26] where σ is the strength, μ is Poisson's ratio, α is thermal expansion, and E is the elastic modulus.

10.1 RESULTS FOR AS-RECEIVED MATERIALS

Five as-received zirconia materials were evaluated in the water quench thermal shock test. Note that a second material from Nilsen was investigated (i.e., TS grade PSZ), since it is purported to possess superior thermal shock resistance. It was expected that, in general, zirconia materials would exhibit relatively poor thermal shock resistance (compared to Si_3N_4 and SiC, for instance) owing to their comparatively high coefficient of thermal expansion. It therefore was of interest to determine if a given vendor could modify the microstructure to yield better thermal shock results. The two materials from Nilsen (MS and TS) permitted this to be investigated.

Samples from these five sets of as-received zirconia materials were quenched into room-temperature water from successively higher initial temperatures (in 25°C increments starting at 200°C). The internal friction, Q^{-1}, was measured after each quench, and the sample was examined in a 160X binocular optical microscope. When no increase in Q^{-1} or surface microcracking was

PAGE 160 INTENTIONALLY BLANK

PRECEDING PAGE BLANK NOT FILMED

observed, a given sample was shocked from the next higher initial temperature. When a significant increase in internal friction or microcracking was observed, testing was resumed with an unshocked sample at an initial temperature one increment (25°C) lower. In this manner, the testing of two to three samples could yield a value of ΔT_c, the critical quench temperature difference. For present purposes, ΔT_c is defined as the temperature difference where the first microcracking or significant increase in internal friction was detected.

The results for the five zirconia materials are contained in Figures 87 through 91, where the change in internal friction, $\Delta Q^{-1}/Q_0^{-1}$, is plotted as a function of quench temperature difference, ΔT. The critical quench temperature difference for each material is shown in Table 19.

TABLE 19. CRITICAL QUENCH TEMPERATURE DIFFERENCE OF ZIRCONIA

Material	ΔT_c, °C
Nilsen MS	375
Nilsen TS	425-450
Feldmuhle ZN-40	300-325
Coors TT-ZrO_2	350-400
NGK Z-191	400

Note, in Figures 87 through 91, that an abrupt large increase in internal friction was always accompanied by the low-magnification optical observation of microcracking. However, the converse was not always true. For instance, Figure 90 exhibits "classic" behavior: a sudden large increase in internal friction (several hundred percent in magnitude) and the associated observation of microcracking. Figure 88, however, exhibits the case where microcracking was observed, thus defining the critical ΔT, prior to any significant internal friction increase. The reason for this is probably that the internal friction is a volume sensitive measurement, where surface effects are minimized. However, the observation of post-quench microcracking is made at the surface, where the largest tensile stresses occur during the sudden thermal downshock.

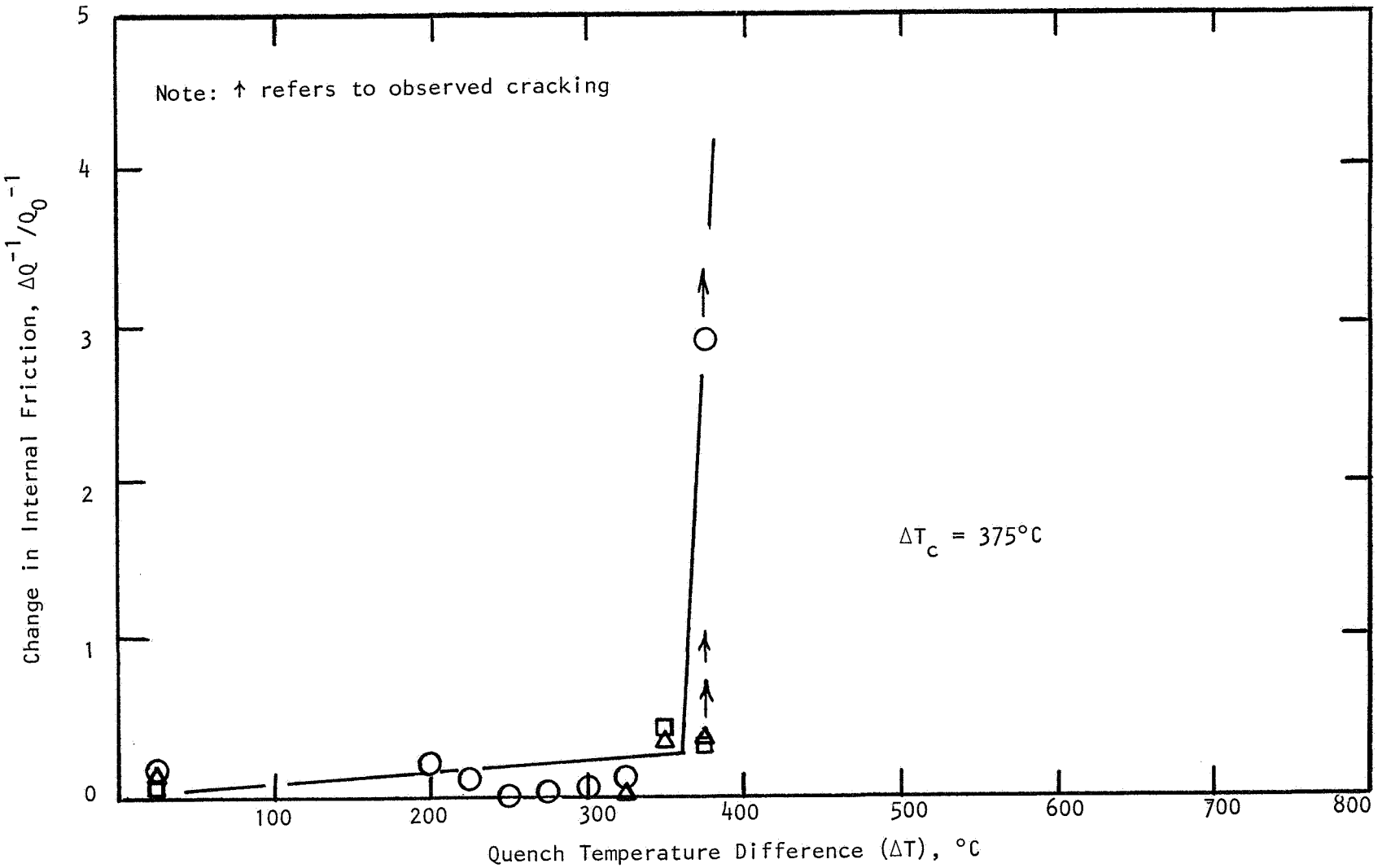

Figure 87. Water-quench thermal shock results for Nilsen MS Mg-PSZ (as-received).

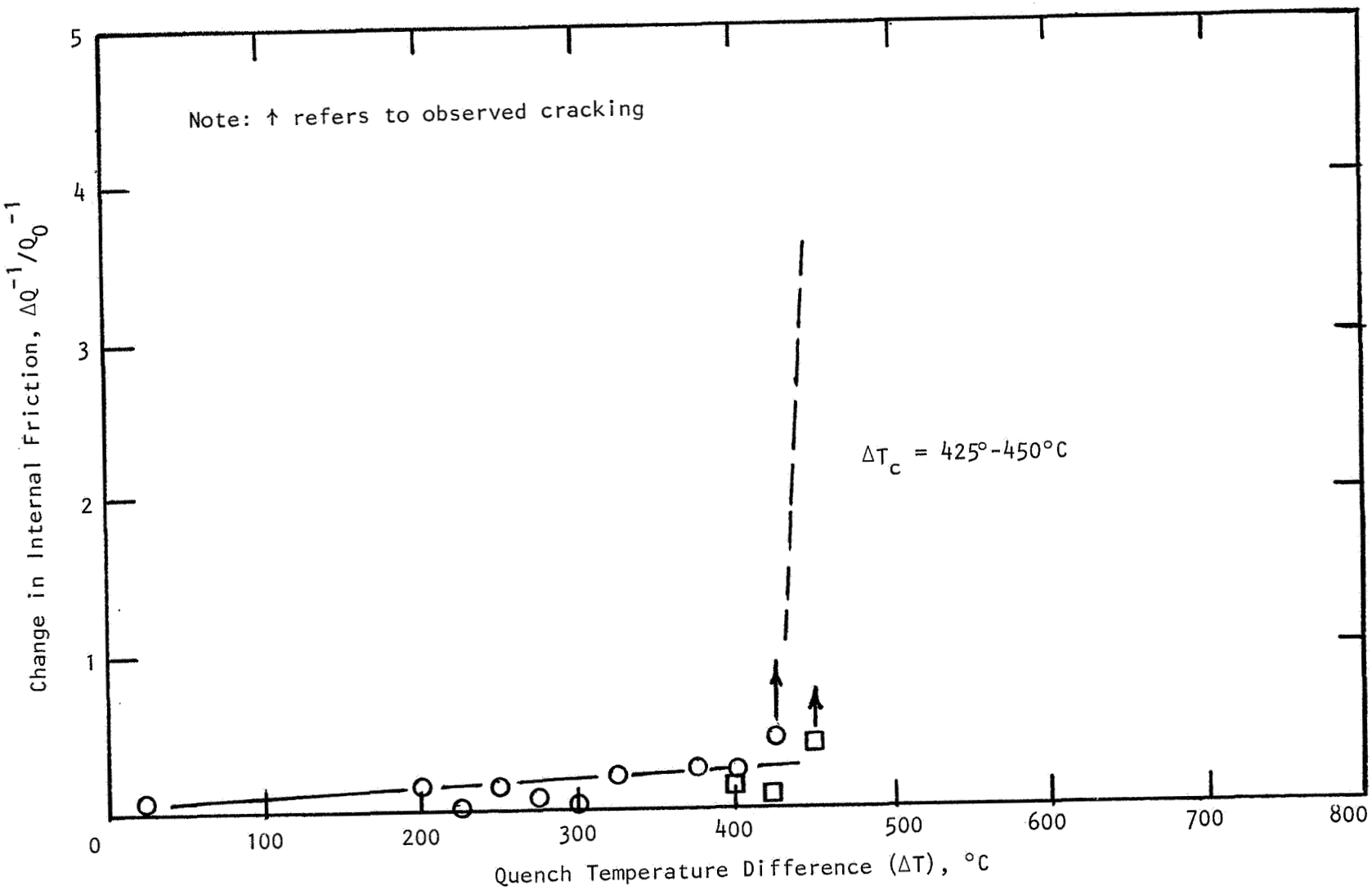

Figure 88. Water-quench thermal shock results for Nilsen TS Mg-PSZ (as-received).

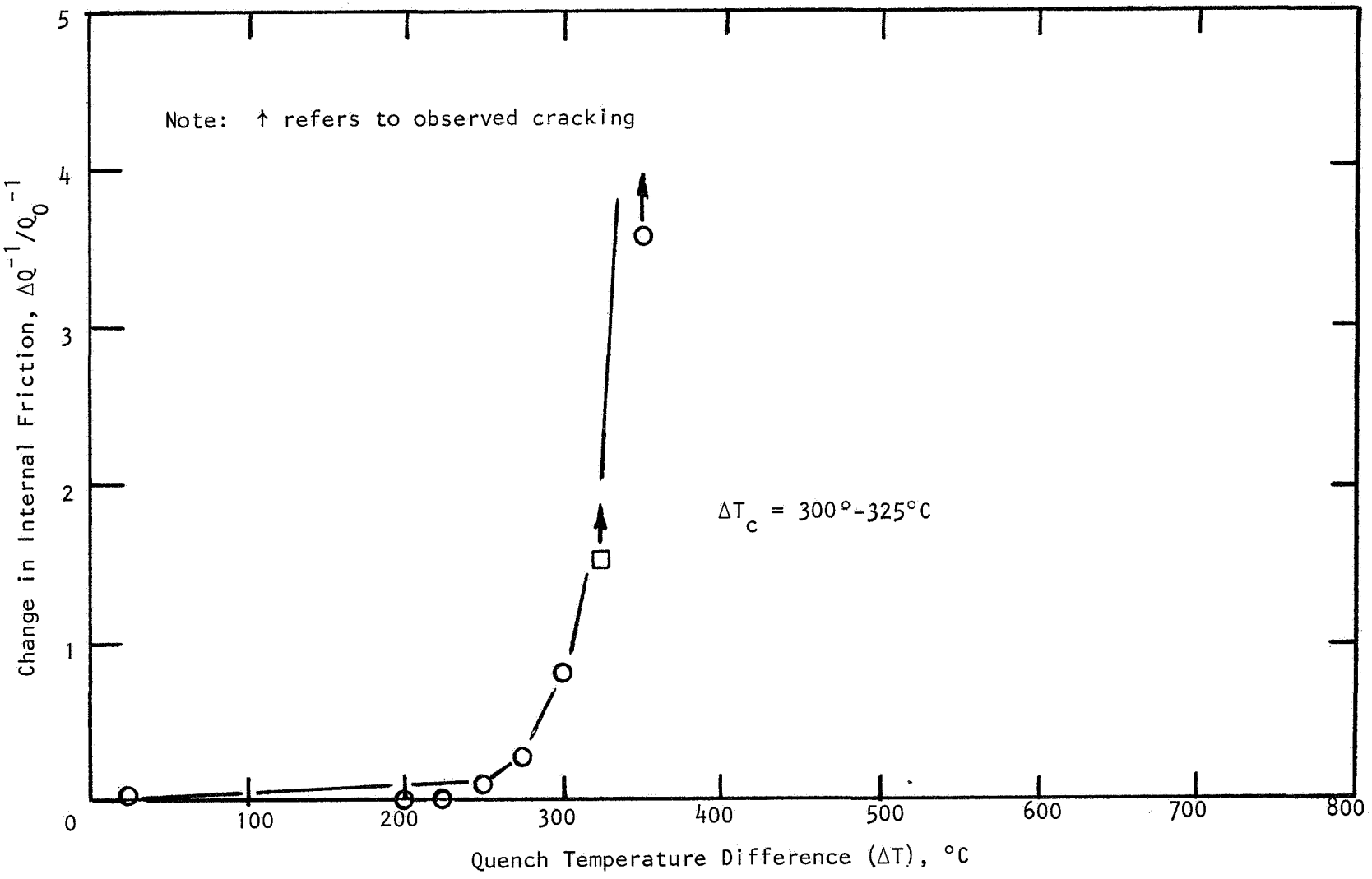

Figure 89. Water-quench thermal shock results for Feldmuhle ZN-40 Mg-PSZ (as-received).

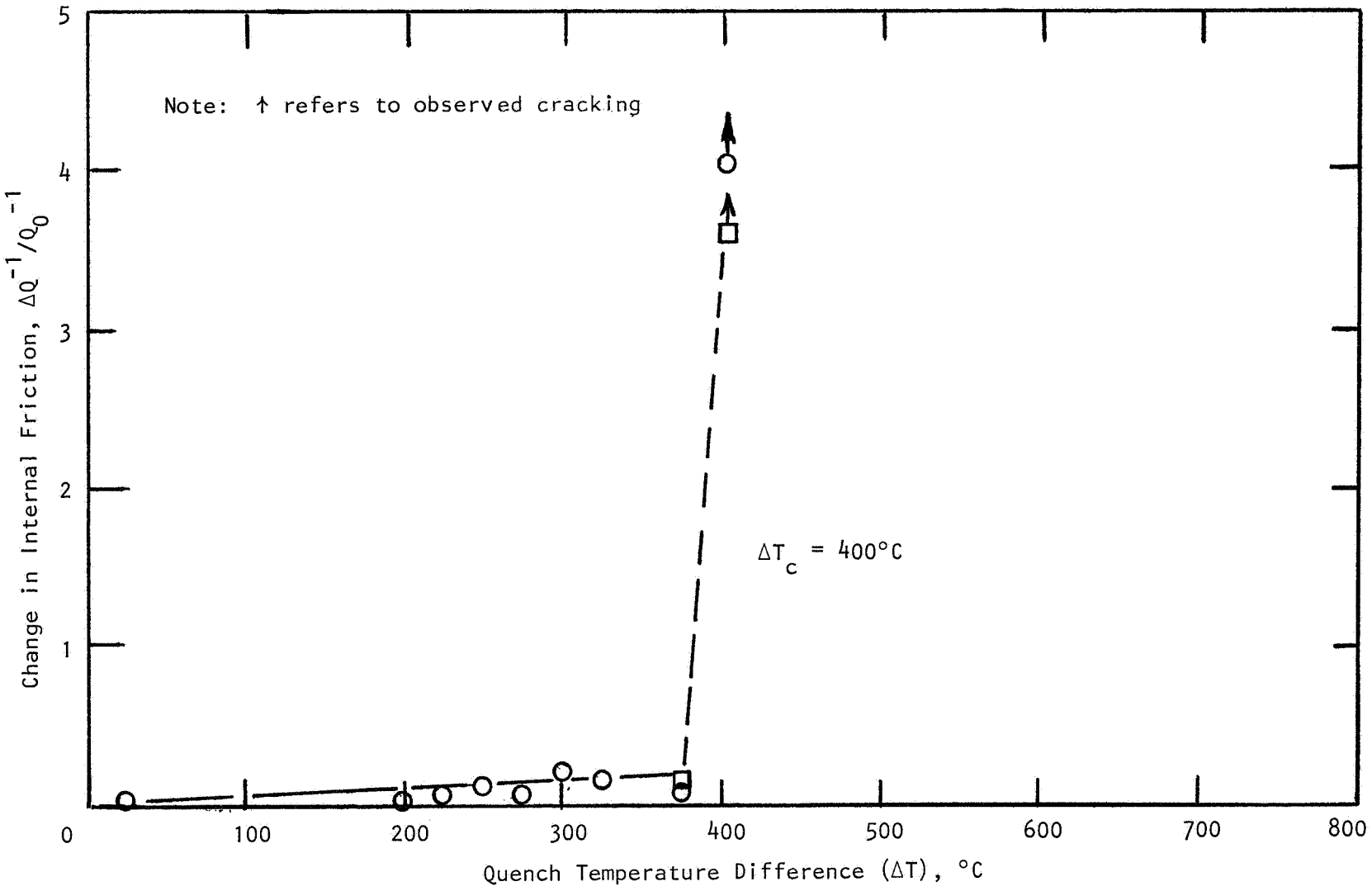

Figure 90. Water-quench thermal shock results for NGK Z-191 Y-TZP (as received).

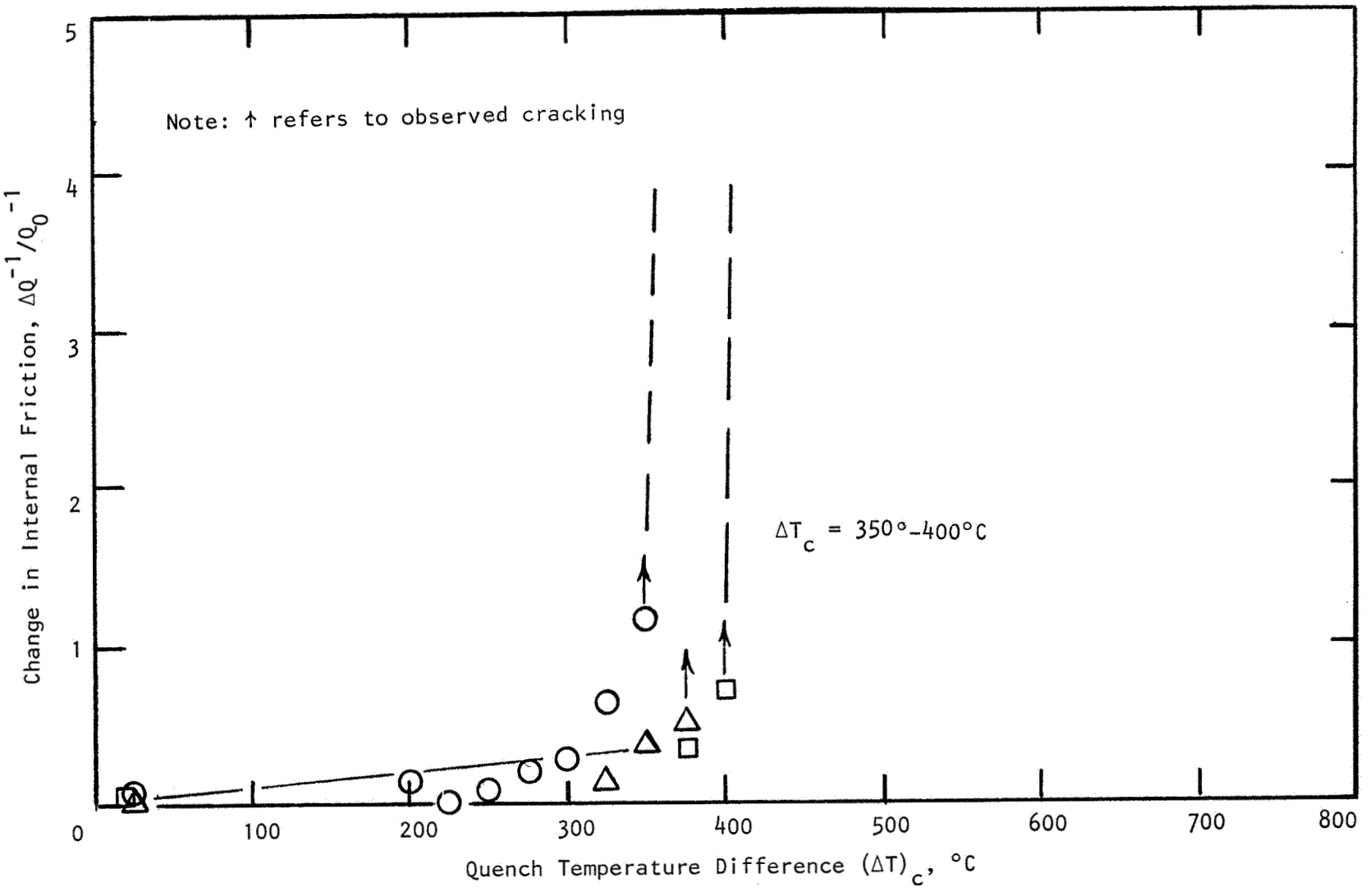

Figure 91. Water-quench thermal shock results for Coors Mg-PSZ (as-received).

This situation is analogous in some ways to the case where internal friction-based thermal shock results are compared with residual strength assessments. The ΔT_c values based on residual strength measurement (i.e., sudden decrease in strength at the critical quench temperature difference) are often found to be slightly higher than ΔT_c data based on internal friction measurement. The reason for this is that the internal friction measurement is an integrated effect, sensitive to all nucleated microcracks of any size throughout the entire sample volume. The residual strength method is usually performed in flexure. Therefore, a decrease in strength subsequent to thermal shock will only be realized when a thermal stress induced microcrack near the tensile surface of the bend bar has grown to a size larger than the original fracture origins in the unshocked material. Thus, internal friction is sensitive to all microcracks of any size which are nucleated prior to one near the surface growing to a certain critical size. The advantage of the internal friction method is that about an order of magnitude fewer test samples are required to accurately define the critical quench temperature difference.

Internal friction-quench temperature results are summarized in Figure 92 for the five as-received transformation-toughened zirconia materials evaluated. Note in Figures 87 through 91 that some materials exhibited a range of ΔT_c for the samples tested. In the summary presented in Figure 92, a conservative approach was taken--a worst case (i.e., lowest ΔT_c) representation is made. Figure 92 illustrates that Nilsen TS PSZ exhibited the highest ΔT_c (425°-450°C). Of the four main materials being investigated on this program, the higher strength materials, NGK Z-191 Y-TZP and Nilsen MS Mg-PSZ, exhibited higher values of the critical quench temperature difference than did the lower strength materials, Coors and Feldmuhle ZN-40 Mg-PSZ. Figure 93 presents low magnification optical photographs of representative cracking patterns of both low and high strength materials. Note the more localized cracking of high strength materials and the more extensive cracking of low strength materials.

Expected thermal shock results for these materials can be computed by employing the appropriate analytical thermal stress resistance parameter. In the case of severe thermal downshock, this parameter is R, which is proportional to the strength, and inversely proportional to the thermal expansion-elastic modulus product as described above. The appropriate thermal and mechanical properties to compute the R parameter were measured on this

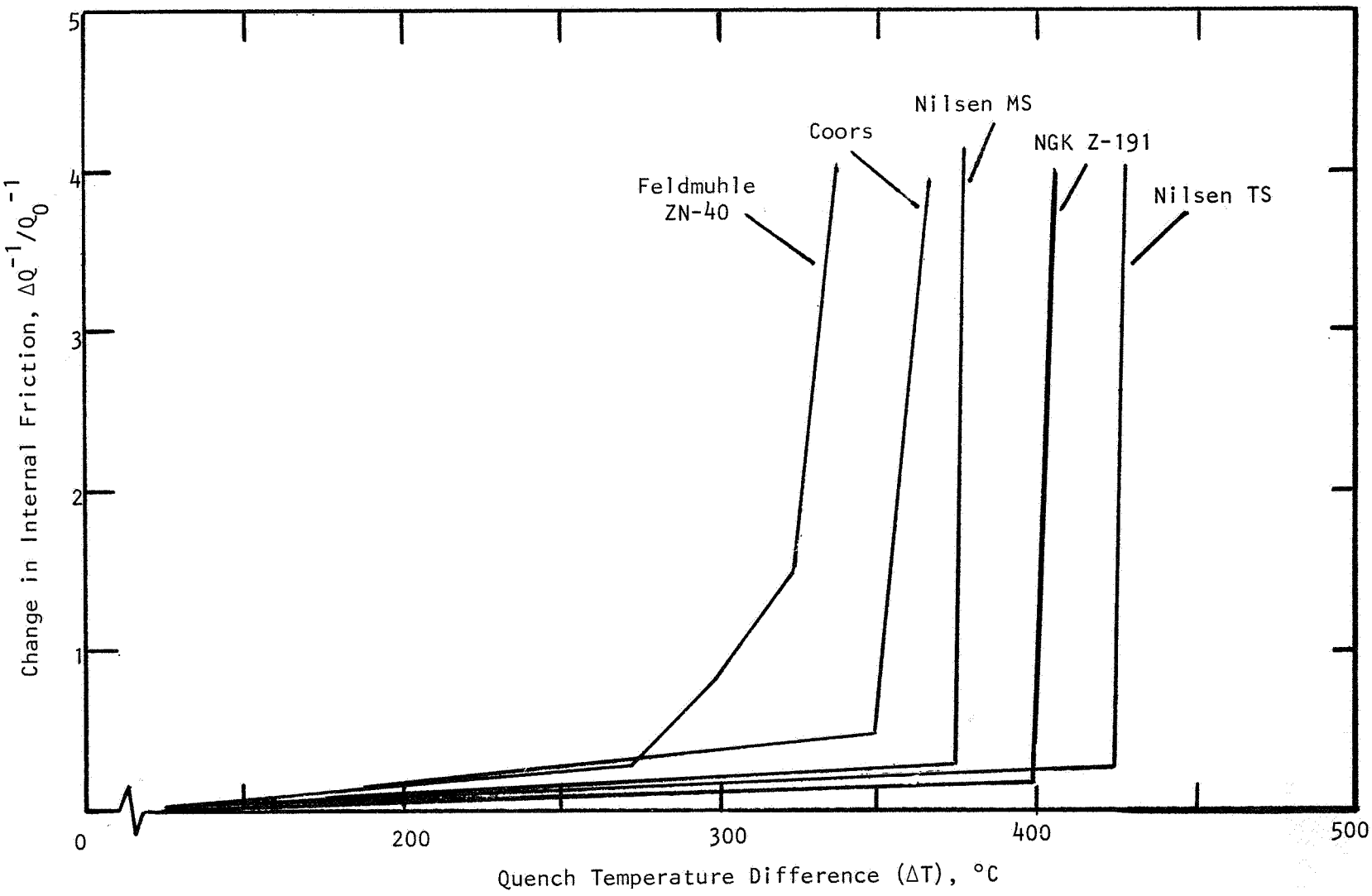

Figure 92. Representative water-quench thermal shock results for various zirconia materials.

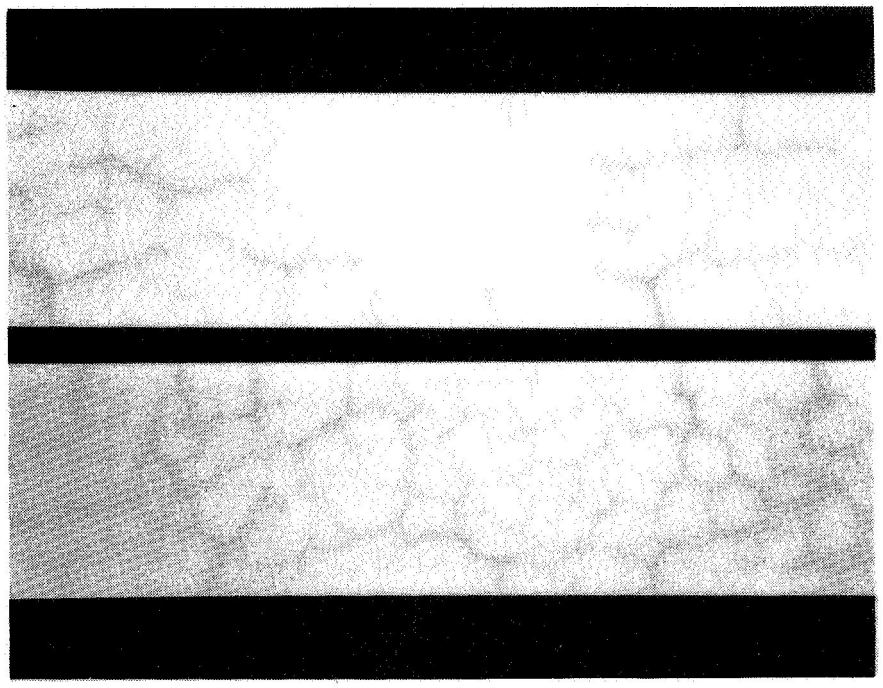

(a) MgO-stabilized zirconia (lower strength)

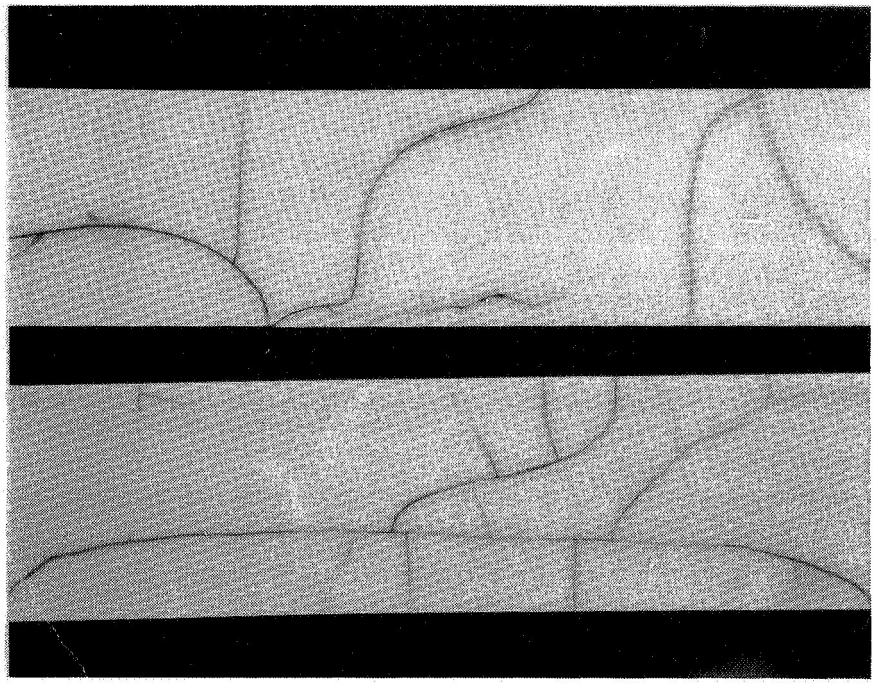

(b) Y_2O_3-stabilized zirconia (higher strength)

Figure 93. Optical photographs of zirconia test bars after water-quench thermal shock.

program, and are tabulated in Table 20. The experimentally obtained critical quench temperature values are also tabulated for each material in Table 20. The computed R parameter has the physical interpretation as the maximum ΔT allowable before thermal shock initiation. The analytical R parameter is directly compared with experimental ΔT_c values from the water quench tests in Figure 94. The trend line is a linear least-squares data fit for the four major materials investigated. Note the excellent agreement in analytical vs. experimental results. Also, note that the Nilsen TS Mg-PSZ falls distinctly away from the trend line established for the other materials.

We can attempt to explain these thermal shock results from the data we have generated. The four main materials evaluated on this program were all designed to optimize the strength and fracture toughness. The MgO-doped materials (i.e., Nilsen MS, Coors, and Feldmuhle ZN-40) consist of relatively large cubic zirconia grains (i.e., 50 μm) with a finely dispersed metastable tetragonal intragranular phase (i.e., 20-50 nm, within the large cubic grains)

TABLE 20. THERMAL STRESS RESISTANCE PARAMETERS FOR TRANSFORMATION-TOUGHENED ZIRCONIA

Material	Flexural Strength,[a] ksi	Estimated Poisson's Ratio	Thermal Expansion,[b] 10^{-6}/°C	Elastic Modulus,[c] 10^6 psi	$R = \sigma(1-\mu)/\alpha E$,[d] °C	ΔT (ΔQ^{-1}),[e] °C
Nilsen MS Mg-PSZ	92.5	0.2	8.3	29.3	304	375
Feldmuhle ZN-40 Mg-PSZ	61.8	0.2	9.1	29.8	182	325
Coors Mg-PSZ	69.9	0.2	8.7	29.5	218	350
NGK Z-191 Y-TZP	129.1	0.2	9.3	28.9	384	400
Nilsen TS Mg-PSZ	75.9	0.2	8.2	29.1	254	425

[a]All properties at 25°C unless otherwise noted; note that 4-point bend strength is used instead of the tensile strength.

[b]At 300°C, using heating cycle data.

[c]Flexural resonant frequency method.

[d]Analytical thermal stress resistance parameters; maximum ΔT allowable for steady heat flow.

[e]Critical ΔT determined either by change in internal friction or visual crack observation after water quench tests.

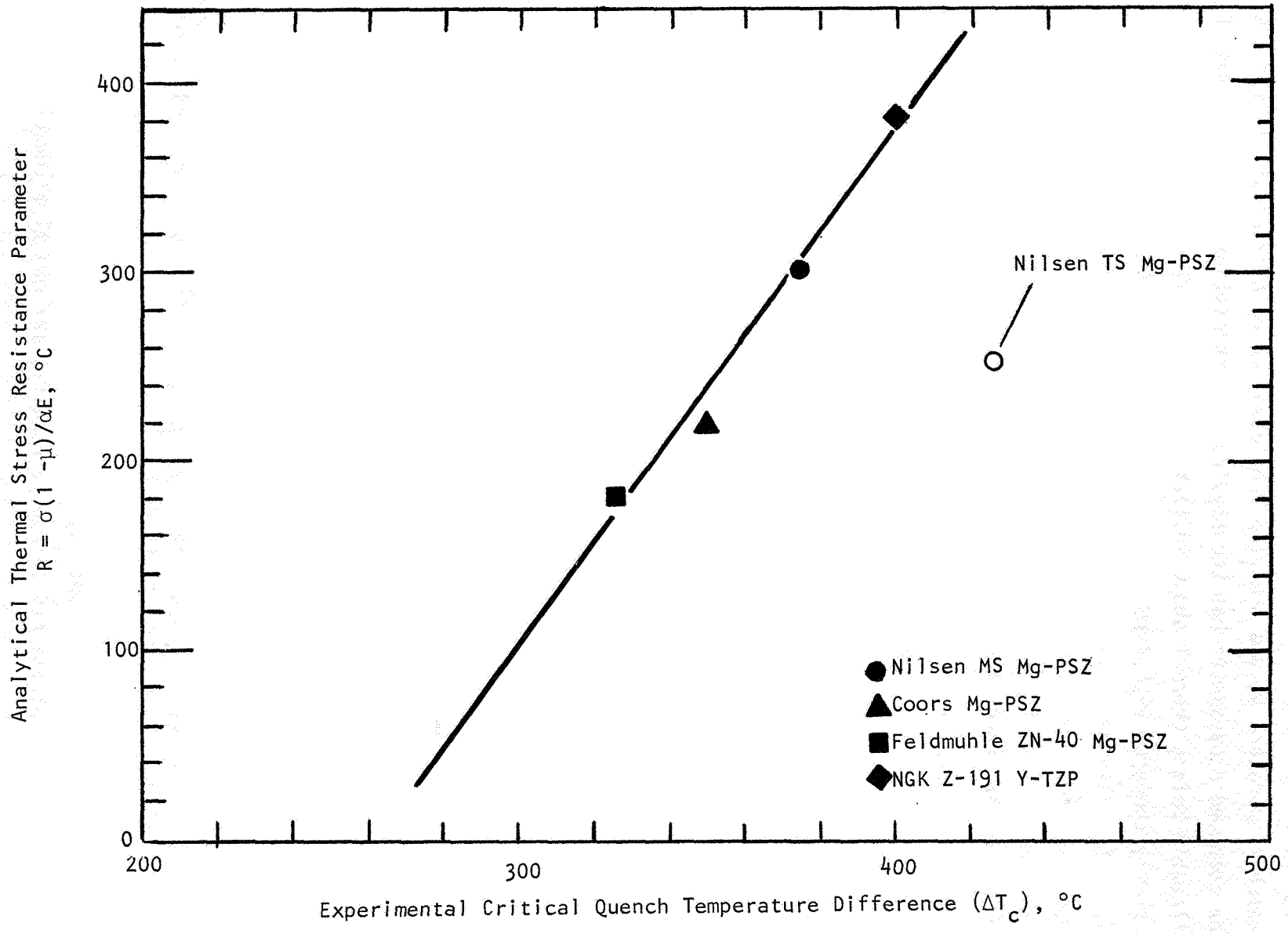

Figure 94. Analytical vs. experimental thermal shock results for transformation-toughened zirconia.

that is responsible for the toughening. The NGK Z-191 material is much finer grained, and consists of discrete tetragonal grains. Table 20 illustrates that these materials all have similar elastic moduli, slightly varying thermal expansion, and widely varying strengths. Therefore, the increasing ΔT_c shown for these materials in Figure 94 is mainly the result of their strength variation. NGK Z-191 is the strongest with the highest ΔT_c, Nilsen MS PSZ is intermediate in strength and ΔT_c, while the Coors and Feldmuhle materials exhibit the lowest strength and ΔT_c values.

The thermal shock behavior of Nilsen TS PSZ requires another explanation, however. The baseline PSZ materials that were designed for optimum toughness and strength (e.g., Nilsen MS PSZ) had poorer thermal shock resistance. The reasons for poor resistance to thermal shock in zirconia include relatively high thermal expansion in general. If higher temperatures than experienced in the water quench tests are involved, then decreasing strength and toughness with temperature also contribute to poor thermal shock resistance (strength and toughness decreasing with temperature as the tetragonal precipitates become more stable). Nilsen's TS PSZ is an attempt to improve the thermal shock resistance of transformation-toughened zirconia. Our present results illustrate their success.

The pertinent thermal and mechanical properties of the materials investigated were presented in Table 20. The strength of TS material (75.9 ksi) is lower than for MS PSZ (92.5 ksi). The elastic moduli of the two materials are virtually identical (29.1, 29.3 x 10^6 psi). At 300°C (a temperature appropriate for analysis of water quench data) the thermal expansions of these two materials are nearly the same. Simple microcracking may be ruled out as an explanation for lower strength and higher ΔT_c when compared to the MS material, since their baseline (unshocked) internal friction values are nearly the same (refer to Table 16). Thus, none of these property considerations can be used to explain the larger ΔT_c observed for the TS material (that is, the properties contained in the thermal stress initiation parameter R, where $R = \sigma[1 - \mu]/\alpha E)$.

The clue to the improved thermal shock resistance of the TS material is in its microstructure. Figure 67 presented the thermal expansion of the MS and TS grades of Nilsen PSZ. The expansion of the TS grade is lower than that

of the MS grade. This is mainly a factor at higher temperatures, and certainly will result in improved thermal shock resistance. However, note the linearity of the MS curve and the inflection in the TS curve heating cycle at ~500°C. This is a strong indication that there is significant monoclinic phase present in the TS grade. XRD analysis confirms that there is 20% monoclinic phase in Nilsen TS Mg-PSZ (as well as 56% cubic and 24% tetragonal). There is only nominally 5% monoclinic zirconia in MS grade material from Nilsen. For high strength and toughness, the presence of monoclinic ZrO_2 is undesirable. However, for thermal shock resistance alone, the monoclinic phase is beneficial. Furthermore, monoclinic zirconia results in thermal shock behavior that does not scale with the water quench thermal shock parameter describing thermal stress induced crack initiation. It appears that an analytical parameter based on propagation rather than initiation is required. The reason for this is apparently the enhanced R-curve behavior exhibited by PSZ, especially in the presence of the monoclinic phase. The term R-curve behavior is not to be confused with the thermal shock R parameters. R-curve behavior is a concept of fracture mechanics, and involves an increase in K_{Ic} with crack extension. These concepts, as applied to transformation-toughened zirconia, are beginning to appear in the literature.[27-29] The presence of monoclinic ZrO_2 in Nilsen TS PSZ explains its lower strength and increased thermal shock resistance. Monoclinic ZrO_2 was expected based on the nature of the thermal expansion curve, and its presence was confirmed by subsequent XRD analysis.

Interestingly, the thermal expansion data for Coors Mg-PSZ presented in Figure 71 showed slight evidence of a phase transformation also. It had previously been shown that substantial monoclinic phase in that material explained the poor strength retention after long-term exposure. The presence of this same monoclinic phase could be responsible for the range of ΔT_c values exhibited by the Coors material as shown in Figure 91. ΔT_c values as high as 400°C are higher than expected considering strength alone (compare inert strength and ΔT_c values obtained for the Coors and Feldmuhle materials). The presence of monoclinic zirconia in the structure of the Coors material either intentional or unintentional, would help explain this. This variability of the Coors Mg-PSZ correlates with its strength and elastic modulus variability, as discussed in Sections 4 and 5.

10.2 RESULTS FOR EXPOSED MATERIALS

Water quench thermal shock tests were also conducted after test samples had undergone a 1000 hr/1000°C static thermal exposure. The results are provided in Figures 95-98. The exposed Coors material was not subjected to the water quench tests since its post-exposure internal friction values were judged to be large enough to perhaps preclude definitive detection of subsequent changes in internal friction upon thermal shock. The microstructure was already severely damaged.

Figures 99-102 summarize the Q^{-1} vs. ΔT data for each material before and after the 1000 hr/1000°C thermal exposure. It is interesting to observe that for the Mg-PSZ materials, the critical quench temperature difference after exposure was ΔT_c = 275°C in all cases. These data are tabulated in Table 21. The 1000 hr/1000°C exposure is severe enough to bring each of the MgO-stabilized materials to equivalent levels of degradation--at least for thermal shock. Each contains significant amounts of transformed monoclinic material. The presence of a certain amount of the monoclinic phase might be expected to be beneficial to thermal shock resistance (e.g., the as-received Nilsen TS material discussed above). However, after 1000°C/1000 hr exposure, much degradation has occurred, and all MgO-stabilized materials exhibit a ΔT_c of 275°C. This may again show the controlling influence of strength on thermal shock behavior--the post-exposure bend strength of all the Mg-PSZ materials was nominally 40 ksi.

Perhaps the most surprising result of the thermal shock testing of exposed materials is the behavior of NGK Z-191 Y_2O_3-stabilized material (Figures 98 and 102). This material also exhibited a ΔT_c of 275°C, although more accurately a range from 275° to 300°C. Recall that its critical quench temperature difference was 400°C prior to the extended 1000 hr/1000°C thermal exposure (Figure 90, Table 19). Therefore, all TTZ materials, both Mg-PSZ and Y-TZP, exhibited ΔT_c = 275°C after the exposure. This is surprising for NGK Z-191 because this material experienced only a 7% strength reduction and no elastic modulus change after the exposure. Its microstructure and phase assemblage, shown in Table 3 and Figure 9, were imperceptibly affected. This is further supported by thermal expansion data that showed no detectable change in thermal expansion after the 1000 hr/1000°C exposure (Figure 68).

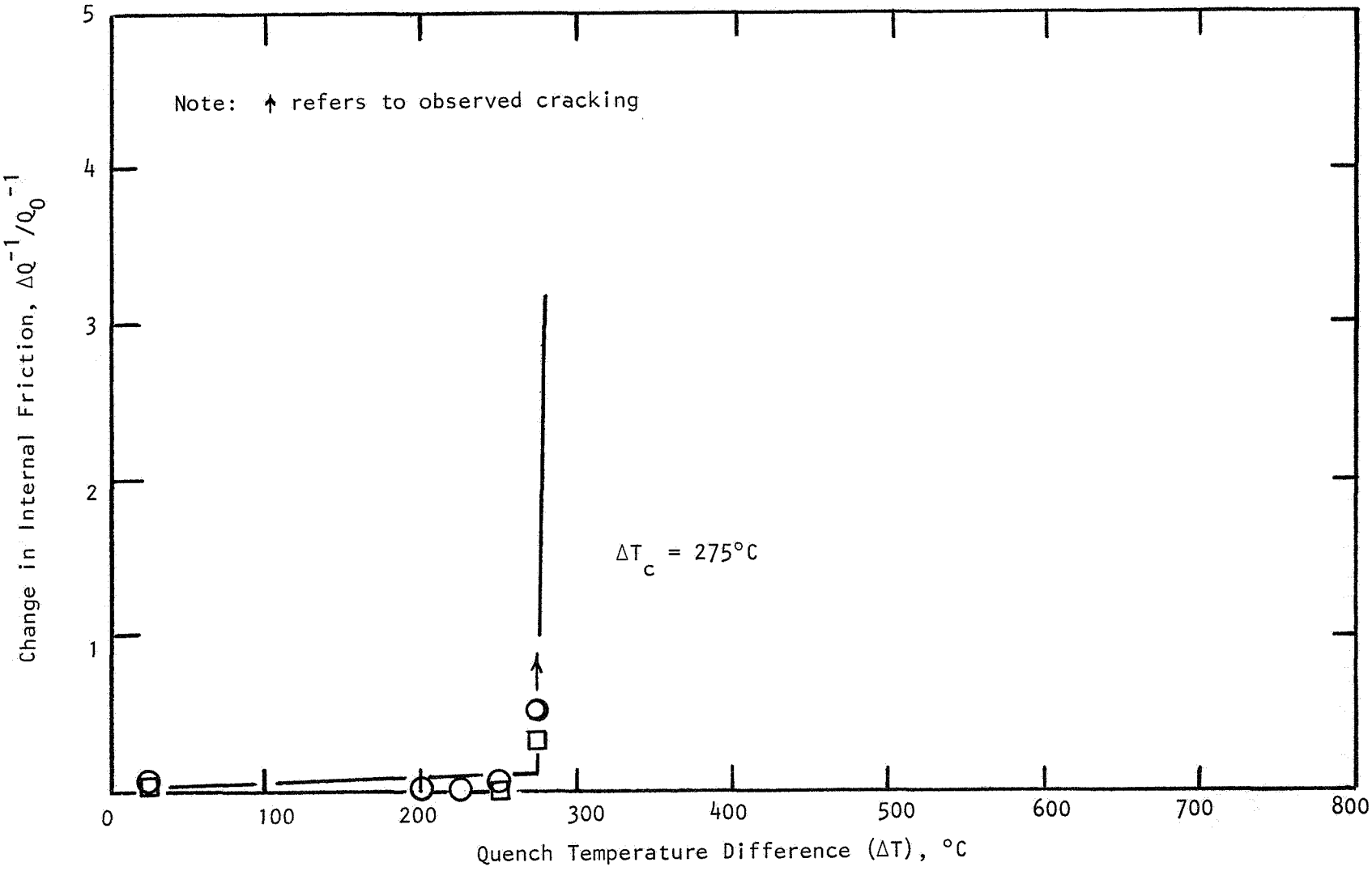

Figure 95. Water-quench thermal shock results for Nilsen MS Mg-PSZ (after 1000 hr/1000°C static exposure).

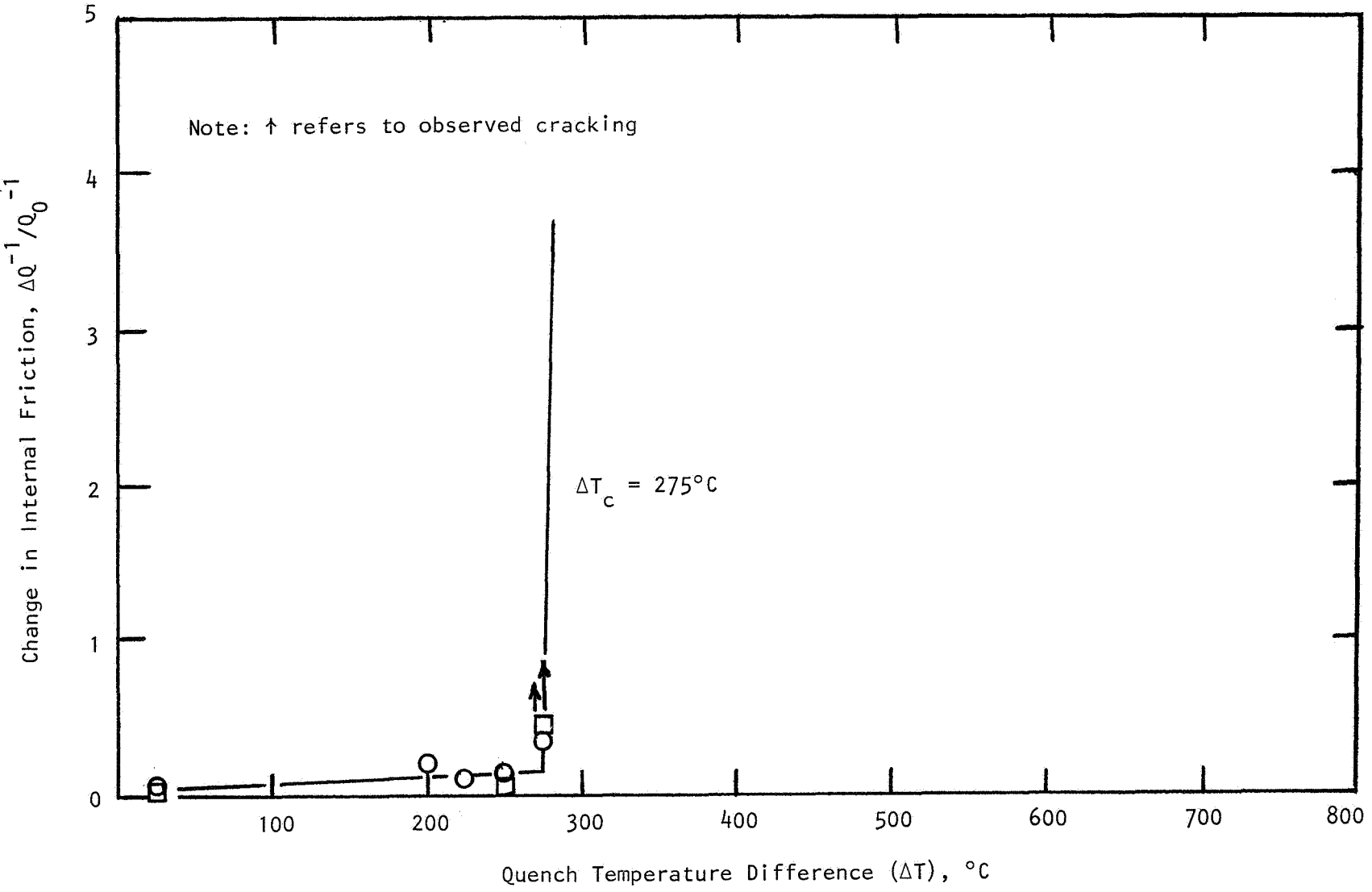

Figure 96. Water-quench thermal shock results for Nilsen TS Mg-PSZ (after 1000 hr/1000°C static exposure).

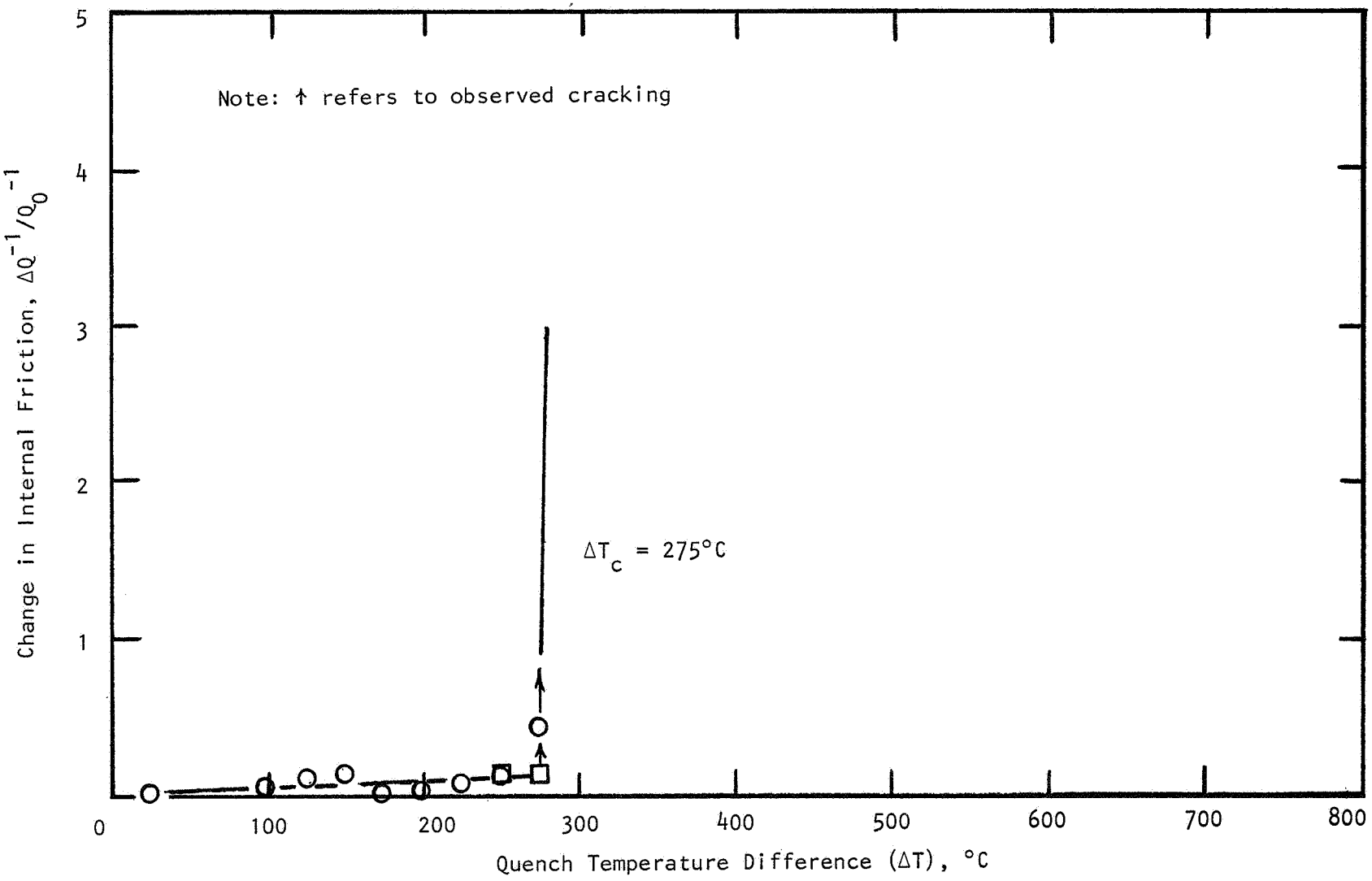

Figure 97. Water-quench thermal shock results for Feldmuhle Zn-40 Mg-PSZ (after 1000 hr/1000°C static exposure).

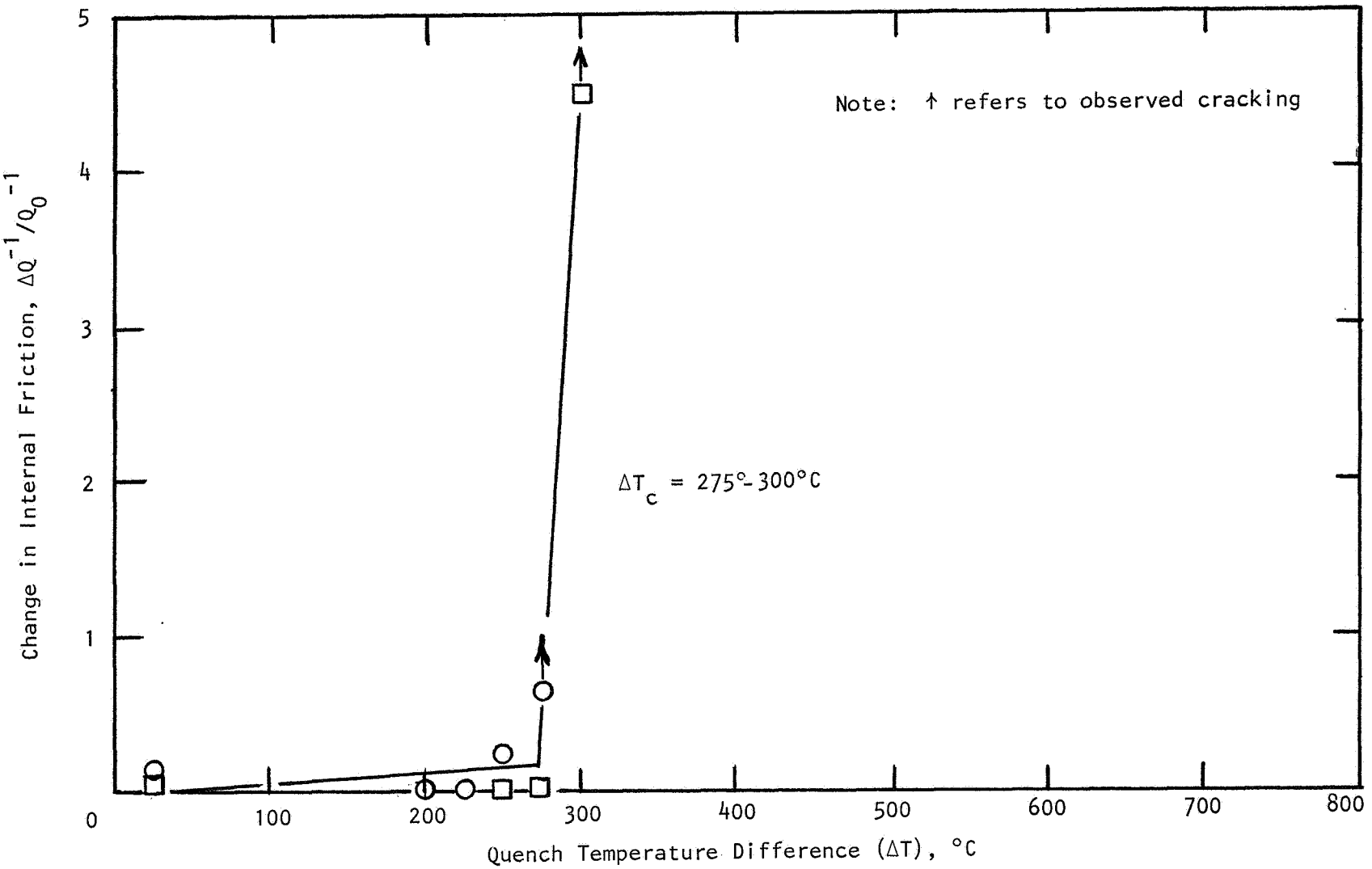

Figure 98. Water-quench thermal shock results for NGK Z-191 Y-TZP (after 1000 hr/1000°C static exposure).

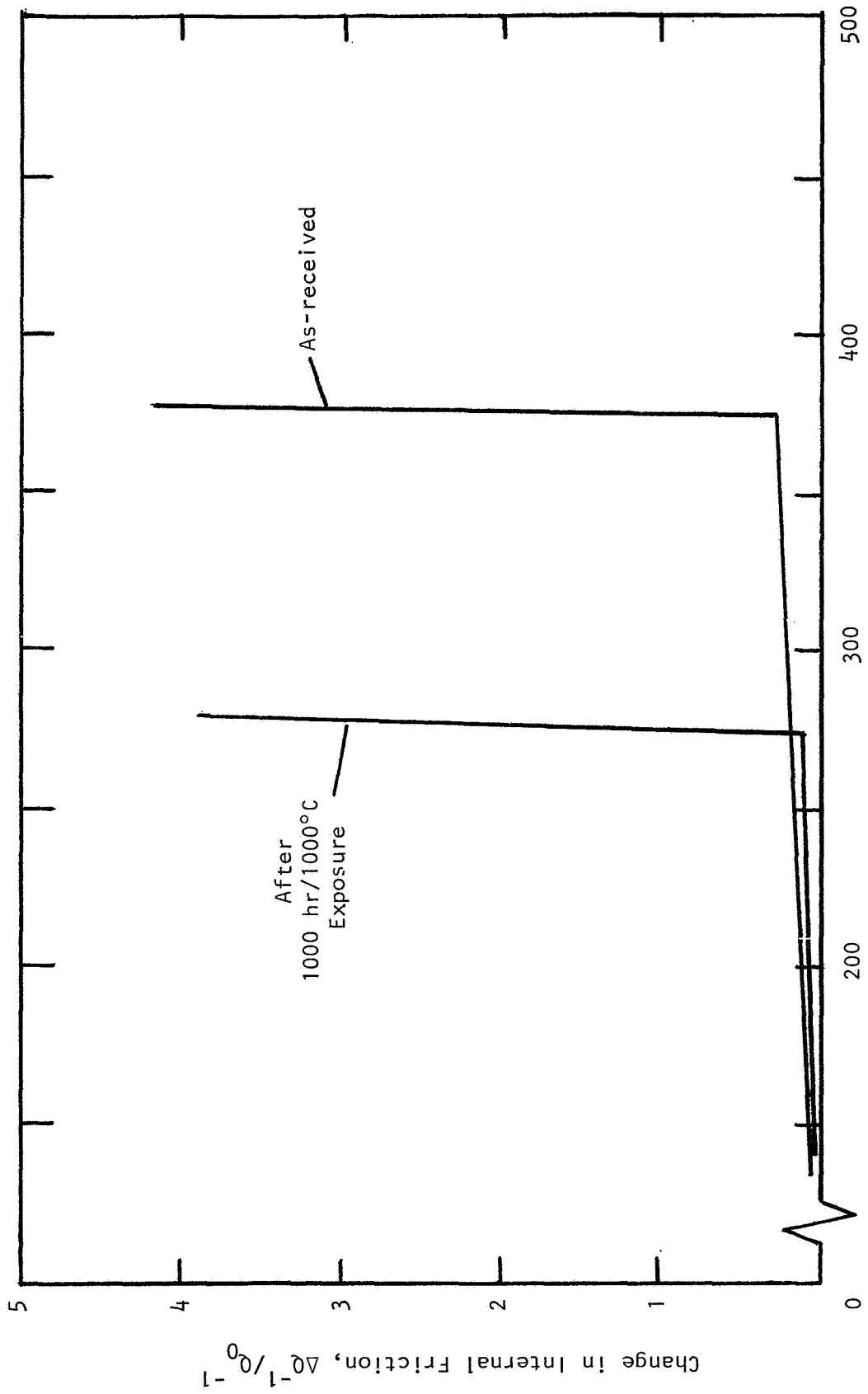

Figure 99. Thermal shock results for Nilsen MS Mg-PSZ before and after 1000 hr/1000°C exposure.

C-3

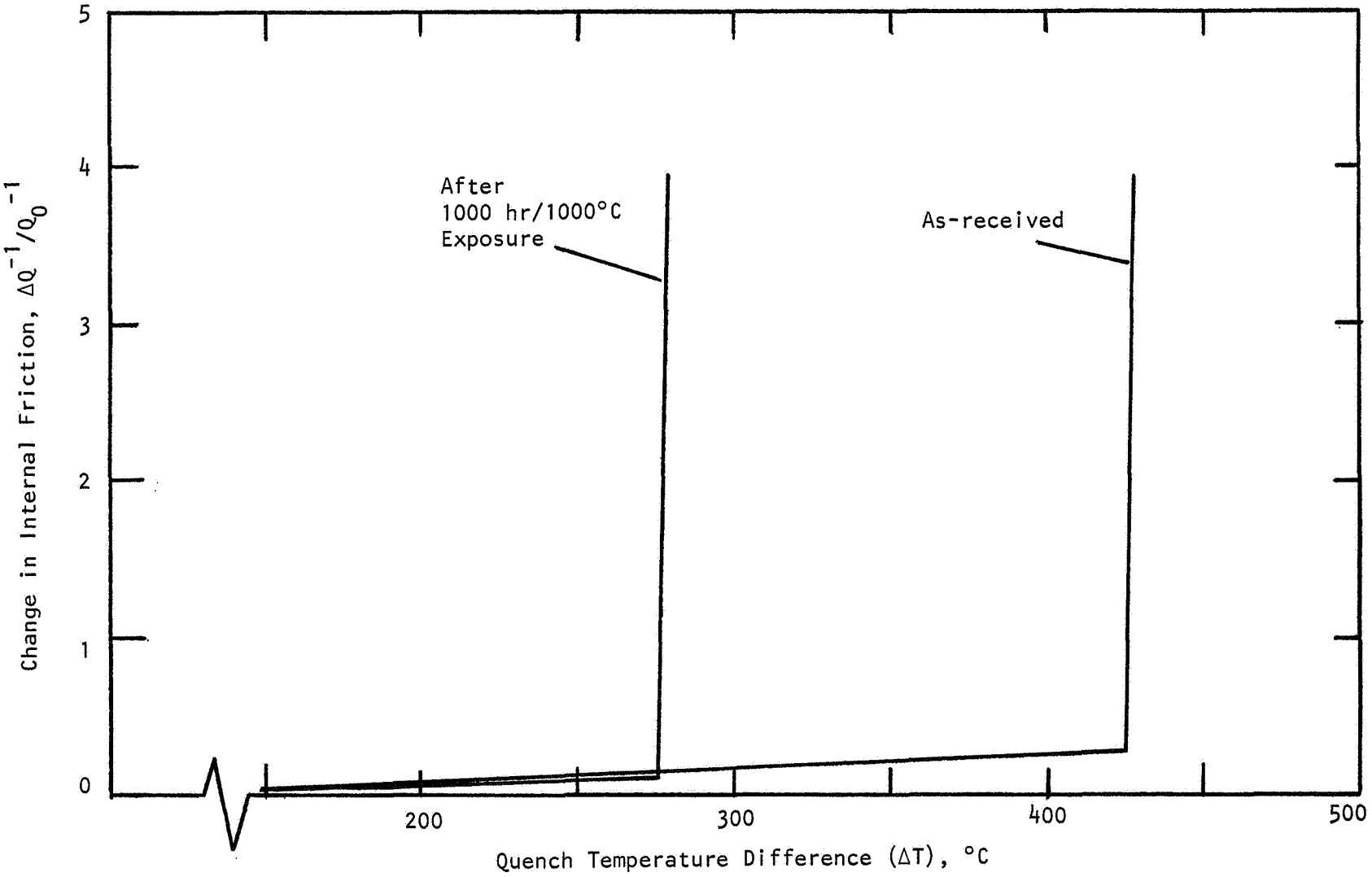

Figure 100. Thermal shock results for Nilsen TS Mg-PSZ before and after 1000 h/1000°C exposure.

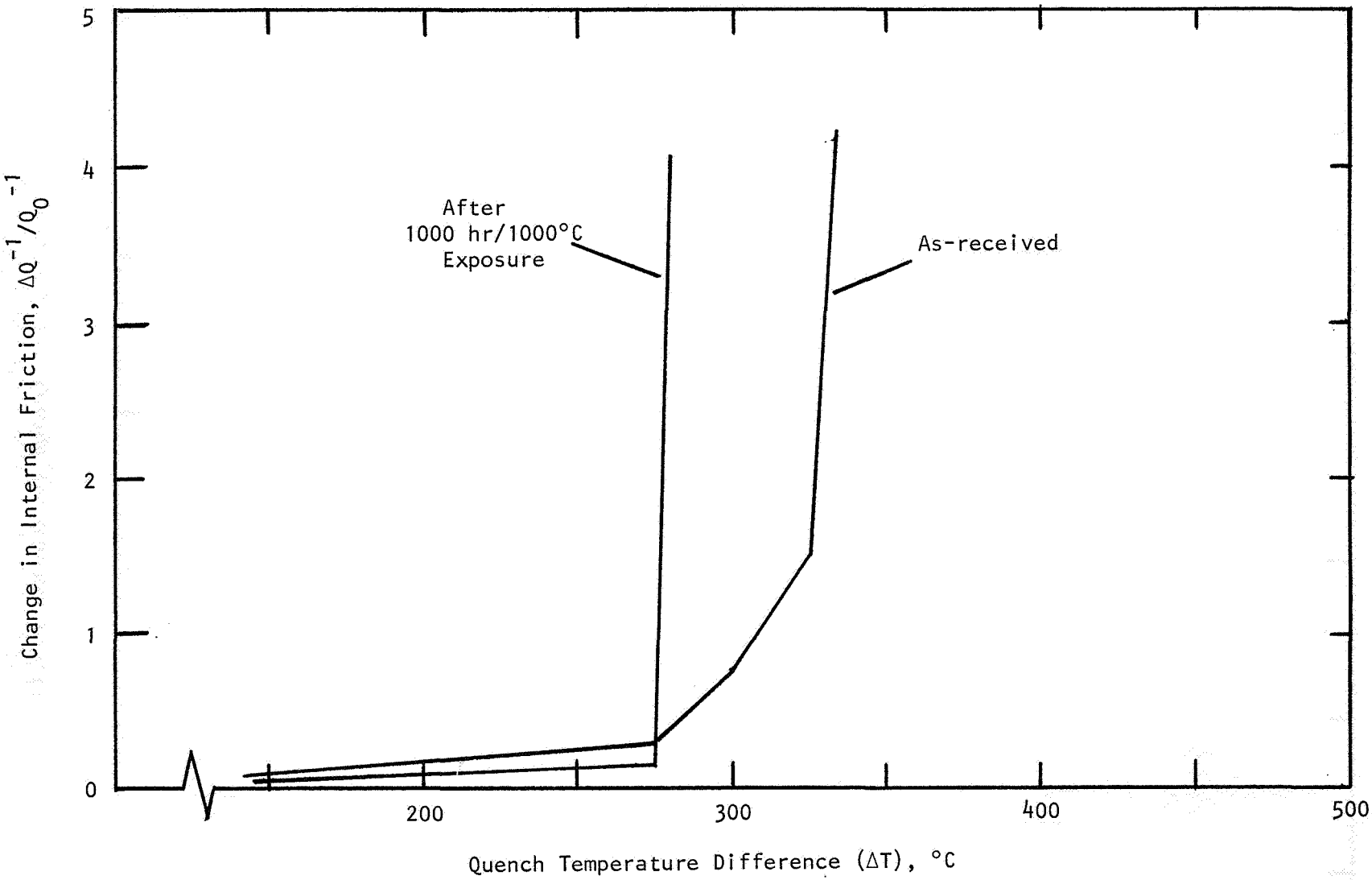

Figure 101. Thermal shock results for Feldmuhle ZN-40 Mg-PSZ before and after 1000 hr/1000°C exposure.

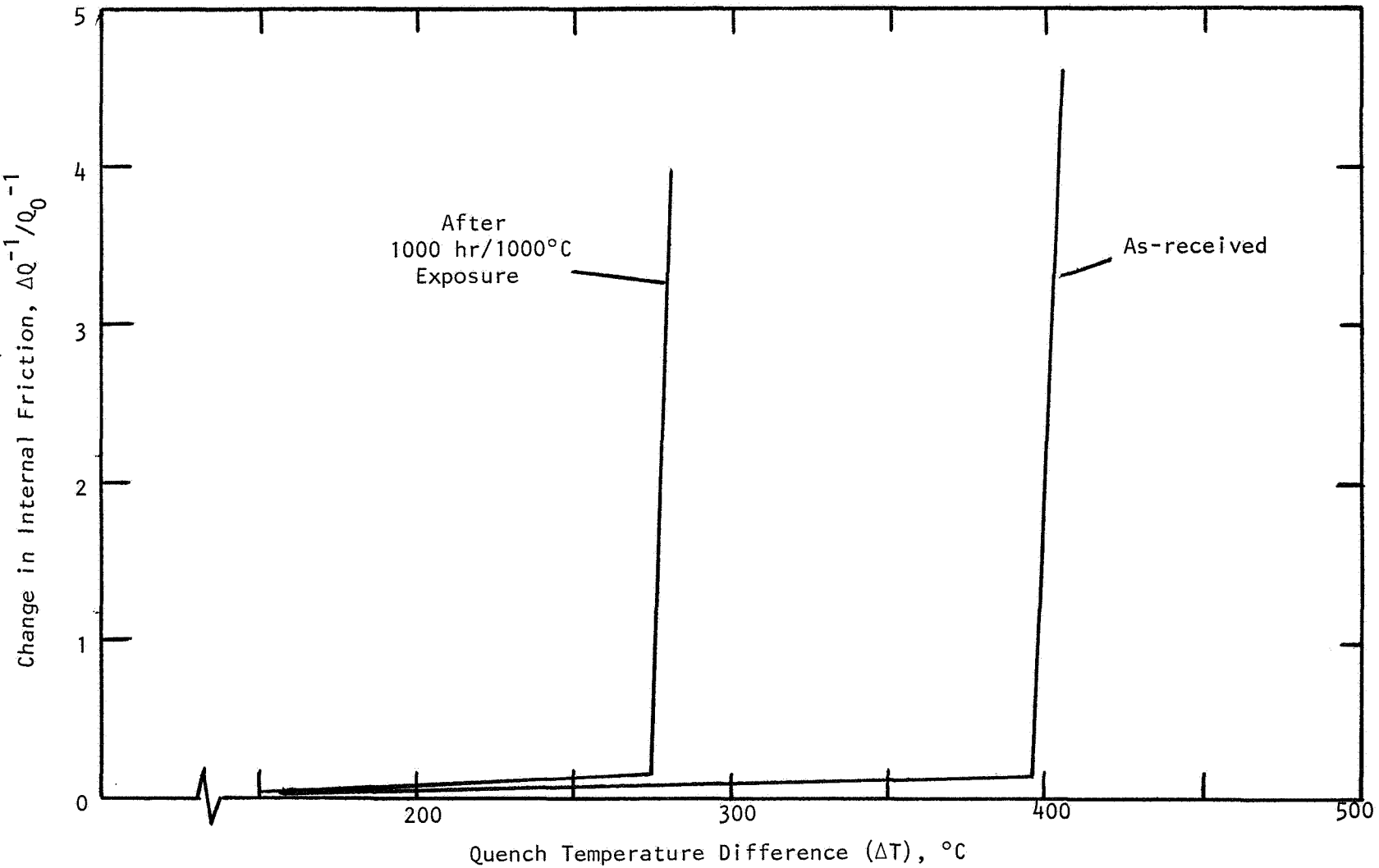

Figure 102. Thermal shock results for NGK Z-191 Y-TZP before and after 1000 hr/1000°C exposure.

TABLE 21. THERMAL SHOCK RESISTANCE OF TRANSFORMATION-TOUGHENED ZIRCONIA BEFORE AND AFTER THERMAL EXPOSURE

Material	Critical Quench Temperature Difference, (ΔT_c), °C	
	As-Received	After 1000 hr/1000°C Exposure
Nilsen Mg-PSZ		
• MS Grade	375	275
• TS Grade	425-450	275
Feldmuhle ZN-40 Mg-PSZ	325	275
NGK Z-191 Y-TZP	400	275-300
Coors Mg-PSZ	350	*

*Coors material judged too altered after 1000 hr/1000°C exposure to definitively measure ΔT_c.

That would tend to further confirm the stability of the Y-TZP microstructure, but it certainly makes interpretation of the post-exposure thermal shock behavior more difficult.

10.3 SUMMARY OF THERMAL SHOCK RESULTS

In summary, water quench thermal shock resistance in Nilsen MS, Coors, and Feldmuhle ZN-40 Mg-PSZ materials, as well as NGK Z-191 Y-TZP, is correlated with the R analytical thermal stress parameter (proportional to $\sigma\alpha^{-1}E^{-1}$) for thermal stress induced crack initiation. These materials have similar thermal expansion and elastic moduli. Resistance to thermal stress induced crack initiation is directly proportional to the tensile strength. Therefore, the NGK material exhibited the highest critical quench temperature difference, ΔT_c = 400°C. The highest thermal shock resistance was obtained for the Nilsen TS PSZ, ΔT_c = 425°-450°C. Thermal expansion results indicate and XRD analysis directly illustrates the higher monoclinic phase content for this material, the microstructure of which was optimized specifically for thermal shock. The monoclinic phase is responsible for the increased thermal shock resistance. Analytically, however, the treatment of such a material may require a thermal stress propagation parameter instead of the usual crack initiation parameter.

The current ceramic literature refers to increased R-curve behavior (increased K_{Ic} with crack extension) for such a material containing the monoclinic phase. This is apparently the reason for its success in water quench tests.

Some monoclinic zirconia in the microstructure may be beneficial, but too much is very detrimental. Test bars of all transformation-toughened zirconia samples that had been exposed to a 1000 hr/1000°C static thermal atmosphere experienced a significant decrease in resistance to sudden thermal downshock. For Mg-PSZ, this correlates with the 30-70% strength reduction resulting from overaging. The loss of thermal shock resistance for the Y-TZP (i.e., NGK Z-191) is not so readily understood since its phase assemblage, microstructure, and mechanical properties were otherwise unaffected by the 1000 hr/1000°C exposure.

ORIGINAL PAGE IS
OF POOR QUALITY

11. THERMAL DIFFUSIVITY

Thermal diffusivity is defined as the ratio of the thermal conductivity to the density-specific heat product. It is of obvious interest for materials being considered for use in the hot-section of the adiabatic diesel engine.

Thermal diffusivity was measured at room temperature (both before and after 1000 hr/1000°C static exposure) by the laser pulse method.[30] The sample was supported by a minimum contact porous zirconia sample holder. The front face of the disk-shaped sample (9/16 in. dia x 0.050 in. thick) was irradiated with a single pulse of laser energy, and the resulting sample rear face temperature transient detected and recorded as shown in Figure 103. Calculation of the thermal diffusivity was made from this temperature-time response. The laser used was a 3 joule Korad K-1 pulsed ruby laser operating at 6943 Å (random lasing, non-Q-switched mode). The pulse duration was nominally 1 msec, which was two orders of magnitude shorter than the transit time for

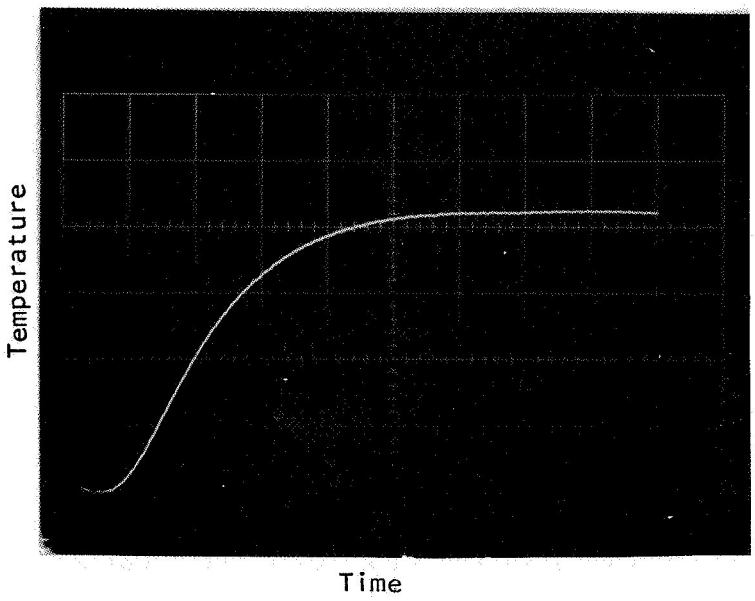

Figure 103. Sample rear face temperature transient in laser pulse method for thermal diffusivity measurement.

PRECEDING PAGE BLANK NOT FILMED
PAGE 186 INTENTIONALLY BLANK

thermal diffusion through the sample, thereby making finite pulse time corrections unnecessary. Fully dense zirconia is translucent at the 0.69 μm wavelength of the laser; this must be considered when using this measurement method since a required boundary condition is that the laser energy be absorbed on the front surface only, or at least in a thickness very small compared to the sample thickness. To accomplish this, a ~0.8 μm thick platinum coating was applied to the zirconia sample front surface by electron-beam evaporation. Additionally, a thin graphite coating* was applied to the front sample surface to increase laser absorption. The sample rear face temperature transient was detected with a liquid nitrogen-cooled indium antimonide infrared detector (Texas Instruments ISV 3105) which is extremely sensititive at long wavelengths corresponding to ambient temperature measurement. The thin graphite film was also applied to the zirconia sample rear surface to avoid below-surface viewing by the detector. Initial time, t_o, for the measurement was determined when lasing occurred through the use of an auxiliary photodiode system monitoring the ruby laser performance.

Thermal diffusivity, α, was computed from the expression:

$$\alpha = \frac{0.1388\ L^2}{t_{1/2}}$$

where L = sample thickness, cm

$t_{1/2}$ = time for rear face temperature to reach half its maximum value.

In making this measurement, it was found necessary to operate the laser at power levels lower than ~75% peak to avoid peeling off the thin Pt coating.**

*"dgf 123," Miracle Power Products, Cleveland, Ohio.

**Additionally it is noted with interest that when an Mg-PSZ sample was repeatedly irradiated with the ~3 kW peak laser pulse, surface damage occurred that consisted of craze cracking of a characteristic size on the order of the grain size, as well as raised areas (i.e., uplifted grains) that might be interpreted as indirect evidence of volume increase associated with a tetragonal to monoclinic phase transformation being activated by the incident laser energy.

TABLE 22. THERMAL DIFFUSIVITY OF TRANSFORMATION-TOUGHENED ZIRCONIA

Material	Room-Temperature Thermal Diffusivity, $cm^2\ sec^{-1}\ (10^{-3})$	
	As-Received[a]	Exposed 1000 h/1000°C[a]
NGK Z-191 Y-TZP	11.1, 11.4	11.7, 11.5
Nilsen MS Mg-PSZ	11.0, 11.1	12.5, 12.4
Feldmuhle ZN-40 Mg-PSZ	10.9, 11.0	12.2, 11.6
Coors Mg-PSZ	10.8, 11.0	15.3, 10.4

[a]Numbers in table are for replicate samples; note that as-received and exposed samples were from different sample sets (i.e., a given sample was not measured in both virgin and exposed conditions).

Thermal diffusivity results for the four transformation-toughened zirconia materials studied are provided in Table 22. The thermal diffusivity of zirconia is very low--nominally 11 x 10^{-3} $cm^2\ sec^{-1}$. Hence, its utility as a thermal insulator for minimum heat rejection or adiabatic diesel engine hot-section components. In general, thermal diffusivity can be affected by porosity, grain size, degree of microcracking, dopant, and crystalline phase. However, for the Mg-PSZ and Y-TZP materials studied, the thermal diffusivity for as-received material varied only ±3%. The thermal diffusivity of NGK Y-TZP was nominally 2% higher than that of the three Mg-PSZ materials. This correlates to its nominally 2% higher density. Apparently, the widely different grain size, dopant, and phase content of Mg-PSZ and Y-TZP do not affect the thermal diffusivity. In other words, thermal diffusivity is not a strong function of crystalline phase in zirconia implying that cubic and tetragonal forms have similar diffusivities. The apparent insensitivity to grain size is not completely understood at present. Therefore, in the as-received condition, commercially available transformation-toughened zirconia materials have nominally equivalent values of thermal diffusivity (and thus also thermal conductivity, since the densities are similar and the specific heat is not expected to vary significantly).

After 1000 h/1000°C static thermal exposure, the thermal diffusivity of the transformation-toughened zirconia materials was more variable, and increased slightly--from nominally 3% increase for NGK Z-191 Y-TZP to nominally

9% and 13% increases for Feldmuhle ZN-40 and Nilsen MS Mg-PSZ materials, respectively. The average value for exposed NGK Z-191 Y-TZP was 11.6 x 10^{-3} cm^2 sec^{-1}, whereas the average value for the exposed Nilsen and Feldmuhle Mg-PSZ materials was 12.2 x 10^{-3} cm^2 sec^{-1}. This increase in thermal diffusivity with the 1000 h/1000°C thermal exposure for the Mg-PSZ materials correlates with the increase in monoclinic content and associated microcracking that result from the degradation processes involved in long-term exposure in magnesia-stabilized PSZ (e.g., decomposition and phase change caused by destabilization and overaging). The thermal diffusivity of the Coors Mg-PSZ, however, increased by as much as 40% (to 15.3 x 10^{-3} cm^2 sec^{-1}) upon the 1000 hr/1000°C static thermal exposure. Also, the Coors material was more variable after exposure. These data correlate with observations of other properties of exposed Coors Mg-PSZ made previously.

It is important to note that when making the laser flash thermal diffusivity measurement on the exposed Mg-PSZ materials, it was necessary to employ heat loss correction methodology to the data reduction procedure. One of the boundary conditions employed to obtain the ideal analytical solution to the conditions of the laser pulse measurement is that there are no heat losses that would alter the shape of the temperature transient. This boundary condition is often violated by radiation transfer at high tempratures.

Taylor[31] discusses a convenient correction for this effect based on Cowan's original work.[32] This correction involves comparison of the shape of the experimentally obtained temperature transient at times out to ~$5t_{1/2}$ to the shape of the ideal rear face temperature transient obtained from the ideal analytical solution (the general shape of the rear face temperature transient is independent of sample thermal diffusivity). This correciton is common in elevated temperature measurement at T > 1000°C. However, for the present low diffusivity materials it was found to be required (about a -7% effect) for the exposed Mg-PSZ materials. Therefore, the apparent increased radiation contribution for exposed Mg-PSZ would suggest that the increase in thermal diffusivity observed upon 1000 hr/1000°C exposure is due more to the degree of increased microcracking that accompanies any degradation than to any grain size changes or increase in the monoclinic zirconia content per se. In other words, the thermal diffusivity of monoclinic zirconia may not be higher than that of tetragonal and/or cubic zirconia (present prior to degradation), but

rather the increase in thermal diffusivity upon degradation is the result of increased microcracking in severely degraded materials.

From the point of view of thermal design with transformation-toughened zirconia for adiabatic diesel engine applications, it is noteworthy that there is no thermal benefit of Y-TZP over Mg-PSZ--both forms of transformation-toughened zirconia have nominally equivalent values of (room temperature) thermal diffusivity. The increase in thermal diffusivity for Mg-PSZ upon long-term degradation, however, is typically nominally 10-13% but can be as high as 40%. This will certainly affect the thermal performance of the adiabatic system (if not first noticeable in the decreased mechanical performance due to the concurrent drastic decreases in strength and toughness associated with the degradation).

12. STRESS RUPTURE/STATIC FATIGUE

Another aspect of the long-term stability of transformation-toughened zirconia was examined--static fatigue. It was of interest to learn the possible time dependence of strength (at stress levels below the fast fracture strength) during extended static exposure at 1000°C. Basically, a constant flexural stress was applied to the test sample at 1000°C, and the failure time recorded. This is referred to as a stress rupture or a static fatigue test (as opposed to dynamic fatigue, where in input stress is time dependent, or cyclic mechanical fatigue).

Several forms of static fatigue have been identified for structural ceramics in general, and silicon-base ceramics (e.g., SiC and Si_3N_4) in particular. The behavior found for zirconia will be compared to the more established data base for silicon-base ceramics. Static fatigue can have a variety of origins and mechanisms, either acting singly or simultaneously operable. For instance, static fatigue can be the result of stress corrosion, which is environmentally assisted strength degradation. Another form is creep fracture, which is diffusion and cavitation-related deformation that results in the formation of extensive microcrack networks. A third form of static fatigue is subcritical crack growth, or the extension of flaws, such as triple point voids, with time. A common cause is grain boundary sliding, or the relative movement of grains surrounded by thin deformable intergranular films. Static fatigue, or strength degradation with time, can also be related to high temperature oxidation or gaseous corrosion mechanisms where the intrinsic volume-distributed flaw population is changed to a surface-related critical flaw population.

For transformation-toughened zirconia, the additional mechanism of phase transformation must be considered when interpreting static fatigue. The goal of the present experiments was to test the materials at 1000°C at applied loads that were lower than the fast fracture strengths at 1000°C. In this manner, we could possibly determine the existence of time-dependent mechanisms of strength reduction other than the primary phase transformation.

PAGE 192 INTENTIONALLY BLANK PRECEDING PAGE BLANK NOT FILMED

The results are presented in Figure 104, where the failure time is plotted for various initial applied stress levels. For NGK Z-191 Y-TZP, the fast fracture strength at 1000°C was 40.3 ksi. Attempts were made to measure the failure times of two samples loaded to 90% of the fast fracture strength (i.e., 36.4 ksi). One sample failed just after loading, and the other failed in nominally 2.3 hr, as shown in Figure 104. To extend this to longer times, the applied stress was then reduced to nominally 80% and 70% of the 1000°C fast fracture strength. As shown in Figure 104, both of these tests were terminated (after 106 and 189 hr, respectively) due to excessive sample deformation. A photograph showing the superplastic behavior is provided in Figure 105. The relatively poor creep resistance of NGK Z-191 Y-TZP was discussed in Section 8, and is a result of the fine grain structure of this material and/or a SiO_2-rich intergranular phase that deforms at elevated temperature. The excessively deformed TZP samples were inked to decorate any cracking, and examined in the low magnification optical binocular microscope. No evidence of creep fracture was observed on the tensile surfaces.

The 1000°C static fatigue results for the Mg-PSZ materials from Nilsen, Feldmuhle, and Coors, however, gave much different results, as shown in Figure 104. The Coors Mg-PSZ survived $\sigma = 0.8\sigma_f$ (i.e., 80% of the 1000°C fast fracture strength) for over 1600 hr without failure. The Coors sample with an applied load of $\sigma = 0.9\sigma_f$ survived over 1500 hr without failure. However, in both instances, the test termination procedure involved furnace-cooling under load, and both samples failed in 2-4 hr during the furnace cool-down.

For the Nilsen MS Grade Mg-PSZ samples, the same phenomenon was observed. Test samples survived a static load, σ, of $0.8\sigma_f \leq \sigma \leq 0.9\sigma_f$ for 1325 and 1510 hr, respectively. Failure then occurred in 1-3 hr while cooling under load from the 1000°C test temperature.

Similar results were obtained for Feldmuhle ZN-40 Mg-PSZ at an applied stress of $0.9\sigma_f$. The test sample survived for 2350 hr at 1000°C under the applied load, only to fail in less than 2 hr while furnace-cooling under load. Static fatigue testing at $0.8\sigma_f$ applied load (i.e., 24.6 ksi) was conducted successfully for 1610 hr for Feldmuhle ZN-40, and this sample was the only one to survive the furnace cooling without incident. The residual strength of that sample was 31.3 ksi. Note that the Feldmuhle material was

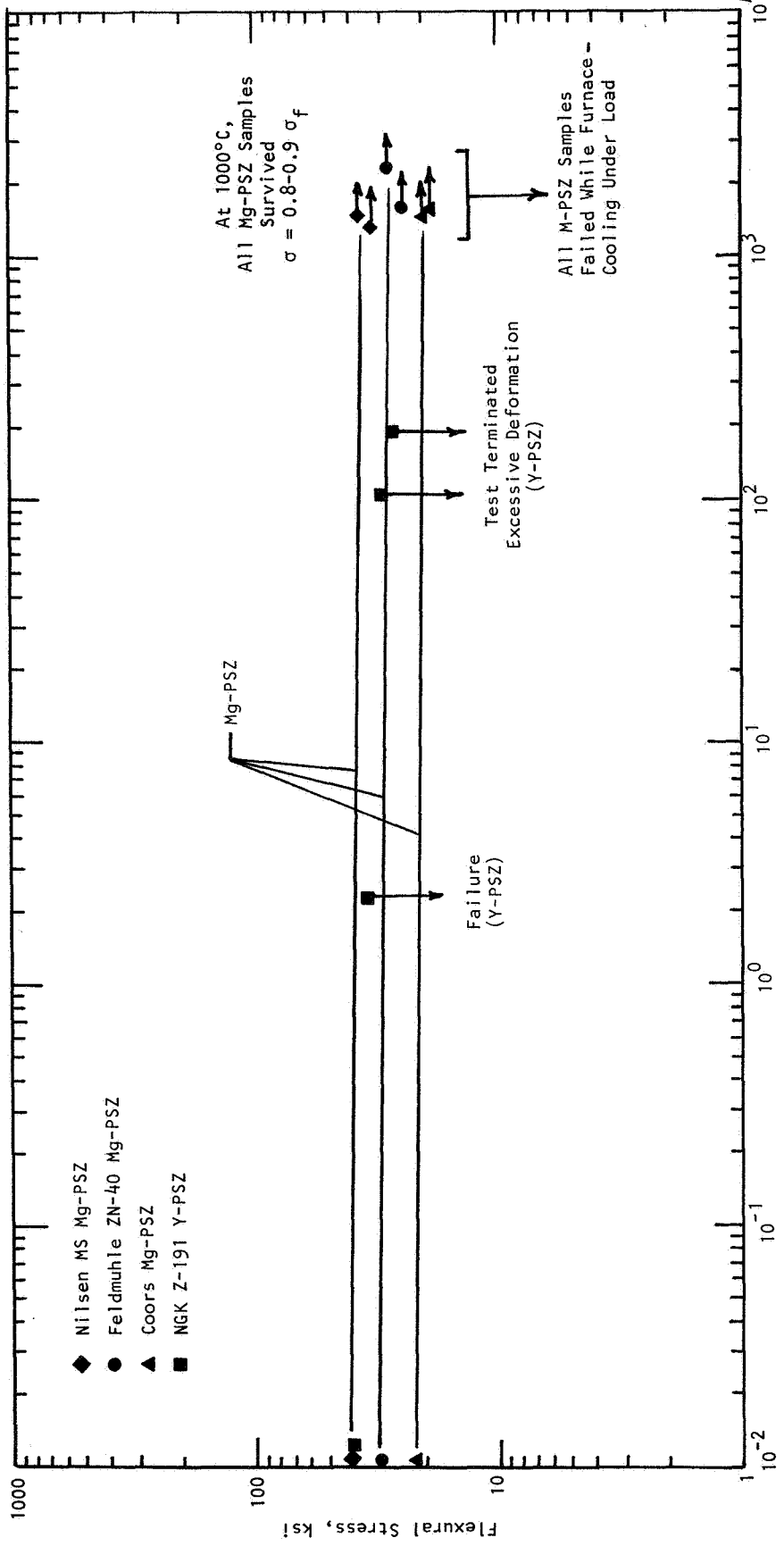

Figure 104. Static fatigue behavior of transformation-toughened zirconia at 1000°C.

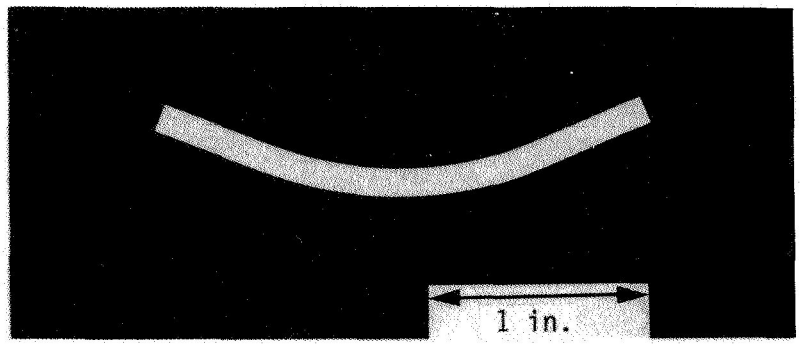

Figure 105. Deflection of NGK Z-191 bend specimen after 1000°C static fatigue test of 189 hr at 28.1 ksi, a stress level that corresponds to ∿70% of the fast fracture strength at 1000°C.

previously found to be less affected by the exposure in terms of its phase assemblage, microstructure, and residual strength. The fact that it was the only Mg-PSZ to survive the static fatigue test correlates with this.

The survival of the Mg-PSZ materials at 1000°C for periods of nominally 2000 hr under applied loads of up to 90% of the fast fracture strength at that temperature is encouraging. This means that classic static fatigue mechanisms such as discussed above may not be operable and performance-limiting in transformation-toughened zirconia. Instead, the problem is in the fractures observed (almost universally) as the test samples furnace-cooled from 1000°C while under load. This will be shown to be the result of a major tetragonal-to-monoclinic phase transformation. It should be noted that the failures were not caused by thermal shock since the samples were furnace-cooled very slowly. Similarly, the fractures were not caused by stresses originating from any possible thermal expansion mismatch between the specimen and loading fixture (SiC). This view is based on the fact that all fractures occurred at the midspan of the specimens, far from any SiC pins.

All Mg-PSZ fractures occurred in ~2-4 hr after terminating the 1000°C static fatigue test. A subsequent cooling rate measurement for the furnace used in this static fatigue test illustrated that the fractures occurred at a temperature almost precisely equivalent to the M_s temperature of each Mg-PSZ. This is illustrated in Figures 106 and 107 for the Coors and Feldmuhle Mg-PSZ materials, where the furnace cooling curve is superimposed on the thermal expansion curve that would be roughly equivalent to the microstructural state of Mg-PSZ after the 1500-2000 hr exposure at 1000°C in the static

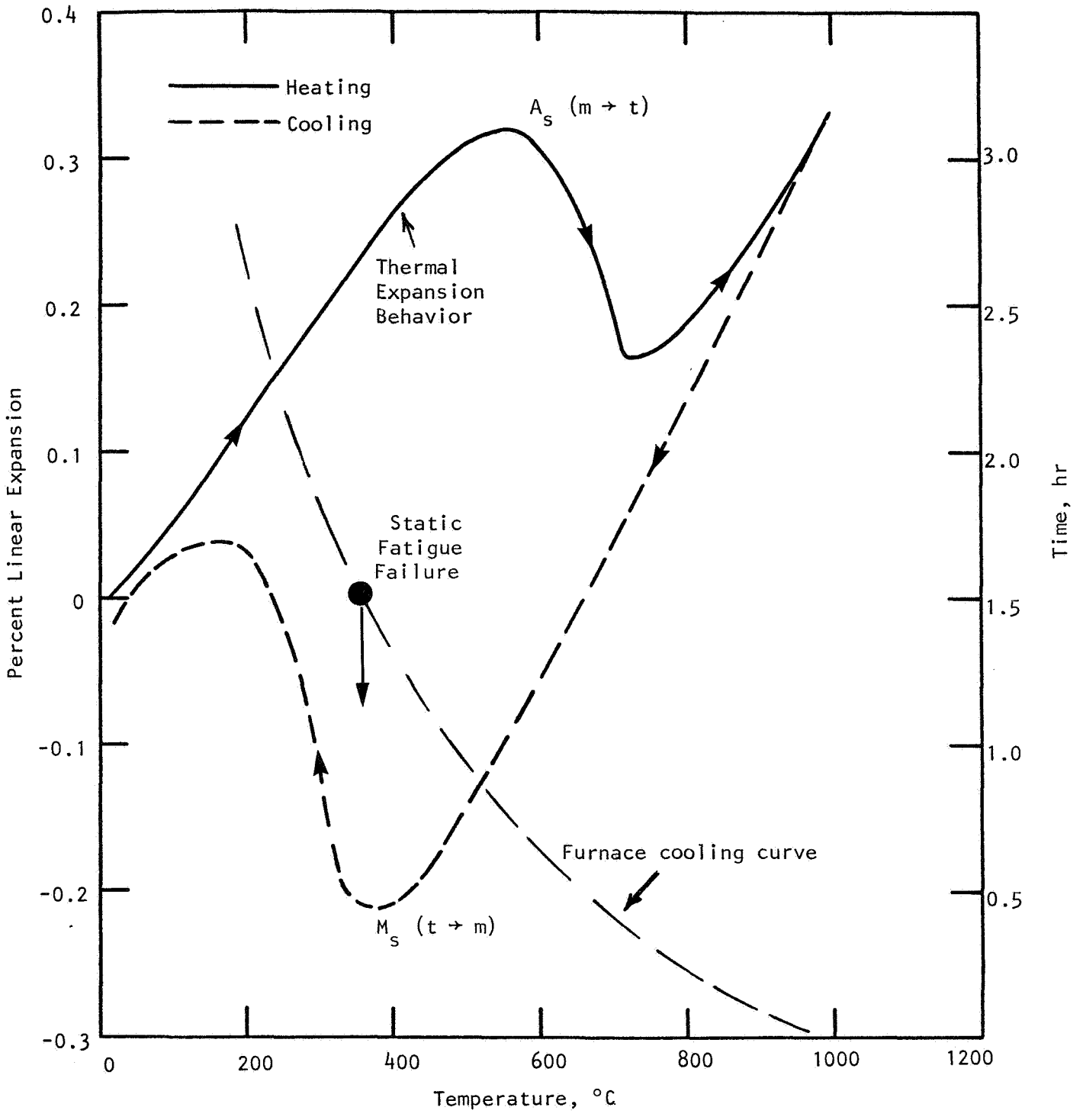

Figure 106. Furnace cooling curve superimposed on Coors Mg-PSZ thermal expansion curve, illustrating that failure at conclusion of static fatigue test occurred as the M_s temperature was passed through.

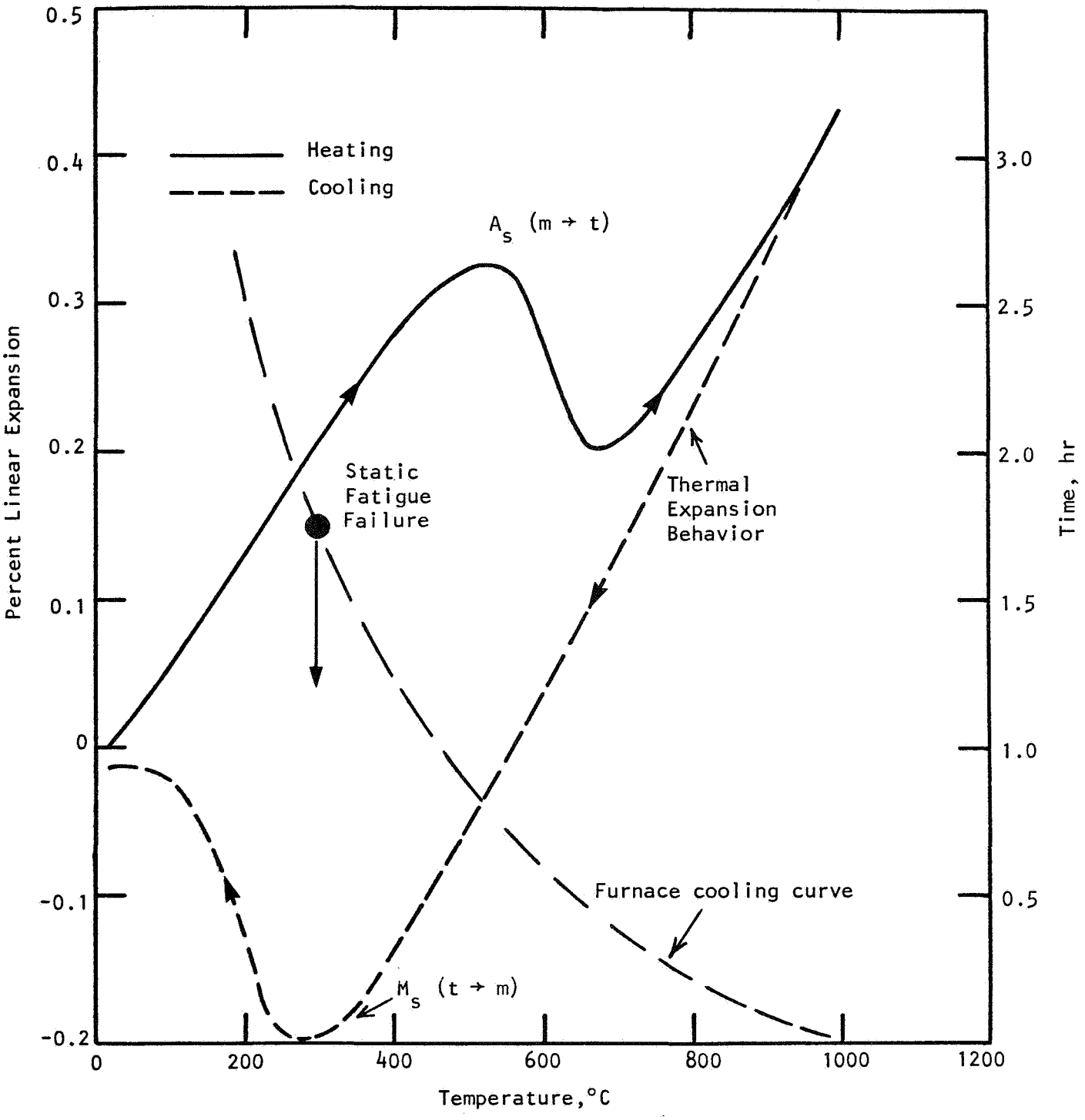

Figure 107. Furnace cooling curve superimposed on Feldmuhle ZN-40 Mg-PSZ thermal expansion curve, illustrating that failure at conclusion of static fatigue test occurred as the M_s temperature was passed through.

fatigue test. The M_s temperature is where the tetragonal → monoclinic phase transformation occurs upon cooling, and is identified on the expansion (contraction) curve in Figures 106 and 107. The time of fracture was recorded. When this time is placed on the furnace cooling curve, it is noted that fracture occurred precisely as the M_s temperature was passed through. Therefore, all Mg-PSZ samples survived the ~2000 hr/1000°C static fatigue, only to fracture upon cooling at the M_s temperature (~300°-400°C).

The microstructural state of the Mg-PSZ materials after the static fatigue test is illustrated in Figure 108, showing Nilsen MS material after 1508 hr at 1000°C at a constant stress corresponding to 0.9 σ_f. The severe degradation is evident. Subsequent XRD phase analysis of this sample indicated the phase composition to be 92% monoclinic, 5% cubic, and 3% tetragonal. Obviously, the degradation involves a combined overaging, destabilization, and decomposition effect. The structure was almost completely converted to monoclinic. Table 23 summarizes the pertinent strength data and stress

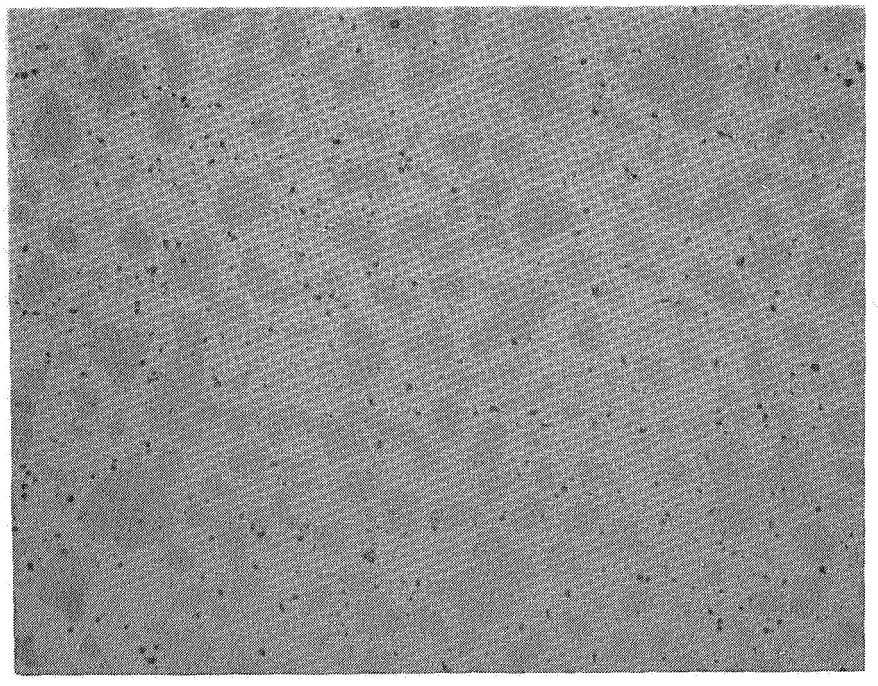

200X

Figure 108. Microstructure of Nilsen MS Mg-PSZ after 1508 hr static fatigue test at 1000°C at a stress corresponding to 0.9 σ_f. XRD analysis indicates a phase composition consisting of 92% monoclinic, 5% cubic, and 3% tetragonal. Combined overaging, destabilization, and decomposition effect.

TABLE 23. FLEXURE STRENGTH AND STATIC FATIGUE STRESS LEVELS FOR ZIRCONIA

Material	4-Point Bend Strength, ksi				
	As-Received 1000°C Fast Fracture Strength[a]	Residual 25°C Strength After 1000 hr/1000°C Exposure[a]	Static Fatigue Applied Stress,[b] ksi		
			$0.7\sigma_f$	$0.8\sigma_f$	$0.9\sigma_f$
Nilsen MS Mg-PSZ	38.5-44.1 (41.6)	34.2-48.9 (39.4)	--	33.2	37.5
Feldmuhle ZN-40 Mg-PSZ	29.1-32.7 (30.9)	40.9-45.4 (43.2)	--	24.6	27.9
Coors Mg-PSZ	17.0-33.2 (23.7)	14.7-25.5 (21.1)	--	19.0	21.4
NGK Z-191 Y-TZP	35.3-44.1 (40.3)	116.5-124.2 (119.8)	28.1	32.4	36.4

[a]Range for 5-sample population, average in parentheses.

[b]70%, 80%, and 90% of the 1000°C fast fracture strength.

levels of the static fatigue experiments. The failures in the static fatigue tests occurred at stress levels significantly lower than the residual strength after the previous static 1000 hr/1000°C exposures, and lower than the previously presented 1000°C fast fracture strengths. This information illustrates that the Mg-PSZ materials degrade during extended elevated temperature exposure, and subsequently fail if under load when the structure undergoes the transformation of the monoclinic phase at the M_s temperature upon cooling.

In summary, the present static fatigue tests illustrate that (a) the conversion of any unconstrained tetragonal phase in the Mg-PSZ structure to the monoclinic form at the M_s temperature as the material cools through the martensitic transformation region, and (b) loss of the cubic phase by destabilization and decomposition, are the most critical parameters for long term strength degradation and the development of associated life prediction methodology and strategies. The limiting long term behavior is not related to bulk diffusion, cavity nucleation, creep fracture, subcritical crack growth, etc. It is simply related to controlling the phase assemblage of the structure, and preventing its conversion to monoclinic as the M_s temperature is passed through upon cooling from the service temperature. Note, however, that

several mechanisms may be involved in the observed degradation (i.e., over-aging [t → m], stress-assisted transformation, decomposition [c → m + Mg], destabilization [c →m] by volatization of MgO stabilizer, etc.).

For Y-TZP, the overriding long term problem is not related to such phenomena involving a tetragonal-to-monoclinic phase transformation. Rather, high-temperature deformation is the critical issue.

13. THERMAL FATIGUE

It was shown in the static fatigue work presented in Section 12 that Y-PSZ (i.e., TZP) materials suffered from excessive deformation while under significant load at 1000°C. For the coarse-grain precipitate structure, Mg-PSZ, it was found that little or no time dependence per se was seen in the strength; however, virtually all of the samples failed after the 2000 hr/1000°C exposure as the sample cooled under load through the M_s temperature, the point at which the tetragonal zirconia transforms to monoclinic in the overaged, destabilized, and decomposed material. This test and its results are significant for diesel engine applications since the maximum temperature expected in certain engine configurations will be ~1000°C (i.e., piston cap), and long service times are projected (much greater than 1000 hr).

Since the problem is related to the tetragonal-to-monoclinic phase transformation, it is very appropriate to examine thermal fatigue behavior, especially in regards to potential degradation from cycling through the A_s ($m \rightarrow t$) and M_s ($t \rightarrow m$) temperatures many times. Accordingly, a thermal fatigue test was conducted on one sample of each of the four transformation-toughened materials, wherein a typical diesel engine start-up and shut-down cycle was simulated. Test samples were slowly cycled under no mechanical load into a furnace maintained at 1000°C in a time of ~20 min; the residence time at 1000°C was 10 min; the sample was slowly withdrawn to ambient conditions over a period of 10 min; the residence time at ambient conditions was 10 min prior to the start of the next thermal cycle. This thermal cycle was repeated a total of 1115 times. The total residence time at 1000°C was 186 hr. The residual bend strength and dynamic elastic modulus were measured after this thermal cycling.

The results for elastic modulus are presented in Table 24, where the as-received modulus and the modulus after 1000 hr/1000°C exposure are also tabulated for reference. The values for thermal-fatigued samples are virtually unchanged. This illustrates that extensive microcracking after repeated cycling did not occur.

PRECEDING PAGE BLANK NOT FILMED

PAGE 202 INTENTIONALLY BLANK

TABLE 24. THERMAL FATIGUE RESULTS--ELASTIC MODULUS

Material	Dynamic Elastic Modulus at 25°C, 10^6 psi		
	As-Received	After 1000 hr/1000°C Exposure	After 1115 Cycles from 25° to 1000°C
NGK Z-191 TZP	28.9	28.9	29.1
Nilsen MS Mg-PSZ	29.3	30.2	29.1
Feldmuhle ZN-40 Mg-PSZ	29.8	29.2	29.8
Coors Mg-PSZ	29.5	18.3-27.0[a]	31.5

[a]Obtained from deformation in bend test.

The thermal fatigue results for bend strength are tabulated in Table 25. Comparison is made to as-received fast fracture strength at 25° and 1000°C, and the residual room temperature strength after 1000 hr/1000°C thermal exposure. As shown in Table 25, the strength of the single thermal-fatigued NGK Z-191 TZP sample is 17% lower than its as-received strength, but still significantly high (107 ksi). As discussed above, the microstructure of TZP is very stable. There was no evidence of phase change in the post 1000 hr/1000°C exposure samples, where the strength was only 7% lower than the original strength. The thermal-fatigued sample exhibited a 17% strength reduction. However, this was on only one sample, and thus the reproducibility of the result is not known. Zirconia is known to have relatively poor thermal shock resistance. Some minimal microcracking may have resulted from the 1115 thermal fatigue cycles. However, the effect is not large based on the residual strength data.

The Mg-PSZ materials are known to suffer severe strength degradation due to overaging and destabilization/decomposition in the static 1000 hr/1000°C exposure. Note in Table 25 that the Nilsen material experienced an identical strength degradation (i.e., 56%) in the thermal fatigue test, where the exposure time was much shorter, i.e., 186 hr. However, the Mg-PSZ materials from Coors and Feldmuhle did not degrade as much due to the 1115-cycle thermal fatigue as they did in the 1000 hr/1000°C static thermal exposure. The total time at 1000°C in the static exposure was 1000 hr. The total time spent at 1000°C in the fatigue test was 186 hr. The strength degradation for these materials appears to correlate with total time at 1000°C. It appears that the

TABLE 25. THERMAL FATIGUE RESULTS--FLEXURAL STRENGTH

Material	4-Point Flexure Strength, ksi			
	As-Received		Residual Strength at 25°C	
	25°C	1000°C	After 1000 hr/1000°C Exposure	After 1115 Cycles from 25° to 1000°C
NGK Z-191 TZP	129.1	40.3	119.8	107.3
Nilsen MS Mg-PSZ	92.5	41.6	39.4	41.4
Feldmuhle ZN-40 Mg-PSZ	61.8	30.9	43.2	64.5
Coors Mg-PSZ	69.9	23.7	21.1	35.8

1115 cycles through the M_s temperature was not in itself detrimental. Presumably, the overaging and destabilization/decomposition is not as severe after only 186 hr at 1000°C, compared to the level of overaging and destabilization/decomposition which occurred after 1000 hr at 1000°C. Note that the thermal fatigue tests were conducted on samples with no mechanical load applied.

These thermal fatigue results suggest that the time at elevated temperature is the most important factor in property degradation. The mechanisms and kinetics of the different degradation modes should therefore be studied. Progressive damage by microcracking as the M_s temperature is repeatedly passed through does not appear to occur to any great extent in transformation-toughened zirconia--either in Mg-PSZ or in Y-TZP forms.

14. COMPONENT SHAPE CAPABILITIES

Transformation-toughened zirconia is recognized to have thermal and mechanical properties that are potentially beneficial for use in the minimum heat rejection diesel engine. As such, a necessary requirement of ceramic vendors is to produce TTZ in the required component configurations. Specific component designs are a function of the particular engine and its performance requirements, and are generally proprietary. Likewise, the details of vendors' production facilities and capabilities are proprietary. However, the diesel engine community can be assured that transformation-toughened zirconia is being scaled to production quantities by current foreign and domestic vendors. A representative sampling of typical transformation-toughened zirconia diesel engine components that have been produced has been provided for the NGK and Nilsen materials, and is presented in Figures 109 and 110.

PRECEDING PAGE BLANK NOT FILMED

PAGE 206 INTENTIONALLY BLANK

ORIGINAL PAGE IS
OF POOR QUALITY

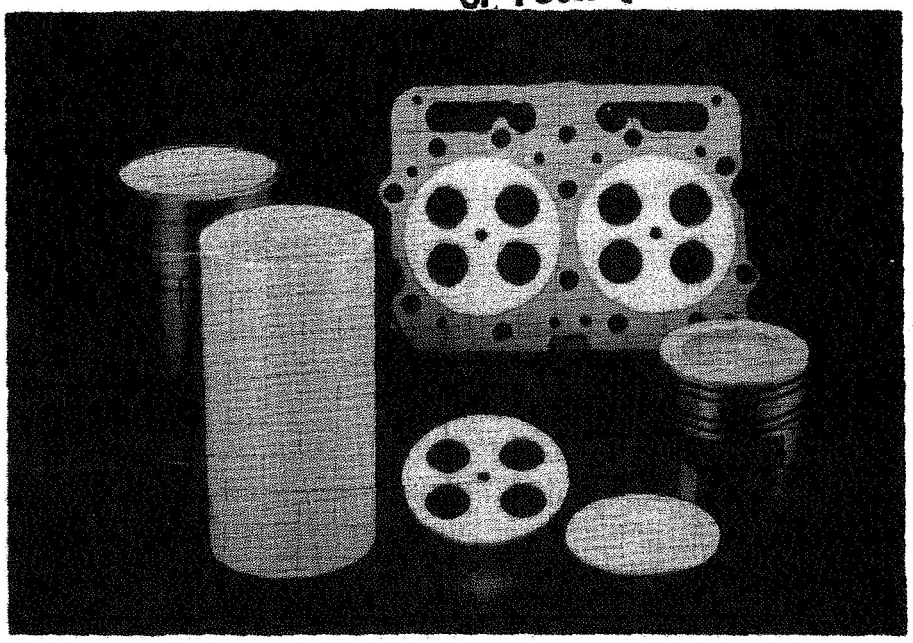

(a)

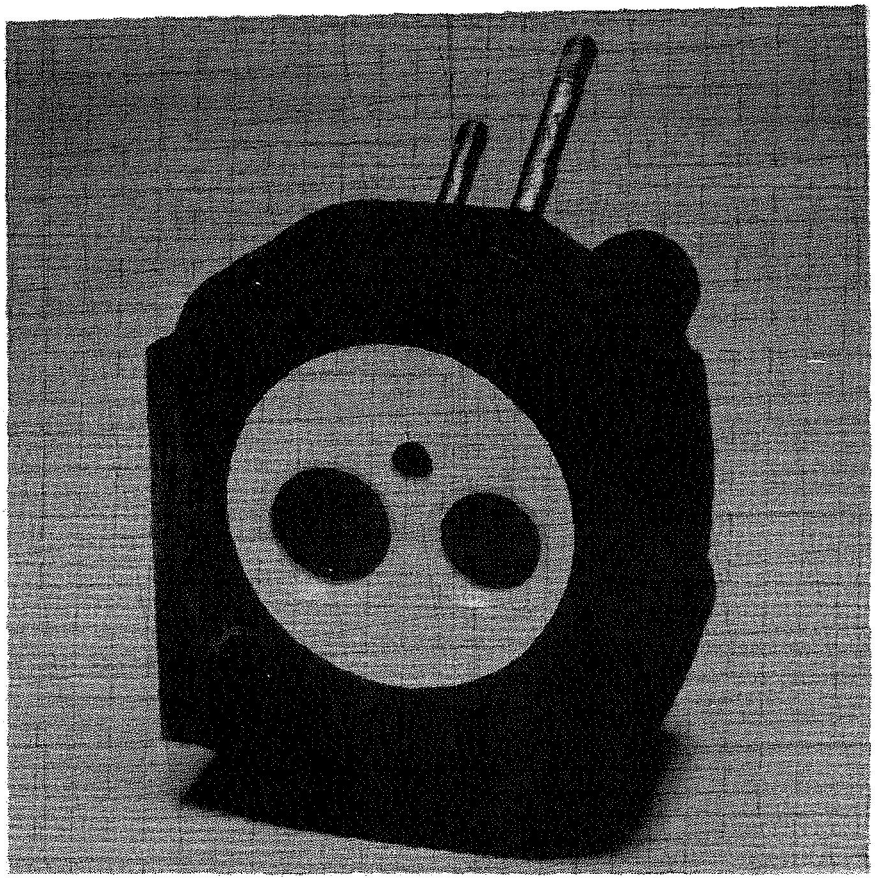

(b)

Figure 109. Zirconia diesel engine components produced by NGK.

ORIGINAL PAGE IS
OF POOR QUALITY

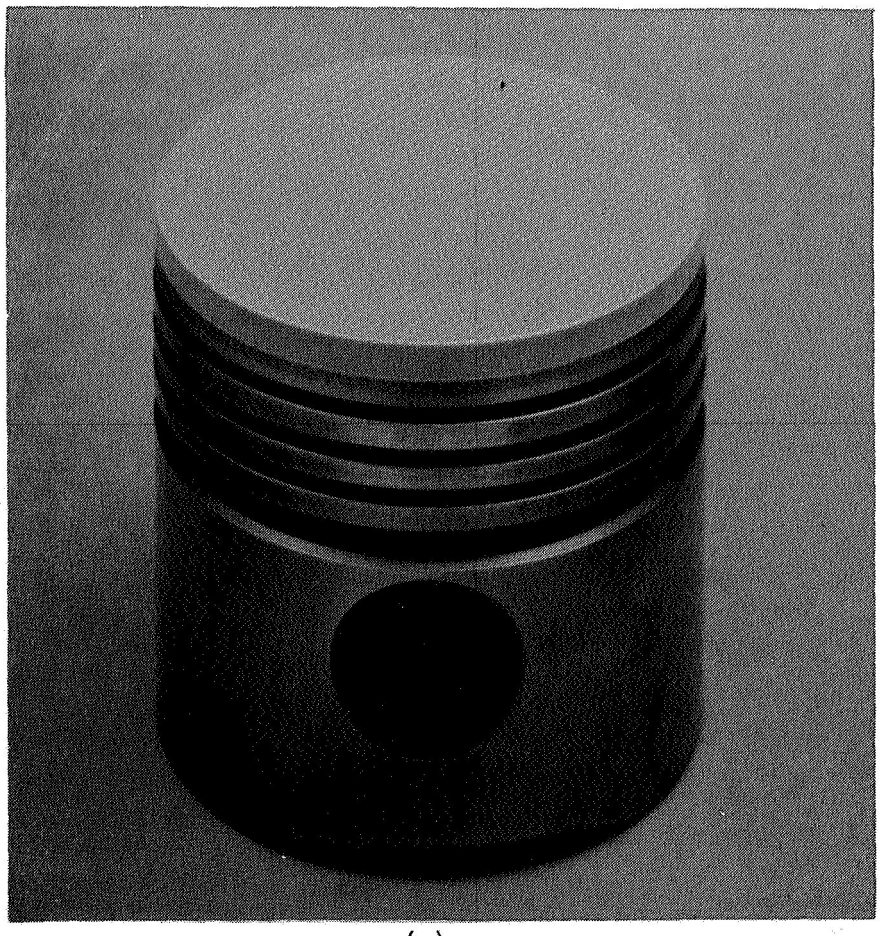

(c)

Figure 109. (cont.)

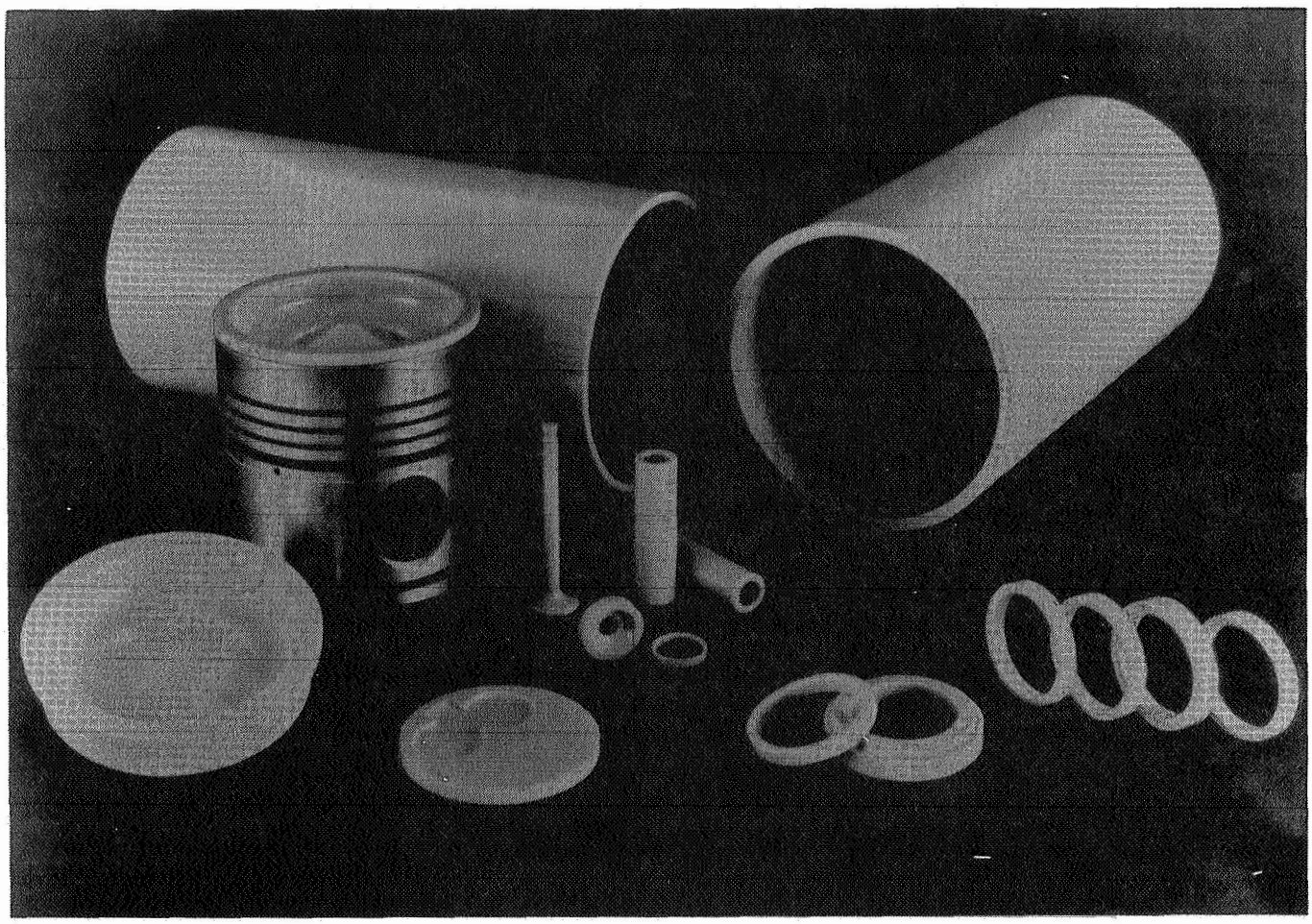

(a)

Figure 110. Zirconia diesel engine components produced by Nilcra Ceramics (Nilsen Mg-PSZ).

ORIGINAL PAGE IS
OF POOR QUALITY

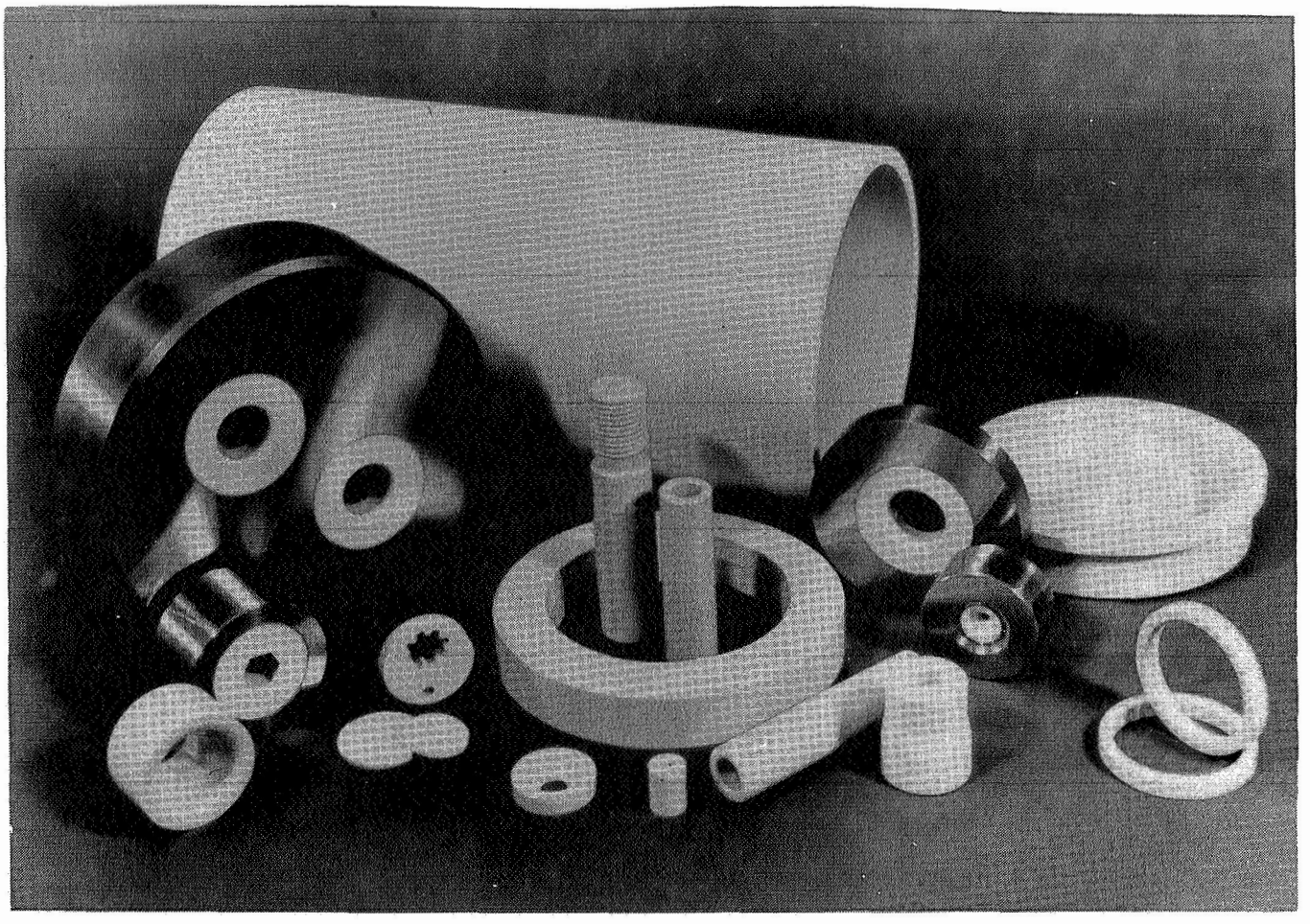

(b)

Figure 110. (cont.)

15. DISCUSSION AND CONCLUSIONS

Transformation-toughened zirconia offers unique benefits for use as a structural component in the adiabatic diesel engine. Besides having low thermal conductivity, this ceramic possesses both high strength and high fracture toughness at moderate temperatures. It is relatively flaw tolerant, exhibiting Weibull moduli, a measure of strength distribution dispersion, that are high for monolithic ceramics. The transformation of the tetragonal zirconia phase in the tensile stress field ahead of an advancing crack tip reduces the severity of the crack tip stresses, thereby shielding it from the applied stress field. More than one mechanism is involved, including microcrack generation, crack deflection, crack bowing, and the energy absorbed by the transformation process. The dispersed tetragonal zirconia phase is the active toughening phase, and its retention and control is the key to maintaining the attributes of TTZ, and a necessary condition of insuring its successful structural use in advanced adiabatic diesel engines.

A comparison of the two major forms of transformation-toughened zirconia, Mg-PSZ and Y-TZP, is provided in Table 26. The items are listed as applied mainly to the two mature forms of these materials investigated on this program (NGK Z-191 Y-TZP and Nilsen MS Mg-PSZ). Mg-PSZ consists of ~37% tetragonal ZrO_2, existing as a fine intragranular dispersion within large cubic grains. Y-PSZ is 100% tetragonal single phase (more correctly referred to as TZP, tetragonal zirconia polycrystals). Both materials are relatively dense, ~5.8 g cm^{-3}, or ~80% more dense than silicon-base ceramics.

The TZP material (Y-PSZ) has a finer grain size (~2 μm vs. ~50 μm) and is ~40% higher strength. Both materials exhibit Weibull moduli that are high for ceramics (m ~20). At 1000°C the Y-TZP suffers ~70% fast fracture strength reduction, whereas the Mg-PSZ strength is reduced ~50%. In both materials, this is the consequence of the tetragonal particles/precipitates becoming more stable with increasing temperature. Magnesia-stabilized zirconia has higher fracture toughness (~10-12 $MPa \cdot m^{1/2}$) than the yttria-stabilized zirconia (~8 $MPa \cdot m^{1/2}$). As a function of temperature, fracture toughness follows the trend of the relative strength degradation. Thermal expansion and elastic modulus

PAGE 212 INTENTIONALLY BLANK

PRECEDING PAGE BLANK NOT FILMED

TABLE 26. COMPARISON OF TWO MAJOR FORMS OF TRANSFORMATION-TOUGHENED ZIRCONIA

3% Mg-PSZ (TTZ)	5% Y-PSZ (TZP)
• Cubic with tetragonal precipitates (58% c, 37% t, 5% m)	• All tetragonal (single phase)
• Large grain size (~50-75 μm)	• Fine grain (1-5 μm)
• High density (5.7 g cm^{-3})	• High density (5.9 g cm^{-3})
• Intermediate strength (90 ksi)	• High strength (130 ksi)
• High Weibull modulus (m = 25)	• High Weibull modulus (m = 19)
• 50% strength and toughness reduction at 1000°C (tetragonal less metastable)	• 70% strength and toughness reduction at 1000°C (tetragonal less metastable)
• Higher toughness (~10-12 MPa·$m^{1/2}$)	• Slightly lower toughness (~8 MPa·$m^{1/2}$)
• Expansion, elastic modulus ~Y-PSZ	• Expansion, elastic modulus ~Mg-PSZ
• Poor thermal stability - overaging	• Long-term stability at temperature
• 30-70% strength reduction after 1000 hr/1000°C	• Only 7% strength and toughness reduction after 1000 hr/1000°C
• 30-50% toughness reduction after 1000 hr/1000°C	
• Good creep resistance	• Thermal expansion unchanged by exposure
• Creep, elastic modulus unaffected by overaging	• Internal friction unchanged, peak at 200°C
• Internal friction peak altered by phase changes	• Thermal diffusivity ~ Mg-PSZ
• Apparent destabilization and decomposition effects	• Potential degradation at 200°C (water vapor) (not investigated on this program)
• Can be optimized for thermal shock	
• Good static fatigue behavior (minimal time dependence; failure on cooling at M_s)	• Poor creep resistance (SiO_2 intergranular phase, fine grain)
• Thermal fatigue minimal (cycling through M_s not detrimental)	
• Most failures relate to t → m transformation: major limitation	• Excessive deformation at temperature a major problem
• Time at temperature most important	

are similar for Mg- and Y-PSZ materials. Yttria-stabilized TTZ exhibits a creep rate more than an order of magnitude higher than magnesia-stabilized TTZ. Water quench thermal shock resistance is higher for Y-PSZ, owing to its higher strength. However, the phase composition of Mg-PSZ can be altered specifically to improve its thermal shock resistance (however, at the expense of strength and toughness).

Y-TZP has much better long-term high temperature microstructural stability compared to Mg-PSZ. This is summarized in Figures 111 and 112. After static thermal exposure for 1000 hr at 1000°C, the residual strength of the TZP material was 93% of the original strength. Conversely, the Mg-PSZ exhibited almost a 60% decrease in strength after 1000 hr/1000°C exposure. Similar behavior is observed for the fracture toughness of these two forms of transformation-toughened zirconia. The MgO-TTZ tetragonal precipitates are very prone to overaging with resultant loss of properties. This is very evident in thermal expansion behavior, which is quite sensitive to detection of any monoclinic zirconia present in the microstructure. However, the elastic modulus and creep behavior are unaffected by such overaging phenomena in Mg-PSZ. Interestingly, both Mg-PSZ and Y-TZP degraded in thermal shock resistance an equivalent amount (to equal ΔT_c).

For Y-TZP, the overriding long-term problem is not overaging and the resulting tetragonal-to-monoclinic phase transformation such as is found in Mg-PSZ. Rather, high temperature deformation is the critical issue, and is thought to be related to the fine grain size and SiO_2-rich intergranular regions. The Y-TZP investigated on this program was single phase (tetragonal). Thus, the active tetragonal phase that is responsible for toughening is unprotected from the environment. Certain forms have shown severe degradation in the presence of water vapor (although this issue was not investigated on this program). The tetragonal phase in Mg-PSZ is an intragranular precipitate, and thus such environmental problems would be expected to be less pronounced.

For Mg-PSZ, all failures or deficiencies appear to be related to unwanted tetragonal-to-monoclinic phase transformation. The Mg-PSZ materials exhibited relatively time-invariant strength during 2000 hr/1000°C static fatigue tests. However, all Mg-PSZ materials failed when cooling under load as they reached

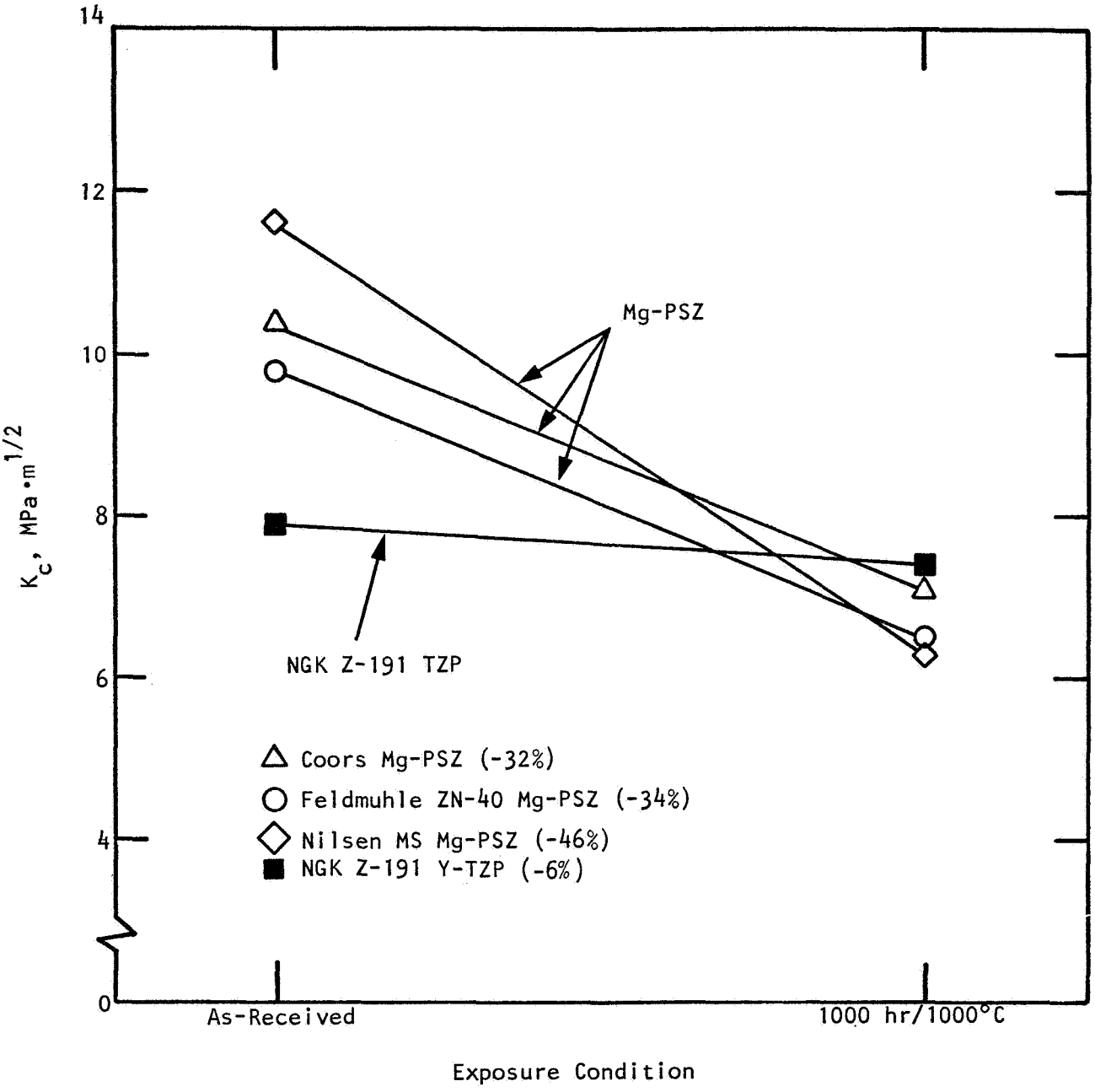

Figure 111. Fracture toughness of zirconia at 25°C before and after 1000 hr/1000°C thermal exposure.

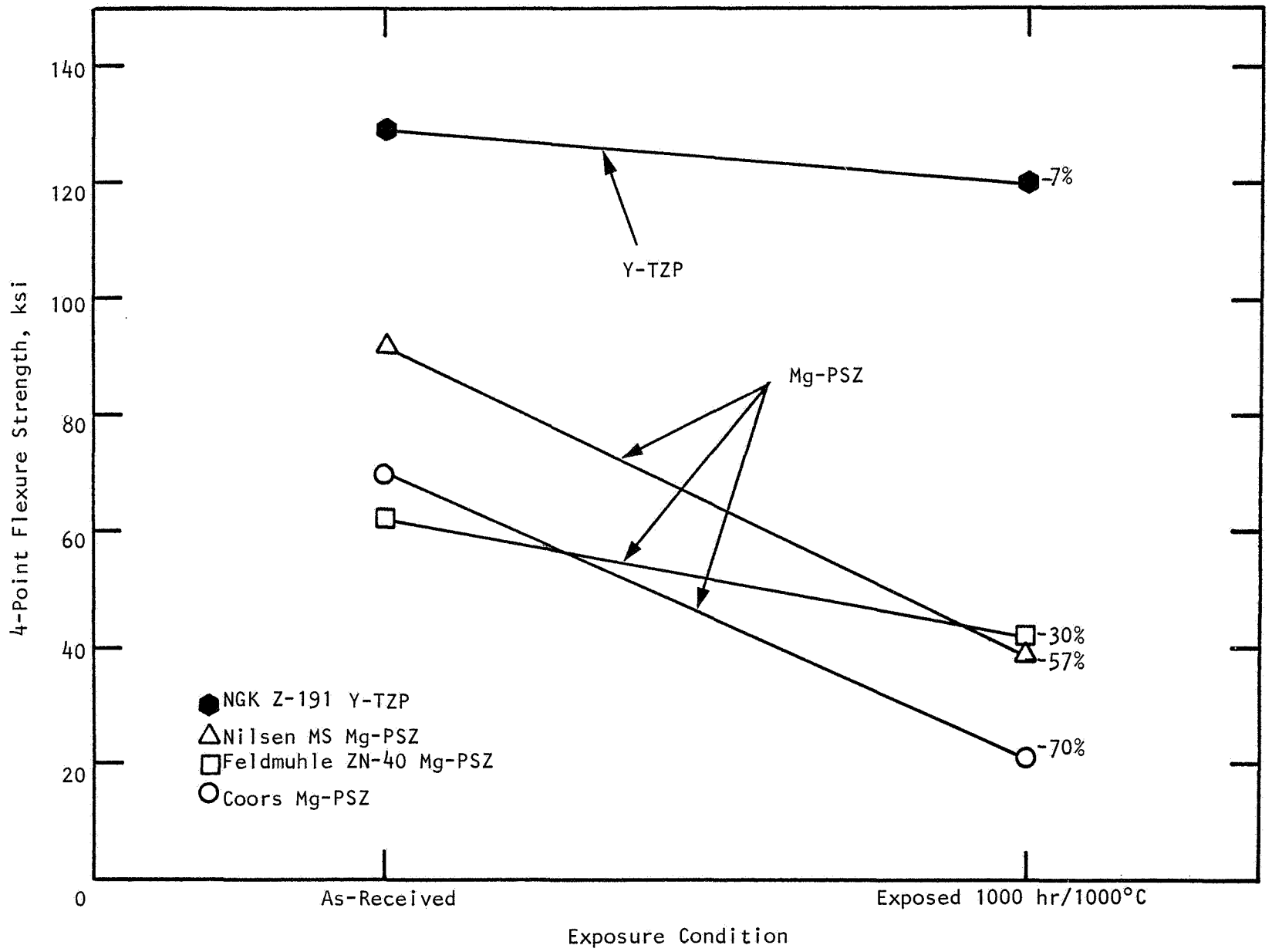

Figure 112. Flexure strength of zirconia at 25°C before and after 1000 hr/1000°C thermal exposure.

the M_s temperature. These static fatigue results illustrate that (a) the conversion of any unconstrained tetragonal phase in the Mg-PSZ structure to the monoclinic form at the M_s temperature as the material cools through the martensitic transformation region, and (b) loss of the cubic phase by destabilization and decomposition are the most critical parameters for long-term property degradation and the development of associated life prediction methodology and strategies. The limiting long-term behavior is not related to bulk diffusion, cavity nucleation, creep fracture, subcritical crack growth, etc. It is simply related to controlling the phase assemblage of the structure, and preventing its conversion to monoclinic as the M_s temperature is reached upon cooling from the service temperature or during in-service temperature excursions while under load.

Thermal fatigue tests were conducted by cycling these materials 1115 times from 25° to 1000°C. The results indicate that the total time at 1000°C is the parameter that is most controlling of the phase degradation. Repeated cycling through the martensitic transformation region, where microcracking can occur, does not appear to be particularly detrimental (however, severely overaged materials were not subjected to the thermal fatigue test on this program).

From the point of view of thermal design with transformation-toughened zirconia for adiabatic diesel engine applications, it is noteworthy that there is no thermal benefit of Y-TZP over Mg-PSZ--both forms of transformation-toughened zirconia have nominally equivalent values of (room temperature) thermal diffusivity. The increase in thermal diffusivity for Mg-PSZ upon long-term degradation, however, is typically nominally 10-13%, but can be as high as 40%. This will certainly affect the thermal performance of the adiabatic system (if not first noticeable in the decreased mechanical performance due to the concurrent drastic decreases in strength and toughness associated with the degradation).

The most useful analytical tool used to assess TT-ZrO_2 is XRD to quantify the phase assemblage. Several mechanisms appear to be involved in the degradation of Mg-PSZ materials. Such mechanisms include overaging, stress-assisted transformation, decomposition, and destabilization. Overaging is explained by the conversion of the original metastable tetragonal to

monoclinic. Destabilization and/or decomposition is indicated by the conversion of the original cubic phase to monoclinic. Both of these phase transformations (e.g., t → m, c → m) were detected for exposed Mg-PSZ materials investigated in this program.

When considering the use of these materials in design of structural components, the ceramic technologist would be wise to consider only relatively low temperature applications. There, the high toughness of TTZ leads to flaw tolerance and high Weibull moduli. Therefore, these materials have perhaps a higher probability of design acceptance compared to monolithic ceramics. Life prediction methodologies should be based on the phase structure (e.g., tetragonal retention) rather than strictly on flaw size.

From a materials development standpoint, a potentially fruitful area of research is to attempt to increase the transformation region to temperatures well above the expected use temperatures. Increased long-term stability would then possibly be achieved.

REFERENCES

1. H. P. Klug and L. E. Alexander, X-Ray Diffraction Procedures, 2nd Ed., John Wiley and Sons, Inc., New York, 1974.

2. B. D. Cullity, Elements of X-Ray Diffraction, Addison-Wesley Publishing Co., Reading, Mass., 1956.

3. Pol Duwez and Francis Odell, "Quantitative Analysis of Cubic and Monoclinic Zirconia by X-Ray Diffraction," J. Am. Ceram. Soc., 32 [5], pp. 180-83 (1949); "Discussion," ibid., pp. 184-85.

4. R. C. Garvie and P. S. Nicholson, "Phase Analysis in ZrO_2 Systems," J. Am. Ceram. Soc., 55 [6], pp. 303-305 (1972).

5. R. C. Garvie, R. H. Hannick, R. T. Pascoe, "Ceramic Steel?," Nature, 258, pp. 703-704 (1975).

6. D. L. Porter and A. H. Heuer, "Microstructural Development in MgO-Partially Stabilized Zirconia (Mg-PSZ)," J. Am. Ceram. Soc., 62 [5-6], pp. 298-305 (1979).

7. R. Hannick, K. A. Johnston, R. T. Pascoe, and R. C. Garvie, "Microstructural Changes During Isothermal Aging of a Calcia Partially Stabilized Zirconia Alloy," in Science and Technology of Zirconia, Advances in Ceramics, Vol. 3, A. H. Heuer and L. W. Hobbs, eds., The American Ceramic Society, Columbus, Ohio, 1981, pp. 116-136.

8. H. G. Scott, "Phase Relationships in the Zirconia-Yttria System," J. Mater. Sci., 10, pp. 1527-1535 (1975).

9. L. J. Schioler and J. W. Adams, "Phase Analysis of Zirconia Systems Using X-Ray Diffraction," to be published.

10. R. T. Pascoe and R. C. Garvie, "Surface Strengthening of Transformation-Toughened Zirconia," in Ceramic Microstructure '76, R. M. Fulrath and J. A. Pask, eds., Westview Press, Boulder, Colo., 1977.

11. C. A. Johnson, "Fracture Statistics in Design and Application," AGARD-CP-276, p. 20-1 (1979).

12. M. Shimada et al., "Temperature Dependence of Young's Modulus and Internal Friction in Alumina, Silicon Nitride, and Partially Stabilized Zirconia Ceramics," C. Am. Ceram. Soc., C23-C24 (February 1984).

13. P. Chantikul, G. R. Anstis, B. R. Lawn, and D. B. Marshall, "A Critical Evaluation of Indentation Techniques for Measuring Fracture Toughness: II, "J. Am. Ceram. Soc. 64 [9], pp. 539-43 (1981).

14. R. F. Cook and B. R. Lawn, "A Modified Indentation Toughness Technique," C. Amer. Ceram. Soc., C200 (1983).

PAGE 220 INTENTIONALLY BLANK

PRECEDING PAGE BLANK NOT FILMED

REFERENCES (cont.)

15. L. J. Schioler, AMMRC, Watertown, Mass., personal communication, 1985.

16. L. J. Schioler, R. N. Katz, A. C. Gonzalez, and B. R. Lawn, "Effect of Overaging on the Room Temperature Strength of Partially Stabilized Zirconia," Amer. Ceram. Soc. Bull., 64 [2], pp. 326-27 (1985).

17. B. R. Lawn, NBS, personal communication, 1985.

18. G. Zener, Elasticity and Anelasticity of Metals, University of Chicago Press, 1948.

19. D. F. Moore, "Internal Friction," Principles and Applications of Tribology, Pergamon Press, New York, 1975.

20. N. F. Astbury and W. R. Davis, "Internal Friction in Ceramics," Trans. Brit. Ceram. Soc., 63, pp. 1-18 (1964).

21. H. Kolsky, Stress Waves in Solids, Oxford-Clarendon Press, 1953.

22. J. B. Wachtman and W. C. Corwin, "Internal Friction in ZrO_2 Containing CaO," NBS J. Res. 69A [5], pp. 457-460 (1965).

23. M. Matsui, T. Soma, and I. Oda, "Effect of Microstructure on Strength of PSZ Components," NGK paper presented at Zirconia-83 Stuttgart, Second International Conference on the Science and Technology of Zirconia, Stuttgart, FRG, June 21-23, 1983. Proceedings to be published by the American Ceramic Society, Advances in Ceramics Series.

24. I. Oda, M. Matsui, and T. Soma, "Strength and Durability of PSZ Ceramics," NGK paper presented at International Symposium on Ceramic Components for Engines, Hakone, Japan, October 17-21, 1983.

25. F. F. Lange, Rockwell International Science Center, private communication, August 1984.

26. D. P. H. Hasselman, "Thermal Stress Resistance Parameters for Brittle Refractory Ceramics: A Compendium," Bull. Am. Ceram. Soc., 49, pp. 1033-1037 (1970).

27. M. V. Swain, "The Effect of Decomposition on the Thermal Shock Behavior of Mg-CSZ," J. Mater. Sci., 2, pp. 279-282 (1983).

28. M. V. Swain, "R Curve Behavior of Magnesia Partially Stabilized Zirconia and Its Significance to Thermal Shock," in Fracture Mechanics of Ceramics, Vol. 6, R. C. Bradt, A. G. Evans, D. P. H. Hasselman, and F. F. Lange, eds., Plenum Press, New York, 1983, pp. 355-368.

REFERENCES (cont.)

29. M. V. Swain and R. H. J. Hannink, "R Curve Behavior in Zirconia Ceramics," paper presented at Zirconia-83 Stuttgart, Second International Conference on the Science and Technology of Zirconia, Stuttgart, West Germany, June 21-27, 1983. Proceedings to be published by the American Ceramic Society, Advances in Ceramics Series.

30. W. J. Parker et al., J. Appl. Phys., 32, p. 1679 (1961).

31. R. E. Taylor, "Critical Review of Flash Method for Measuring Thermal Diffusivity," Thermophysical Properties Research Center Report PRF-6764, Purdue University, to National Science Foundation, October 15, 1973.

32. R. D. Cowan, "Pulse Method for Measuring Thermal Diffusivity at High Temperature," J. Appl. Phys., 34, pp. 926-927 (1963).

APPENDIX

TABULAR DATA: FLEXURAL STRENGTH, MODULUS, FAILURE STRAIN

PRECEDING PAGE BLANK NOT FILMED

PAGE 224 INTENTIONALLY BLANK

A1. FLEXURE TEST RESULTS FOR NGK Z-191 ZrO_2 (Y_2O_3)

Condition: Unexposed, As-Received
Test Temperature: 25°C

SAMPLE	BULK DENSITY (GM/CC)	STRENGTH (PSI)	STRENGTH (MPA)	STRAIN-TO-FAILURE (IN/IN X 10E-3)	SECANT MODULUS (10E6 PSI)	SECANT MODULUS (GPA)	Fracture Origin
NG1F 01	5.858	120,500	830.8	—	—	—	Subsurface pore
NG1F 02	5.861	133,800	922.6	—	—	—	Subsurface pore
NG1F 03	5.831	129,800	895.0	—	—	—	Subsurface pore
NG1F 04	5.855	136,700	942.5	—	—	—	Subsurface pore
NG1F 05	5.837	130,000	896.4	—	—	—	Open pore
NG1F 32	5.847	134,800	929.4	4.99	26.9	185.3	Open pore
NG1F 33	5.843	120,500	830.8	4.37	27.8	191.4	Open pore
NG1F 34	5.842	126,600	872.9	4.57	27.6	190.0	Subsurface pore
MEAN	5.846	129,090	890.0	4.64	27.4	188.9	
ST.DEV	0.010	6,190	42.6	—	—	—	
MAX.	5.861	136,700	942.5	—	—	—	
MIN.	5.830	120,500	830.8	—	—	—	

WEIBULL MODULUS(STRENGTH) = 19.4

TABLE A2. FLEXURE TEST RESULTS FOR NGK Z-191 ZrO_2 (Y_2O_3)

Condition: Unexposed, As-Received
Test Temperature: 500°C

SAMPLE	BULK DENSITY (GM/CC)	STRENGTH (PSI)	(MPA)	STRAIN-TO-FAILURE (IN/IN X 10E-3)	SECANT MODULUS (10E6 PSI)	(GPA)	Fracture Origin
NG1F 06	5.849	97,540	672.5	3.01	31.3	215.9	Subsurface pore cluster
NG1F 07	5.865	86,490	596.3	3.05	28.0	193.1	Subsurface pore
NG1F 08	5.860	89,310	615.8	2.78	31.6	218.0	Large grain
NG1F 09	5.839	66,470	458.3	2.22	29.8	205.2	Subsurface pore cluster
NG1F 10	5.842	77,100	531.6	2.70	28.4	195.5	Large grain
MEAN	5.851	83,380	574.9	2.75	29.8	205.5	

TABLE A3. FLEXURE TEST RESULTS FOR NGK Z-191 ZrO_2 (Y_2O_3)

Condition: Unexposed, As-Received
Test Temperature: 750°C

SAMPLE	BULK DENSITY (GM/CC)	STRENGTH (PSI)	(MPA)	STRAIN-TO-FAILURE (IN/IN X 10E-3)	SECANT MODULUS (10E6 PSI)	(GPA)	Fracture Origin
NG1F 11	5.846	67,570	465.9	2.11	32.1	221.1	Pore cluster
NG1F 12	5.842	58,010	400.0	1.83	31.5	217.3	Open pore
NG1F 13	5.844	64,390	444.0	2.21	29.2	201.5	Undetermined
NG1F 14	5.837	49,980	344.6	1.55	31.7	218.4	Subsurface pore
NG1F 15	5.845	64,320	443.5	2.32	27.6	190.5	Subsurface pore
MEAN	5.842	60,850	419.5	2.00	30.4	209.7	

TABLE A4. FLEXURE TEST RESULTS FOR NGK Z-191 ZrO_2 (Y_2O_3)

Condition: Unexposed, As-Received
Test Temperature: 1000°C

SAMPLE	BULK DENSITY (GM/CC)	STRENGTH (PSI)	(MPA)	STRAIN-TO-FAILURE (IN/IN X 10E-3)	SECANT MODULUS (10E6 PSI)	(GPA)	Fracture Origin
NG1F 16	5.834	39,660	273.5	1.75	22.3	153.8	Undetermined
NG1F 17	5.840	41,110	283.5	1.62	25.2	173.5	Subsurface pore agglomerate
NG1F 18	5.832	41,370	285.2	1.88	22.0	151.3	Subsurface pore
NG1F 19	5.838	44,130	304.3	2.08	21.0	144.9	Subsurface pore
NG1F 20	5.839	35,320	243.5	1.54	23.4	161.1	Subsurface pore
MEAN	5.836	40,320	278.0	1.77	22.7	156.9	

TABLE A5. **FLEXURE TEST RESULTS FOR NGK Z-191 ZrO_2 (Y_2O_3)**

Condition: After 1000hr/1000°C Exposure
Test Temperature: 25°C

SAMPLE	BULK DENSITY (GM/CC)	STRENGTH (PSI)	STRENGTH (MPA)	STRAIN-TO-FAILURE (IN/IN X 10E-3)	SECANT MODULUS (10E6 PSI)	SECANT MODULUS (GPA)	Fracture Origin
NG1F 21	5.921	120,300	829.5	4.34	27.7	191.3	Open pore
NG1F 22	5.911	124,200	856.4	4.46	27.8	191.5	Subsurface pore cluster
NG1F 23	5.919	120,000	827.4	4.35	27.5	190.0	Open pore
NG1F 24	5.904	118,200	815.0	4.44	26.7	183.9	Open pore
NG1F 25	5.899	116,500	803.3	4.15	28.1	193.5	Open pore
MEAN	5.910	119,840	826.2	4.34	27.5	190.0	

TABLE A6. FLEXURE TEST RESULTS FOR NILSEN MS GRADE PSZ (MgO)

Condition: Unexposed, As-Received
Test Temperature: 25°C

SAMPLE	BULK DENSITY (GM/CC)	STRENGTH (PSI)	STRENGTH (MPA)	STRAIN-TO-FAILURE (IN/IN X 10E-3)	SECANT MODULUS (10E6 PSI)	SECANT MODULUS (GPA)	Fracture Origin
NV1F 01	5.731	93,540	645.0	—	—	—	Subsurface pore
NV1F 02	5.729	92,320	636.5	—	—	—	Subsurface pore
NV1F 03	5.710	89,270	615.5	—	—	—	Subsurface pore
NV1F 04	5.725	94,380	650.8	—	—	—	Undetermined
NV1F 05	5.727	89,890	619.8	—	—	—	Large grain
NV1F 32	5.716	86,940	599.5	3.43	27.1	186.9	Large grain
NV1F 33	5.688	97,580	672.8	4.13	27.4	188.6	Open pore
NV1F 34	5.693	95,680	659.7	4.02	27.2	187.5	Undetermined
MEAN	5.714	92,450	637.4	3.86	27.2	187.7	
ST.DEV	0.016	3,560	24.5	—	—	—	
MAX.	5.730	97,580	672.8	—	—	—	
MIN.	5.688	86,940	599.4	—	—	—	

WEIBULL MODULUS(STRENGTH) = 24.7

TABLE A7. FLEXURE TEST RESULTS FOR NILSEN MS GRADE PSZ (MgO)

Condition: Unexposed, As-Received
Test Temperature: 500°C

SAMPLE	BULK DENSITY (GM/CC)	STRENGTH (PSI)	STRENGTH (MPA)	STRAIN-TO-FAILURE (IN/IN X 10E-3)	SECANT MODULUS (10E6 PSI)	SECANT MODULUS (GPA)	Fracture Origin
NV1F 06	5.725	63,180	435.6	2.06	30.7	211.6	Undetermined
NV1F 07	5.700	64,950	447.8	2.20	30.0	206.5	Open pore
NV1F 08	5.697	66,790	460.5	2.18	30.9	212.8	Subsurface pore
NV1F 09	5.695	66,620	459.3	2.32	28.4	195.7	Poorly sintered region, intragranular fracture origin
NV1F 10	5.693	65,610	452.4	2.37	28.2	194.2	Subsurface pore
MEAN	5.702	65,430	451.1	2.22	29.6	204.1	

TABLE A8. FLEXURE TEST RESULTS FOR NILSEN MS GRADE PSZ (MgO)

Condition: Unexposed, As-Received
Test Temperature: 750°C

SAMPLE	BULK DENSITY (GM/CC)	STRENGTH (PSI)	(MPA)	STRAIN-TO-FAILURE (IN/IN X 10E-3)	SECANT MODULUS (10E6 PSI)	(GPA)	Fracture Origin
NV1F 11	5.680	54,360	374.8	1.84	29.6	203.8	Subsurface pore
NV1F 12	5.709	54,920	378.7	1.74	31.3	216.0	Open pore
NV1F 13	5.689	54,220	373.8	1.73	31.0	214.0	Open pore
NV1F 14	5.718	53,390	368.1	1.74	30.6	211.1	Open pore
NV1F 15	5.707	48,040	331.2	1.63	29.4	202.9	Open pore
MEAN	5.700	52,990	365.3	1.73	30.3	209.5	

TABLE A9. FLEXURE TEST RESULTS FOR NILSEN MS GRADE PSZ (MgO)

Condition: Unexposed, As-Received
Test Temperature: 1000°C

SAMPLE	BULK DENSITY (GM/CC)	STRENGTH (PSI)	(MPA)	STRAIN-TO-FAILURE (IN/IN X 10E-3)	SECANT MODULUS (10E6 PSI)	(GPA)	Fracture Origin
NV1F 16	5.718	38,510	265.5	1.58	24.2	167.2	Subsurface pore
NV1F 17	5.705	44,140	304.3	1.61	27.2	187.6	Open pore
NV1F 18	5.715	42,460	292.8	1.65	25.5	175.7	Large grain
NV1F 19	5.697	41,080	283.2	1.47	27.9	192.5	Open pore
NV1F 20	5.727	41,790	288.1	1.74	24.1	166.0	Subsurface pore
MEAN	5.712	41,600	286.8	1.61	25.7	177.8	

TABLE A10. FLEXURE TEST RESULTS FOR NILSEN MS GRADE PSZ (MgO)

Condition: After 1000hr/1000°C Exposure
Test Temperature: 25°C

SAMPLE	BULK DENSITY (GM/CC)	STRENGTH (PSI)	(MPA)	STRAIN-TO-FAILURE (IN/IN X 10E-3)	SECANT MODULUS (10E6 PSI)	(GPA)	Fracture Origin
NV1F 21	5.728	37,130	256.0	1.37	27.3	188.0	Undetermined
NV1F 22	5.692	40,720	280.8	1.52	27.0	185.9	Undetermined
NV1F 23	5.674	48,920	337.3	1.79	27.7	190.9	Large grain
NV1F 24	5.692	35,790	246.8	1.35	26.8	184.5	Subsurface pore
NV1F 25	5.690	34,180	235.7	1.28	27.2	187.9	Open pore
MEAN	5.695	39,350	271.3	1.46	27.1	187.4	

TABLE A11. FLEXURE TEST RESULTS FOR FELDMUHLE ZN-40 ZrO_2 (MgO)

Condition: Unexposed, As-Received
Test Temperature: 25°C

SAMPLE	BULK DENSITY (GM/CC)	STRENGTH (PSI)	STRENGTH (MPA)	STRAIN-TO-FAILURE (IN/IN X 10E-3)	SECANT MODULUS (10E6 PSI)	SECANT MODULUS (GPA)	Fracture Origin
KF1F 01	5.785	53,650	369.9	—	—	—	Subsurface porous region
KF1F 02	5.775	67,520	465.6	—	—	—	Subsurface pore
KF1F 03	5.777	58,810	405.5	—	—	—	Subsurface pore/ large grain
KF1F 04	5.782	56,500	389.6	—	—	—	Undetermined
KF1F 05	5.773	66,730	460.1	—	—	—	Undetermined
KF1F 32	5.785	64,480	444.6	2.26	28.6	197.1	Undetermined
KF1F 33	5.779	67,690	466.7	2.41	28.1	193.8	Undetermined
KF1F 34	5.796	59,240	408.5	2.13	27.2	187.8	Undetermined
MEAN	5.781	61,830	426.3	2.27	28.0	192.9	
ST.DEV	0.007	5,460	37.6	—	—	—	
MAX.	5.796	67,690	466.7	—	—	—	
MIN.	5.772	53,650	369.9	—	—	—	

WEIBULL MODULUS(STRENGTH) = 10.5

TABLE A12. FLEXURE TEST RESULTS FOR FELDMUHLE ZN-40 ZrO_2 (MgO)

Condition: Unexposed, As-Received
Test Temperature: 500°C

SAMPLE	BULK DENSITY (GM/CC)	STRENGTH (PSI)	(MPA)	STRAIN-TO-FAILURE (IN/IN X 10E-3)	SECANT MODULUS (10E6 PSI)	(GPA)	Fracture Origin
KF1F 06	5.782	39,950	275.5	1.33	29.8	205.3	Undetermined
KF1F 07	5.787	45,110	311.0	1.49	30.1	207.4	Subsurface porous region
KF1F 08	5.782	43,070	297.0	1.53	28.0	193.3	Subsurface pore
KF1F 09	5.795	42,490	293.0	1.49	28.0	193.2	Undetermined
KF1F 10	5.773	43,120	297.3	1.50	28.6	197.0	Undetermined
MEAN	5.783	42,750	294.7	1.46	28.8	199.2	

TABLE A13. FLEXURE TEST RESULTS FOR FELDMUHLE ZN-40 ZrO_2 (MgO)

Condition: Unexposed, As-Received
Test Temperature: 750°C

SAMPLE	BULK DENSITY (GM/CC)	STRENGTH (PSI)	(MPA)	STRAIN-TO-FAILURE (IN/IN X 10E-3)	SECANT MODULUS (10E6 PSI)	(GPA)	Fracture Origin
KF1F 11	5.771	39,030	269.1	1.24	30.6	211.3	Large grain
KF1F 12	5.789	38,490	265.4	1.40	27.4	189.0	Undetermined
KF1F 13	5.766	38,700	266.8	1.45	26.5	182.4	Large grain
KF1F 14	5.775	40,030	276.0	1.36	29.5	203.2	Open pore
KF1F 15	5.744	37,720	260.1	1.29	28.8	198.7	Undetermined
MEAN	5.769	38,790	267.4	1.34	28.5	196.9	

TABLE A14. FLEXURE TEST RESULTS FOR FELDMUHLE ZN-40 ZrO_2 (MgO)

Condition: Unexposed, As-Received
Test Temperature: 1000°C

SAMPLE	BULK DENSITY (GM/CC)	STRENGTH (PSI)	(MPA)	STRAIN-TO-FAILURE (IN/IN X 10E-3)	SECANT MODULUS (10E6 PSI)	(GPA)	Fracture Origin
KF1F 16	5.793	30,950	213.4	1.39	22.1	152.1	Poorly sintered region of intragranular fracture
KF1F 17	5.781	31,270	215.6	1.28	24.0	165.8	Subsurface pore
KF1F 18	5.768	29,070	200.4	1.16	25.0	172.7	Undetermined
KF1F 19	5.792	32,720	225.6	1.53	21.4	147.8	Poorly bonded grains perpendicular to tensile surface
KF1F 20	5.776	30,300	208.9	1.14	26.2	180.7	Undetermined
MEAN	5.782	30,860	212.7	1.30	23.7	163.8	

TABLE A15. FLEXURE TEST RESULTS FOR FELDMUHLE ZN-40 ZrO_2 (MgO)

Condition: After 1000hr/1000°C Exposure
Test Temperature: 25°C

SAMPLE	BULK DENSITY (GM/CC)	STRENGTH (PSI)	(MPA)	STRAIN-TO-FAILURE (IN/IN X 10E-3)	SECANT MODULUS (10E6 PSI)	(GPA)	Fracture Origin
KF1F 21	5.777	43,720	301.4	1.61	27.2	187.5	Undetermined
KF1F 22	5.775	40,910	282.1	1.47	28.1	193.6	Pore cluster
KF1F 23	5.772	45,350	312.7	1.67	27.2	187.3	Undetermined
KF1F 24	5.805	44,270	305.2	1.65	27.0	186.3	Undetermined
KF1F 25	5.811	41,780	288.1	1.55	27.0	186.1	Undetermined
MEAN	5.788	43,210	297.9	1.59	27.2	188.1	

TABLE A16. FLEXURE TEST RESULTS FOR COORS TT-ZrO_2 (3% MgO)

Condition: Unexposed, As-Received
Test Temperature: 25°C

SAMPLE	BULK DENSITY (GM/CC)	STRENGTH (PSI)	STRENGTH (MPA)	STRAIN-TO-FAILURE (IN/IN X 10E-3)	SECANT MODULUS (10E6 PSI)	SECANT MODULUS (GPA)	Fracture Origin
CB1F 01	5.750	56,290	388.1	—	—	—	Undetermined processing defect
CB1F 02	5.764	75,850	523.0	—	—	—	Poorly bonded intragranular fracture origin
CB1F 03	5.752	74,380	512.9	—	—	—	Open pore/subsurface pore
CB1F 04	5.780	79,000	544.7	—	—	—	Subsurface pore
CB1F 05	5.748	61,090	421.2	—	—	—	Open pore
CB1F 32	5.720	64,080	441.8	2.25	28.5	196.4	Open pore
CB1F 33	5.728	59,260	408.6	2.14	27.5	189.5	Subsurface pore
CB1F 34	5.742	83,380	574.9	3.02	28.0	193.1	Subsurface pore
CB1F 64	5.727	75,610	521.3	—	—	—	
MEAN	5.745	69,880	481.8	2.47	28.0	193.0	
ST.DEV	0.019	9,760	67.2	—	—	—	
MAX.	5.780	83,380	574.9	—	—	—	
MIN.	5.719	56,290	388.1	—	—	—	

WEIBULL MODULUS(STRENGTH) = 6.6

ORIGINAL PAGE IS OF POOR QUALITY

TABLE A17. FLEXURE TEST RESULTS FOR COORS TT-ZrO_2 (3% MgO)

Condition: Unexposed, As-Received
Test Temperature: 500°C

SAMPLE	BULK DENSITY (GM/CC)	STRENGTH (PSI)	(MPA)	STRAIN-TO-FAILURE (IN/IN X 10E-3)	SECANT MODULUS (10E6 PSI)	(GPA)	Fracture Origin
CB1F 06	5.732	55,330	381.5	1.98	30.4	209.7	Subsurface pore
CB1F 07	5.729	48,270	332.8	1.56	31.3	216.2	Undetermined
CB1F 08	5.739	45,870	316.3	1.60	29.5	203.6	Pore cluster
CB1F 09	5.759	46,200	318.5	1.56	27.2	187.3	Subsurface pore
CB1F 10	5.730	43,700	301.3	1.44	30.5	210.5	Undetermined
MEAN	5.737	47,870	330.0	1.62	29.7	205.4	

TABLE A18. FLEXURE TEST RESULTS FOR COORS TT-ZrO_2 (3% MgO)

Condition: Unexposed, As-Received
Test Temperature: 750°C

SAMPLE	BULK DENSITY (GM/CC)	STRENGTH (PSI)	STRENGTH (MPA)	STRAIN-TO-FAILURE (IN/IN X 10E-3)	SECANT MODULUS (10E6 PSI)	SECANT MODULUS (GPA)	Fracture Origin
CB1F 11	5.738	33,160	228.6	1.16	28.4	195.8	Open pore
CB1F 12	5.725	29,820	205.6	0.98	30.3	208.8	Subsurface pore
CB1F 13	5.741	31,680	218.4	1.18	26.4	182.2	Open pore
CB1F 14	5.750	40,230	277.4	1.42	28.1	193.5	Open pore
CB1F 15	5.751	37,130	256.0	1.24	29.7	204.6	Subsurface pore
MEAN	5.741	34,400	237.1	1.19	28.5	196.9	

TABLE A19. FLEXURE TEST RESULTS FOR COORS TT-ZrO_2 (3% MgO)

Condition: Unexposed, As-Received
Test Temperature: 1000°C

SAMPLE	BULK DENSITY (GM/CC)	STRENGTH (PSI)	STRENGTH (MPA)	STRAIN-TO-FAILURE (IN/IN X 10E-3)	SECANT MODULUS (10E6 PSI)	SECANT MODULUS (GPA)	Fracture Origin
CB1F 16	5.730	17,040	117.5	0.74	22.9	158.1	Poorly sintered region of intergranular fracture
CB1F 17	5.752	33,150	228.6	1.49	22.0	151.8	Open pore
CB1F 18	5.753	22,930	158.1	1.04	21.7	149.9	Subsurface pore
CB1F 19	5.741	24,680	170.2	0.94	26.5	182.6	Subsurface pore
CB1F 20	5.734	20,880	144.0	0.84	24.6	169.3	Subsurface pore
MEAN	5.742	23,740	163.6	1.01	23.5	162.3	

TABLE A20. FLEXURE TEST RESULTS FOR COORS TT-ZrO_2 (3% MgO)

Condition: After 1000hr/1000°C Exposure
Test Temperature: 25°C

SAMPLE	BULK DENSITY (GM/CC)	STRENGTH (PSI)	(MPA)	STRAIN-TO-FAILURE (IN/IN X 10E-3)	SECANT MODULUS (10E6 PSI)	(GPA)	Fracture Origin
CB1F 21	5.744	24,040	165.8	0.96	25.1	173.0	Undetermined
CB1F 22	5.750	25,540	176.1	1.11	26.8	185.0	Subsurface pore
CB1F 23	5.744	25,490	175.8	1.06	27.0	185.8	Subsurface pore
CB1F 24	5.781	15,900	109.6	0.75	19.1	131.7	Subsurface pore
CB1F 25	5.773	14,710	101.4	0.82	18.3	126.0	Subsurface pore
MEAN	5.758	21,140	145.7	0.94	23.2	160.2	

REPORT DISTRIBUTION LIST

General Electric Company
Building 7, Advanced Energy
Program Department
P.O. Box 527
King of Prussia, PA 19406
Attn: J. A. Bledsoe
S. Musikant

Oak Ridge National Laboratory
Conservation & Advanced Systems
Programs
Metals and Ceramics Division
P.O. Box X
Oak Ridge, TN 37830
Attn: A. C. Schaffhauser

Department of Energy
FE-22
Germantown, MD 20545
Attn: John Fairbanks

Concept Analysis Corporation
9145 General Court
Plymouth, MI 48170
Attn: P. C. Glance

Department of Energy
MS 5E-091
Washington, DC 20585
Attn: J. J. Eberhardt

Aerospace Corporation
2350 East El Segundo Blvd.
El Segundo, CA 90009
Attn: W. U. Roessler

Allison Gas Turbine Operations
P.O. Box 420
Indianapolis, IN 46206-0420
Attn: D. L. Clingman-W5

Garrett Corporation
One First National Plaza
Suite 1900
Dayton, OH 45402
Attn: A. E. Hause

IIT Research Institute
10 W. 35th Street
Chicago, IL 60616
Attn: D. C. Larsen

United Technologies Research
Center
Silver Lane
East Hartford, CT 06108
Attn: G. S. Hausmann

Battelle Pacific N.W.
P.O. Box 999
Richland, WA 99352
Attn: Paul Koehnstead

Garrett Turbine Engine Company
P.O. Box 5217
Phoenix, AZ 85010
Attn: Jere Castor

Howmet Turbine Components Corp
1600 Warner Road
Whitehall, MI 49461
Attn: L. G. McCoy

Teledyne Continental
76 Getty Street
Muskegon, MI 49442
Attn: Richard Roy

Mueller Associates
1401 South Edgewood Street
Baltimore, MD 21227
Attn: T. Timbario

General Atomic Company
P.O. Box 81608
San Diego, CA 92138
Attn: F. Warner

John Deere and Company
John Deere Road
Moline, IL 61265
Attn: J. D. Spuller

October 1985

PAGE 246 INTENTIONALLY BLANK

Thermo Electron Corporation
101 First Avenue
Waltham, MA 02154
Attn: Mr. Michael Koplow

Mechanical Technology Inc.
968 Albany-Shaker Road
Latham, NY 12110
Attn: Wilbur Shapiro

Cummins Engine Company
P.O. Box 3005
Columbus, IN 47201
Attn: Michael Brands, 50165

International Harvester
10400 W.N. Avenue
Melrose Park, IL 60160
Attn: J. J. Egan

SKF Technology Services
SKF Industries, Inc.
P.O. Box 515
King of Prussia, PA 19406
Attn: P. A. Madden

Jet Propulsion Laboratory
4800 Oak Grove Drive
Pasadena, CA 91103
Attn: M. Dowty

Ford Motor Company
P.O. Box 2053
Dearborn, MI 48121
Attn: Wally Wade

GM Research Lab
Engine Research Department
Warren, MI 48090
Attn: Chuck Amann

E-F Tech. Assoc.
P.O. Box 189
St. Johns, MI 48879
Attn: R. R. Tison

Alex C. Alkidas
Staff Research Engineer
General Motors Research Labs
Warren, MI 48090-9055

Imperial Clevite, Inc.
Technical Library
Technology Center
540 E. 105th Street
Cleveland, OH 44108

Caterpillar Tractor Company
Research Department
Technical Center
Peoria, IL 61629
Attn: John M. Bailey

Eaton Corporation
Engine and Research Center
26201 Northwestern Highway
P.O. Box 766
Southfield, MI 48037
Attn: Richard Chute

Detroit Diesel Allison
13400 West Outer Drive
Detroit, MI 48228
Attn: R. B. Wallace

Perkins Engines, Inc.
24175 Research Drive
Farmington, MI 48024
Attn: Engineering Department

Richardo Consulting Engineers, Ltd
Bridge Works
Shoreham-by-Sea
Sussex
BN45FG
ENGLAND
Attn: Simon R. Norris-Jones

Energy Systems
Sundstrand Energy Systems
4747 Harrison Avenue
Rockford, IL 61101
Attn: D. Lacey

Army Materials and Mechanics
Research Center
Arsenal Street
Watertown, MA 02172
Attn: Dr. Robert N. Katz

Dr. Charles Church
HQDA (DAMA-ARA)
Washington, DC 20310

Detroit Diesel Allison
Speed Code RO3B
36880 Ecorse Road
Romulus, MI 48239-4001
Attn: Nabil Hakim

October 1985

GTE Laboratories Incorporated
40 Sylvan Road
Waltham, MA 02254
Attn: C. O. Dugger

Westinghouse Electric Corporation
R&D Center
1310 Beulah Road
Pittsburgh, PA 15235
Attn: D. J. Boes

Carborundum Company
P.O. Box 832
Niagara Falls, NY 14302
Attn: R. Storm

A. D. Little, Inc.
Acorn Park
Cambridge, MA 02140
Attn: R. G. Colello

Coors Porcelain Company
Director, Technical Operations
Golden, CO 80401
Attn: D. G. Wirth

PACCAR Inc.
Business Center Building
P.O. Box 1518
Bellevue, WA 98009
Attn: J. M. Dunn
Vice President

Freightliner Corporation
Research & Development
4747 N. Channel Avenue
P.O. Box 4849
Portland, OR 97208
Attn: R. Murphy, Director

Mack Trucks, Inc.
Engineering and Product
Box M
Allendale, PA 18105
Attn: W. M. May
Executive Vice President

TRW
One Space Park
Redondo Beach, CA 90278
Attn: J. W. Martin

Barber Nichols Engineering
6365 W. 55th Street
Arvada, CO 80002
Attn: R. Barber

Southwest Research Institute
Department of Material Sciences
Post Office Drawer 28570
6220 Culebra Drive
San Antonio, TX 78284
Attn: James Lankford

American Trucking Associations, Inc.
Engineering Department
1616 P Street NW
Washington, DC 20036
Attn: V. Suski

Battelle Pacific Northwest Laboratories
2030 M Street NW
Washington, DC 20036
Attn: J. C. Franke

Integral Technologies, Inc.
415 E. Plaza Drive
Westmont, IL 60559

Louis Peck and Associates
176 Congress Avenue
Rochester, NY 14611

Ramsey Corporation
1233 Manchester Road
Manchester, MO 63011
Attn: H. E. McCormick

Timoney Research Limited
Dublin Road, Trim Co.
Meath, Ireland
Attn: S. G. Timoney

October 1985

Adiabatics, Inc.
630 S. Mapleton
Columbus, IN 47201
Attn: R. Kamo, President

Massachusetts Institute of Tech.
Department of Mechanical Engrg.
Sloan Laboratory
Cambridge, MA 02139
Attn: Dr. J. Ekchian, Bldg 31

U.S. Army Tank Automotive Command
and Development Center
Warren, MI 48090
Attn: W. Brysik (DRSTA/RGED)

NASA
Lewis Research Center
21000 Brookpark Road
Cleveland, OH 44135
Attn: Report Control
M.S. 60-1

Library (2 copies)
M.S. 60-3

Patent Counsel
M.S. 60-2

M. Bailey, 77-6
H. Yacobucci, 77-6
J. Wood, 77-6
D. Evans, 77-6
R. Evans, 77-6
H. Sliney, 23-2
T. Strom, 77-6
W. Wintucky, 77-6
E. Willis, 77-6
W. Sanders, 49-3
G. Prok, 77-6
R. Barrows, 77-6
J. Ziemianski, 86-1
G. Reck, 86-1

NASA Headquarters
Washington, DC 20546
Attn: RJP/John Facey (5)

Department of Energy
CE-131-1000 Independence Ave., S.W.
Washington, DC 20585
Attn: S. Goguen(10)

NASA Scientific & Technical
Information Facility
P.O. Box 8757
Baltimore/Washington Intl. Airport
MD 21240
Attn: Accessioning Department (25)

David Dimick
Advanced Product Engineering
GM Technical Center
Warren, MI 48090

Dr. Michael Dubeck
Ethyl Corporation
451 Florida Street
Baton Rouge, LA 70801

Argonne National Laboratory
9700 South Cass Avenue
Argonne, IL 60439
Attn: Robert Holtz
CT-331

White Engines, Inc.
Attn: Enrico J. Caruso
Vice President, Engineering
Canton, OH 44707

Adapco
Analysis & Design
Application Co., Ltd
60 Broadhollow Road
Melville, NY 11747
Attn: P. S. MacDonald
President

October 1985

D. Groghan
NAVSEA
1000 Jefferson Davis Highway
Washington, DC 20007

David Mann
ARO
P. O. Box 12211
Research Triangle Park, NC 27709

Dr. Michal Dyer
Combustion Applications Division
Sandia National Laboratories
Livermore, CA 94550

Mr. Frank Crotelli
U.S. Maritime Administration
Room 7330, Code MAR-760
400 7th. Street, SW
Washington, DC 20590

Mr. James McCandless
Kohler Company
Kohler, WI 53044

Mr. Ronald Graves
P. O. Box Y
Building 9108
Oak Ridge National Laboratory
Oak Ridge, TN 37831

Mr. Ralph McGill
P. O. Box Y
Building 9108
Oak Ridge National Laboratory
Oak Ridge, TN 37831

Mr. Larry K. Carpenter
Morgantown Energy Technology Center
P. O. Box 880
Morgantown, WV 26505

Ms. Terry M. Levinson
DOE
Mail Stop 5E-052
Washington, DC 20585

Mr. Marvin Gunn
Energy Systems Research, ECUT
DOE
Mail Stop 5E-052
Washington, DC 20585

Mr. L. B. Mann
Chrysler Corporation
P. O. Box 1118
Detroit, MI 48288

Mr. N. Richard Dunteman
Electromotive Division
General Motors Corporation
La Grange, IL 60525

Dr. Warren E. Snyder
Waukesha Engine Division
Dresser Industries
P.O. Box 379
Waukesha, WI 53167

Dr. K. Subramanian
Norton Company
1 New Bond Street
Worcester, MA 01606

Sverdrup Technology, Inc.
P. O. Box 30650 Midpark Branch
Middleburg Heights, OH 44130
Attn: R. G. Ragsdale

Dr. Roy Rice
W. R. Grace and Company
7379 Route 32
Columbia, MD 21044

Dr. Max Bentele
XAMAG, Inc.
259 Melville Avenue
Fairfield, CT 06430

October 1985

SUPPLEMENTAL DISTRIBUTION LIST

Mr. John M. Bailey
Research Department
Technical Center
Caterpillar Tractor Co.
Peoria, IL 61629

Dr. Paul F. Becher
Oak Ridge Natl. Laboratory
Metals & Ceramics Div.
P. O. Box X
Oak Ridge, TN 37831

Dr. Paul Becker
Allied Automotive Tech Ctr.
900 W. Maple
Troy, MI 48083

Dr. Paul N. Blumberg
Integral Technologies, Inc.
415 E. Plaza Drive
Westmont, IL 60559

Mr. Edward J. Borto
U.S. Army Tank-Automotive Command
Attn: AMSTA-RCKM
Warren, MI 48090

Dr. Richard Bradt
University of Washington
318 Roberts Hall, FB-10
Seattle, WA 98195

Mr. Terrence K. Brog
University of Michigan
Dow Building
Ann Arbor, MI 48109

Dr. Bernard J. Busovne, Jr.
AC Spark Plug Division
General Motors Corporation
1300 N. Dort Highway
Flint, MI 48556

Dr. W. Roger Cannon
Department of Ceramics
College of Engineering
Rutgers University
P.O. Box 909
Piscataway, NJ 08854

Dr. Jenn Chang
G. M. Corporation
Allison Gas Turbine Div.
P. O. Box 420
Speed Code W5
Indianapolis, IN 46206-0420

Professor I-Wei Chen
Rm. 13-5118
Massachusetts Institute of Technology
Cambridge, MA 02139

Dr. David R. Clarke
IBM Corporation
Thomas J. Watson Research Center
P.O. Box 218
Yorktown Heights, NY 10598

Mr. Raymond A. Cutler
Ceramatec, Inc.
163 W. 1700 S.
Salt Lake City, UT 84115

Dr. A. G. Evans
Materials Services Engineering Dept.
Hearst Mining Building
University of California/Berkeley
Berkeley, CA 94720

Dr. K. T. Faber
Ceramic Engineering Department
Ohio State University
2041 College Road
Columbus, OH 43210

Dr. James Floyd, President
American Feldmuehle Corporation
Box 2090
Hendersonville, NC 28739

Mr. F. D. Gac
Los Alamos National Laboratory
Los Alamos, NM 87545

Mr. George Gazza
Army Materials & Mechanics Res. Ctr.
Attn: AMXMR-MCS
Watertown, MA 02172

PAGE 252 INTENTIONALLY BLANK

Dr. Donald L. Guile
Ceramics Research
Corning Glass Works
Sullivan Park
Corning, NY 14831

Mr. M. D. Gurney
IIT Research Institute/NIPER
Post Office Box 2128
Bartlesville, OK 74005

Dr. D.P.H. Hasselman
Virginia Polytechnic Institute
and State University
Dept. of Materials Engineering
Blacksburg, VA 24061

Dr. Norman L. Hecht
University of Dayton Research Inst.
300 College Park
Dayton, OH 45469-0001

Dr. Peter W. Heitman
Detroit Diesel Allison Div.
General Motors Corp.
P.O. Box 894
Mail Stop W-5
Indianpolis, IN 46206

Prof. Arthur H. Heuer
Dept. Metallurgy and Materials Science
Case Western Reserve University
500 White Building
Cleveland, OH 44106

Dr. Thomas V. Hynes
Army Materials & Mechanics Res. Ctr.
Attn: AMXMR-OC
Watertown, MA 02172

Dr. Robert P. Ingel
U.S. Naval Research Laboratory
Code 6360
Washington, D.C. 20375

Dr. Herb Johns
Zircoa Products
Division of Corning Glass Works
Ceramic Products Division
31501 Solon Road
Solon, OH 44139

Dr. D. R. Johnson
Oak Ridge National Laboratory
P. O. Box X
Building 4508, M/S 113
Oak Ridge, TN 37831

Dr. Robert Katz
Army Materials & Mechanics Res. Ctr
Attn: AMXMR-MC
Watertown, MA 02172

Dr. Frederick L. Kennard
AC Spark Plug Division
General Motors Corporation
1300 N. Dort Highway
Flint, MI 48556

Mr. M. R. Kibbe
Molycorp, Inc.
709 Westchester Avenue
White Plains, NY 10604

Dr. E. H. Kraft
Kyocera International, Inc.
8611 Balboa Avenue
San Diego, CA 92123

Ms. Sarah M. Kunz
Sohio Chemicals & Ind. Prod. Co.
(Carborundum)
P. O. Box 832
Niagara Falls, NY 14302

Mr. Richard B. Lancashire
NASA-Lewis Research Center
21000 Brookpark Road
Cleveland, OH 44135

Dr. Brian Lawn
National Bureau of Standards
Physical Properties Section
Washington, DC 20234

Dr. David Lewis
U.S. Naval Research Laboratory
Code 6360
Washington, D.C. 20375

Dr. Winston W. Liang
Advanced Industrial Materials
and Components
Gas Research Institute
8600 West Bryn Mawr Avenue
Chicago, IL 60631

Ms. Laura J. Lindberg
Garrett Turbine Engine Co.
111 South 34th Street
P. O. Box 5217
Phoenix, AZ 85010

Dr. David Marshall
Rockwell International Science Center
1049 Camino Dos Rios
Thousand Oaks, CA 91360

Mr. Keith Matsuhiro
Technical Service
Automotive Ceramics
NGK-LOCKE, Inc.
3000 Town Center, Suite 1140
Southfield, MI 48075

Mr. A. F. McLean
Ford Motor Co.
P. O. Box 2053
Dearborn, MI 48121-2053

Mr. Carl H. McMurtry
Sohio Chemicals & Ind. Prod. Co.
(Carborundum)
P. O. Box 832
Niagara Falls, NY 14302

Dr. Robert M. McNally
Research Manager
Corning Glass Works
Sullivan Park
Painted Post, NY 14870

Dr. Jack Mecholsky
Pennsylvania State University
Applied Research Laboratory
P.O. Box 30
State College, PA 16801

Dr. Terry Mitchell
Case Western Reserve University
10900 Euclid Ave.
Cleveland, OH 44106

Mr. A. J. Moorhead
Metals and Ceramics Division
Oak Ridge National Laboratory
Oak Ridge, TN 37830

Mr. Michael E. Moynihan
Teledyne Continental Motors
General Products Division
76 Getty Street
Muskegon, MI 49442

Dr. Solomon Musikant
General Electric
Space Systems Division
Valley Forge Space Center
P. O. Box 8555
Philadelphia, PA 19101

Mr. Jeffrey Neil
GTE Laboratories, Inc.
40 Sylvan Road
Waltham, MA 02254

Mr. Richard C. Novak
M.S. 22
UTRC
East Hartford, CT 06108

Mr. R. J. Palicka
General Manager
Ceradyne, Inc.
3030-A South Red Hill Ave.
Santa Ana, CA 92705

Dr. James Patten
Cummins Engine Co.
Mail Code 50183
Box 3005
Columbus, IN 47202

Dr. Arvid Pasto
GTE Laboratories, Inc.
40 Sylvan Road
Waltham, MA 02254

Mr. David B. Quinn
G.M. Corporation
AC Spark Plug Division
1300 N. Dort Highway
Flint, MI 48556

Mr. George Quinn
Army Materials & Mechanics Res. Ctr.
Attn: AMXMR-MCP
Watertown, MA 02172

Mr. David Reed
Ceradyne, Inc.
43 Hopkinton Road
Westborough, MA 01581

Dr. Paul Rempes/Mr. R. Insley
Ceramic Division
Champion Spark Plug Company
20000 Conner Avenue
Detroit, MI 48234

Dr. Seong Rhee
Allied Automotive Tech. Center
900 West Maple
Troy, MI 48083

Mr. R. W. Rice
W. R. Grace & Company
7379 Route 32
Collumbia, MD 21044

Dr. Giulio A. Rossi
Norton Co.
HPC, R&D #5
1 New Bond St.
Worcester, MA 01606

Dr. Robert Ruh, AFWAL/MLLM
Air Force Materials Laboratory
Wright Aeronautical Laboratories
Wright-Patterson AFB, OH 45433

Dr. Arthur L. Ruoff
Director, Dept. of Materials Science
Cornell University
Ithaca, NY 14850

Dr. Liselotte J. Schioler
Department 9990
Aerojet Tech Systems Co.
P.O. Box 13222
Sacramento, CA 95813

Dr. Matt Schreiner
Mechanical Technology, Inc.
968 Albany Shaker Road
Latham, NY 12110

Mr. Robert B. Schulz
U.S. Department of Energy
Forrestal Bldg., CE-131
Washington, D.C. 20585

Mr. Brian Seegmiller
Coors Porcelain Co.
600 9th Street
Golden, CO 80401

Mr. J. Sisson
Howmet Corporation
1600 S. Warner Road
Whitehall, MI 49461

Mr. Michael Slavin
Army Materials & Mechanics Res. Ctr
Attn: AMXMR-MCP
Watertown, MA 02172

Dr. M. Srinivasan
Materials Characterization
Engineered Materials Sector
SOHIO R&D Center
P.O. Box 832
Niagara Falls, NY 14302

Mr. Gordon Starr
Cummins Engine Co.
Box 3005
Columbus, IN 47202-3005

Mr. Patrick Stephan
Norton Co.
High Performance Ceramics
1 New Bond St.
Worcester, MA 01606

Mr. Harold L. Stocker
G.M. Corporation
Allison Gas Turbine Div.
P. O. Box 420
Indianapolis, IN 46206

Mr. Thomas N. Strom
NASA-Lewis Research Center
21000 Brookpark Road
Cleveland, OH 44135

Dr. V. J. Tennery
Oak Ridge Natl. Laboratory
P. O. Box X
Oak Ridge, TN 37831

Dr. T. Y. Tien
University of Michigan
Dow Building
1500 Hayward Street
Ann Arbor, MI 48109

Dr. Nancy J. Tighe
National Bureau of Standards
Institute for Materials Science
Gaithersburg, MD 20899

Dr. Maurice L. Torti
Norton Co.
1 New Bond Street
Worcester, MA 01606

Mr. Frank T. Traceski
Army Materials & Mechanics Res. Ctr.
Attn: AMXMR-SMS
Watertown, MA 02172

Mr. Rudy Vallee
Nilcra Ceramics (U.S.A.) Inc.
St. Charles Business Park
3755 East Main Street, Suite 120
St. Charles, IL 60174-2496

Dr. Thomas Vasilos
AVCO Systems Division
201 Lowell Street
Wilmington, MA 01887

Dr. Jay S. Wallace
University of Michigan
Dow Building
1500 Hayward Street
Ann Arbor, MI 48109

Dr. Dale E. Wittmer
GTE Products Corporation
Hawes Street
Towanda, PA 18848

Mr. Tom Yonushonis
Cummins Engine Co.
Mail Code 50183
Box 3005
Columbus, IN 47202

Dr. Takaki Masaki
Technical Development Dept.
Toray Industries Inc.
2-2, 3-chome Sonoyama
Otsu Shiga, 520, JAPAN

Dr. Shigeyuki Somiya, Director
Laboratory for Advanced Ceramics
Tokyo Institute of Technology
4259 Nagatsuta
Midori-ku
Yokohama, 227, JAPAN

Dr. Isao Oda, General Manager
Materials Research Laboratory
NGK R&D Laboratories
NGK Insulators, Ltd.
2-56 Suda-cho Mizuho-ku
Nagoya, 467, JAPAN

Dr. P. Morrell
University of Manchester
Metallurgy Building
Grosvenor Street
Manchester, M1 7HS
United Kingdom

Asahi Glass Company, Ltd.
1-2, Marunouchi, 2-chome
Chiyoda-ku
Tokyo, JAPAN

D. T. Ochiai, Manager
Technical Development Dept.
Metal Products Division
Toshiba Corporation
Yokohama Metal Works
No. 8 Shinsugitacho, Isogo-ku
Yokohama, 235, JAPAN

Dr. Keisuke Kobayashi
Toray Industries, Inc.
3-chome Sonoyama
Otsu, Shiga 520, JAPAN

Dr. Nils E. Claussen
Max-Planck Institute
Heisenbergstrasse 5
D-7000 Stuttgart 80
FEDERAL REPUBLIC OF GERMANY

Dr. Chris Knapp
Norton Company
8001 Daly Street
Niagara Falls, Ontario, CANADA

Y. Hamano, Dr. Eng.
Managing Dir./General Manager
Central Research Laboratory
Kyocera Corporation
1-4 Yamashita-cho Kokubu
Kagoshima, 899-43, JAPAN

Dr. Michael Swain
CSIRO
Division of Material Science
Box 4331, G.P.O
Melbourne, Vic. 3001, AUSTRALIA

Dr. Hiroshige Suzuki
Emeritus Professor
Tokyo Institute of Technology
2-39-9, Kitasenzoku, Ota-ku
Tokyo, 145, JAPAN

Dr. Ing. Dieter Fingerle
Manager, Automotive Ceramic
Research and Development
Feldmuhle Aktiengesellschaft
Fabrikstrasse 23-29
7310 Plochigen
FEDERAL REPUBLIC OF GERMANY